

ISSN 0914-9244
CODEN JSTEEW

Journal of
Photopolymer
Science and Technology
Volume 34 Number 1

2021

JOURNAL OF PHOTOPOLYMER SCIENCE AND TECHNOLOGY

Home Page <http://www.spst-photopolymer.org>
<https://www.jstage.jst.go.jp/browse/photopolymer>

Journal of Photopolymer Science and Technology publishes papers on the scientific progress and the technical development of photopolymers.

Editorial Board

Editor-in-Chief and Founding Editor:

Minoru TSUDA, *SPST & Chiba University*

Editors:

Masayuki ENDO, *Osaka University*

Yoshihiko HIRAI, *Osaka Prefecture University*

Taku HIRAYAMA, *Hoya Co., Ltd.*

Hideo HORIBE, *Osaka City University*

Takanori ICHIKI, *University of Tokyo*

Masaaki KAKIMOTO, *Tokyo Institute of Technology*

Takashi KARATSU, *Chiba University*

Masayuki KUZUYA, *Chubu Gakuin University*

Seiji NAGAHARA, *Tokyo Electron Ltd.*

Editor-in-Chief:

Hiroyuki MAYAMA, *Asahikawa Medical University*

Tomoki NAGAI, *JSR Corporation*

Tomoki NISHINO, *Ritsumeikan University*

Haruyuki OKAMURA, *Osaka Prefecture University*

Itaru OSAKA, *Hiroshima University*

Shu SEKI, *Kyoto University*

Atsushi SEKIGUCHI, *Litho Tech Japan Corporation*

Takumi UENO, *Shinshu University*

Takeo WATANABE, *University of Hyogo*

Masashi YAMAMOTO, *Nat. Inst. Tech. Kagawa College*

International Advisory Board

Robert D. ALLEN, *IBM Almaden Research Center*

Paul F. NEALEY, *University of Chicago*

C. Grant WILLSON, *The University of Texas*

Ralph R. DAMMEL, *EMD Performance Materials*

Christopher K. OBER, *Cornell University*

The Editorial Office

Assoc. Prof. Hiroyuki MAYAMA

Department of Chemistry, Asahikawa Medical University, 2-1-1-1 Midorigaoka-Higashi, Asahikawa, Hokkaido 078-8510, Japan.

FAX: +81-166-68-2782, e-mail: mayama@asahikawa-med.ac.jp

Information for Contributors

Submit Manuscripts to the SPST Homepage (Journal --> Submission of Papers --> Editorial Manager). Submission is a representation that the manuscript has not been published previously elsewhere. The manuscript should be accompanied by a statement transferring copyright from the authors (or their employers-whoever holds the copyright) to the Society of Photopolymer Science and Technology. A suitable form for copyright transfer is available from the SPST Homepage. This written transfer of copyright, which previously was assumed to be implicit in the act of submitting a manuscript, is necessary under the Japan copyright law. Further information may be obtained from the "Manual for Manuscript Writing" at the SPST Homepage.

Proofs and All Correspondence: Concerning papers in the process of publication should be addressed to the Editorial Office.

Manuscript Preparation: All the papers submitted are reproduced electronically as they were. For this reason, the manuscripts should be prepared according to

the Manual for Manuscript Writings shown at the SPST Homepage.

Subscription Price (Airmail Postage included):

¥12,000 (in Japan), US\$ 150.00 (for Foreign)

Subscriptions, renewals, and address changes should be addressed to the Editorial Office. For the address changes, please send both old and new addresses and, if possible, include a mailing label from the wrapper of recent issue. Requests from subscribers for missing journal issues will be honored without charge only if received within six months of the issue's actual date of publication; otherwise, the issue may be purchased at the single-copy price.

Publication Charge (Reprint Order): To support a part of the cost of publication of journal pages, the author's institution is requested to pay a page charge of ¥3,000 per page (with a one-page minimum) and an article charge of ¥12,000 per article. The page charge (if honored) entitles the author to 50 free reprints. For Errata the minimum page charge is ¥3,000, with no articles charge and no free reprints.

JOURNAL
OF
PHOTOPOLYMER
SCIENCE
AND
TECHNOLOGY

Volume 34 Number 1

2021

Published by

THE SOCIETY OF PHOTOPOLYMER SCIENCE AND TECHNOLOGY

THE SOCIETY OF PHOTOPOLYMER SCIENCE AND TECHNOLOGY (SPST)

<http://www.spst-photopolymer.org>

President:

Minoru TSUDA
SPST & Chiba University

Director of Publication:

Hiroyuki MAYAMA
Asahikawa Meical University

Director of Scientific Program:

Masayuki ENDO
Osaka University

Director of International Affairs:

Takeo WATANABE
University of Hyogo

Director of Administration:

Takashi KARATSU
Chiba University

Office of the Administration

c/o Prof. Takashi KARATSU
*Department of Applied Chemistry
and Biotechnology,
Chiba University
1-33 Yayoi-cho, Inage-ku,
Chiba 263-8522, Japan
Phone: +81-43-290-3366
Fax +81-43-290-3401
e-mail:office@spst-photopolymer.org*

THE SPST REPRESENTATIVES 2021

Robert ALLEN, *IBM*

Tsukasa AZUMA, *Toshiba Co., Ltd.*

Teruaki HAYAKAWA, *Tokyo Institute of Technology*

Takashi HIRANO, *Sumitomo Bakelite Co., Ltd.*

Hideo HORIBE, *Osaka City University*

Masaaki KAKIMOTO, *Tokyo Institute of Technology*

Yoshio KAWAI, *Shin-Etsu Chemical Co., Ltd.*

Hiroto KUDO, *Kansai University*

Jun MIZUNO, *Waseda University*

Tomoki NAGAI, *JSR Corporation*

Hideo OHKITA, *Kyoto University*

Hiroaki OIZUMI, *Gigaphoton Inc.*

Itaru OSAKA, *Hiroshima University*

Atsushi SEKIGUCHI, *Litho Tech Japan Corporation*

Akinori SHIBUYA, *Fuji Film, Co., Ltd.*

Kuniharu TAKEI, *Osaka Prefecture University*

Minoru TSUDA, *SPST & Chiba University*

Takeo WATANABE, *University of Hyogo*

Takashi YAMASHITA, *Tokyo University of Technology*

Hitoshi ARAKI, *Toray Co., Ltd.*

Masayuki ENDO, *Osaka University*

Yoshihiko HIRAI, *Osaka Prefecture University*

Taku HIRAYAMA, *Hoya Co., Ltd.*

Takanori ICHIKI, *University of Tokyo*

Takashi KARATSU, *Chiba University*

Shin-ichi KONDO, *Gifu Pharmaceutical University*

Masayuki KUZUYA, *Chubu Gakuin University*

Seiji NAGAHARA, *Tokyo Electron Ltd.*

Tomoki NISHINO, *Ritsumeikan University*

Yasunobu OHNISHI, *University of Tokyo*

Haruyuki OKAMURA, *Osaka Prefecture University*

Shu SEKI, *Kyoto University*

Takehiro SESHIMO, *Tokyo Ohka Co., Ltd.*

Kohei SOGA, *Tokyo University of Science*

Jun TANIGUCHI, *Tokyo University of Science*

Takumi UENO, *Shinshu University*

Shinji YAMAKAWA, *University of Hyogo*

Wang YUEH, *Intel*

Notice about photocopying

Prior to photocopying any work in this publication, the permission is required from the following organization which has been delegated for copyright clearance by the copying owner of this publication.

- In the USA

Copying Clearance Center Inc.

222 Rosewood Drive, Danvers MA 01923, USA

Tel: 1-978-750-8400, Fax: 1-978-750-4744, e-mail: info@copyright.com

<http://www.copyright.com>

- Except in the USA

Japan Academic Association for Copyright Clearance (JAACC)

9-6-41 Akasaka, Minato-ku, Tokyo 107-0052, Japan

Tel: 81-3-3475-5618, Fax: 81-3-3475-5619, e-mail: info@jaacc.jp

<http://www.jaacc.org>

Experimental Evaluation and Modeling of Adsorption Phenomena of Nanoliposomes on Poly(dimethylsiloxane) Surfaces

Sylvan Sunny Koyagura¹, Virendra Majarikar¹, Hiroaki Takehara^{1,2*},
and Takanori Ichiki^{1,2**}

¹ Department of Materials Engineering, School of Engineering, The University of Tokyo,
7-3-1 Hongo, Bunkyo-ku, Tokyo 113-8656, Japan

² Innovation Center of NanoMedicine (iCONM), 3-25-14 Tonomachi, Kawasaki,
Kanagawa 210-0821, Japan

*takehara@bionano.t.u-tokyo.ac.jp

**ichiki@bionano.t.u-tokyo.ac.jp

Nanoparticles, such as exosomes or liposomes, have been widely studied using poly(dimethylsiloxane) (PDMS) microchannels. The interaction between nanoparticles and solid surfaces is an important subject for basic and applied research on nanoparticles, but there have been few reports on the use of microchannels for this purpose. Micro-scale systems serve as a useful platform for adsorption analysis because of their large surface-to-volume ratio. In this study, we attempted to develop a platform to study the adsorption phenomena of nanoparticles on solid surfaces using a microchannel, in which a model that analyzes dynamic (i.e., non-equilibrium) adsorption was used. This model allowed quantitative analysis of nanoliposome adsorption onto the surface of a PDMS microchannel.

Keywords: Solid surface adsorption, Analytical model, Non-equilibrium adsorption, nanoliposome, PDMS microchannel

1. Introduction

Nanoparticles (NPs) such as exosomes and liposomes have been examined for their biomedical applications [1, 2], using poly(dimethylsiloxane) (PDMS) microchannels as a platform for analysis [3–5]. In the analysis, NPs can be characterized to obtain properties such as size and zeta potential, which provide important details for future applications [6–10].

Another property that is important for understanding the behavior of NPs is their interaction with solid surfaces [11]. Adsorption phenomena are crucial in many applications and studies involving NPs [12]. Moreover, adsorption depends on the properties of both NPs and solid surfaces; accordingly, there are different types of interactions, such as hydrophobic or electrostatic interactions [13, 14].

For adsorption analysis, a microchannel is a

suitable setup as it is a micro-scale system that has a higher surface-to-volume ratio (S/V ratio) compared with macro-scale systems, which allows adsorption to be more easily observed [15, 16].

Quantitative analysis of the adsorption experiment data can be performed to understand the interactions between NPs and solid surfaces. Conventionally, adsorption models such as the Freundlich isotherm or Langmuir isotherm have been used to quantitatively measure the adsorption phenomena of particles [17–19]. These prove to be accurate in describing the rate of particle adsorption and are highly useful in applications involving the adsorption of NPs [20, 21]. However, one drawback is that these models typically require a longer observation time (such as one or two hours) to observe the NPs adsorb onto the adsorbents until an equilibrium state is reached. Moreover, multiple experiments with different initial NP concentrations

are required to gather a range of data points to accurately measure the adsorption rate of these NPs, which involves expending more time.

In this study, we attempted to establish a platform for analyzing the adsorption of NPs on solid surfaces using a microchannel setup. The adsorption of nanoliposomes observed under light-sheet illumination was quantitatively analyzed using the experimental data reported in our previous study [13]. An adsorption model was developed to analyze the transient adsorption phase of the nanoliposomes on the PDMS surface under a shorter observation time. The functionality of this model was compared with that of traditional adsorption models.

2. Experimental

The nanoliposomes were prepared using the thin-film hydration method [10, 13]. An appropriate molar ratio of lipids and cholesterol was dissolved in chloroform and the lipid film was deposited on a vial by evaporating the solvent. Subsequently, the lipid film was hydrated with PBS buffer with pH 7.4 for 24 h and original liposomes were prepared. Prior to performing adsorption experiments, the original liposomes were extruded through a polycarbonate membrane with 100 nm pore size using an Avanti® mini-extruder to form nanoliposomes with around 100 nm in diameter. Three different liposomes were prepared using 1,2-dilauroyl-sn-glycero-3-phosphocholine (DLPC), 1,2-di-O-octadecenyl-3-trimethylammonium propane (chloride salt) (DOTMA), and L- α -phosphatidylserine (Brain, Porcine) (sodium salt) (PS). The molar ratios were DLPC and cholesterol at 4:1 for the DLPC liposomes, DOTMA and cholesterol at 1:1 for the DOTMA liposomes, and DLPC, PS, and cholesterol at 5.55:0.45:4 for the PS liposomes. The measured average size of DLPC, DOTMA, and PS nanoliposomes were 117.0 nm, 117.3 nm, and 111.7 nm, whereas the polydispersity indexes were 0.10, 0.08, and 0.08, respectively. The adsorption data of three different nanoliposomes in microchannels (200 μm width, 200 μm height, and 10 mm length,) were obtained from light-sheet illumination [13]. All three nanoliposomes were found to have particle numbers in the region of interest (ROI). DLPC and DOTMA nanoliposomes adsorbed onto the PDMS surface, while PS nanoliposomes were adsorbed onto the polyethylenimine (PEI)-coated PDMS surface. A calibration curve to convert particle number in ROI (particles) into concentration (particles/mL) was obtained using polystyrene

nanobeads (NIST particle size standard, 100 nm). Using the calibration curve (Fig. 1), the particle number in ROI was correlated with the particle concentration in the bulk sample.

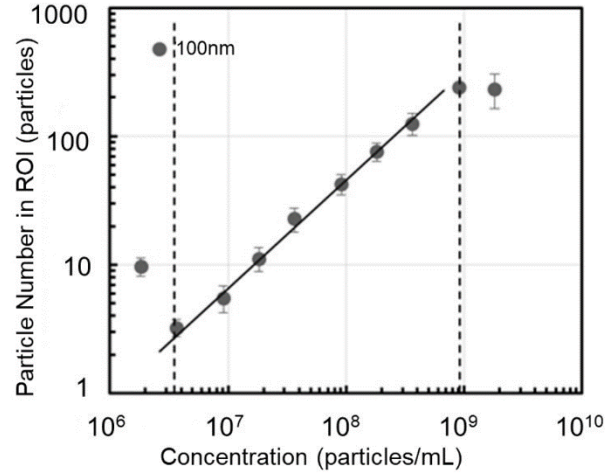


Fig. 1. Calibration curve used to convert particles in ROI, obtained by light-sheet illumination, into particle concentration.

3. Model

The adsorption data [13] decreased exponentially, and therefore, to set up the adsorption model, we analyzed the mass transfer of nanoliposomes as the concentration decays over time. This is similar to the integrated first-order rate law as shown in Equation 1 [22].

$$\frac{dC}{dt} = -kC \quad (1)$$

Where C is the concentration of nanoliposomes (particles/mL), t is the time (min), and k is the rate constant (min^{-1}). Equation 1 can be rearranged and integrated using the following conditions: when $t = 0$ min, $C = C_0$, and when $t = t$, $C = C_t$, to give Equation 2.

$$\int_{C_0}^{C_t} \frac{dC}{C} = \int_0^t -k dt \quad (2)$$

which gives Equation 3:

$$\ln\left(\frac{C_t}{C_0}\right) = -kt. \quad (3)$$

By taking the exponential and rearranging, we can obtain the final exponential decay Equation 4 as follows:

$$C_t = C_0 e^{-kt}. \quad (4)$$

Additionally, we can obtain the time constant τ (min) using Equation 5:

$$\tau = \frac{1}{k} \quad (5)$$

The values of τ and k provide key details of the nanoliposome properties and their interactions with the surface of the PDMS microchannel. Owing to their different properties, each nanoliposome has different types of interactions with the PDMS surface. Accordingly, the values of τ and k can quantitatively describe these interactions. Equation 4 was used to obtain the values of τ and k by fitting to the adsorption data.

4. Results and discussion

4.1. Quantitative analysis

The data obtained in the form of particles in the ROI [13] were converted to concentration (particles/mL) using the calibration curve shown in Fig.1. Accordingly, the calibrated data were plotted in Figs. 2, 3, and 4.

Based on the data from Figs. 2, 3, and 4, it was determined that as the particle number in the ROI decreased, the corresponding particle concentration also decreased by approximately 52% to 75%, depending on the type of nanoliposome. This large decrease in particle concentration over time implied that adsorption of the particles likely occurs not only in the ROI, but also in the bulk solution, such that fewer particles are observed in the microchannel.

Next, Equation 4 was rearranged, and the natural logarithm was used to find k , where C_0 is the concentration at the initial time of 4 min, C_t is the

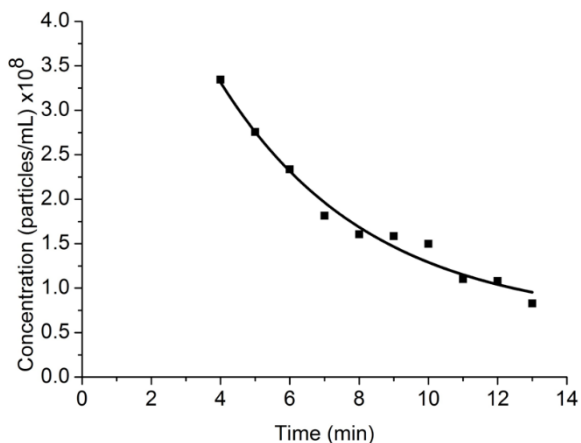


Fig. 2. Adsorption curve of DLPC nanoliposomes onto PDMS microchannel surface over time. The adsorption data was fitted using Equation 4.

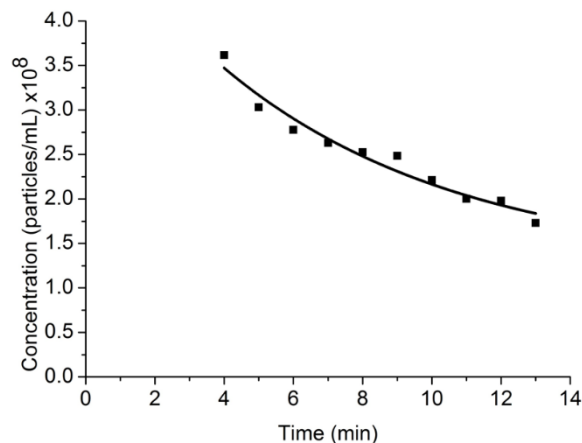


Fig. 3. Adsorption curve of DOTMA nanoliposomes onto PDMS microchannel surface over time. The adsorption data was fitted using Equation 4.

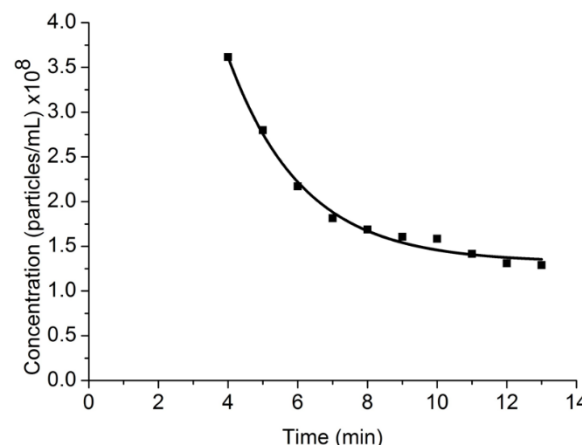


Fig. 4. Adsorption curve of PS nanoliposomes onto PEI coated PDMS microchannel surface over time. The adsorption data was fitted using Equation 4.

concentration at the final time of 13 min, and t is the difference between the initial and final time which is 9 min. Subsequently, Equation 5 was used to determine τ . The results of these calculations are provided in Table 1.

Table 1. k and τ calculated for each nanoliposome analyzed.

Nanoliposome	k (min^{-1})	τ (min)
DLPC	0.155	6.45
DOTMA	0.0820	12.2
PS	0.115	8.72

DLPC nanoliposomes had the highest k value, which means that it had the fastest adsorption rate, implying that the interaction between DLPC nanoliposomes and the PDMS surface is the

strongest, when compared to the other two types of nanoliposomes. In addition, the τ value for DLPC nanoliposomes was the lowest, further indicating that it had the fastest adsorption rate and that a larger percentage of nanoliposomes were adsorbed onto the surface, compared to the other nanoliposomes. It is known that DLPC nanoliposomes have hydrophobic interactions with the PDMS surface, while DOTMA and PS nanoliposomes have electrostatic interactions [13]. Therefore, based on the analysis, it was determined that hydrophobic interactions have a stronger effect on the adsorption of nanoliposomes on the surface of PDMS, when compared with electrostatic interactions.

4.2. Other adsorption models

Traditionally, adsorption models such as the linear model, Freundlich isotherm, and Langmuir isotherm are widely used for adsorption analysis [18]. By analyzing the data gathered from repeated adsorption experiments, the equilibrium concentrations from different initial concentrations can be obtained. Accordingly, these models can be used to identify key parameters that help to quantitatively describe the observed adsorption phenomena. However, these adsorption experiments require an adsorption equilibrium state that has to be reached, and accordingly, the observation times are long (one or two hours). Moreover, several experiments need to be carried out so that sufficient data is available to generate an adsorption curve, which increases the overall time and resources required.

Adsorption analysis in the transient phase is possible using the proposed model described in this paper, which allows for quicker analysis and requires less time and resources. By calculating k and τ values, we obtained parameters that can inform us about the adsorption capabilities of nanoparticles onto a solid surface.

5. Conclusion

With the use of a PDMS microchannel, a platform to analyze the adsorption of NPs on a solid surface was developed. In this study, an adsorption model using the exponential decay equation to find parameters such as the k and τ values was set up and used to quantitatively analyze the non-equilibrium adsorption of nanoliposomes in a PDMS microchannel. The DLPC nanoliposomes had the highest adsorption rate with a k value of 0.155 min^{-1} and a τ value of 6.45 min. This implied that the hydrophobic interactions between the DLPC

nanoliposomes and the PDMS surface were stronger than the electrostatic interactions between the other nanoliposomes and PDMS surface. The proposed model can be used for quicker adsorption experiments to quantitatively describe the adsorption of nanoparticles onto a solid surface, in comparison with traditional adsorption models, which require a greater time investment.

Acknowledgement

This research was supported by the Center of Innovation Program (COI STREAM), from the Japan Science and Technology Agency (JST).

References

1. G. Bozzuto and A. Molinari, *Int. J. Nanomedicine*, **10** (2015), 975.
2. Y. Zhou, Z. Ma, M. Tayebi, and Y. Ai, *Anal. Chem.*, **91** (2019) 4577.
3. K. Mogi, K. Hayashida, and T. Yamamoto, *Anal. Sci.*, **34** (2018) 875.
4. M. He and Y. Zeng, *J. Lab. Autom.*, **21** (2016) 599.
5. G. Li, W. Tang, and F. Yang, *Biotechnol. J.*, **15** (2020) 1900225.
6. H. Deschout, K. Raemdonck, S. Stremersch, P. Maoddi, G. Mernier, P. Renaud, S. Jiguet, A. Hendrix, M. Bracke, R. V. den Broecke, M. Rödning, M. Rudemo, J. Demeester, S. C. De Smedt, F. Strubbe, K. Neyts, and K. Braeckmans, *Nanoscale*, **6** (2014) 1741.
7. S. S. Koyagura, H. Takehara, and T. Ichiki, *J. Photopolym. Sci. Technol.*, **33** (2020) 485.
8. K. Kato, M. Kobayashi, N. Hanamura, T. Akagi, N. Kosaka, T. Ochiya, and T. Ichiki, *Jpn. J. Appl. Phys.*, **52** (2013) 06GK10.
9. V. Majarikar, H. Takehara, and T. Ichiki, *Microfluid. Nanofluidics*, **22** (2018) 110.
10. K. Kato, M. Koido, M. Kobayashi, T. Akagi, and T. Ichiki, *Electrophoresis*, **34** (2013) 1212.
11. R. Chen, Y. Zhang, F. D. Sahneh, C. M. Scoglio, W. Wohlleben, A. Haase, N. A. Monteiro-Riviere, and J. E Riviere, *ACS Nano*, **8** (2014), 9446.
12. A. Verma and F. Stellacci, *small*, **6** (2010), 12.
13. V. Majarikar, H. Takehara, and T. Ichiki, *J. Photopolym. Sci. Technol.*, **32** (2019) 107.
14. V. Majarikar, H. Takehara, and T. Ichiki, *Biomed. Microdevices*, **22** (2020) 1.
15. A. Lionello, J. Jossierand, H. Jensen, and H. H. Girault, *Lab Chip*, **5** (2005) 254.
16. K. Kawazoe and Y. Takeuchi, *J. Chem. Eng. Japan*, **7** (1975) 431.

17. B. Samiey, S. Abdollahi Jonaghani, and J. Pollut. *Eff. Cont.*, **3** (2015) 1.
18. J. Wang and X. Guo, *Chemosphere*, **258** (2020) 127279.
19. L. Largette and R. Pasquier, *Chem. Eng. Res. Des.*, **109** (2016) 495.
20. A. Sebastian, A. Nangia, and M. N. V Prasad, *J. Hazard. Mater.*, **371** (2019) 261.
21. A. Basu, S. S. Behera, S. Dash, S. Banerjee, S. Sarkar, C. K. Mohanty, N. K. Dhal, P. K. Parhi, and S. K. Tripathy, *J. Taiwan Inst. Chem. Eng.*, **102** (2019) 118.
22. P. Atkins and J. de Paula, *Atkins' Physical Chemistry*, 10th ed. Oxford: Oxford University Press, 2014.

Polymer-Based Near-Infrared Afterglow Fluorescent Complex of Dye and Rare-Earth-Doped Ceramics

Shengjie Fang¹, Masakazu Umezawa¹, Kyohei Okubo¹, and Kohei Soga¹

¹ Department of Materials Science and Technology, Tokyo University of Science,
6-3-1 Niijuku, Katsushika, Tokyo 125-8585, Japan
*masa-ume@rs.tus.ac.jp

Near-infrared (NIR) light has been used for in vivo deep imaging in the biomedical field owing to its high permeability in biological tissues. Conventional fluorescence bioimaging requires simultaneous optical excitation, which can induce undesired results such as autofluorescence. In the present study, we report a polymer-based NIR afterglow fluorescent complex by using NIR dye, LDS 821, and SrAl₂O₄: Eu, Dy powder. To obtain the complex, SrAl₂O₄: Eu, Dy was first mixed with LDS 821 solution and dried at 65 °C for 12 h. Then, they were further mixed with pentaerythritol tetraacrylate (PETA) and photopolymerization initiator and then subjected to photopolymerization reaction. Poly-PETA was effective for not only retain both the dye and inorganic powder but also preventing the denaturation of SrAl₂O₄: Eu, Dy by water. The obtained polymer-based complex emits NIR afterglow fluorescence (wavelength: 760–780 nm) with a long fluorescence lifetime (5.0 min). This material design will provide a choice of obtaining NIR luminescent imaging phosphors for deep tissues without simultaneous light irradiation during image acquisition.

Keywords: Afterglow fluorescence, Near-infrared, Rare-earth-doped ceramics, Polymer

1. Introduction

Fluorescent bioimaging has been a major technique to dynamically visualize biological phenomena and tissue structures by using fluorescence probes. The light in near-infrared (NIR) wavelength region (700–2400 nm) shows less optical loss and scattering by biological tissues than those of visible and ultraviolet regions. Thus, the NIR window has been used for in vivo deep imaging [1, 2]. While indocyanine green has been used as the most major NIR fluorescent probe in clinical field, various types of NIR phosphors that work in longer wavelength (>1000 nm) have been developed [3] such as single-walled carbon nanotubes [4–8], quantum dots [9,10], rare-earth-doped ceramics [11–15], and organic dyes [16–20]. Although they are useful for in vivo fluorescent imaging of deep tissues, conventional fluorescence bioimaging with these phosphors requires simultaneous optical excitation, which can also induce autofluorescence and decrease the signal-to-noise ratio. To solve this problem, an NIR optical

imaging method free from simultaneous light irradiation during image acquisition has been studied.

Afterglow fluorescence is a phenomenon in which a luminescent material continues to emit light for several seconds to hours after the irradiation for excitation is removed. This is useful for realizing the imaging free from simultaneous irradiation for excitation. The most representative and commercially available afterglow phosphor is rare-earth-doped ceramics, SrAl₂O₄: Eu, Dy marketed as Luminova, which emits visible light with a peak wavelength of 540 nm. In this phosphor, Dy and Eu work as a trap center and emitting center, respectively [21]. Recently, zinc gallogermanate co-doped with Cr³⁺/Pr³⁺ [22] and LaAlO₃ perovskite co-doped with Cr³⁺/Er³⁺ [23] were reported as NIR afterglow phosphors emitting 700 and 1550 nm, respectively. Red shifting of the afterglow fluorescence of SrAl₂O₄: Eu, Dy has also been reported. Coating the surface of SrAl₂O₄: Eu, Dy with poly(methyl methacrylate) and red-emitting

coumarin converted the wavelength peak of the afterglow fluorescence from 525 nm (green) to 610 nm [24]. However, the color conversion of the afterglow fluorescence of SrAl₂O₄: Eu, Dy from green to NIR has not been reported. Moreover, the potential of denaturation of SrAl₂O₄: Eu, Dy by water should be investigated to prevent its quenching in the physiological environment.

In the present study, we chose an organic dye, LDS 821, as a color converter from green to NIR. To design a material that emits NIR afterglow luminescence, fixing of the LDS 821 at the surface of SrAl₂O₄: Eu, Dy with poly-PETA, a hydrophobic polymer that can shield rare-earth-doped ceramics from surrounding aqueous environment [25]. The spectra and the decay rate of the afterglow fluorescence were investigated for the obtained polymer-based complex with LDS 821 and SrAl₂O₄: Eu, Dy.

2. Experimental

2.1. Materials

A ceramic-based green afterglow fluorophore SrAl₂O₄: Eu, Dy (Luminova; G-300L700) was purchased from Nemoto & Co., Ltd. (Kanagawa, Japan). LDS 821 (excitation: 532 nm, emission: 825 nm) and Irgacure 784 were purchased from Lambda Physik Inc. (FL, USA) and Ciba Specialty Chemicals Inc. (Basel, Switzerland), respectively. Pentaerythritol tetraacrylate (PETA) and dimethyl sulfoxide (DMSO) were purchased from Tokyo Chemical Industry Co., Ltd. (Tokyo, Japan). LDS 821 was used as a solution in DMSO at the concentration of 100 mg/mL. All the reagents were used without further purification.

2.2. Preparation of polymer-based complex of rare-earth-doped ceramics and dye

SrAl₂O₄: Eu, Dy (0.15 g) and LDS 821 (100 μL) were mixed and dried by incubating at 65 °C for 12 h. After cooling to room temperature, the dried mixture was mixed with PETA (0.14 g) and Irgacure 784 (2 mg) and then placed on a 1-mm-thick glass slide (Matsunami Glass Ind., Ltd., Osaka, Japan). The sample was irradiated by a light of halogen lamp (25 W/cm², LA-150UE; Hayashi-Repic Co., Ltd., Tokyo, Japan) for 12 h to photopolymerize the PETA.

2.3. Optical characterization of the polymer-based complex

The afterglow fluorescent spectra of samples were analyzed by using a spectrometer (Flame-S;

Ocean Optics Inc., Tokyo, Japan) at 0–20 min after switching off the 2-min irradiation of light from a halogen lamp (25 W/cm²; LA-150UE).

3. Results and discussion

3.1. Polymerization of PETA with dye and rare-earth-doped ceramics

First, we tried to prepare polymer-based complex of LDS 821 and SrAl₂O₄: Eu, Dy by mixing them with PETA and the photopolymerization initiator, Irgacure 784, without the process for drying the dye-ceramics mixture followed by lamp irradiation. In this case, the blue color of LDS 821 was severely lost by the photopolymerization process (Fig. 1). This result was also observed when 2,2'-azodiisobutyronitrile was used for photopolymerization initiator (data not shown).

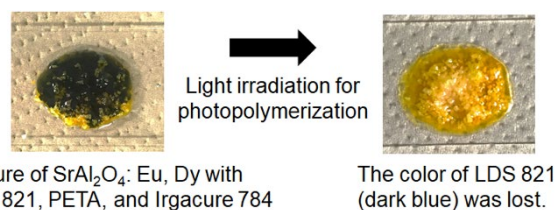


Fig. 1. A false example of preparation of the polymer-based complex. The LDS 821 dye was severely denatured (thus its dark blue color was lost) via radical generation from Irgacure 784 by irradiation for photopolymerization.

This denaturation of LDS 821 was suppressed by immersing SrAl₂O₄: Eu, Dy in LDS 821 solution in DMSO at 65 °C for 12 h before adding PETA and Irgacure 784. The results suggest that LDS 821 was denatured by radicals generated from Irgacure 784 during the light irradiation in the first case. Therefore, we mixed SrAl₂O₄: Eu, Dy with LDS 821 and dried before the photopolymerization to obtain polymer-based complex for following experiments (Fig. 2a).

3.2. Effect of poly-PETA coating on the luminescence of rare-earth-doped ceramics in water

The quenching of SrAl₂O₄: Eu, Dy has been reported following denaturation in water [26]. The quenching is likely due to the hydroxylation of SrAl₂O₄ [26]. To investigate the effect of poly-PETA coating on the luminescence, we first prepared a polymer-based complex without the NIR dye, LDS 821. The afterglow fluorescence intensity of pure SrAl₂O₄: Eu, Dy decreased to 12.5% by exposure to water for 24 h, while the intensity of poly-PETA-coated SrAl₂O₄: Eu, Dy maintained at 87.2% after the incubation in water (Fig. 2b). The results showed that poly-PETA successfully coated

SrAl₂O₄: Eu, Dy via photopolymerization and prevented its denaturation and quenching by water. The shift of luminescence spectral peak was observed by sample coating with poly-PETA possibly due to the effect of optical absorption of Irgacure 784 used as a photopolymerization initiator.

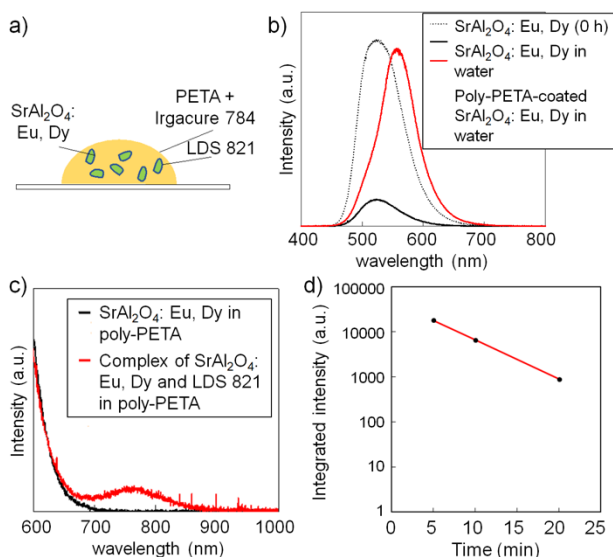


Fig. 2. Optical property of the poly-PETA complex prepared with SrAl₂O₄: Eu, Dy and LDS 821. (a) A schematic illustration of the polymer-based complex. It was prepared by immersing SrAl₂O₄: Eu, Dy in LDS 821 solution followed by mixing with PETA and Irgacure 784 for photopolymerization. (b) Effect of poly-PETA coating of SrAl₂O₄: Eu, Dy on its fluorescence. The fluorescence was measured by a spectrometer at 10 s after light irradiation of halogen lamp (25 W/cm²) for 2 min. (c) The spectrum and (d) the decay of NIR afterglow luminescence of the poly-PETA complex with SrAl₂O₄: Eu, Dy and LDS 821.

3.3. Near-infrared afterglow fluorescence of the dye-ceramics complex in poly-PETA

Finally, we investigated the NIR afterglow fluorescence of the polymer-based complex. As shown in Fig. 2c, it emits NIR light from LDS 821 excited by afterglow fluorescence of SrAl₂O₄: Eu, Dy in the complex for several tens of minutes after switching off the irradiation for excitation of SrAl₂O₄: Eu, Dy. The fluorescence lifetime determined by the decay curve (Fig. 2d) was 5.0 min, which is similar to visible afterglow fluorescence of SrAl₂O₄: Eu, Dy [21]. Although further investigations are needed to enhance the afterglow fluorescence of NIR and to increase the biocompatibility to allow various applications, the concept presented in this paper will provide a new choice of obtaining NIR luminescent imaging phosphors for deep tissues without simultaneous

light irradiation during image acquisition.

4. Conclusion

In the present study, we developed a polymer-based NIR afterglow luminescent complex using rare-earth-doped ceramics, SrAl₂O₄: Eu, Dy, and an NIR dye, LDS 821. The coating of poly-PETA resulted in protecting the SrAl₂O₄: Eu, Dy from quenching by water. By excitation with afterglow luminescence (wavelength: 540 nm) of SrAl₂O₄: Eu, Dy, the complex obtained shows NIR fluorescence (wavelength: 760–780 nm) with slow decay rate (lifetime: 5.0 min) that is similar to the afterglow luminescence of the original SrAl₂O₄: Eu, Dy. This concept of designing afterglow NIR phosphor may develop new NIR luminescence bioimaging techniques for deep tissues without simultaneous irradiation for excitation during image acquisition.

Acknowledgement

This work was partly supported by a MEXT Grant-in-Aid for Scientific Research on Innovative Areas (Resonance Bio), no. 15H05950, a MEXT Grant-in-Aid for Scientific Research(A), no. 19H01179, of Japan, and the Center of Innovation Program “COINS” from Japan Science and Technology Agency (JST).

References

1. A. M. Smith, A. C. Mancini, and S. Nie, *Nat. Nanotechnol.*, **4** (2009) 710.
2. K. Soga, M. Umezawa, and K. Okubo (Eds.), “Transparency in Biology: Making the Invisible Visible” Springer (2021).
3. K. Soga, M. Kamimura, K. Okubo, M. Umezawa, T. K. D. Doan, and K. Nigghossian, *J. Imaging Soc. Jpn.*, **58** (2019) 602.
4. S. M. Bachilo, M. S. Strano, C. Kittrell, R. H. Hauge, R. E. Smalley, and R. B. Weisman, *Science*, **298** (2002) 2361.
5. S. Ghosh, S. M. Bachilo, R.A. Simonette, K.M. Beckingham, and R. B. Weisman, *Science*, **330** (2010) 1656.
6. G. Hong, S. Diao, J. Chang, A. L. Antaris, C. Chen, B. Zhang, S. Zhao, D. N. Atochin, P. L. Huang, K. I. Andreasson, C. J. Kuo, and H. Dai, *Nat. Photonics*, **8** (2014) 723.
7. Y. Iizumi, M. Yudasaka, J. Kim, H. Sakakita, T. Takeuchi, and T. Okazaki, *Sci. Rep.*, **8** (2018) 6272.
8. S. Sekiyama, M. Umezawa, Y. Iizumi, T. Ube, T. Okazaki, M. Kamimura, and K. Soga, *Langmuir*, **35** (2019) 831.

9. B. del Rosal, D. Ruiz, I. Chaves-Coira, B. H. Juárez, L. Monge, G. Hong, N. Fernández, and D. Jaque, *Adv. Funct. Mater.*, **28** (2018) 1806088.
10. J. Lifante, Y. Shen, I. Z. Gutierrez, I. Rubia-Rodríguez, D. Ortega, N. Fernandez, S. Melle, M. Granado, J. Rubio-Retama, D. Jaque, and E. Ximendes, *Adv. Sci.*, (2021) in press.
11. D. J. Naczynski, M. C. Tan, M. Zevon, B. Wall, J. Kohl, A. Kulesa, S. Chen, C. M. Roth, R. E. Riman, and P.V. Moghe, *Nat. Commun.*, **4** (2013) 2199.
12. M. Kamimura, T. Matsumoto, S. Suyari, M. Umezawa, and K. Soga K, *J. Mater. Chem. B*, **5** (2017) 1917.
13. D. H. Ortgies, M. Tan, E. C. Ximendes, B. del Rosal, J. Hu, L. Xu, X. Wang, E.M. Rodríguez, C. Jacinto, N. Fernandez, G. Chen, and D. Jaque, *ACS Nano*, **12** (2018) 4362.
14. S. Sekiyama, M. Umezawa, S. Kuraoka, T. Ube, M. Kamimura, and K. Soga K, *Sci. Rep.*, **8** (2019) 16979.
15. T. Chihara, M. Umezawa, K. Miyata, S. Sekiyama, N. Hosokawa, K. Okubo, M. Kamimura, and K. Soga, *Sci. Rep.*, **9** (2019) 12806.
16. A. L. Antaris, H. Chen, K. Cheng, Y. Sun, G. Hong, C. Qu, S. Diao, Z. Deng, X. Hu, B. Zhang, X. Zhang, O. K. Yaghi, Z. R. Alamparambil, X. Hong, Z. Cheng, and H. Dai, *Nat. Mater.*, **15** (2016) 235.
17. X. D. Zhang, H. Wang, A. L. Antaris, L. Li, S. Diao, R. Ma, A. Nguyen, G. Hong, Z. Ma, J. Wang, S. Zhu, J. M. Castellano, T. Wyss-Coray, Y. Liang, J. Luo, and H. Dai, *Adv. Mater.*, **28** (2016) 6872.
18. M. Kamimura, S. Takahiro, M. Yoshida, Y. Hashimoto, R. Fukushima, and K. Soga, *Polym. J.*, **49** (2017) 799.
19. M. Kamimura, Y. Ueya, E. Takamoto, K. Iso, M. Yoshida, M. Umezawa, and K. Soga, *J. Photopolym. Sci. Technol.*, **32** (2019) 93.
20. M. Umezawa, M. Haruki, M. Yoshida, M. Kamimura, and K. Soga, *Anal. Sci.*, **37** (2021) 365.
21. Y. Murayama, *J. Soc. Inorg. Mater. Jpn.*, **8** (2001) 160. (in Japanese)
22. A. Abdukayum, J.T. Chen, Q. Zhao, and X.P. Yan, *J. Am. Chem. Soc.*, **135** (2013) 14125.
23. J. Xu, D. Murata, Y. Katayama, J. Ueda, and S. Tanabe, *J. Mater. Chem. B*, **5** (2017) 6385.
24. Z. Chen, X. Guo, and M. Ge. *J. Lumin.*, **194** (2018) 200.
25. K. Okubo, T. Yamada, H. Haraguchi, M. Kamimura, M. Umezawa, and K. Soga, *J. Photopolym. Sci. Technol.*, under review.
26. M. Ohkawa, H. Kominami, Y. Nakanishi, and K. Hara, *IEICE Tech. Rep.*, (2017) EID2016-38 (in Japanese).

Multifunctional Top-Coats Strategy for DSA of High- χ Block Copolymers

Xavier Chevalier^{1,*}, Cindy Gomes Correia², Gwenaelle Pound-Lana³, Philippe Bézard^{3,4}, Matthieu Sérégé³, Camille Petit-Etienne³, Guillaume Gay³, Gilles Cunge³, Benjamin Cabannes-Boué², Célia Nicolet¹, Christophe Navarro¹, Ian Cayrefourcq^{1,5}, Marcus Müller⁶, Georges Hadziioannou², Ilias Iliopoulos⁷, Guillaume Fleury², and Marc Zelsmann³

¹ ARKEMA FRANCE, GRL, Route Nationale 117, BP34 64170 Lacq, France.

² Univ. Bordeaux, CNRS, Bordeaux INP, LCPO, UMR 5629, F-33600, Pessac, France.

³ Univ. Grenoble Alpes, CNRS, CEA/LETI Minatec, Grenoble INP, LTM, 38000 Grenoble, France.

⁴ IMEC, Kapeldreef 75, 3001 Leuven, Belgium.

⁵ I-TEN SA, 12 Chemin du Jubin, F69570, Dardilly, France.

⁶ Georg-August Universität Göttingen, Institute for Theoretical Physics, 37077 Göttingen, Germany.

⁷ Laboratoire PIMM, Arts et Métiers Institute of Technology, CNRS, Cnam, HESAM Université, 151 Boulevard de l'Hôpital, 75013 Paris, France.

*xavier.chevalier@arkema.com

A concept of patternable top-coats dedicated to directed self-assembly of high- χ block copolymers is detailed, where the design enables a crosslinking reaction triggered by thermal or photo-activation. Nanostructured BCP areas with controlled domains orientation are selected through a straightforward top-coat lithography step with unique integration pathways. Additionally, the crosslinked nature of the material enables the suppression of the BCP dewetting, while exhibiting exceptional capabilities for the construction of 3D stacks.

Keywords: Lithography, Block copolymers, Self-assembly, Cross-linkable top-coats, Top-coat patterning, Nanopatterning, Dewetting

1. Introduction

The directed self-assembly (DSA) of block copolymers (BCPs) is a potential method of choice to obtain regular arrays of predetermined patterns, owing to their intrinsic periodic nature, ease of processing, and nanometer-scale dimensions of features. However, reaching aggressive dimensions below 10 nm, *i.e.* below the ultimate resolution of polystyrene-*b*-poly(methyl methacrylate) (PS-*b*-PMMA) system [1], necessitates the use of high- χ BCPs (χ being the Flory-Huggins segregation parameter). Such BCPs are very often constituted of blocks presenting a large difference in their intrinsic surface energy at the targeted annealing temperature, promoting the self-assembly process. These BCPs necessitate the use of top-coats (TC) materials to balance the interfacial tension between the blocks

and achieve the perpendicular orientation of nanometric features [2]. In our previous works we proposed a new design of TCs able to circumvent key challenges posed by the integration of DSA into microelectronic nodes [3,4]. Here we highlight the specific properties of these TCs enabling their multifunctional use for nano-manufacturing.

2. Experimental

2.1. Synthesis of TC material

The synthesis of the TC material was performed by radical polymerization in solution with AIBN as initiator [3]. All the monomers, solvent, initiator and terminating agent were used as received.

2.2. Synthesis of poly(1-1dimethylsilacyclobutane)-*b*-polystyrene (PDMSB-*b*-PS BCP)

The synthesis of the BCP material was performed as previously reported [5].

2.3. Preparation of thin films

0.9 wt% PDMSB-*b*-PS solutions in methyl isobutyl ketone (MIBK) were spin-coated (2 krpm) on neutralized 3x3cm Si-substrate, followed by a soft-bake at 60 °C for 1 min to produce BCP layers with approximatively 30 nm thickness. The TC material dissolved into absolute ethanol at 2 wt%, is spin-coated on the BCP thin film at 1500 rpm. The stack is baked at 90 °C for 3 minutes, and the BCP is self-assembled at 240 °C for 5 minutes.

2.4. Ellipsometry

The film thicknesses were determined using spectroscopic ellipsometry in reflection mode with a phase modulated spectroscopic ellipsometer (UVISEL, from Horiba Scientific) on the spectral range 200-800 nm.

2.5. Patterning

UV lithography was carried out with a KarlSüss MJB4 equipment equipped with a mercury arc lamp having a power of 20 mW/cm² at a wavelength of 365 nm.

Electron-beam (e-beam) lithography was performed on a JEOL6300FS equipment at an acceleration voltage of 100 kV, with a current of 500 pA and a dose of 80 μC/cm².

2.6. Microscopy

Top-view SEM images were acquired on a Hitachi CD-SEM H-9300 microscope with 0.5 kV electron acceleration voltage and a 6 μA current. FIB-STEM cross-sections were carried out using a Helios 450s-FEI dual-beam equipment.

3. Results and discussion

3.1. Macromolecular design

The BCP used is based on the PDMSB-*b*-PS platform (Fig. 1, left) [5]. It presents a large difference in the surface free energy of its blocks, and is able to reach dimensions below 12 nm in period as previously demonstrated [3]. The silicon, present in the PDMSB block, enables to increase the etch performances for the final transfer step into the underlying substrate. It avoids the use of a time-consuming sequential-infiltration-synthesis step to provide a decent etch contrast between the two blocks.

The TC material designed is based on a methacrylic terpolymer, with a statistical architecture of poly(2,2,2-trifluoroethylmethacrylate-*co*-glycidylmethacrylate-*co*-hydroxyethylmethacrylate) hereafter abbreviated “FGH” (Fig. 1, middle). This TC is thus entirely organic and exhibits a great etch selectivity with respect to the Si-containing BCP under O₂-based plasma. The FGH material presents low *M_w* (~3000 g/mol.) and polar comonomers, favoring its solubility into alcoholic solvents (pure ethanol or IPA for instance), while the BCP material is insoluble in such solvents. Its inexpensive and available constituents, readiness of synthesis through radical polymerization, and easiness of compositional tuning, make it a material of choice for DSA applications. Moreover, FGH material can also be used as grafted or cross-linked underlayer, thanks to hydroxyl and epoxy chemical functions respectively.

The FGH solution is readily spin-coated and cross-linked on top of the BCP, the interfacial

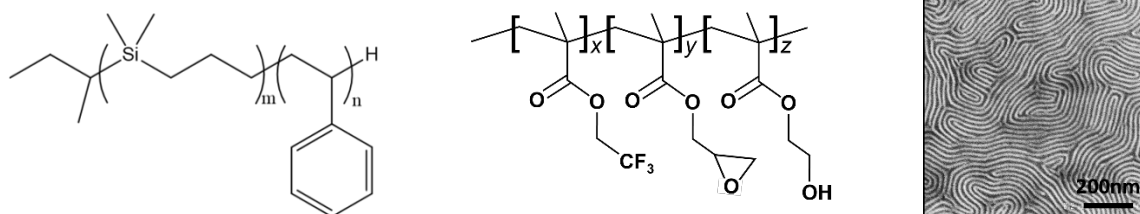


Fig. 1. Chemical structure of PDMSB-*b*-PS block copolymer (left); Structure of FGH top-coat material (middle); Top-view SEM picture showing the self-assembly of a lamellae-forming 18 nm period PDMSB-*b*-PS BCP obtained by using a neutral FGH material as TC and a neutralized substrate, with a 240 °C/5 minutes thermal annealing process (right).

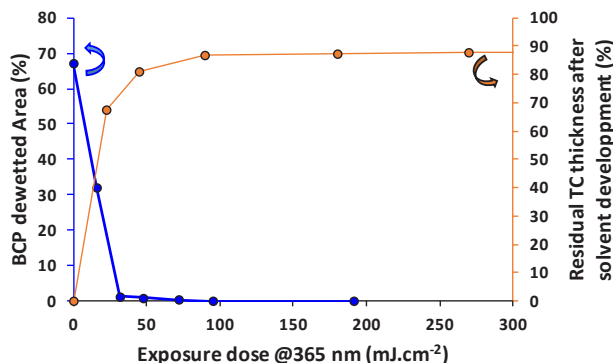


Fig. 2. Evolution of the remaining FGH thickness, after exposure to various doses of UV light ($\lambda=365$ nm) and subsequent rinse in ethanol for 2 mins (orange plot). Evolution of the dewetted area on the sample of a neutralized substrate/PDMSB-*b*-PS/neutral FGH stack as a function of the UV light ($\lambda=365$ nm) exposure dose, a PEB performed at 90 °C for 3 minutes, and subsequent thermal annealing at 260 °C for 5 minutes to promote the self-assembly of the block copolymer layer (blue plot).

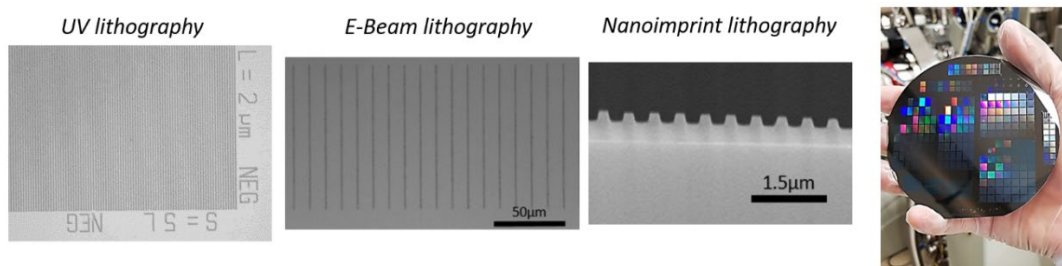


Fig. 3. Examples of FGH patterning on top of PDMSB-*b*-PS film with different techniques. A 4 inch wafer of a BCP/TC stack, where the FGH –TC material is patterned with UV light ($\lambda=365$ nm) exposure, is shown on the right.

tension of both PDMSB and PS blocks are subsequently well-balanced upon thermal annealing and, as a result, it drives the perpendicular orientation of the domains (Fig.1, right). This first functionality as “neutral” material is found for adjusted composition of FGH comonomers, selected through the synthesis.

3.2. Cross-linking

One of the most interesting functionalities of the FGH material is their ability to be cross-linked. Owing to the epoxy functions in FGH, the cross-linking process can be triggered either by thermal stimulus with a latent catalyst, or by photoactivation with a photoacid generator (PAG) followed by a post-exposure bake (PEB), and completed within few minutes. This particular property, and the methacrylic nature of the backbone, leads to a stiff material and confers to the FGH layer a tremendous mechanical strength. This mechanical cohesion enables to freeze the dewetting kinetic of the underlying BCP material, and thus locks the BCP film in its initially flat configuration. Although the amplification of the capillary waves responsible of

the dewetting [6] is suppressed by the cross-linking of the FGH, the BCP material is still able to self-assemble into a lamellar microphase, as proven in Fig. 1, right. This unique property owned by FGH materials is illustrated in Fig. 2. It can be seen that the FGH material blended with (4-phenylthiophenyl) diphenylsulfonium triflate as PAG is easily photo-cross-linked at low UV doses, even for a 365nm wavelength. The FGH thickness is indeed constant for doses as low as 100 mJ/cm², followed by a 3 minutes PEB at 90 °C, and then rinsed in ethanol (Fig. 2, orange plot). Meanwhile, the dewetting of the BCP film is progressively mitigated when the UV dose is increased, and is entirely suppressed for UV dose of ~100 mJ/cm², even with a subsequent high temperature self-assembly annealing process as 260 °C for 5 minutes (Fig. 2, blue plot).

3.3. Patterning

The most appealing property of the FGH material is their ability to be patterned like a standard lithographic resist. Indeed, the chosen methacrylic platform enables the FGH materials to be patterned

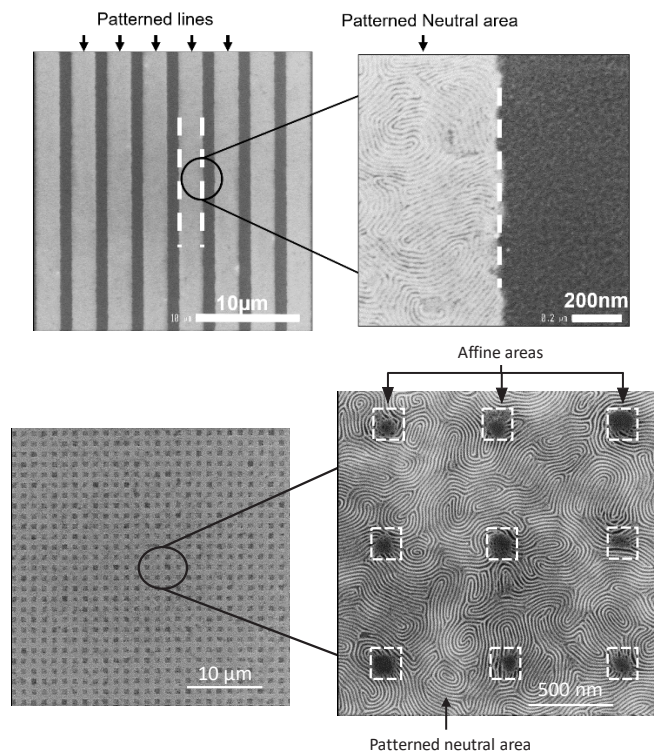


Fig. 4. Example of FGHPatterning results, demonstrating the selection of perpendicular and parallel areas of a lamellae-forming 18 nm period PDMSB-*b*-PS BCP with UV light ($\lambda=365$ nm) exposure (top panel) or e-beam exposure (bottom panel). The thermal annealing step was performed at 240 °C for 5 minutes.

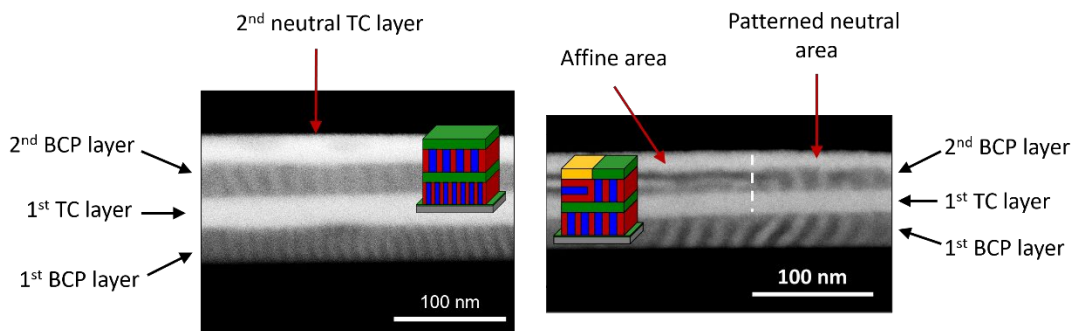


Fig. 5. Examples of 3D-multilayered PDMSB-*b*-PS film stack obtained with the specific FGHPatterning as neutral interface material, where the cross-sections are characterized with FIB-STEM technique. The first BCP layer is a lamellae-forming 12 nm period PDMSB-*b*-PS BCP, and the second is a lamellae-forming 18 nm period PDMSB-*b*-PS BCP (left). Example of a combination of BCP multilayers stack with the patterning ability of the FGHPatterning material (right). The upper patterned FGHPatterning film leads to different orientational order of the 2nd lamellar BCP layer. A lamellae-forming 18 nm period PDMSB-*b*-PS was used as first and second BCP layer.

with most of advanced lithographic techniques, as illustrated on Fig. 3 with the examples of UV ($\lambda=365$ nm), e-beam and nanoimprint techniques. In the case of UV lithography, it is worth mentioning that methacrylates are transparent down to 193 nm wavelength as they are the basis of many chemically amplified resist materials [7]. Moreover, the possibility of sensitization [8] even opens up a compatibility with EUV technique for advanced nodes. It is also of interest to mention that the FGHPatterning

material and patterning processes can be easily scaled up to wafer sizes, as demonstrated with a BCP/TC stack on a 4 inches wafer where the TC is patterned with UV light ($\lambda=365$ nm) on the Fig. 3, right.

The FGHPatterning material, blended with a PAG as latent catalyst, behaves as a chemically amplified negative resist, due to the nature of the cross-linking reaction through the epoxy moieties [9]. Thanks to the ease of their compositional tuning with the synthesis, the

user is able to readily choose either the neutral or affine nature of the TC material to be patterned. This unique patterning ability of the FGH opens up new integration schemes for the DSA of block copolymers, leading to the selection of areas of interest with either perpendicular or parallel orientation of BCP domains directly through the TC material. Examples of such a selection of areas of perpendicular or parallel orientations for BCP through TC patterning are given in Fig. 4 with UV and e-beam lithography techniques. This intrinsic property leads to processes and integrational paths, which cannot be achieved with classical schemes and materials, and thus further increase the available process-flows, aiming to control and use the self-assembled morphologies.

3.4. Multilayers stacking

Another interesting functionality offered by the unique FGH design is tied to their cross-linked and controlled surface energy nature. Indeed, these two features naturally open up the way of an original multilayer stacking process of BCPs films. Previously reported techniques [10] use time-consuming processes to coat an extra-layer of a material to encapsulate and protect the BCP film form a potential stripping or lift-off with an upper layer of a second BCP material. In the case of the FGH material, thanks to their spin-coatable nature, the protection of the first BCP layer with its neutral TC is very quickly achieved (few minutes for the cross-linking step) before being able to coat the second layer of BCP. Moreover, the self-assembly bake can be performed either all along or at the end of the stacking process, as the BCP keeps here its own viscoelastic properties along the whole stacking process, conversely to other techniques [11]. Therefore, the overall process is very swift, and a functional two-layer stack can be achieved within less than 10 minutes, as illustrated on the Fig. 5, left. The stacking process can also include a patterning step, as evidenced in the Fig. 5, right, which can hardly be achieved with other techniques, rendering thus the FGH materials quite appealing for investigations in photonic and metamaterials applications with BCPs.

4. Conclusion

We have detailed the design of an innovative TC material combining multiple functionalities. While being able to balance the interfacial tension of a given BCP material, it demonstrates a high efficiency to suppress the dewetting of the BCP

material through the trapping of its initially flat state, without hindering its phase-separation process. The unique patternable ability of this TC design enables new processing schemes for the self-assembly of BCP to select areas of interest in the film and their integration into useful process-flows for nanolithography. Finally, the cross-linked nature opens up interesting potential into photonic/metamaterials applications with BCP, owing to the swift stacking of multiple BCPs layers.

Acknowledgments

This work was supported by the REX-7 project from Région Rhône Alpes and BPI France, by the French RENATECH network and by the LabEx Minos ANR-10-LABX-55-01. C.G.C., G. H. and G.F. acknowledge financial support from the LCPO/Arkema industrial chair "HOMERIC" (ANR-13-CHIN-0002-01), the Equipex ELORPrintTec ANR-10-EQPX-28-01 with the help of the French state's Initiative d'Excellence IdEX ANR-10-IDEX-003-02. I.I. acknowledges financial support from the Industrial Chair Arkema/CNRS-ENSAM-Cnam.

References

1. X. Chevalier, C. Nicolet, R. Tiron, A. Gharbi, M. Argoud, J. Pradelles, M. Delalande, G. Cunge, G. Fleury, G. Hadziioannou, and C. Navarro, *Proc. SPIE*, **8680** (2013) 868006.
2. C. M. Bates, T. Seshimo, M. J. Maher, W. J. Durand, J. D. Cushen, L. M. Dean, G. Blachut, C. J. Ellison, and C. G. Willson, *Science*, **338** (2012) 775.
3. X. Chevalier, C. G. Correia, G. Pound-Lana, P. Bézard, M. Sérégé, C. Petit-Etienne, G. Gay, G. Cunge, B. Cabannes-Boué, C. Nicolet, C. Navarro, I. Cayrefourcq, M. Müller, G. Hadziioannou, I. Iliopoulos, G. Fleury, and M. Zelsmann, *ACS Appl. Mater. Interfaces*, **13** (2021) 11224.
4. X. Chevalier, C. G. Correia, G. Pound-Lana, P. Bézard, M. Sérégé, C. Petit-Etienne, G. Gay, G. Cunge, B. Cabannes-Boué, C. Nicolet, C. Navarro, I. Cayrefourcq, M. Müller, G. Hadziioannou, I. Iliopoulos, G. Fleury, and M. Zelsmann, *Proc. SPIE*, **11612** (2021) 1161200.
5. A. Legrain, G. Fleury, M. Mumtaz, C. Navarro, J. Arias-Zapata, X. Chevalier, I. Cayrefourcq, M. Zelsmann, *ACS Appl. Mater. Interfaces*, **9** (2017) 43043.
6. F. Brochard Wyart, P. Martin, and C. Redon, *Langmuir*, **9** (1993) 3682.

7. D. P. Sanders, *Chem. Rev.*, **110** (2010) 321.
8. S. Nagahara, C. Q. Dinh, G. Shiraishi, Y. Kamei, K. Nafus, Y. Kondo, M. Carcasi, M. Minekawa, H. Ide, Y. Yoshida, K. Yoshihara, R. Shimada, M. Tomono, K. Takeshita, S. Biesemans, H. Nakashima, D. De Simone, J. S. Petersen, P. Foubert, P. De Bisschop, G. Vandenberghe, H.-J. Stock, and B. Meliorisz, *Proc. SPIE*, **10960**, (2019) 109600A.
9. H. Ito, H. “*Advances in Polymer Science*” Springer, Berlin, Heidelberg, 2005, Vol. **172**, p. 37.
10. A. Rahman, P. W. Majewski, G. Doerk, C. T. Black, and K. G. Yager, *Nat. Commun.* **7** (2016) 13988.
11. H. Jung, D. Hwang, E. Kim, B.-J. Kim, W. B. Lee, J. E. Poelma, J. Kim, C. J. Hawker, J. Huh, D. Y. Ryu, J. Bang, *ACS Nano*, **5** (2011) 6164.

Resist Thickness Dependence of Latent Images in Chemically Amplified Resists Used for Electron Beam Lithography

Takahiro Kozawa^{1*} and Takao Tamura²

¹*The Institute of Scientific and Industrial Research, Osaka University,
8-1 Mihogaoka, Ibaraki, Osaka 567-0047, Japan*

²*NuFlare Technology, Inc., 8-1 Shinsugita, Isogo, Yokohama, 235-8522, Japan*

**kozawa@sanken.osaka-u.ac.jp*

Transistors have been miniaturized to increase their integration. With miniaturization, the thickness of the patterning material, called a resist, has been decreased to prevent them from collapsing. In this study, the resist film thickness dependence of the latent images of chemically amplified electron beam resists was investigated using the simulation on the basis of their sensitization and reaction mechanisms. The decompositions of sensitizers (photoacid generators) were significantly affected by the dynamics of low-energy electrons at the interfaces of resist films. The subsequent deprotection was also affected by the initial acid distribution. Simulation results indicated that such interfacial effects basically increased with the decrease of resist film thickness.

Keywords: EB lithography, Chemically amplified resist, Interface effect, Low-energy electron

1. Introduction

The electron beam (EB) lithography is an indispensable technology for the information-oriented society. It has been used for the fabrication of photomasks, extreme ultraviolet (EUV) masks, and nanoimprint molds for the high-volume production of semiconductor devices. The requirement for photomasks becomes severe with the miniaturization of electronic devices. When the critical dimension was decreased, the resist patterns tend to collapse due to the surface tension of rinse liquid (pure water) [1-3]. The collapse prevention measures such as freeze drying process, supercritical drying, and dry development rinse process have been investigated [4-8]. They are, however, still inadequate or impose additional costs. Therefore, the reduction of resist film thickness is required for the high-resolution patterning. However, the quality of resist patterns is degraded with the decrease of the initial resist film thickness for the sub-100

nm thickness range, even if the pattern collapse is avoided [9-12].

A highly sensitive resist, called a chemically amplified resist, has been used for the fabrication of photomasks [13]. The sensitization mechanism has been reported as follows. The resist molecules are ionized and secondary electrons are emitted upon by the irradiation of electron beam. The counteranions of acids are generated through the dissociative electron attachment to acid generators after the secondary electrons are thermalized [14,15]. The protons of acids are mainly generated through the deprotonation of polymer radical cations [16,17]. The generated acids catalyze the deprotection of polymer molecules during the postexposure baking (PEB). The deprotection induces the polarity change of polymer molecules, which leads to the solubility change of resist film in the tetramethylammonium hydroxide (TMAH) aqueous developer. The low-energy electrons play an essential role in the sensitization of

chemically amplified EB resists.

The resist film is roughly divided into three layers (near-surface, bulk, and near-substrate layers). With the decrease of initial resist film thickness, the volume of bulk layer decreases and the effects of near-surface and near-substrate layers on the resist performance increase. For the near-surface layer, the segregation of low molecular weight components was investigated [18-23]. Such surface segregation was reported to lead to the fast deprotection at the near-surface layer [18]. The segregation at the near-substrate layer was weaker than that at the near-surface layer [19-23].

The film thickness dependence of glass transition temperature T_g , which reflects the strength of polymer-substrate interaction, has been investigated [24-27]. When the polymer-substrate interaction is strong, the mobility of acids decreases. The dynamics of low-energy electrons at the interface has been also reported to affect the acid distribution in the depth direction for chemically amplified EUV resists [28]. In this study, the resist film thickness dependence of the latent images of chemically amplified EB resists was investigated, assuming eight patterns for the low-energy electron dynamics at the interfaces. The latent images of 100 nm line-and-space patterns were calculated for the initial resist film thickness of 20 and 70 nm on the basis of the sensitization and reaction mechanisms of chemically amplified EB resists [29]. The effect of low-energy electron dynamics at the interfaces on the latent image formation is discussed.

2. Simulation model and method

The chemically amplified resist assumed consisted of the triphenylsulfonium nonaflate (TPS-nf) as an acid generator, the trioctylamine (TOA) as a quencher, and a partially protected poly(4-hydroxystyrene) (PHS). The TPS-nf concentration was $0.257 / \text{nm}^3$. The TOA concentration was $0.128 / \text{nm}^3$. A *tert*-butoxycarbonyl group was assumed as a protecting group. The protected ratio was 31.2%.

The latent images of line-and-space patterns were calculated on the basis of the sensitization and reaction mechanisms of chemically amplified EB resists. The

Table I. Parameters used in the simulation.

Acceleration voltage of electron beam (kV)	125
Beam blur (σ_b) (nm)	2
Backscattering coefficient[38]	0.31
Half-pitch (nm)	100
Initial resist film thickness (nm)	20,70
Stopping power (eV/nm)	0.418
Resist film density (g/cm^3)[21]	1.2
Thermalization distance (nm)[30]	3.2
Acid generator concentration ($/\text{nm}^3$)	0.257
Quencher concentration ($/\text{nm}^3$)	0.128
Reaction radius of acid generator (nm)[30,31]	0.70
Effective reaction radius for neutralization (nm)	0.5
Effective reaction radius for deprotection (nm)	0.1
Protection ratio (%)	31.2
Deprotonation efficiency of proton source[39]	1.0
Deprotonation efficiency of nonproton source[32]	0.59
Diffusion constant of acids (nm^2/s)	1.0
PEB time (s)	600
PEB temperature ($^\circ\text{C}$)	130

acceleration voltage of the electron beam was 125 kV. The beam blur was approximated using a Gaussian function. The beam blur ($1\sigma_b$) was set to 2.0 nm. The pitch was 200 nm and the calculated area was $200 \times 150 \text{ nm}^2$. The thickness of resist films was 20 and 70 nm. The reaction radius of TPS-nf with thermalized electrons were assumed to be the same as that of triphenylsulfonium triflate (TPS-tf) [30,31]. The thermalization distance of secondary electrons in PHS has been reported to be 3.2 nm.[30] The deprotonation efficiency of *tert*-butoxycarbonyl protected unit radical cations was set to 0.59 [32]. The trajectories of secondary electrons and the reaction of thermalized electrons with acid generators were calculated by a Monte Carlo method. The low-energy (<ionization potential) electron dynamics at the surface (the interface between vacuum and a resist layer) was categorized into two patterns. The low-energy electron dynamics at the interface between a resist layer and an underlayer (UL) was categorized into four patterns, as later explained. The other details of the calculation procedure have been reported elsewhere [33].

Using the acid distribution after the preneutralization [34,35] as the initial condition, the catalytic chain deprotection during PEB was also calculated by solving the reaction-diffusion equations. The details

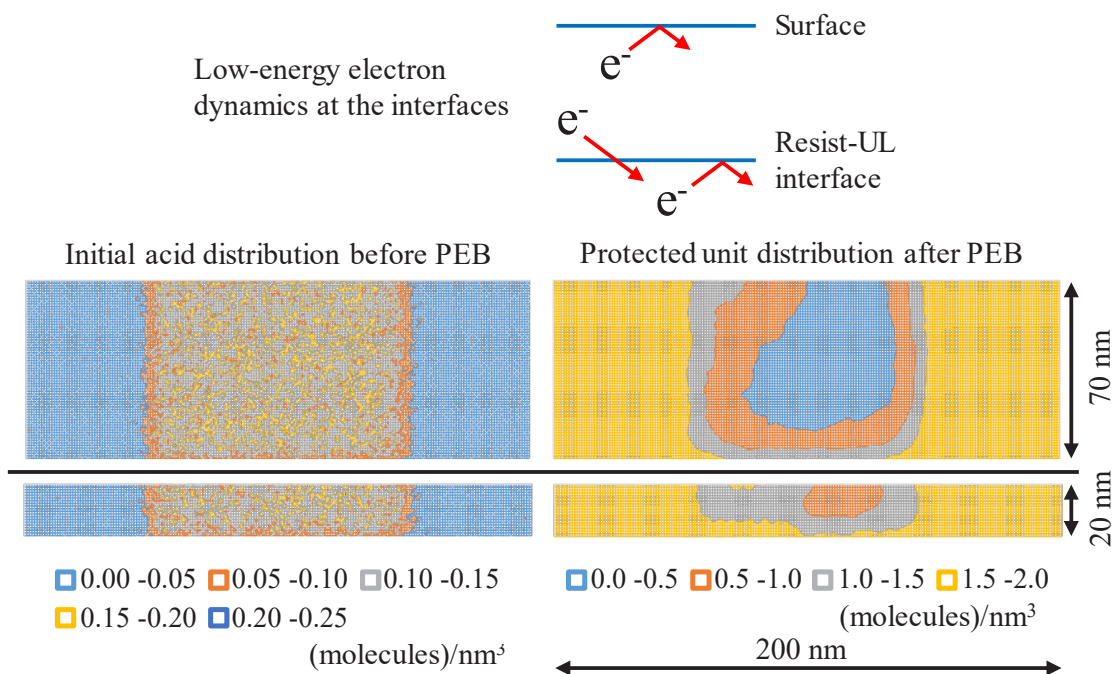


Fig. 1. Initial resist film thickness dependence of initial acid distribution before PEB and protected unit distribution after PEB, obtained by the simulation. The features were line-and-space patterns with 100 nm half-pitch. The film thicknesses were 20 and 70 nm. The boundary conditions were reflection (from resist layer to vacuum), transmission (from resist to UL), and reflection (from UL to resist). The figures for 20 nm film thickness were reprinted from Ref. 12.

of the calculation procedure have been reported elsewhere [36]. The effective reaction radius for neutralization was set to 0.5 nm. The effective reaction radius for deprotection was assumed to be 0.1 nm [37]. The periodic boundary condition was applied in the horizontal direction. The reflective boundary condition was applied in the vertical direction. The backscattering coefficient was assumed to be 0.31 [38]. The parameters used in the simulation are summarized in Table I [21,30-32,38,39]. The validity of the simulation method has been examined by comparison with the experimental results obtained by using EBM-9000 of NuFlare [37]. Other details of the reaction mechanisms have been reported elsewhere [29].

3. Results and discussion

The resist film thickness dependence of the pattern formation of chemically amplified EB resists was investigated using Si wafers (p type, electrical resistance of $\leq 0.02 \Omega \text{ cm}$) in our previous study [12]. Using an EB writer (125 keV), the line-and-space patterns with 100 nm half-pitch were fabricated. The line

width roughness (LWR) of line-and-space patterns was analyzed. The dissolution kinetics of resist films was also analyzed using a quartz crystal microbalance (QCM) method. Figure 1 shows the initial resist film thickness dependence of initial acid distribution before PEB and protected unit distribution after PEB, obtained by the simulation on the basis of the sensitization and reaction mechanisms of chemically amplified EB resists. The simulated latent images well explained the resist film thickness dependence of LWR and dissolution kinetics. In the simulation, the low-energy electrons were assumed to be able to move from the resist layer to UL and to be unable to move from UL to the resist layer because both Au and Si wafer used are electrically conductive. For the resist surface, the low-energy electrons were assumed to be unable to escape to the vacuum from the comparison with the crosssectional SEM images of line-and-space patterns. Thus, the boundary conditions for the simulation were set to be the reflection (from resist layer to vacuum), the transmission (from resist to UL), and the reflection (from UL to resist). Under such conditions, the acid concentration

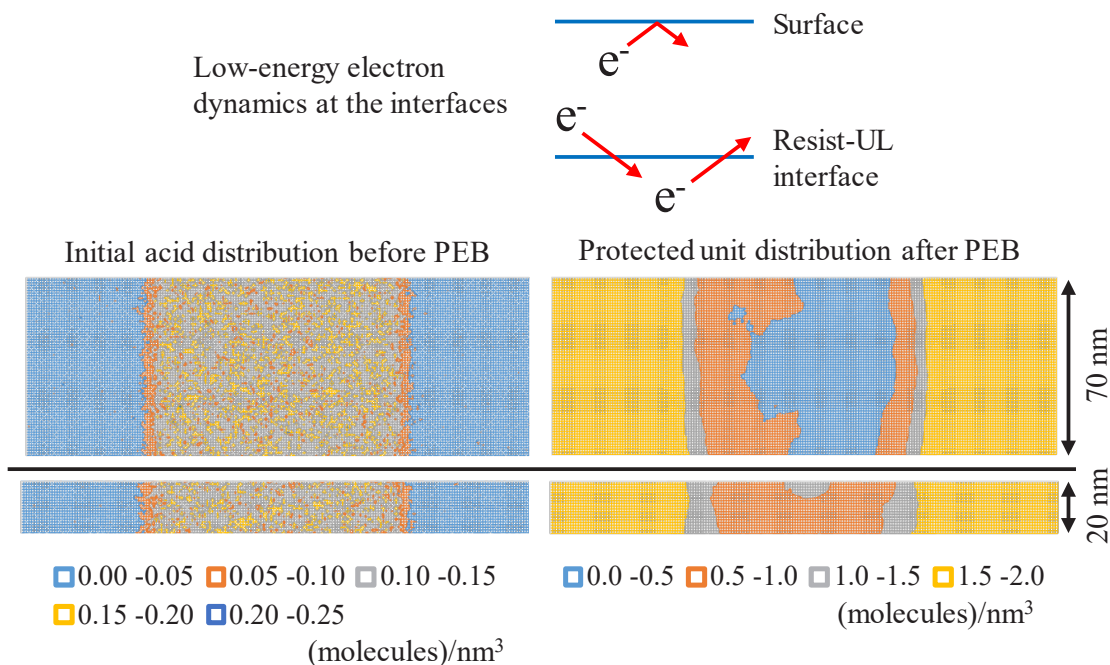


Fig. 2. Initial resist film thickness dependence of initial acid distribution before PEB and protected unit distribution after PEB, obtained by the simulation. The boundary conditions were reflection (from resist layer to vacuum), transmission (from resist to UL), and transmission (from UL to resist).

decreased near UL because of the loss of low-energy electrons. There was no difference between the acid distributions near UL for the resists with 20 and 70 nm film thickness. The acids diffuse in the resist matrix during PEB. The amount of acids supplied from the bulk layer decreased with decreasing the resist film thickness. Consequently, the protected unit concentration near UL for the resist with 20 nm film thickness became higher than that for the resist with 70 nm film thickness [12].

Figure 2 shows the initial resist film thickness dependence of initial acid distribution before PEB and protected unit distribution after PEB, obtained by the simulation. The boundary conditions were set to be the reflection (from resist layer to vacuum), the transmission (from resist to UL), and the transmission (from UL to resist). The difference from the case shown in Fig. 1 is the low-energy electron dynamics from UL to the resist layer. The initial acid concentration near UL increased owing to the supply of low-energy electrons from UL. The protected unit concentration near UL became lower than those shown in Fig. 1 because of the increased acids. However, the dependence of protected unit concentration near UL on the initial resist film thickness was still observed.

The reflection boundary condition was applied to both interfaces. The initial acid distribution before PEB and the protected unit distribution after PEB are shown in Fig. 3 for the initial resist film thicknesses of 20 and 70 nm. In this study, the material properties of UL associated with the secondary electron generation and electron deceleration were assumed to be the same as those of the resists. In addition, the penetrating power of 125 keV electron is significantly high. Therefore, the simulation results should be the same as those shown in Fig. 2. The observed difference in the protected unit distribution (Figs. 2 and 3) is a calculation error originated from the stochasticity of Monte Carlo method applied to the calculation of acid distribution. The dependence of protected unit concentration near UL on the initial resist film thickness was decreased, unlike the case shown in Fig. 2. With the same reason, the thickness dependence shown in Fig. 3 should be the same as the case shown in Fig. 2. This discrepancy is considered to be caused because the stochasticity strongly affected the protected unit distribution with the decrease of resist film thickness. That is, the number of acids in the target feature decreased with the decrease of resist film thickness. The decrease in the number of acids led to the increase in the stochasticity.

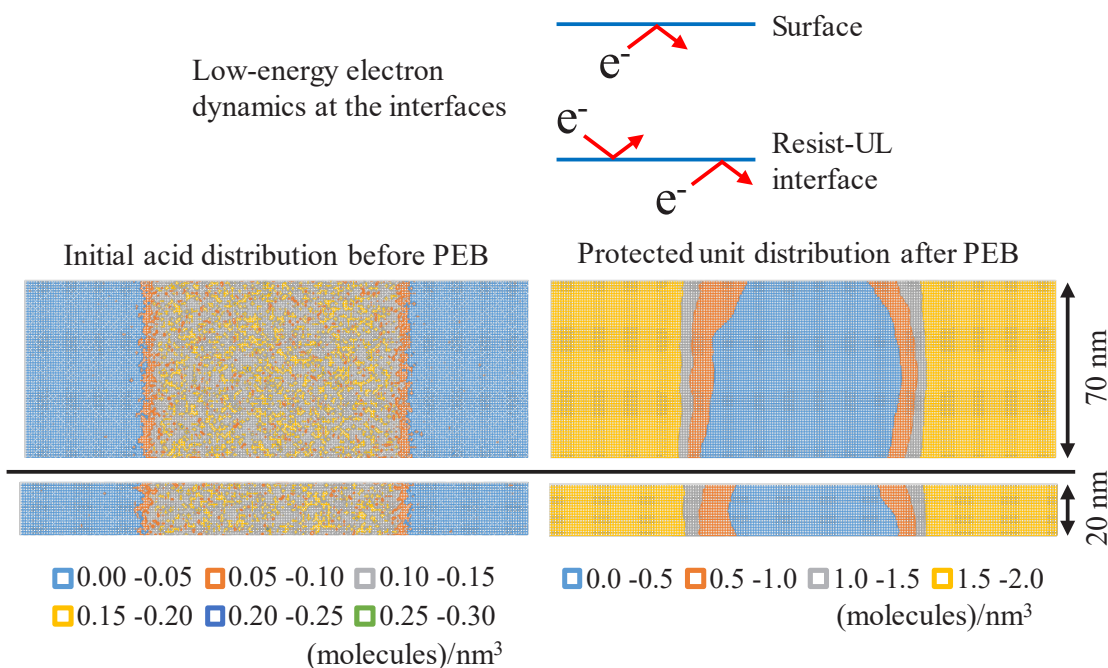


Fig. 3. Initial resist film thickness dependence of initial acid distribution before PEB and protected unit distribution after PEB, obtained by the simulation. The boundary conditions were reflection (from resist layer to vacuum), reflection (from resist to UL), and reflection (from UL to resist).

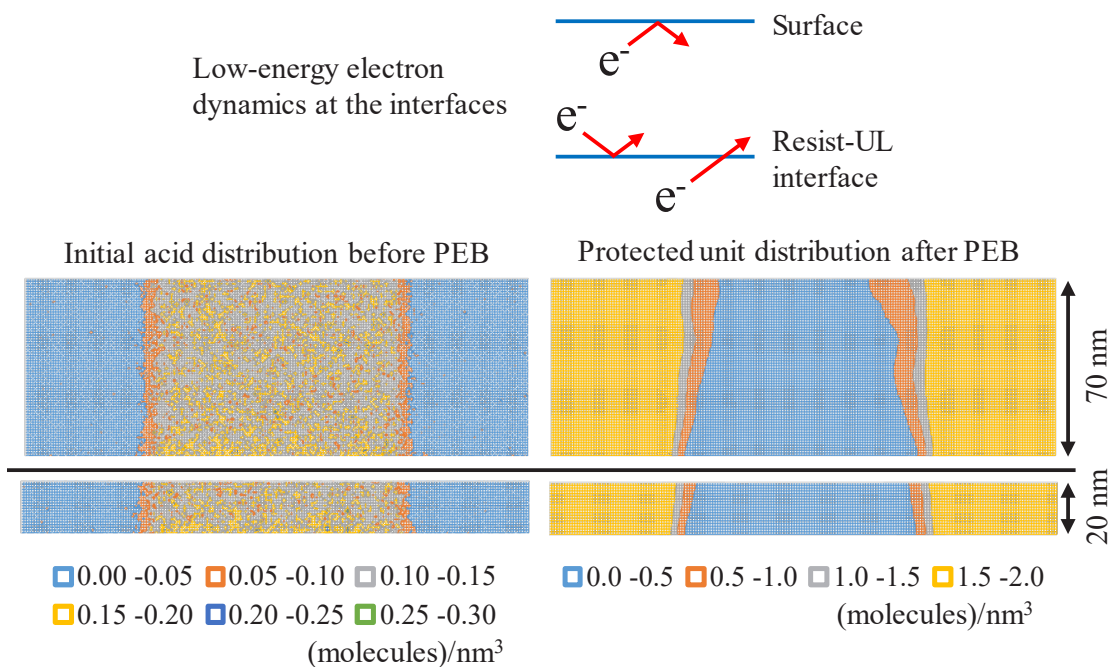


Fig. 4. Initial resist film thickness dependence of initial acid distribution before PEB and protected unit distribution after PEB, obtained by the simulation. The boundary conditions were reflection (from resist layer to vacuum), reflection (from resist to UL), and transmission (from UL to resist).

Figure 4 shows the initial resist film thickness dependence of initial acid distribution before PEB and protected unit distribution after PEB, calculated with the boundary condition that the low-energy electrons can move from UL to the resist layer. The reflection was assumed for the other

boundary conditions. The acid concentration near UL increased owing to the influx of low-energy electrons from UL. Consequently, the pattern shape became an inverse tapered shape. The dependence of protected unit concentration near UL on the initial resist film thickness was not observed.

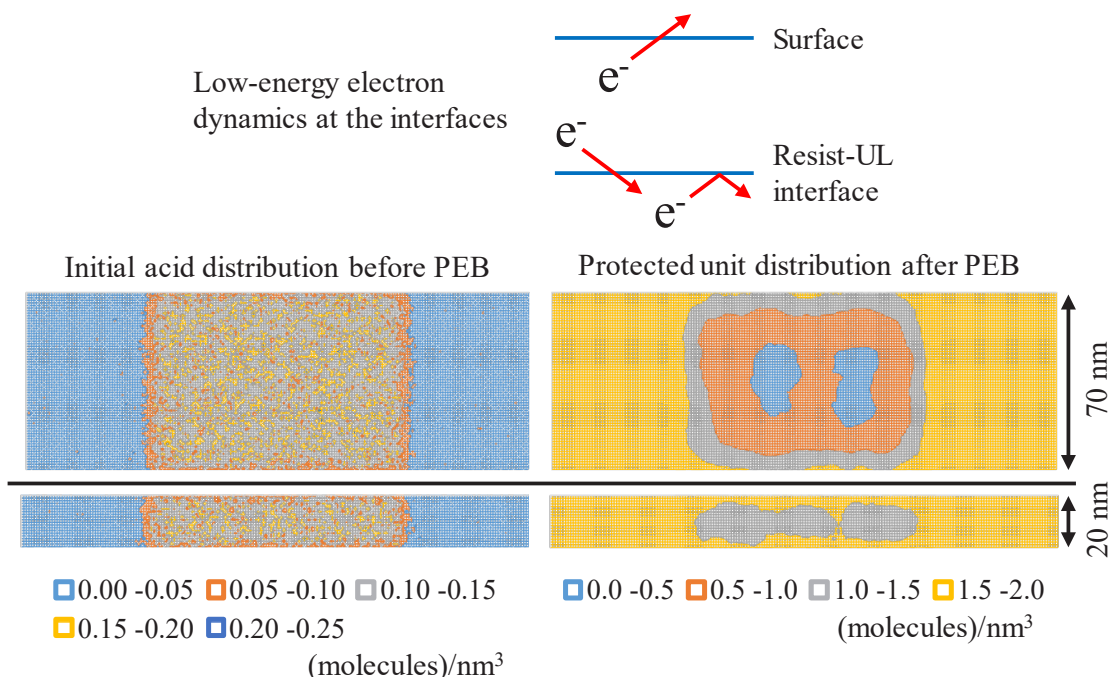


Fig. 5. Initial resist film thickness dependence of initial acid distribution before PEB and protected unit distribution after PEB, obtained by the simulation. The boundary conditions were transmission (from resist layer to vacuum), transmission (from resist to UL), and reflection (from UL to resist).

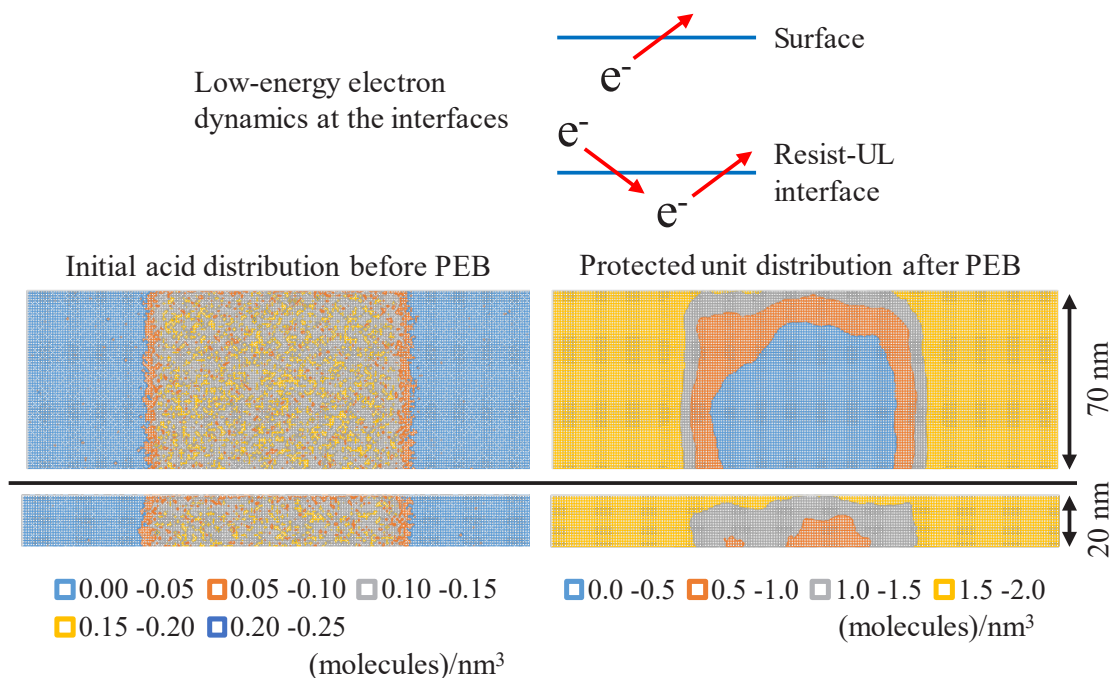


Fig. 6. Initial resist film thickness dependence of initial acid distribution before PEB and protected unit distribution after PEB, obtained by the simulation. The boundary conditions were transmission (from resist layer to vacuum), transmission (from resist to UL), and transmission (from UL to resist).

Thus far, the effect of interface between resist film and UL on the initial resist film thickness dependence was discussed. Next, the effect of surface condition is discussed. The boundary conditions of the surfaces were reflection for the cases shown in Figs. 1-4.

Changing the boundary condition of the surface from reflection to transmission, the similar calculation was carried out for all the cases. Figs. 5, 6, 7, and 8 correspond to Figs. 1, 2, 3, and 4, respectively. The protected unit concentration near the surface decreased

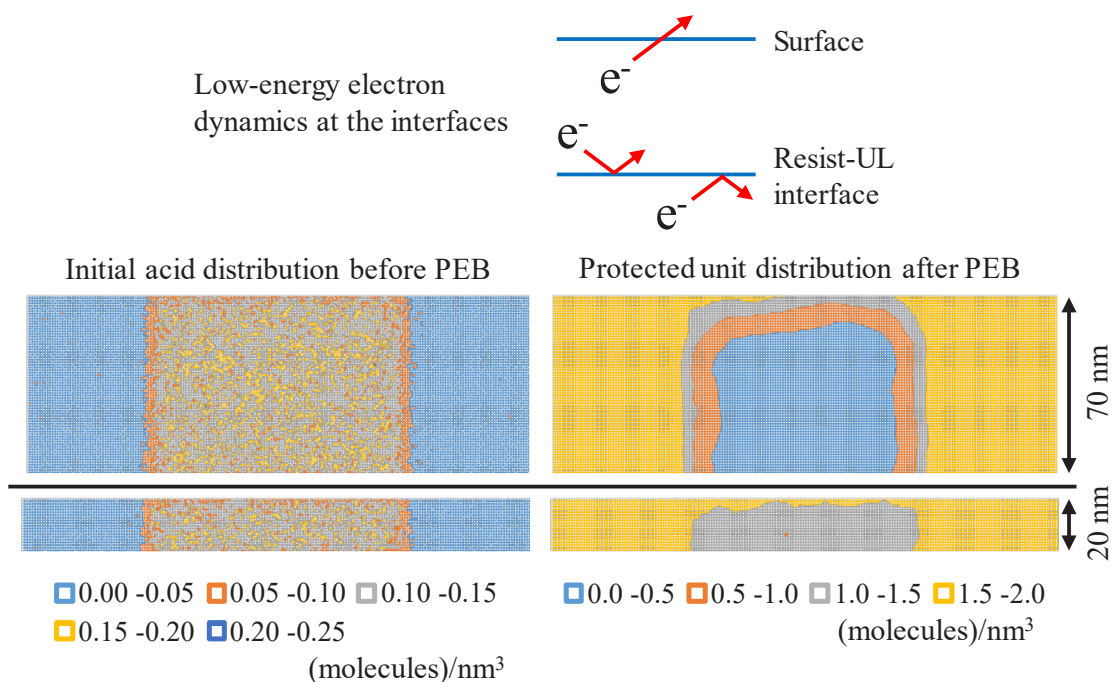


Fig. 7. Initial resist film thickness dependence of initial acid distribution before PEB and protected unit distribution after PEB, obtained by the simulation. The boundary conditions were transmission (from resist layer to vacuum), reflection (from resist to UL), and reflection (from UL to resist).

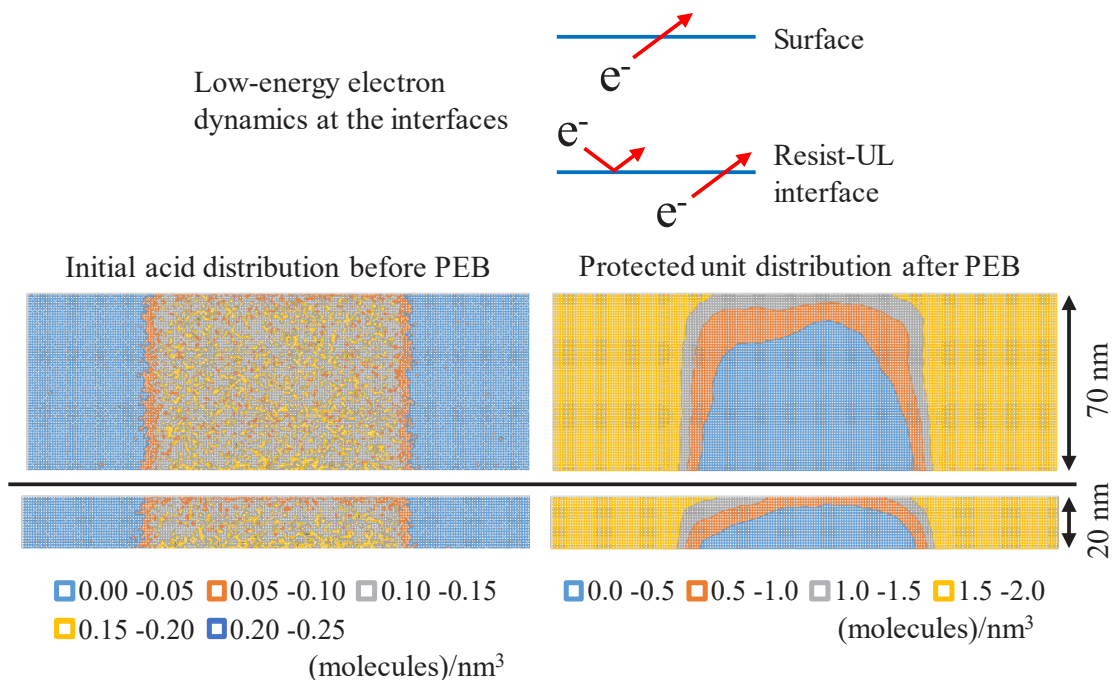


Fig. 8. Initial resist film thickness dependence of initial acid distribution before PEB and protected unit distribution after PEB, obtained by the simulation. The boundary conditions were transmission (from resist layer to vacuum), reflection (from resist to UL), and transmission (from UL to resist).

owing to the loss of acids caused by the escape of low-energy electrons from the surface. With the reduction of resist film thickness, this effect increased with the same reason discussed previously except for the case shown in Fig. 8. The situation is

complicated for the case shown in Fig. 8, because the interfaces at the top and bottom of resist layer have opposite effects. Both effects increase by decreasing the resist film thickness. Consequently, the effects of interfaces seemed to decrease with the

decrease of initial resist film thickness. The discussion about the comparison between Figs. 2 and 3 described above can also be applied to Figs. 6 and 7. The simulation results in Fig. 6 should be approximately the same as those in Fig. 7. The discrepancy was caused by the stochasticity of Monte Carlo method applied to the calculation of acid distribution. The same discussion can be applied to the real cases.

4. Conclusion

The resist film thickness dependence of the latent images of chemically amplified EB resists was investigated using the simulation on the basis of their sensitization and reaction mechanisms. The low-energy electron dynamics at the surface (the interface between vacuum and a resist layer) was categorized into two patterns. The low-energy electron dynamics at the interface between a resist layer and UL was categorized into four patterns. The decomposition of sensitizers (photoacid generators) were significantly affected by the dynamic of low-energy electrons at the interfaces of resist films. The subsequent deprotection was also affected by the initial acid distribution. Such interfacial effects basically increased with the decrease of resist film thickness. These results suggest that the resist formula should be optimized in accordance with the conditions of interfaces when the resist film thickness is reduced.

References

1. T. Tanaka, M. Morigami, and N. Atoda, *Jpn. J. Appl. Phys.*, **32** (1993) 6059.
2. S. F. Chini and A. Amirfazli, *Langmuir*, **26** (2010) 13707.
3. A. Kawai and K. Suzuki, *Jpn. J. Appl. Phys.*, **45** (2006) 5429.
4. H. Namatsu, *J. Photopolym. Sci. Technol.*, **15** (2002) 381.
5. T. Tanaka, M. Morigami, H. Oizumi, and T. Ogawa, *Jpn. J. Appl. Phys.*, **32** (1993) 5813.
6. K. Shin and G. Lee, *J. Photopolym. Sci. Technol.*, **16** (2003) 363.
7. R. Sakamoto, Y. Sakaida, and B. -C. Ho, *Proc. SPIE*, **8682** (2013) 868205.
8. M. Harumoto, T. Motono, A. F. Santos, C. Mori, Y. Tanaka, H. Stokes, M. Asai, J. Santillan, T. Itani, and T. Kozawa, *Jpn. J. Appl. Phys.*, **60** (2021) SCCA03.
9. T. Yamaguchi, K. Yamazaki, M. Nagase, and H. Namatsu, *Jpn. J. Appl. Phys.*, **42** (2003) 3755.
10. J. H. Kim, N. Choi, Y. -H. Kim, and T. -S. Kim, *Proc. SPIE*, **6153** (2006) 615337.
11. L. Singh, I. Matthew, A. Pawloski, and A. Minvielle, *Proc. SPIE*, **6153** (2006) 61530W.
12. N. Maeda, A. Konda, K. Okamoto, T. Kozawa, and T. Tamura, *Jpn. J. Appl. Phys.*, **59** (2020) 086501.
13. H. Ito and C. G. Willson, *Polym. Eng. Sci.*, **23** (1983) 1012.
14. T. Kozawa, Y. Yoshida, M. Uesaka, and S. Tagawa, *Jpn. J. Appl. Phys.*, **31** (1992) 4301.
15. K. Natsuda, T. Kozawa, K. Okamoto, A. Saeki, and S. Tagawa, *Jpn. J. Appl. Phys.*, **48** (2009) 06FC05.
16. A. Nakano, T. Kozawa, K. Okamoto, S. Tagawa, T. Kai, and T. Shimokawa, *Jpn. J. Appl. Phys.*, **45** (2006) 6866.
17. K. Okamoto, R. Matsuda, H. Yamamoto, T. Kozawa, S. Tagawa, R. Fujiyoshi, and T. Sumiyoshi, *Jpn. J. Appl. Phys.*, **52** (2013) 06GC04.
18. J. L. Lenhart, D. A. Fischer, S. Sambasivan, E. K. Lin, R. L. Jones, C. L. Soles, W. Wu, D. L. Goldfarb, and M. Angelopoulos, *Langmuir*, **21** (2005) 4007.
19. T. Hirayama, D. Shiono, S. Matsumaru, T. Ogata, H. Hada, J. Onodera, T. Arai, T. Sakamizu, A. Yamaguchi, H. Shiraishi, H. Fukuda, and M. Ueda, *Jpn. J. Appl. Phys.*, **44** (2005) 5484.
20. T. Hirayama, D. Shiono, J. Onodera, A. Yamaguchi, and H. Fukuda, *Polym. Adv. Technol.*, **17** (2006) 116.
21. T. Fukuyama, T. Kozawa, S. Tagawa, R. Takasu, H. Yukawa, M. Sato, J. Onodera, I. Hirosawa, T. Koganesawa, and K. Horie, *Appl. Phys. Express*, **1** (2008) 065004.
22. T. Fukuyama, T. Kozawa, K. Okamoto, S. Tagawa, M. Irie, T. Mimura, T. Iwai, J. Onodera, I. Hirosawa, T. Koganesawa, and K. Horie, *Jpn. J. Appl. Phys.*, **48** (2009) 06FC03.
23. T. Fukuyama, T. Kozawa, H. Yamamoto, S. Tagawa, M. Irie, T. Mimura, T. Iwai, J. Onodera, I. Hirosawa, T. Koganesawa, and K. Horie, *J. Photopolym. Sci. Technol.*, **22** (2009) 105.
24. K. C. Tseng, N. J. Turro, and C. J.

- Durning, *Phys. Rev.*, **E 61** (2000) 1800.
25. D. S. Fryer, P. F. Nealey, and J. J. Pablo, *J. Vac. Sci. Technol.*, **B 18** (2000) 3376.
 26. D. R. Medeiros, W. M. Moreau, K. Petrillo, M. Chauhan, W. S. Huang, C. Magg, D. Goldfarb, M. Angelopoulos, and P. Nealey, *Proc. SPIE*, **4345** (2001) 241.
 27. L. Singh, P. J. Ludovice, and C. L. Henderson, *Proc. SPIE*, **5039** (2003) 1008.
 28. T. Kozawa, S. Tagawa, R. Ohnishi, T. Endo, and R. Sakamoto, *Jpn. J. Appl. Phys.*, **50** (2011) 016504.
 29. T. Kozawa and S. Tagawa, *Jpn. J. Appl. Phys.*, **49** (2010) 030001.
 30. T. Kozawa and S. Tagawa, *Jpn. J. Appl. Phys.*, **50** (2011) 030209.
 31. R. Hirose, T. Kozawa, S. Tagawa, T. Kai, and T. Shimokawa, *Appl. Phys. Express*, **1** (2008) 027004.
 32. Y. Ikari, K. Okamoto, A. Konda, T. Kozawa, and T. Tamura, *Jpn. J. Appl. Phys.*, **59** (2020) 086506.
 33. T. Kozawa, *Jpn. J. Appl. Phys.*, **54** (2015) 056501.
 34. K. Natsuda, T. Kozawa, K. Okamoto, and S. Tagawa, *Jpn. J. Appl. Phys.*, **45** (2006) L1256.
 35. K. Natsuda, T. Kozawa, K. Okamoto, and S. Tagawa, *Jpn. J. Appl. Phys.*, **46** (2007) 7285.
 36. T. Kozawa and S. Tagawa, *Jpn. J. Appl. Phys.*, **50** (2011) 106502.
 37. T. Kozawa, *Jpn. J. Appl. Phys.*, **55** (2016) 056503.
 38. G. P. Watson, D. Fu, S. D. Berger, D. Tennant, L. Fetter, A. Novembre, and C. Biddick, *J. Vac. Sci. Technol.*, **B 14** (1996) 4277.
 39. H. Yamamoto, T. Kozawa, A. Nakano, K. Okamoto, Y. Yamamoto, T. Ando, M. Sato, H. Komano, and S. Tagawa, *Jpn. J. Appl. Phys.*, **43** (2004) L848.

Investigations of Matrix-Exposure Lithography Using Stacked Linear Arrays of Squared Optical Fibers

Toshiyuki Horiuchi*, Jun Watanabe, Jun-ya Iwasaki, and Hiroshi Kobayashi

*Department of Advanced Machinery Engineering, Graduate School of Engineering,
Tokyo Denki University, 5 Senju-Asahi-cho, Adachi-ku, Tokyo 120-8551, Japan*

**horiuchi@cck.dendai.ac.jp*

Plastic optical fiber matrices with squared ends were investigated. Such fiber matrices are particularly required for printing two dimensional code marks by using them as new lithography tools combining with light emitting diodes. A large number of fibers with a diameter of 500 μm were packed in an oblong slit of a jig, and fiber ends were simultaneously transformed into square shapes by heating the jig on a hotplate. Next, three linear arrays, each composed of 10 fibers, were simply stacked and bound without coating any adhesives and/or opaque films. It was anticipated that light leaks from neighbored bright fibers degraded the printed pattern qualities. However, checker patterns were normally printed without influenced by neighbored bright fibers when the fiber ends were projected on a wafer through a 1/10 projection lens. Considering the advantages, a regularly arranged 10 \times 10 fiber matrix was fabricated on trial for demonstrating the availability of the matrix required for developing a matrix-exposure lithography system.

Keywords: Squared optical fiber, Optical fiber matrix, LED exposure, Projection lithography, Code mark printing

1. Introduction

Matrix-exposure lithography using a plastic optical fiber matrix with squared ends was proposed in our past research earlier than 2010 [1-4]. Each fiber in the matrix was led individually to a light emitting diode (LED) for supplying exposure light. Bright and dark conditions of the fiber ends were assigned by lighting the LEDs arbitrarily using a personal computer, and patterns corresponding to a brightness map of the fiber matrix were projected on a wafer by reducing the sizes in 1/10 through a projection lens.

It is thought that such a method is simple and low-cost, and effective for printing two dimensional (2D) code marks. In particular, lithographic printing of 2D code marks is practically used in actual production lines of display panels. That is, code marks including serial numbers, lot numbers and others are frequently printed at an early process step, and they are used for quality controls. However, commercially available exposure systems for the exclusive use of code mark printing [5,6] are rare and expensive.

It has been demonstrated that 2D code marks were successfully printed using a 10 \times 10 fiber matrix fabricated by binding plastic optical fibers with a diameter of 1 mm and squared ends. The marks are readable using a commercial code mark reader without failures [7-11]. However, it is worried that printed code mark patterns with a unit size of 1mm \times 1/10=100 μm were too large to increase the matrix scale to 22 \times 22, 44 \times 44, and others [12,13]. It is required to control the 2D code mark sizes less than approximately 2 mm square.

For this reason, in this research, fibers with a diameter of 500 μm are used instead for reducing printable element pattern sizes in a half. In addition, to fabricate precise fiber matrices efficiently using such fine fibers, a new method is developed for fabricating linear arrays of optical fibers with squared ends. Fibers are contacted and arrayed in an oblong slit of a jig, and fiber ends are simultaneously transformed into square shapes by heating the jig on a hotplate [14]. Next, linear arrays of squared fibers obtained by the new method are simply stacked and bound together

without coating any adhesives and/or opaque films. Then, using the 3×4 fibers in a 3×10 fiber-matrix, patterning characteristics are investigated. Besides, fabrication feasibility of a precise 10×10 fiber matrix is also investigated.

The system will also be applicable to maskless lithography for fabricating various microstructures such as bio-devices [15,16], micro fluidic devices [17-19], micro-lenses [20,21] and others in the future. On the other hand, lithography using LEDs is also watched with keen interest depending on the recent developments of ultra-violet and short visible light LEDs with strong intensities [22,23].

2. Lithography using squared fibers

A basic structure of the exposure system to be developed is shown in Fig. 1. A matrix of fine optical fibers is used in place of a reticle, and the brightness distribution of fiber ends assigned by a bright LED map is projected on various substrates such as panel boards, glass sheets and wafers coated with resist films. As a result, arbitrary patterns are printed on the substrates.

Printing of 2D code mark patterns is the primary application of this exposure method. To improve the quality and readability of code marks, the optical fiber ends should be square, and printed square unit patterns of dots or holes should be stitched precisely. Sizes and pitches of unit patterns should be kept uniform, and neighbored unit patterns should be printed closely each other.

In the past research, two methods for transforming circular fiber ends to square ones were developed. In the method developed at first, each optical fiber end was transformed by heating the fiber end one by one using a jig with the

structure shown in Fig. 2. The heated fiber end expanded in the jig to be transformed into a square shape and shrank in the axial direction instead. As a result, the fiber end was successfully transformed. However, it took a long time to get a lot of squared fibers required for fabricating a matrix. In addition, it was very difficult to assemble a lot of separated fibers in a regularly and precisely arranged matrix.

For this reason, a new method was developed next. In the new method, circular optical fibers were inserted in an oblong slit, and tightly arrayed in a line using a jig with the structure shown in Fig. 3. Fibers inserted in the jig slit were pushed from both sides not to make any gaps between neighbored fibers. Therefore, when the jig was heated on a hot plate, all of the heated fiber ends were simultaneously transformed into squared shapes. Heights of the squared fibers became almost uniform though the widths slightly fluctuated at random.

In this research, the new method was adopted. As a 0.5-mm plastic optical fiber, a commercial general-purpose fiber (Mitsubishi Chemical, ESKA, CK20) was used. It was demonstrated in the past research that at most 40 fibers were simultaneously transformed into square shapes within width and height errors of ±7.2 and ±6.5 nm, respectively, using the same fiber [14].

Moreover, in addition to the convenience for fabricating the fiber arrays, another advantage of the new method was found. That was the decrease of the fiber damages during the heat treatment.

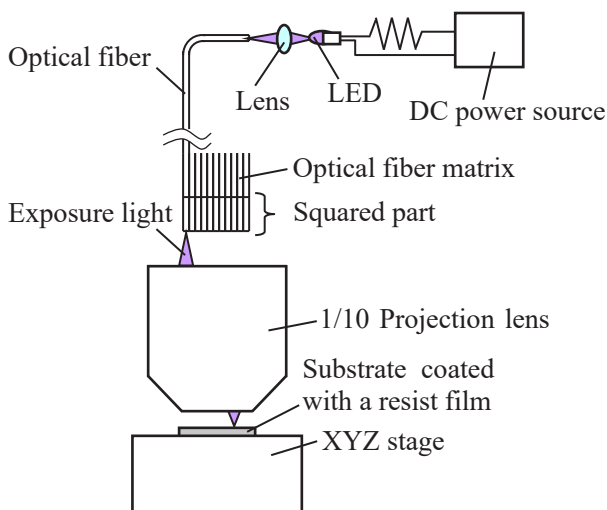


Fig. 1 Basic structure of aimed exposure system.

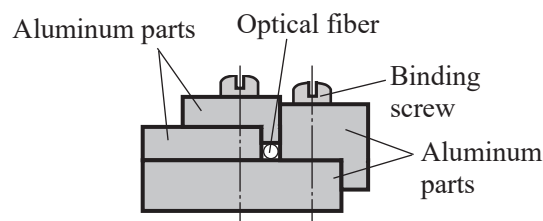


Fig. 2 Structure of the jig for transforming an optical fiber end to a square shape one by one.

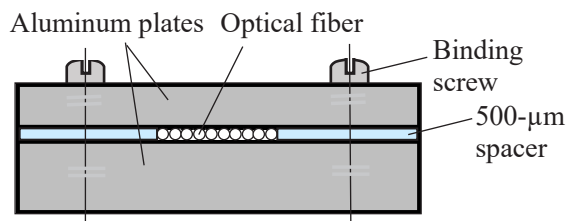


Fig. 3 Structure of the jig for transforming a large number of optical fiber ends into square shapes simultaneously.

When fibers were transformed into squares one by one, heated fiber clads were separated from cores, and light from LEDs leaked much from the damaged fibers. In comparison, in the new method, damages between neighbored fibers were almost prevented, and average light leak of 10 fibers was decreased from 34.4% to 20.4% [14].

For this reason, patterning characteristics of a fiber array and a matrix fabricated by the new method were investigated. The heating temperature was kept at 120°C.

3. Patterning Characteristics

Lithography performances of a linear fiber array composed of 10 fibers was investigated at first. Actually, the 8 fibers except 2 fibers with irregular shapes at both sides were used, as shown in Fig. 4. Exposure light rays from blue LEDs with a central wavelength of 405 nm were supplied to fibers through condenser lenses. Each fiber was paired with a LED (OptoSupply, OSSV5111A). The squared fiber array was placed at the reticle position of a test exposure system equipped with a 1/10 projection lens [7-11]. The numerical aperture of the lens was 0.4. As a resist, positive THMR iP-3300 (Tokyo Ohka Kogyo) with a thickness of approximately 1 μm was used.

Thus, when square patterns were printed using each fiber one by one solely, the sizes varied depending on the exposure time, as shown in Fig. 5. The sizes were the widths and heights measured crossing the pattern centers. The trends of size changes were normal and regular. Pattern widths and heights of 8 fibers at the appropriate exposure time of 2.2 s were $49.7 \pm 1.0 \mu\text{m}$, and $51.0 \pm 1.0 \mu\text{m}$, respectively. Width and height fluctuations were almost similar.

Typical shapes of printed squared hole patterns are shown in Fig. 6. Although the side edges of squared fibers were almost straight, pattern shapes were rather round. It was considered that the light intensity was strong at the center and weak at the

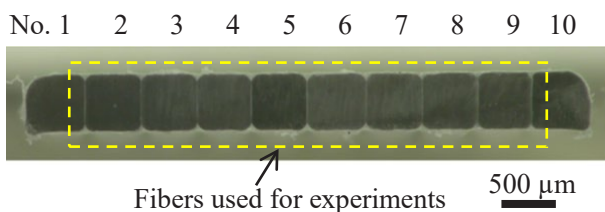


Fig. 4 The fiber array used for investigating patterning characteristics. Fibers except irregular ones at both sides were practically used.

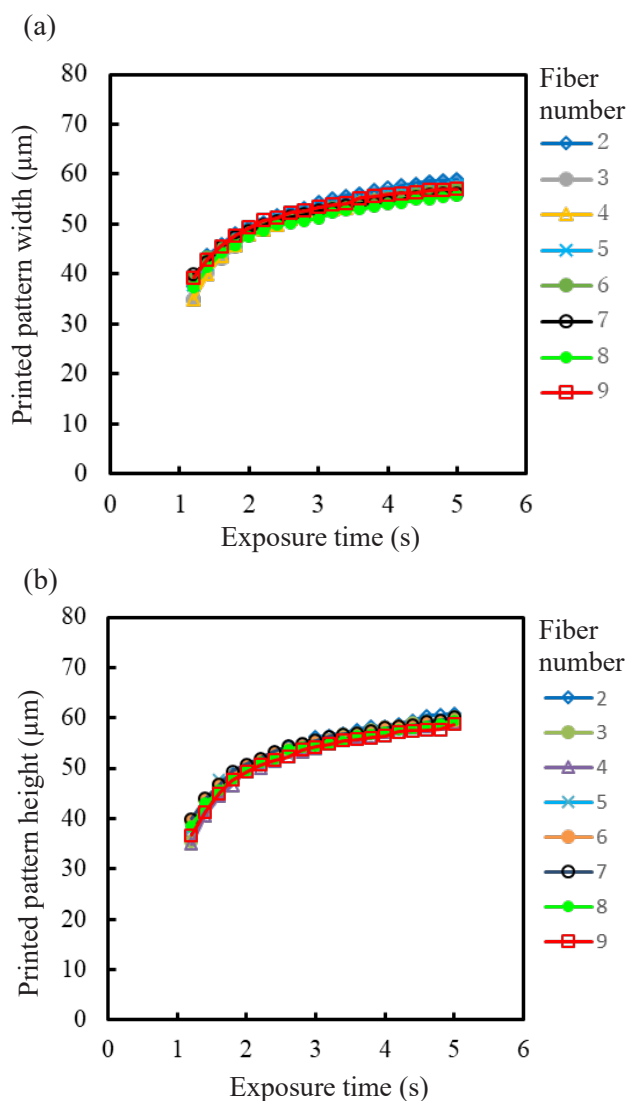


Fig. 5 Size dependence of printed square hole patterns on the exposure time. Pattern width dependence (a) and pattern height dependence (b) are compared.

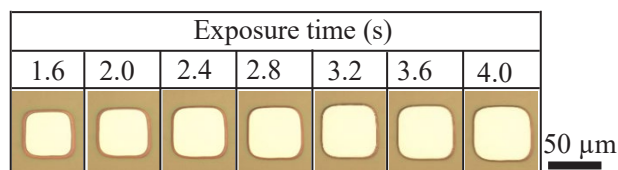


Fig. 6 Typical shapes of printed square hole patterns.

corners, because the length of the squared parts of fibers were as short as 30 mm.

Next, patterning characteristics were investigated using a small-scale fiber matrix fabricated by stacking and binding the fiber arrays. Because fibers were tightly assembled without gaps in the array (row) direction, it was expected that fiber arrays were stacked without gaps also in

the column direction.

For this reason, a small-scale matrix was fabricated on trial by simply stacking and binding 3 linear fiber arrays composed of 10 fibers without coating any opaque films and/or adhesive materials. The fabricated fiber matrix is shown in Fig. 7. The matrix was assembled by sandwiching the linear arrays using a pair of parallel aluminum plates bound by 2 pairs of a screw and a nut.

All the squared fibers obtained simultaneously were weakly adhered each other, and they are easily separated by pulling the fibers to be removed. Therefore, wrongly deformed fibers at both sides were peered off from regularly transformed inner fibers.

Although the fiber damage during the heating process was fairly reduced by the adoption of the new method, it was anticipated if patterns were faithfully printed as assigned by an on-off map of the LEDs. That is, it was worried that exposure light might leak through the slightly damaged fiber clads, and patterns different from the assigned ones might be printed. Therefore, it was investigated whether the light leaks badly influenced on the patterning or not. Using the 3×4 fibers shown in Fig. 7, checker patterns assigned in bright and dark alternately were printed under various exposure time conditions.

The results are shown in Fig. 8. Before the experiments, it was thought that the dark square parts surrounded by the bright square parts might be sensitized by the light leaked from the bright parts. However, the resist was correctly sensitized under appropriate exposure-time conditions as assigned by the bright fiber map, as shown in Fig. 8(a). Even if a very large exposure dose of 10 times larger than the appropriate one was given, parts corresponding to the dark fibers were not sensitized, as shown in Fig. 8(b).

Next, linear continuous patterns in the row

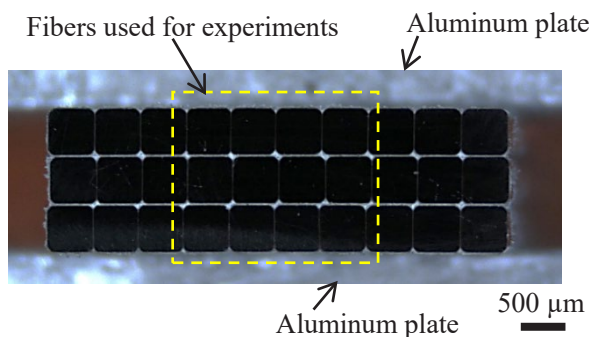


Fig. 7 Small-scale matrix fabricated by simply stacking and binding 3 linear 10-fiber arrays.

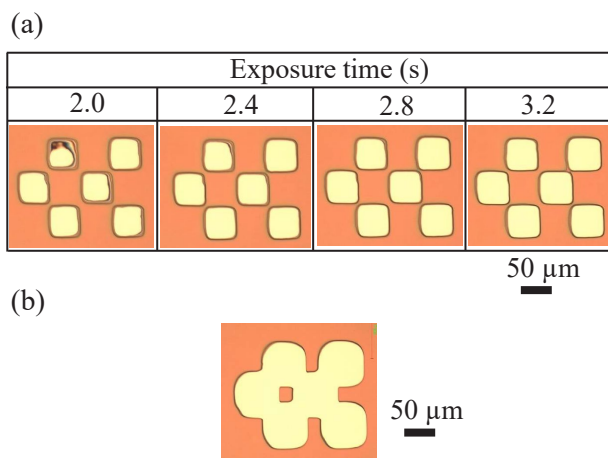


Fig. 8 Checker patterns printed using the 3×4 fiber matrix. Patterns printed under appropriate exposure-time conditions (a) and patterns printed under over exposure-dose condition of 30 s (b) are shown.

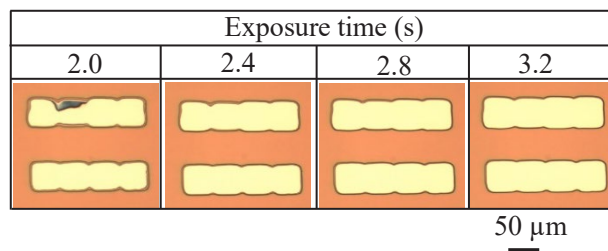


Fig. 9 Linear continuous patterns in the row direction printed using the 3×4 fiber matrix.

direction were printed using the same 3×4 fiber matrix. The results are shown in Fig. 9. It was confirmed that straight linear patterns with almost uniform widths of approximately 50 μm were printed though fine notches were observed periodically corresponding to the corner roundness of each element fiber.

4. Fabrication of 10×10 Fiber Matrix

It was demonstrated in the previous chapter that a fiber matrix fabricated by simply stacking and binding without using any opaque films and/or adhesive materials was applicable to matrix-exposure lithography. For this reason, availability of a quite large-scale fiber matrix was investigated by fabricating a 10×10 fiber matrix.

As the first step, 10 linear arrays, each of which was composed of 10 fibers with squared regular shapes, were fabricated. Next, the 10 linear fiber arrays were stacked by sandwiching them by 2 flat aluminum plates, and binding by 2 pairs of a screw and a nut at both sides. As a result, a well-assembled fiber matrix was obtained, as

shown in Fig. 10.

Fiber sizes were evaluated next. Because all the fibers were tightly contacted with the neighbored ones, the fiber sizes were equal to the fiber pitches. Measured fiber sizes in horizontal and vertical directions, or the fiber widths and heights are shown in Figs. 11 and 12. The widths and heights are plotted only for No. 1, 4, 7, 10 row from the top, because it became difficult to detect size fluctuations in each row, if all the size data were plotted together. Distribution or fluctuations of fiber widths and heights for all the 10×10=100 fibers were 489±20 μm and 500±5 μm, respectively. Uniformity of the widths was inferior to that of the heights. It was considered that this result was caused by the simultaneous deformation process of a large number of fibers from circular cross sections to square ones.

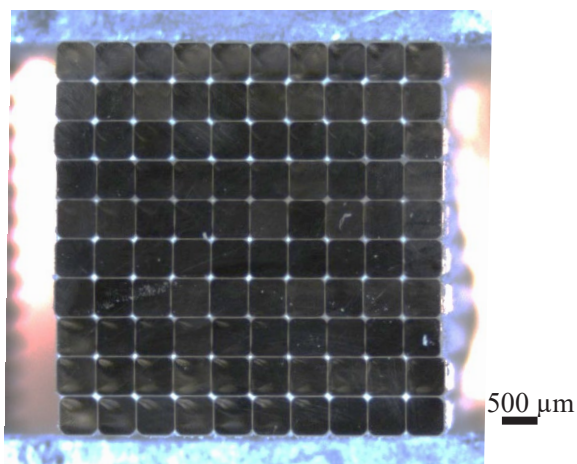


Fig. 10 10×10 fiber matrix assembled by stacking and bounding 10-fiber linear arrays.

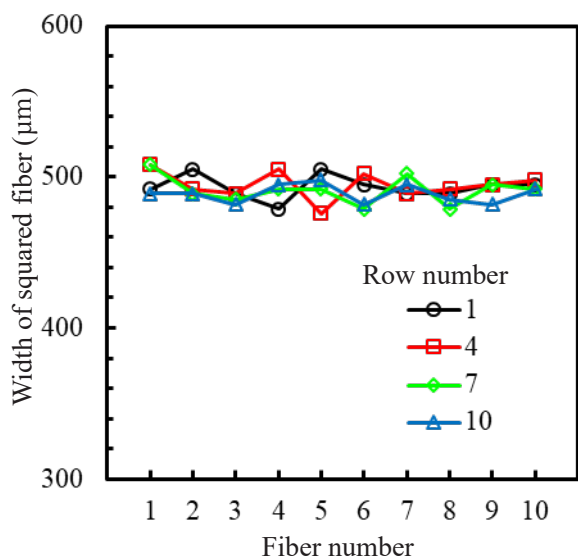


Fig. 11 Measured fiber width uniformity.

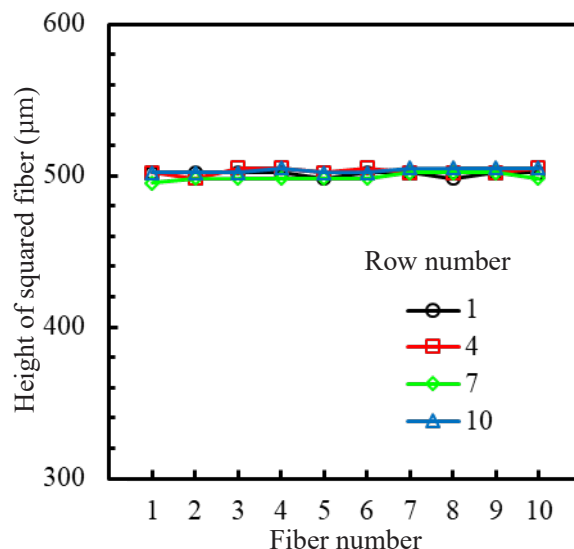


Fig. 12 Measured fiber height uniformity.

On the other hand, square ratio S defined by Eq. (1) was also evaluated [4]. Here, d_1 and d_2 are the diagonal lengths, w is the width, and h is the height of a fiber cross section. S becomes 0 for a circular shape, and S becomes 1 for a square shape. Calculated S values were distributed between 0.49-0.75, and differed from row to row, as shown in Fig. 13. The average value was 0.64. The ratio should be improved up to 0.70 by making some more progresses in the array fabrication processes or preparing spare fiber arrays and selecting superior ones.

$$S = \frac{1}{\sqrt{2}-1} \frac{(d_1 + d_2) - (w + h)}{w + h} \quad (1)$$

In the past research, a 10×10 fiber matrix composed of individually squared 1-mm fibers was

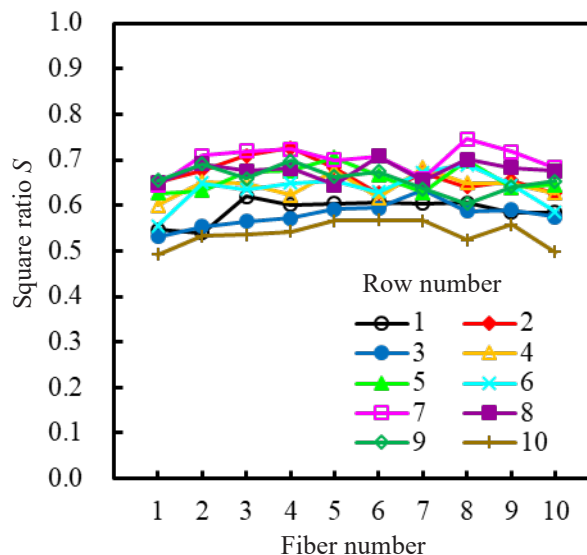


Fig. 13 Square ratios of all the squared fibers.

Silver lacquer and adhesive coated on fibers

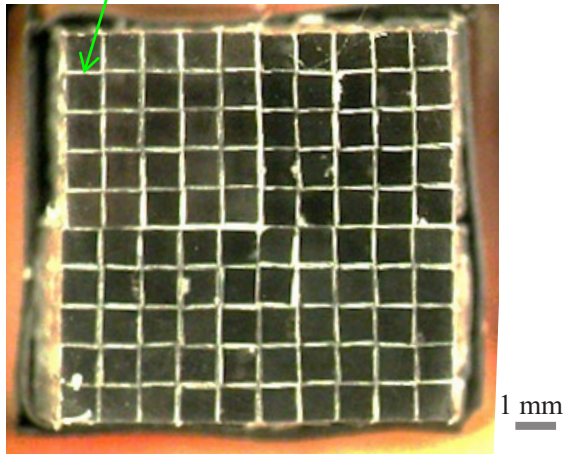


Fig. 14 Fiber matrix composed of 1-mm square fibers fabricated in the past research [8, 10].

fabricated, as shown in Fig. 14 [8, 10]. The fiber matrix was used for printing 2D code marks on Si wafers using the same 1/10 projection exposure system and resist processes, and the 2D code marks were certainly read without fails by a commercial code mark reader [8-11]. The size uniformity and regulation of the fiber matrix obtained in this research and shown in Fig. 10 is obviously superior to the fiber matrix obtained in the past research and shown in Fig. 14. It is considered that the size errors and fluctuations shown in Figs. 10-12 are within allowable ranges.

5. Discussion

In the new method, fibers were deformed almost symmetrically in both width and height directions of fiber cross sections, because all the fibers were tightly packed, and all fiber sides became straight. In addition, squared fiber corners became almost circular. Considering these facts, relationship between the square ratio and the corner roundness was investigated assuming all the fiber corners were geometrically circular.

In the past research, the square ratio S was defined by Eq. (1). However, if the fiber corners are circularly round, it was found that S is calculated by a very simple equation.

The diagonal lengths $d_1=d_2=d$ are expressed by the side length a and the corner radius r , as shown in Eq. (2), referring to Fig. 15.

$$d_1 = d_2 = d = \sqrt{2}(a - 2r) + 2r \quad (2)$$

If Eq. (2) is substituted in Eq. (1) assuming

both the fiber width w and the height h are equal to a , S is calculated by Eq. (3).

$$\begin{aligned} S &= \frac{1}{\sqrt{2}-1} \frac{2\sqrt{2}(a-2r) + 4r - 2a}{2a} \\ &= \frac{1}{\sqrt{2}-1} \frac{(\sqrt{2}-1)a - 2(\sqrt{2}-1)r}{a} \\ &= 1 - \frac{2r}{a} \end{aligned} \quad (3)$$

This relationship between S and r is shown in Fig. 16. It is known from Eq. (3) and Fig. 16 that S decreases linearly in proportion to r . The square ratio S was defined by Eq. (1) in the past research at first as a parameter expressing the normalized difference between the average diagonal length and side length of a fiber cross section. However, this time, it was clarified that S related directly and

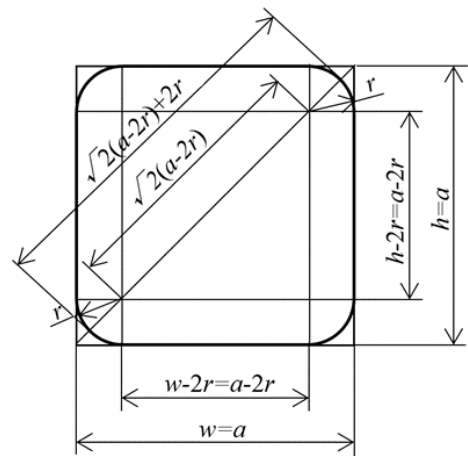


Fig. 15. Figure prepared for explaining the parameters for calculating the square ratio.

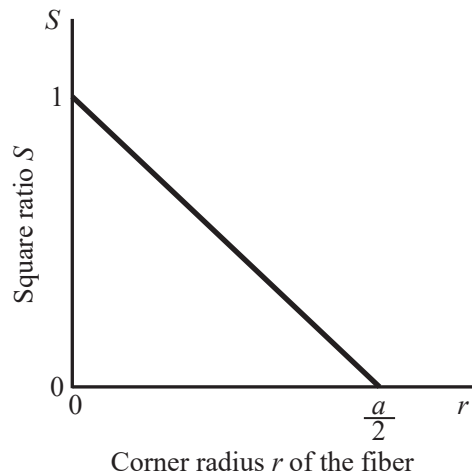


Fig. 16 Newly found relationship between the square ratio and the corner radius of the fiber.

linearly to the corner radius r . It was found that S was a more qualified, reasonable and eligible parameter than it had been recognized.

5. Conclusion

A new method for transforming end parts of plastic optical fibers with a diameter of 500 μm into square ones simultaneously in a line was applied to the fabrication of fiber matrices. In addition, applicability of the matrices to the matrix-exposure lithography was investigated.

It had been anticipated if arbitrary patterns were regularly printable using a fiber matrix fabricated by simply stacking and binding linear arrays of squared fibers without coating any opaque films and/or adhesives. However, it was verified that checker patterns were exactly printed without influenced by neighbored bright fibers.

In addition, availability of a regularly and precisely arranged 10×10 fiber matrix was demonstrated. Moreover, it was clarified that the square ratio S proposed in the past research was simply expressed by $S=1-r/2a$, when corners of squared fibers with a side length of a were circularly rounded to a radius of r . It was found that S is a qualified parameter expressing the corner roundness relevantly.

Prospects for the reduction of pattern size unit to a half are promising if the new method is adopted. Further research efforts should be made.

Acknowledgement

This work was partially executed in the collaboration research with JI engineering, and partially supported by the contributed funds from Shonan Instruments.

References

1. J. Iwasaki and T. Horiuchi, *Techn. Dig., ODF'10, 7th Int. Conf. Optics-photonics Design & Fabrication*, (2010) 341.
2. J. Iwasaki and T. Horiuchi, *Opt. Rev.* **19** (2012) 198.
3. J. Iwasaki and T. Horiuchi, *Rev. Sci. Instrum.* **83** (2012) 045445.
4. J. Iwasaki and T. Horiuchi, *J. Photopolym. Sci. Technol.*, **25** (2012) 461.
5. http://www.toray-eng.com/products/fpd/fpd_011.html, TNT Series Optical Mask Type Marking Titlers (2021).
6. http://www.toray-eng.com/products/fpd/fpd_012.html TRT-iW/gW/hW Series Laser Type Marking Titlers (2021).
7. J. Watanabe, K. Kato, J. Iwasaki, and T. Horiuchi, *Dig. Pap., Photomask Japan 2014, 21st Symp. Photomask and NGL Mask Technol.*, (2014) 40.
8. J. Watanabe, K. Kato, J. Iwasaki, and T. Horiuchi, *Dig. 27th Int. Microprocesses and Nanotechnol. Conf.* (2014) 6P-7-96.
9. J. Watanabe, J. Iwasaki, and T. Horiuchi, *Dig. Pap., Photomask Japan 2015, 22nd Symp. Photomask and NGL Mask Technol.* (2015) 44.
10. J. Watanabe, K. Kato, J. Iwasaki, and T. Horiuchi, *Jpn. J. Appl. Phys.*, **54** (2015) 06FP11.
11. J. Watanabe, J. Iwasaki, and T. Horiuchi, *Proc. SPIE*, **9658** (2015) 965817.
12. <http://www.idautomation.com/barcode-faq/2d/data-matrix/>, Data Matrix 2D Barcode ISO/IEC 16022 FAQ (2021).
13. <http://whatis.techtarget.com/definition/QR-code-quick-response-code>, QR code (quick response code) (2021).
14. T. Horiuchi, J. Watanabe, Y. Suzuki, and J. Iwasaki, *Proc. SPIE*, **10232** (2017) 102320D.
15. I. Byun, J. Yang, and S. Park, *Microelectronics J.*, **39** (2008) 717.
16. J. Watanabe, J. Iwasaki and T. Horiuchi, *9th Int. Joint Conf. Biomed. Eng. Sys. Technol., Proc. I, Biodevices* (2016) 203.
17. J. He, R. Chen, Y. Lu, L. Zhan, Y. Liu, D. Li, and Z. Jin, *Materials Sci. and Eng. C*, **59** (2016) 53.
18. I. Doh, S. Youn, Y. H. Jin, and Y. H. Cho, *Current Appl. Phys.*, **12** (2012) 1596.
19. L. Wang, R. Kodzius, X. Yi, S. Li, Y. S. Hui, and W. Wen, *Sens. Act. B*, **168** (2012) 214.
20. C. T. Pan, T. L. Yang, Y. C. Chen, C. M. Chang, J. H. Hsu, and J. C. Huang, *Optik*, (2016) 6850.
21. H. Kim, J. Kim, J. Kim, B. Lee, S. D. Lee, *Optics. Commun.*, **357** (2015) 52.
22. K. Zhong, Y. Gao, F. L. N. Luo, and W. Zhang, *Optics Laser Techn.*, **56** (2014) 367.
23. H. L. Chien, Y. H. Chiu, and Y. C. Lee, *Optics Lasers Eng.*, **136** (2021) 106313.

Research on a New Lithography Method Utilizing Laser Speckles for Printing Random Patterns

Hiroshi Kobayashi*, Iwaoka Tomoki, Kazuki Oi
and Toshiyuki Horiuchi

*Graduate School of Engineering, Tokyo Denki University,
5 Senju-Asahi-cho, Adachi-ku, Tokyo 120-8551, Japan*

**h_kobayashi@mail.dendai.ac.jp*

A new simple and low-cost optical lithography method utilizing speckles was developed for printing random patterns on surfaces of three-dimensional objects with various shapes, and patterning characteristics were investigated by assembling a handmade exposure system. In the system, a laser beam was irradiated on a transparent diffuser plate, and generated speckles were projected onto a wafer coated with a resist. As a result, resist patterns with random shapes were successfully formed after the development. The size and number of patterns were controllable by adjusting the exposure time. Pattern sizes were between several tens microns and a few hundred microns. It was demonstrated also that the pattern sizes were controlled by changing the wafer position from the diffuser plate. However, the sizes and numbers of patterns were varied together when the exposure time or the distance between the diffuser and the wafer was changed.

Keywords: Random pattern, Lithography, Speckle

1. Introduction

Lotus leaves and rose petals have minute surface structures barely observable without using a microscope, and it causes their hydrophobic properties [1-7]. Similar hydrophobic performances have been discovered in various plants and insects though modified surface structures and the performances are different [8-17].

If water-repellent surfaces are obtained by giving some surface modifications on various things used outdoors daily or casually, utilities and values of the things will be much improved. The purpose of this research is to print random patterns with sizes of between tens microns and a few hundred microns on silicon wafers, stainless steel plates or other material objects with arbitrary shapes easily and inexpensively using an original lithography method utilizing laser speckles. If the patterned objects are etched, the surfaces are modified, and changes of hydrophobic properties are expected.

Generally speaking, in various optical systems, speckles are disliked because they cause fine uneven brightness distribution, and efforts for decreasing speckles are made vigorously [18-21]. In

contrast, in this research, patterns are printed by positively utilizing high-contrast speckles. As a related research, speckle lithography is applied to creation of non-reflective silicon structure [22]. However, applications to improvements of hydrophobic properties have hardly been reported.

By using the speckle lithography, it is possible to provide simple and inexpensive exposure systems with large exposure fields for printing random patterns. In addition, though patterns are printed only on flat surfaces in most of the conventional lithography systems, it is considered that patterns can be formed on curved or stepped surfaces of objects with three-dimensional shapes.

It is expected that fine structures formed by etching substrates or objects using the random resist patterns as etching masks improve the hydrophobic properties. The idea of forming hydrophobic structures on non-planar objects utilizing speckles is novel and looks promising.

2. Properties of speckles

Speckles are light spots with irregular light intensity distributions generated by interference of

reflected or transmitted light from a rough material surface irradiated by a laser beam. Light scattered at the rough surface is radiated in various directions. When coherent light is used, the scattered light is complicatedly interfered each other, and high-contrast spot-like patterns with random shapes are generated in space. Because the speckle patterns are not formed by the imaging such as the projection using a lens or a mirror, they are clearly projected even if the distance between the rough surface and the object is changed. Therefore, they are thought applicable to the lithography onto arbitrary objects including three-dimensional ones, as shown in Fig. 1.

It was considered that if the bright and dark light distributions of speckles were projected on an object coated with a photosensitive resist film, patterns with random shapes were formed on the object after developing the exposed resist. Just to make sure, speckle patterns are projected on a flat white board, and taken by a camera before investigating the lithography. The photograph shown in Fig. 2 is a binarized image. White parts are places irradiated strongly, and black parts are places irradiated weakly. It was confirmed that patterns with various sizes between 10 and 100 μm and random shapes were observed.

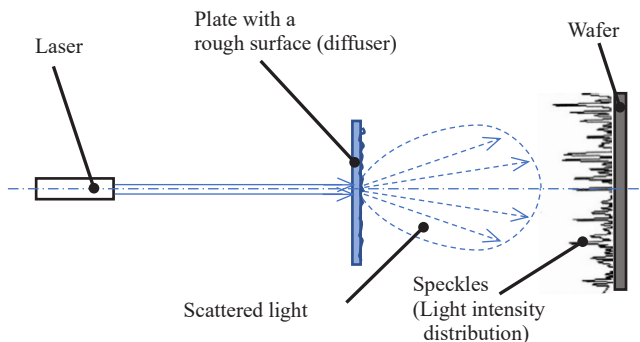


Fig. 1. Principle of exposure using speckles

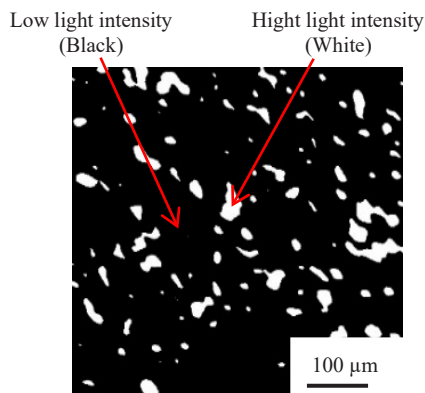


Fig. 2. Image of speckles captured by a camera and binarized.

3. Principle of exposure utilizing speckles

To confirm the principle, a simple experimental exposure system was assembled, and basic exposure characteristics of speckle lithography were investigated. An appearance of the system is shown in Fig. 3. The system consists of a laser diode with a wavelength of 405 nm and a power of 7 mW, a diffuser (# 1000 SIGMAKOKI Co., Ltd.), and a wafer stage. The wafer was held by a vacuum chuck. They are fixed on a guide rail in a line.

To efficiently and systematically grasp the patterning characteristics, it was decided to execute many experiments on one wafer under various exposure conditions. Therefore, a light-shading plate was placed in front of the wafer stage for limiting the exposure area to a 10 mm square. The space between the laser and the diffuser is prepared for mounting additional optical lenses, if necessary.

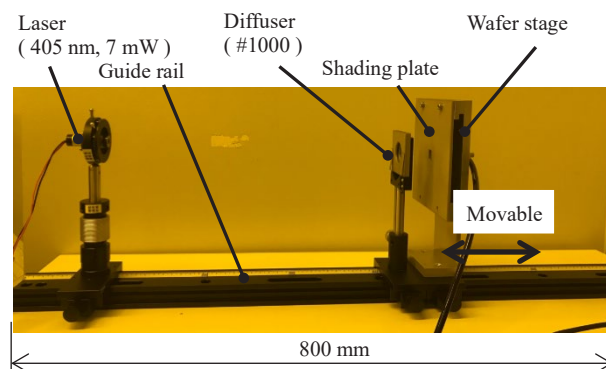


Fig. 3. Handmade exposure system assembled in this research.

4. Patterning results and discussion

4.1. Influence of exposure time

In this research, all the wafers were coated with a positive resist THMR-iP3300 (Tokyo Ohka Kogyo Co., Ltd.) in approximately 1 μm thick using a spin coater. The wafer diameter was 4 inches.

At first, influences of the exposure time on patterning characteristics were investigated. The exposure time was adjusted by turning the laser on and off. The distance between the diffuser plate and the wafer was set to 45 mm, and the exposure time was changed between 4 and 12 s. Printed patterns under each exposure time conditions are shown in Fig. 4.

Because the positive resist was used, the resist at the place where the speckle light intensity was strong disappeared in the development process, and patterns with irregular shapes were formed randomly. To evaluate the patterns quantitatively, the pattern size and the number of patterns were measured.

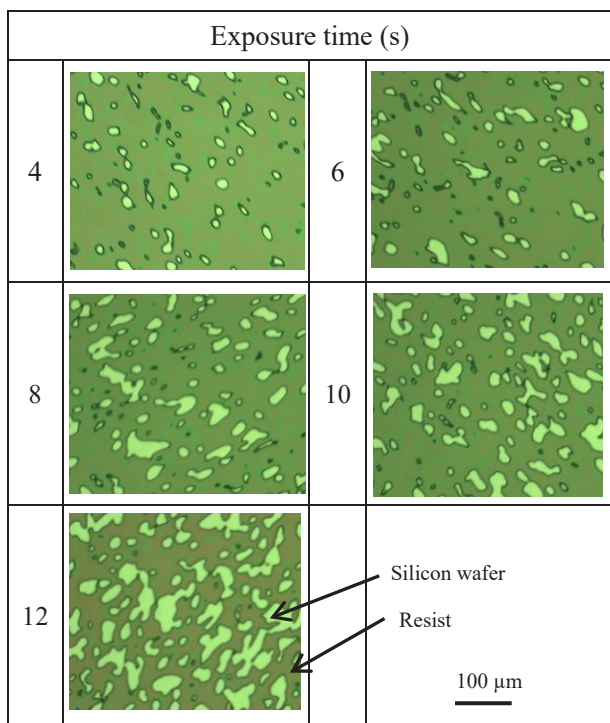


Fig. 4. Speckle patterns printed under various exposure time conditions.

Measurement methods of the size and the number of patterns are shown in Fig. 5.

As the pattern size, the maximum size of the largest pattern in the microscope image field of approximately $75 \times 10^{-3} \text{ mm}^2$ was measured. And, the number of independent patterns in which the resist was completely removed was counted in the microscope image field of 1 mm square.

Fig. 6 shows the relationship between the pattern size and the exposure time, and Fig. 7 shows the relationship between the number of patterns and the exposure time.

The pattern size increased as the exposure time was extended. Similarly, the number of patterns increased as the exposure time was lengthened.

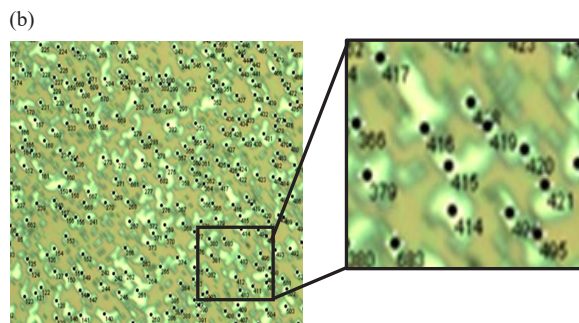
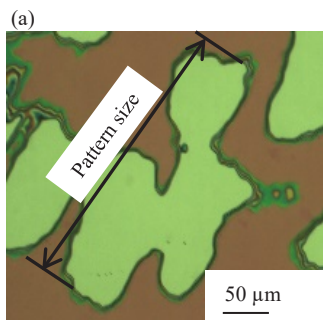


Fig. 5. Methods used for evaluating sizes and numbers of speckle patterns.

(a); An example of measured speckle pattern size. The largest size was measured.

(b); An example of number counting of speckle patterns.

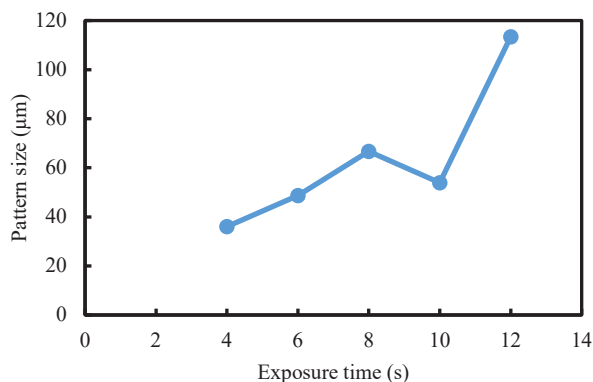


Fig. 6. Relationship between the pattern size and the exposure time.

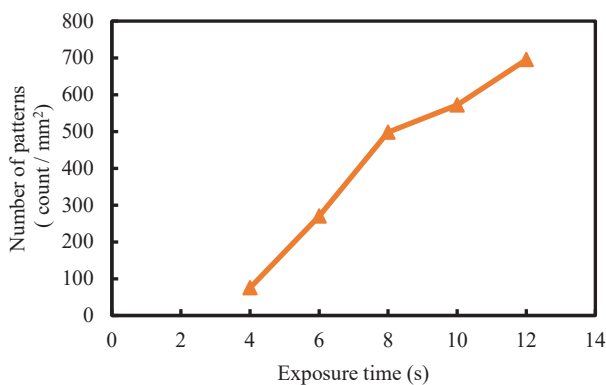


Fig. 7. Relationship between the number of patterns and the exposure time.

It was found possible to adjust the pattern size and the number of patterns to some extent by controlling the exposure time. However, it was difficult to control both the pattern size and the number of patterns independently.

4.2. Influence of diffuser-wafer distance

Patterns were printed changing the distance L between the diffuser and the wafer. L was changed between 45 and 200 mm. Because the exposure system was required to have a large exposure field, an optical element such as a reduction projection lens was not inserted between the diffuser and the wafer. Therefore, the scattered light spread and the intensity of speckle light decreased as the wafer was moved away from the diffuser. For this reason, the light intensity I on the wafer surface was measured. And the exposure time t was adjusted as the exposure dose D was almost constant using the following equation.

$$D = It \tag{1}$$

Patterns printed at various distances are shown in Fig. 8. It seemed that the pattern size increased and the number of patterns decreased as the distance was lengthened. To clarify the relationship between the diffuser-wafer distance and the size, or the number of patterns, pattern sizes and numbers of patterns were evaluated quantitatively. The change of pattern sizes depending on the distance is shown in Fig. 9.

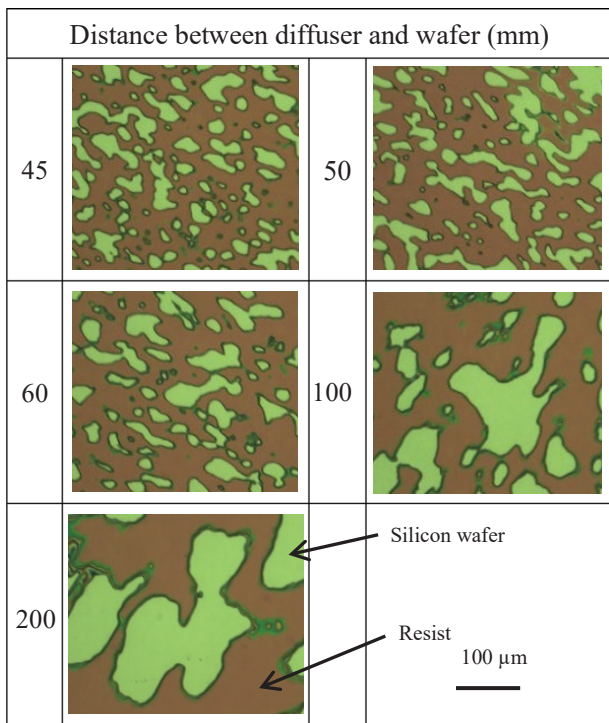


Fig. 8. Speckle patterns printed under various conditions of distance between diffuser and wafer.

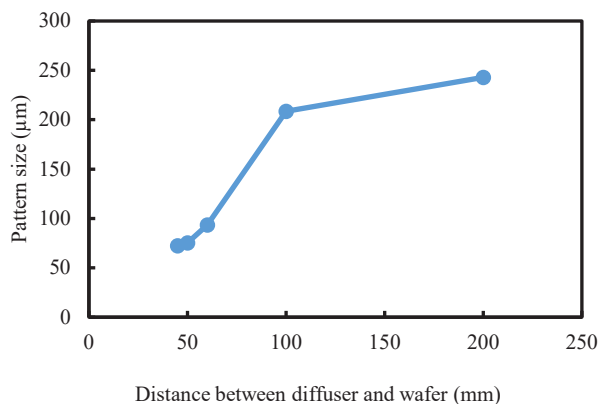


Fig. 9. Relationship between the pattern size and the distance between diffuser and wafer.

It was clarified that the pattern size could be controlled also by changing the distance between diffuser and wafer.

Next, the numbers of printed speckle patterns for various distances between diffuser and wafer were counted. Because the pattern density depended on the exposure time, the numbers were counted for various exposure times. Patterns used for the evaluation are shown in Figs. 10-12.

Figures show the results of exposures under different exposure-time conditions when the distance between diffuser and wafer is 45 mm, 100 mm, and 200 mm.

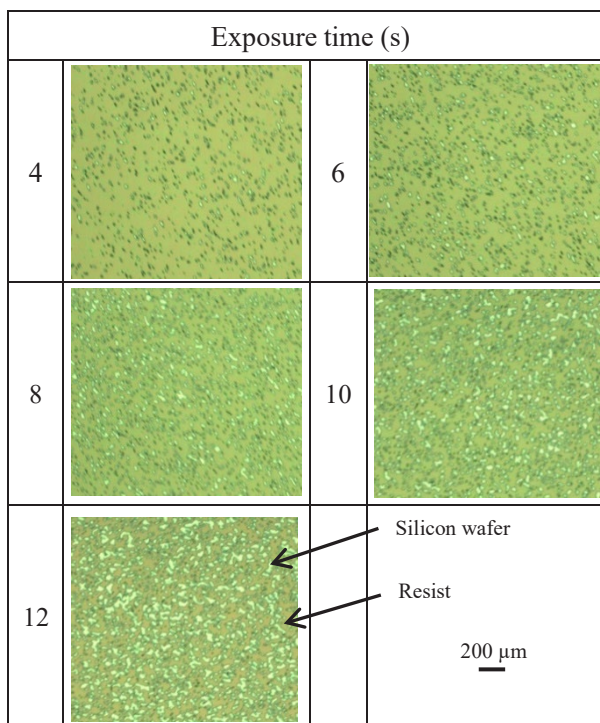


Fig. 10. Speckle patterns printed under various exposure time conditions when the distance between diffuser and wafer was 45 mm.

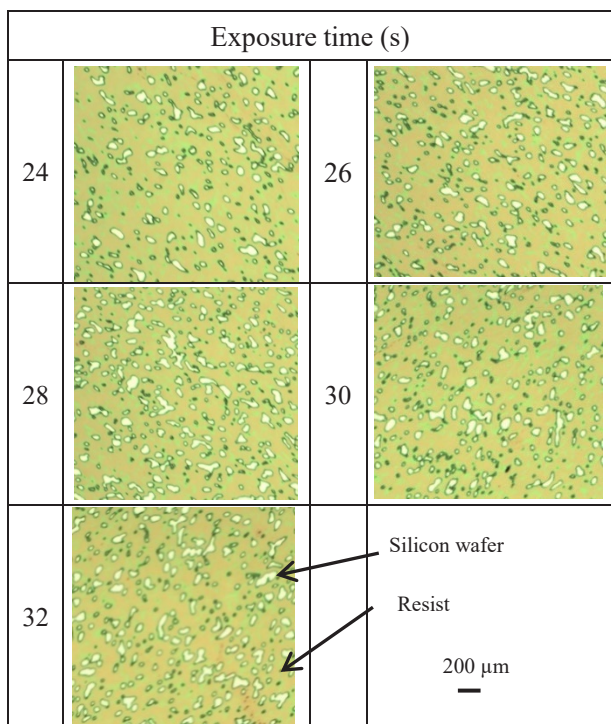


Fig. 11. Speckle patterns printed under various exposure time conditions when the distance between diffuser and wafer was 100 mm.

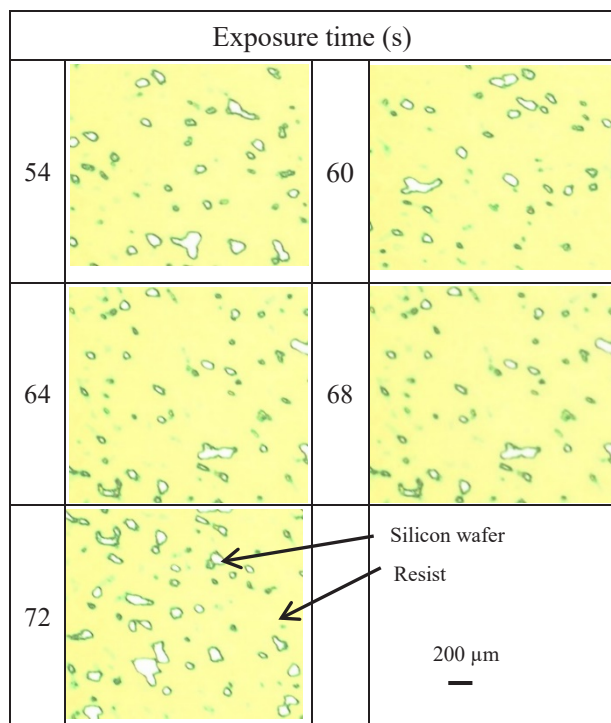


Fig. 12. Speckle patterns printed under various exposure time conditions when the distance between diffuser and wafer was 200 mm.

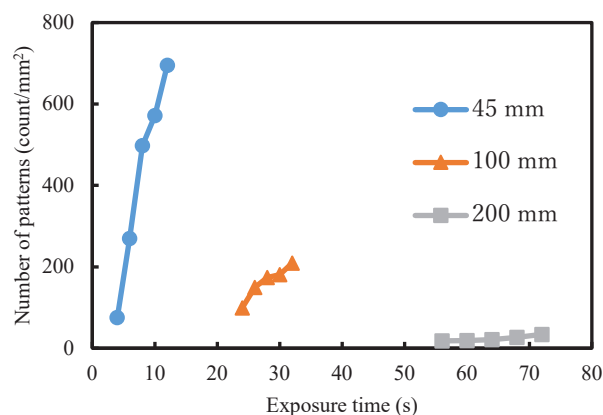


Fig. 13. Relationship between the exposure time and the number of patterns for each distance.

Counted pattern numbers for each distance and exposure time are shown in Fig. 13. It was clarified quantitatively that the number of patterns decreased as the distance between diffuser and wafer was lengthened. It was verified also that the number of patterns increased as the exposure time was extended regardless of the distance between diffuser and wafer.

5. Conclusion

It was demonstrated that random patterns were printed on the resist by using the light intensity distribution of laser speckles. Both the pattern sizes and the number of patterns increased as the exposure time was extended.

On the other hand, by lengthening the distance between diffuser and wafer, the pattern sizes increased and the numbers of patterns decreased.

It is expected that the new lithography method utilizing speckles is applicable to printing of random minute patterns on curved surfaces of three-dimensional structures with various unique shapes. It is prospected that hydrophobic properties and/or other surface characteristics may be improved, if the surfaces are etched or modified by using the resist patterns as masking materials.

References

1. T. Horiuchi, Y. Imon, K. Sumimoto, A. Yanagida, and H. Kobayashi, *Key Eng. Mater.*, **813** (2019) 19.
2. U. U. Ghosh, S. Nair, A. Das, R. Mukherjee, and S. Das Gupta, *Coll. Surf. A*, **561** (2019) 9.
6. T. Wang, L. Chang, B. Hatton, J. Kong, G. Chen, Y. Jia, D. Xiong, and C. Wong, *Mater. Sci. Eng. C*, **43** (2014) 310.
4. M. Karaman, N. Çabuk. D. Özyurt, and Ö.

- Köysuren, *Appl. Surf. Sci.*, **259** (2012) 542.
5. K. Koch, B. Bhushan, Y. C. Jung and W. Barthlott, *Soft Matter*, **5** (2009) 1386.
 6. B. L. Feng, S. Li, Y. Li, H. Li, L. Zhang, J. Zhai, Y. Song, B. Liu, L. Jiang, and D. Zhu, *Adv. Mater.*, **14** (2002) 1857.
 7. W. Barthlott, and C. Neinhuis, *Planta*, **202** (1997) 1.
 8. Z. Chen, Z. Zhang, Y. Wang, D. Xu, and Y. Zhao, *Mat. Sci. Eng. R*, **144** (2021) 100605.
 9. F. Wang, and S. Li, L. Wang, *Coll. Surf. A Phy. Eng.*, **513** (2017) 389.
 10. J. Nickerl, M. Tsurkan, R. Hensel, C. Neinhuis, and C. Werner, *J. R. Soc. Interface*, **11** (2014) 0619.
 11. P. P. Goodwyn, Y. Maezono, N. Hosoda, and K. Fujisaki, *Naturwissenschaften*, **96** (2009) 781.
 12. Y. Zhu, Y. Gao, C. Zhang, X. Zhao, Y. Ma, and F. Du, *Coll. Surf. A*, **547** (2018) 148.
 13. K. Koch, B. Bhushan, and W. Barthlott, *Soft Matter*, **4** (2008) 1943.
 14. X. Gao, X. Yan, X. Yao, L. Xu, K. Zhang, J. Zhang, B. Yang, and L. Jiang, *Adv. Mater.*, **19** (2007) 2213.
 15. Y. Zheng, X. Gao, and L. Jiang, *Soft Matter*, **3** (2007) 178.
 16. W. Lee, M. K. Jin, W. C. Yoo, and J. K. Lee, *Langmuir*, **20** (2004) 7665.
 17. A. Otten, and S. Herminghaus, *Langmuir*, **20** (2004) 2405.
 18. V. Kumar, A. k. Dubey, M. Gupta, V. Singh, A. Butola, and D. S. Mehta, *Opt. Laser Technol.*, **141** (2021) 107079.
 19. C. K. Lo, and J. W. Pan, *Opt. Commun.*, **454** (2020) 124301.
 20. K. Oleg, R. Slava, P. Bill, L. F. Bruno, F. Nigel, and L. Harry, *J. Vac. Sci. Technol. B*, **26** (2008) 2145.
 21. X. Cai, *Optik*, **125** (2014) 4389.
 22. J. Bingi, and V. M. Murukeshan, *Report*. **5** (2016) 18452.

Development of Materials Informatics Platform

Yasumitsu Orii^{1*}, Shuichi Hirose², Akihiro Fujita³, and Masakazu Kobayashi¹

¹ *New Value Creation Office, NAGASE & Co., LTD,*

5-1 Nihonbashi-Kobunacho, Chuo-ku, Tokyo, 103-8355, Japan

² *NAGASE R&D Center, New Value Creation Office, Nagase & Co., LTD*

2-2-3, Murotani, Nishi-ku, Kobe city, Hyogo, 651-2241, Japan

³ *R&D Center, HAYASHIBARA & CO., LTD.*

675-1, Fujisaki, Naka-ku, Okayama, 702-8006, Japan

**yasumitsu.orii@nagase.co.jp*

As the use of IT increases importance with big data and AI, the issue of power consumption has been highlighted. Under these circumstances, the development of new materials is more and more important. Materials Informatics (MI) is one of the hottest technologies in the material development field, because of its potential to reduce the time and costs of discovering innovative materials. To achieve this, the key is to collect data that has been accumulated for many years at research institutions and companies, and to make information extracted from the data into knowledge. This article introduces the development of two methods based on AI: the “cognitive approach”, which reads vast amounts of literature information and digitizes data, and the “analytic approach”, which theoretically estimates the structure and physical properties of chemical substances from predictive models.

Keywords: Materials Informatics, Cognitive approach, Analytics approach

1. Introduction

In terms of “data volume”, the total amount of digital information generated worldwide in 2010 exceeded 1 ZB (Zettabyte) per year and reached at 44 ZB in 2020[1]. The Internet of Things (IoT) is key factor of the data volume increasing. Conventionally, humans created data, but these days, machines and sensors create data on behalf of humans. And then, the data volume will expand to 163 ZB in 2025[2].

However, among this immense amount of data, only about 20% of the data used by companies is structured data, and it is easy to manage with conventional computers. On the other hand, unstructured data accounts for about 80% of the total data, and it is expected that this percentage will increase furthermore soon. And that huge amounts of data will not be used. It is no exaggeration to say that AI has emerged to take full advantage of this buried unstructured data.

Regarding the “network”, an increase in communication speed is a major interest. The data created by sensors is stored in various places, but

most of them are stored in the cloud environment via wireless communication. At present, the communication band and speed are problems, and there are cases and situations where it is impossible to use, even if it is desired by users. The fifth-generation mobile communication system (5G) is expected as a breakthrough. It is assumed that a maximum transmission speed of 20 Gbps, that is 20 times faster than current LTE, and low latency. Therefore, remote robot operation and surgery in real time can be performed. In addition, the problem of multiple simultaneous connections will be solved. 5G will be the key technology for acceleration of big data.

As for “hardware”, along with Moore's Law, semiconductors have evolved, that is, the performance of computers is one trillion times higher in 60 years and has evolved overwhelmingly. This is exactly following “The Law of Accelerating Returns”[3] proposed by Ray Kurzweil (Fig.1.). One important invention is linked to another, it can be shortening the time between the appearance of the next important invention and accelerating the

speed of innovation. Thus, the performance of computers has been improved based on the rule of thumb that science and technology advance exponentially instead of linearly. Moore's law in the law of accelerating returns is said to be the fifth paradigm shift. The history of semiconductor starts from punch cards, relays, vacuum tubes, transistors, and integrated circuits. It is exactly that integrated circuits have evolved along with Moore's law. However, following Moore's law has also become more difficult due to the physical limitations of transistor integration. That means the improvement of AI performance requires the sixth paradigm shift. In order to bring about the sixth paradigm in the law of accelerating returns, the discovery of new materials is an important factor, and Materials Informatics (MI) [4],[5] is the powerful method to make it happen.

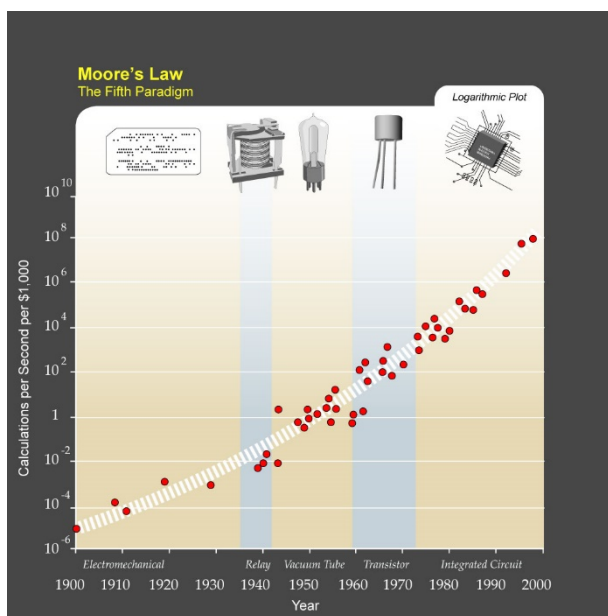


Fig. 1. The Law of Accelerating Returns.

2. Cognitive approach and analytics approach

According to Nature report about Chemical Space, there are 10^9 (one billion) materials known to the world. On the other hand, there are 10^{62} unknown materials [6]. AI can find suitable materials from such a huge unknown materials. To achieve it, we developed the “cognitive approach” [7] and “analytic approach” [8] and their features are summarized in Fig. 2.

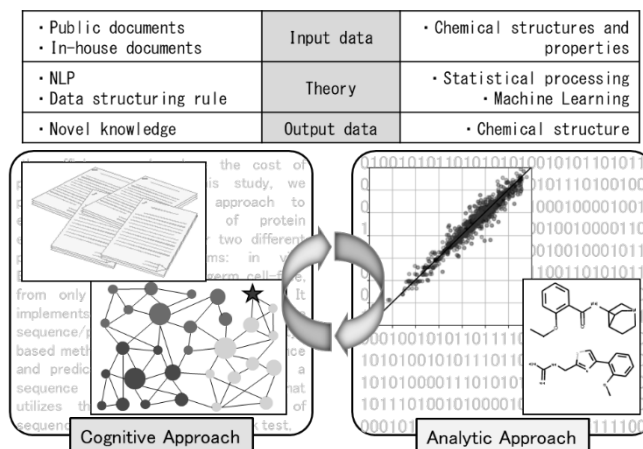


Fig. 2. Overview of cognitive and analytic approach.

The cognitive approach consists of three steps: "converting document information into structural data", "extracting facts by natural language processing", and "transforming facts into a knowledge graph (KG) expressing their correlation" (Fig. 3).

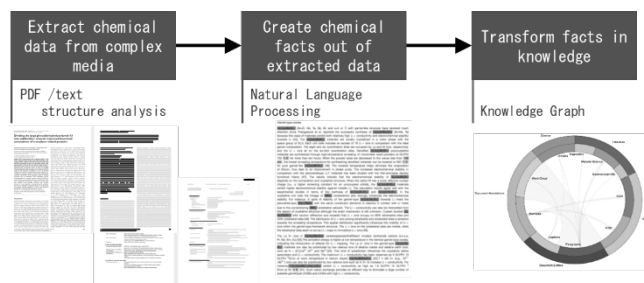


Fig. 3. Workflow for cognitive approach.

As a first step, the document information, which is unstructured data, is converted into structured data so that the computer can process it. For example, scientific papers, patents, and in-house documents are usually stored in pdf format, therefore those data are often difficult for computer to process. One of the solutions for document processing is the Corpus Conversion Service (CCS) reported by Staar et al. [9]. CCS can recognize titles and authors (labels) in scientific papers and extract text information along with the labels. In the next step, facts (entities) related to materials and their relationships (relation) are extracted from the text. Here, in addition to commonly used natural language processing, a dictionary that describes technical terms such as material names and physical property values and the relevance of those terms in the field of material is required to get entity. The final step is to develop the KG by joining the relations extracted from the document. The KG can

represent data obtained from various resources as one graph structure.

While the cognitive approach has the advantage of handling volumes that humans can hardly read, it can only extract facts in documents. In the future, it is expected that cognitive approach will infer new knowledge not written in documents by combining KG and machine learning. That is, we call Inference Model (IM).

The analytic approach includes two processes. The one is called a forward problem that analyzes a correlation between chemical structures and their physical property values, and the other is called an inverse problem that generates a chemical structural formula satisfying a target property value (Fig. 4).

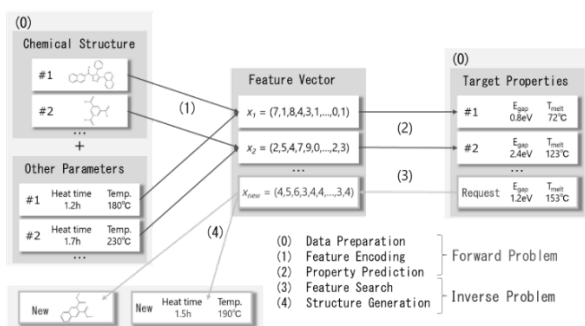


Fig. 4. Workflow for analytic approach.

First, the chemical structural formulas read as input information are converted into feature vectors using by a set of descriptors. For instance, the number of atoms, the number of partial structures, and so on are employed for descriptors. They need to be able to capture features of molecular structure exactly, and to generate a chemical structural formula from the features.

Next, model for predicting a physical property value is constructed. Generally, regression model is applied for such cases. The model with high prediction accuracy can be constructed, then it is possible to proceed to the next process called the inverse problem. In this step, a feature vector that satisfies a target property value is explored from a prediction model using a particle swarm optimization (PSO) method or other similar methods at the beginning.

Next, based on the given feature vector, chemical structural formulas that can exist mathematically are generated employing graph theory, and so on. As an application example of this method, Takeda et al. reported the design of drug candidate compounds [10]. In this research, candidate compounds which meet the target values for two contradictory

property values (LogP(Octanol/water partition coefficient), TPSA(polar envelope)) are designed, some of them were not included in the input data set. The potential of analytic approach to discover novel materials is of great interest.

However, it is difficult for the inverse problem to design material with large molecular weight due to their limitation of the calculation cost of search space. In this case, designing sub-structure having a high correlation with the target property value is one of the solutions.

While analytic and cognitive approaches seem at first glance to be entirely different approaches, combining the two approaches is expected to further accelerate material discovery.

3. KG construction

3.1. Biochemical KG

In recent years, biochemistry, which mainly focuses on cells, microorganisms, viruses and biomolecules such as proteins, sugars, lipids, DNA and RNA, has become increasingly important in contributing to human health and solving medical problems. In the field of biochemistry, it is widely practiced to register research data in public databases on the Internet after publishing papers and patents. Each of these public databases has its purposes, and the data which meet those purposes are registered in the databases. For example, Uniprot[11] and Genbank[12] are comprehensive databases on proteins and genes. CAZy[13] is a database which specializes in enzymes related to the degradation and production of carbohydrates. BRENDA[14] is a comprehensive database specialized for enzymatic reaction. Searching in single database will not yield sufficient results because each database has only the data that meet the purposes. Therefore, biochemists need to search multiple databases to obtain the data they need. Furthermore, some data are only described in papers and not registered in databases, making it difficult to obtain the necessary information. To address these issues, it is necessary to construct a queryable knowledge graph where research data retrieved from multiple databases and a large number of papers are systematically organized. NAGASE CO., LTD., HAYASHIBARA CO., LTD and IBM Zurich constructed the BioChemical Knowledge Graph (BCKG) from seven databases, papers and books. Furthermore, in this paper, we demonstrated an efficient and comprehensive search for carbohydrate-active enzymes using the constructed BCKG.

To construct the BCKG, we ingested data from a comprehensive list of structured databases: Uniprot,

Genbank, CAZY, BRENDA, Pfam[15], PubChem[16], KEGG[17]. Furthermore, unstructured data such as dictionary of carbohydrate and scientific papers related to carbohydrates and enzymes were also ingested via CCS. Using NLP process and entity recognition, scientific data described in papers and books were extracted. Data extracted from databases, books and papers were aggregated, and links between extracted items were created on the knowledge graph using common concepts (e.g., EC number). Thus, BCKG shown in Fig. 5. was created.

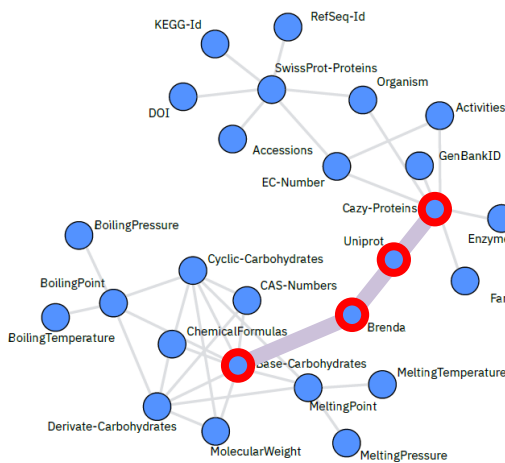


Fig. 5. An example of the BCKG.

To demonstrate the usefulness of the BCKG, we searched for EC numbers of the enzymes synthesizing and degrading lactose which is the

main cause of stomachache in adults when they drink milk. In the search using the BCKG, 6 EC numbers were obtained (Table.1). On the other hand, the search using expasy [18], which is general database for enzymatic reaction, obtained only 3 EC numbers. The BCKG found 3 EC numbers which could not be discovered by the search using Expasy. This result shows the usefulness and advantages of the BCKG on search by human and search using single database.

Table 1. Search results using the BCKG.

Search using the BCKG	Human search using Expasy	EC number
hit	No hit	1.1.99.13
hit	Hit	2.4.1.22
hit	Hit	2.7.1.207
hit	No hit	3.2.1.23
hit	Hit	3.2.1.108
hit	No hit	3.2.1.140

3.2. Polymers KG

Fig. 6 shows the results that CCS process the data. Subtitles, text and tables (which are regarded as labels) can be recognized. Then, the information with labels are retrieved as an output data. The approach for analyzing document structure is trained by machine learning method, so error correction enables their capability improve recognition accuracy. The recognition accuracy is over 99% in the case of applying for similar formatted documents.

The image shows a document page with various annotations. On the left, there are chemical structures labeled 13 and 14. The main text describes the synthesis of polyacetylenes. A table (Table 1) is present, showing data for different examples. The table has columns for 'Ex. (no.)', 'THP (mol %)', 'IBP (mol %)', 'IBP (mol %)', 'Average MW', and 'Average number of repeating units'. The table data is as follows:

Ex. (no.)	THP (mol %)	IBP (mol %)	IBP (mol %)	Average MW	Average number of repeating units
1	0.50	0.50	0.50	276	2.0
2	0.50	0.50	0.50	938	4.2
3	0.50	0.50	0.50	610	3.0
4	0.50	0.50	0.50	1708	8.0
5	0.50	0.50	0.50	1708	8.0
6	0.50	0.50	0.50	1708	8.0
7	0.50	0.50	0.50	1708	8.0
8	0.50	0.50	0.50	2488	11.0

Annotations include dashed boxes with 'X' marks around text and table elements, and a blue box at the bottom right labeled 'Annotate table'.

Fig. 6. Results of CCS process.

The next step is to extract the facts that related to material development from text data. For this purpose, two technologies are needed, the commonly used natural language processing method and dictionary including technical terms (called entities) such as material names and physical property values and their relationships in the specific materials fields2 [19],[20]. In the case of text analysis, each entity is firstly extracted, the relationship among [polymer-X] to [viscosity] to [1,000 centistokes] is then generated as shown in Fig. 7.

To the reaction vessel is added under nitrogen sparge, at 85°C and with stirring, a mixture of 300 g of a poly(vinylmethyl-co-dimethylsiloxane) having 1 percent random vinyl methyl groups and having a viscosity of 1,000 centistokes and which is sold commercially as PS 426 by Petrarch Systems, Incorporated, and 3.8 g of t-butylperoxoate catalyst.

Fig. 7. Extraction of technical terms by natural language process .

Fig.8. is an example of KG consisting of patents related to polymers, which contains more than 400,000 data extracted from 782 patents. The entire process from ingesting patent document to build KG took one hour on 10 CPUs. The blue circles (nodes) are a set of entities with the same type of information, and the lines (edges) represent the relationships between entities. Paragraph node locates in the central of the KG and is connected to Structural information, physical properties, process conditions, and so on. Fig.9. shows the number of chemicals and their values of each property contained in KG on the left side. The word cloud on the right side presents the compounds associated with the glass transition temperature.

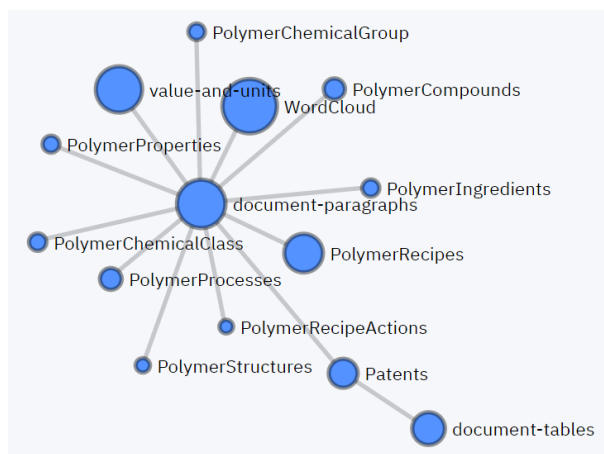


Fig. 8. KG consisting of Polymers patents.

Property name	# of chemical	# of value
Glass transition temperature	49	2006
Thermal stability	26	511
Viscosity	65	5954
Tensile strength	51	3076

polyacrylicacid
Cellulose Acetate
polyethylenesebacate
polyethylene
nylon66 polystyrene
polyacrylamide
polypropylene
polyvinylacetate
polylactacid
polymethylmethacrylate
polybisphenolcarbonate

Fig. 9. statistical information stored in the KG.

4. Overview of Platform Services for MI system

Our Materials Informatics (MI) system is intended to be provided as SaaS (Software as a service). Since this system uses the service built on the server via the Internet, multiple authorized members can use the system in the same state. Software is regularly updated by cloud administrators and is always up to date. Since the clients' data is not stored in the terminal, the risk of data leakage can be dramatically reduced.

In Fig. 10, it shows an overview of the MI system. The MI system is managed in the cloud as a domain for each client. Each domain can only be accessed by the designated client who has been granted an account. Since the clients' private data are ingested by the clients, the private data cannot be viewed by anyone other than them, including the cloud administrator. Public data such as patents can be viewed only by the clients when the data are ingested. If there is a request from them, a service for collecting and ingesting public data will be considered in the future.

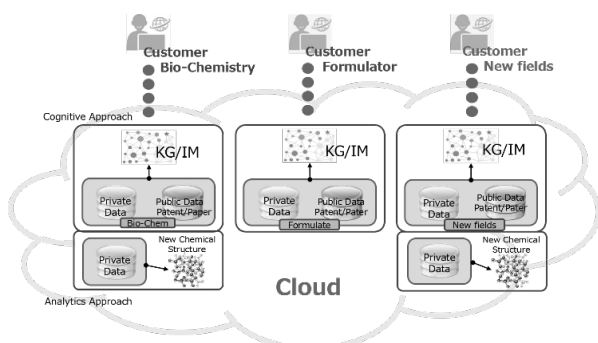


Fig. 10. Schematic image of Materials Informatics.

5. Summary and Conclusion

With the evolution of IoT, the advancement of 5G, and the growth of energy consumption due to the enormous amount of data processing on servers, the increasing needs for new material development and intensifying competition in material development are inevitable. MI technology must be an indispensable technology for improving the speed of development in the search and design of such new materials, not only organic materials but also inorganic materials. And also, MI will certainly be the source of future corporate competitiveness. MI can search for target materials directly from the database which is based on conventional method depending on the intuition and experience of researchers. And it also enables efficient or direct way to develop materials to meet the needs of users. There are many advantages of MI, however we should do more for improving the systems for commonly using. For example, further improvement of data analysis technology, accumulation of data, and establishment of support system for MI introduction to users, is needed. The training of data scientists who can analyze data is also urgent. The future direction of MI evolution is the accumulation of unstructured data collected from sensing devices, combined with clustering processing by AI, and new material simulation using quantum computers as accelerators. The field of quantum chemical calculation is also expected to be actively developed with MI field, as a more effective way to find out materials properties compare to conventional calculation methods [21].

References

1. EMC Digital Universe with Research & Analysis by IDC, "The Digital Universe of Opportunities: Rich Data and the Increasing Value of the Internet of Things" (2014).
2. D. Reinsel, J. Grantz, and J. Rydning, "Data Age 2025, IDC (2017).
3. R. Kurzweil, "The Singularity Is Near" P.68, (2005).

4. R. Ramprasad, R. Batra, G. Pilia, A. Mannodi-Kanakithodi, and C. Kim, "Machine learning in materials informatics: recent applications and prospects", *npj Computational Materials* **3**, 54 (2017).
5. A. Agrawal and A. Choudhary, "Perspective: Materials informatics and big data: Realization of the "fourth paradigm" of science in materials science", *APL Materials* **4**, 053208 (2016).
6. C. Kirkpatrick and W. C. McMartin, *Guida Chemical Space*, *Nature*.**432(7019):823-865** (2004).
7. M. Matteo, C. Auer, V. Weber, F. Zipoli, M. Dolfi, P. Staar, T. Laino, C. Bekas, A. Fujita, H. Toda, S. Hirose, and Y. Orii, *An Information Extraction and Knowledge Graph Platform for Accelerating Biochemical Discoveries, Workshop on Applied Data Science for Healthcare at KDD* (2019).
8. S. Takeda, T. Hama, H. H. Hsu, V. Piunova, D. Zubarev, D. Sanders, J. Pitera, M. Kogoh, T. Hongo, Y. Cheng, W. Bocanett, H. Nakashika, Y. Tsuchiya, K. Hino, K. Yano, S. Hirose, H. Toda, Y. Orii, and D. Nakano, *Molecular Inverse-Design Platform for Material Industries, KDD'20:Proceedings of the 26th ACM SIGKDD International Conference on Knowledge Discovery & Data Mining* (2020).
9. P. Staar, M. Dolfi, C. Auer, and C. Bekas, "Corpus Conversion Service: A machine learning platform to ingest documents at scale", *the 24th ACM SIGKDD International Conference on Knowledge Discovery & Data Mining* (2018).
10. S. Takeda, H. Han Hsu, T. Hama, T. Yamane, K. Masuda, and D. Nakano: "New Material Search Method by Artificial Interagency", *The Japan Society for Artificial Intelligence* (2018).
11. A. Bateman, UniProt: a worldwide hub of protein knowledge. *Nucleic Acids Research* **47**, D1 (2018).
12. D. A. Benson, M. Cavanaugh, K. Clark, I. Mizrahi, D.J. Lipman, J. Ostell, and E.W. Sayers, *GenBank. Nucleic Acids Research* **45**, D1 (2017).
13. B. L. Cantarel, P. M. Coutinho, C. Rancurel, T. Bernard, V. Lombard, and B. Henrissat, *The Carbohydrate-Active EnZymes database (CAZy): An expert resource for glycogenomics. Nucleic Acids Research* **37**, SUPPL. 1 (2009).
14. S. El-Gebali, J. Mistry, A. Bateman, S. R. Eddy, A. Luciani, S. C. Potter, M. Qureshi, L. J. Richardson, G. A. Salazar, A. Smart, E. L. Sonnhammer, L. Hirsh, L. Paladin, D. Piovesan, S. C. E. Tosatto, and R. D. Finn, *A European*

- ELIXIR core data resource. Nucleic Acids Research* **47**, **D1** (2019).
15. J. Mistry, S. Chuguransky, L. Williams, M. Qureshi, G. A. Salazar, E. L. L. Sonnhammer, S. C. E. Tosatto, L. Paladin, S. Raj, L. J. Richardson, R. D. Finn, and A. Bateman, "Pfam: The protein families database in 2021", *Nucleic Acids Research*. **49(D1):D412-D419** (2020).
 16. S. Kim, J. Chen, T. Cheng, A. Gindulyte, J. He, S. He, Q. Li, B. A. Shoemaker, P. A. Thiessen, B. Yu, L. Zaslavsky, J. Zhang, and E. E. Bolton, "PubChem in 2021: new data content and improved web interfaces", *Nucleic Acids Research*. **47(D1):D1388-D1395** (2019).
 17. M. Kanehisa, M. Furumichi, Y. Sato, M. Ishiguro-Watanabe, and M. Tanabe. "KEGG: integrating viruses and cellular organisms" *Nucleic Acids Research*. **49(D1):D545-D551** (2021).
 18. P. Artinmo, M. Jonnalagedda, K. Arnold, D. Baratin, G. Csardi, E. de Castro, S. Duvaud, V. Flegel, A. Fortier, E. Gasteiger, A. Grosdidier, C. Hernandez, V. Ioannidis, D. Kuznetsov, R. Liechti, S. Moretti, K. Mostaguir, N. Redaschi, G. Rossier, I. Xenarios, and H. Stockinger, *SIB bioinformatics resource portal, Nucleic Acids Res*, **40(W1):W597-W603** (2012).
 19. G. Lample, M. Ballesteros, S. Subramanian, K. Kawakami, and C. Dyer, *Neural Architectures for Named Entity Recognition, proceedings of NAACL-HLT2016* (2016).
 20. M. Honnibal and I. Montani, *spaCy2: Natural language understanding with Bloom embeddings, convolutional neural networks and incremental parsing, To appear* (2017).
 21. H. Nishimori and M. Ozeki "Quantum computer accelerates artificial intelligence", *Nikkei Business Publications, Inc.* (2016) (in Japanese).

Fundamental Evaluation of Resist on EUV Lithography at NewSUBARU Synchrotron Light Facility

Takeo Watanabe*, Tetsuo Harada, and Shinji Yamakawa

Center for EUVL, Laboratory of Advanced Science and Technology for Industry, University of Hyogo, 3-1-2 Kouto, Kamigori-cho, Akou-gun, Hyogo 678-1205, Japan

**takeo@lasti.u-hyogo.ac.jp*

Extreme ultraviolet lithography was started to use for the production of 7-nm node-logic-semiconductor devices in 2019. And it was adapted to use for high volume manufacturing (HVM) of 5-nm logic devices in 2020. EUVL is required to be extended to use in 1.5-nm-node-device fabrications. However, it still has many technical issues. Especially, for EUV resists, simultaneous achievement of high sensitivity and low line edge width are required. To solve the EUV resist issue, the fundamental work using synchrotron in soft X-ray region is necessary. The fundamental evaluation study of EUV resist at NewSUBARU synchrotron light facility is described in this paper.

Keywords: EUVL, Resist, Sensitivity, Line edge roughness, EUV, Soft X-ray, Resonant scattering, Reflectivity measurement, Out of band patterning, Photo-electron emission microscopy

1. Introduction

Extreme ultraviolet lithography (EUVL) was started to use for the production of 7-nm-node-logic-semiconductor devices. In addition, EUVL technology has finally begun to be used as high-volume-mass-production technology since 2020. EUV technology is going to extend to use in the fabrication of 1.5-nm node devices. EUVL still has technical issues such as EUV resist development, defect free mask fabrication including metrology and pellicle, and EUV high power and stable light source. Especially, it is required that EUV resist which has high resolution and sensitivity, low line width roughness (LWR), and low outgassing [1]. In the EUV resist technical issues, the simultaneous achievement of high resolution and sensitivity, and low LWR is very significant and not so easy. Thus, more fundamental studies are still needed.

Even if the resist material itself has high resolution, as trying to replicate a resist pattern which has narrower width, the pattern collapse interferes the fine-pattern replication. In order to increase the resolution, preventing from the pattern collapse is necessary. Thus, the fundamental study

of the structure analysis of resist films using synchrotron is necessary.

In order to increase the sensitivity, studying the whole chemical reactions which occur by the EUV irradiation is necessary. And the development of EUV resist material with high sensitivity based on this study is significant. Since, the wavelength of EUV light and EUV photon energy is 13.5 nm and 91.8 eV, respectively, secondary electron ionization reaction occurs by the high energy electron region. To clarify the reaction by low energy region, it is necessary to use the fundamental evaluation using synchrotron radiation in soft X-ray region.

In addition, to achieve the low LWR resist, the fundamental study of the origin of LWR is necessary. In this study, it is also necessary to use the fundamental evaluation using synchrotron radiation in soft X-ray region as describe later. As above reasons, the fundamental evaluation studies of EUV resist at NewSUBARU synchrotron light facility [2], University of Hyogo, are described in this paper. Total nine beamlines are operating, and three beamlines which are BL03, BL09, and

BL10 of NewSUBARU as shown in Fig. 1. We have the EUV flood exposure tool for the resist sensitivity evaluation by the actual EUV light spectrum, interference lithographic exposure tool for the patterning 10 nm and below, outgassing and contamination growth evaluation tools by ellipsometry, and chemical reaction analysis by the

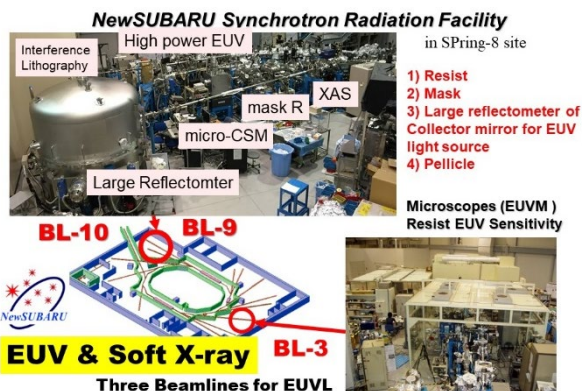


Fig. 1. EUVL R&D at NewSUBARU.

soft X-ray spectroscopy (XAS). In addition, recently it is prepared additional tools for the fundamental studies of EUV resists. This paper focuses that 1) resist-film layer analysis by the resonant soft X-ray reflectivity method in soft-X-ray energy region, 2) stochastic origin analysis in EUV resist by resonant soft X-ray scattering to achieve low LWR, 3) out of band systematic analysis, and 4) preparation of the photo-electron emission microscopy for the chemical content spatial distribution analysis.

2. Layer Analysis by the Resonant Soft X-ray Reflectivity Method in soft-X-ray Energy Region

For the layer analysis [3, 4] of the single layer resist material which has a thickness of 20 – 50 nm, the resonant soft X-ray reflectivity (RSoXR) method in soft-X-ray energy region is a powerful method for the chemical layer analysis of the resist film [5]. This method is the hybrid method using soft X-ray absorption spectroscopy [6, 7] and soft X-ray reflectance measurement. By the soft X-ray absorption spectroscopy, the incident energy of the photon is selected for the soft X-ray reflectance measurement to evaluate refractive index of n and k values, and thickness of a resist film coated on a wafer. The examples of the measured reflective fringe and fitting results are shown in Fig. 2. The reflectivity fringe spectrum can be fit by n and k values, and thickness of the layers.

The commercial chemical amplified (CA) resist was employed for the layer analysis. The resist was

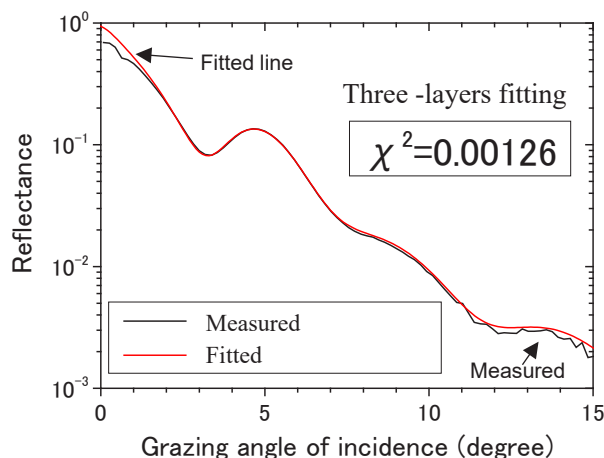


Fig. 2. Fitting result of the reflectance fringe.

spin-coated on a 4 inches silicon wafer to have 26-nm thick. Then the layer analysis was carried out. As a result, the fitting result is shown in Table.1. Even if the CA resist for a single layer process, the thin resist film consists of three layers. The bottom, main body, and top layers have the thickness of 4.5 nm, 14.1 nm, and 7.4 nm, respectively. And these layers have the complex refractive index of k value of 0.0007, 0.0003, and 0.0004, respectively. The bottom layer between the main body layer might be a pattern collapse region.

Table 1. Result of fitting

Layer names	Thickness (nm)	n	k	Roughness (nm)
Top	7.4	0.9996	0.0004	0.22
Main body	14.1	0.9996	0.0003	3.51
Bottom	4.5	0.9999	0.0007	4.83
SiO ₂	0.8	0.9946	0.0018	0.1
Si wafer	--	0.9951	0.0028	--

3. Stochastic Origin Analysis in EUV Resist by Resonant Soft X-ray Scattering

The low LWR is necessary to maintain the electronic characteristics of semiconductor device, such as logic and memory devices.

The origin of the LWR might be 1) spatial distribution of functional material in resist functional groups, photosensitizers (acid generators), additives such as amines, and so on, 2) spatial distribution of free volume caused by the solvent distribution in prebake process, 3) EUV

photon shot noise, 4) secondary electron blur, 5) solvent effect in PEB process acid diffusion, 6) spatial distribution of developer penetration and development process yield caused by developer and rinse effects, and 7) out of band (OoB) light effect.

In order to reduce LWR of the resist pattern, the controls of the above stochastics are significant. In the above list, in order to control the chemical reaction fluctuation within the nanometer dimensions, the special distribution control of the chemical contents is very significant. However, up to now the measurement of the chemical-contents distribution has not been carried out. Thus, the method of resonant soft X-ray scattering (RSoXS) is used for the measurement. This method is the hybrid method using soft X-ray absorption spectroscopy [6, 7] and soft X-ray scattering as shown in Fig.3. The scattering vector is defined by the following equation.

$$q = |\vec{q}| = \frac{4\pi}{\lambda} \sin \frac{\theta}{2} \quad (1)$$

By the soft X-ray absorption spectroscopy, the incident energy of the photon is selected for the soft X-ray scattering to obtain the selected chemical-

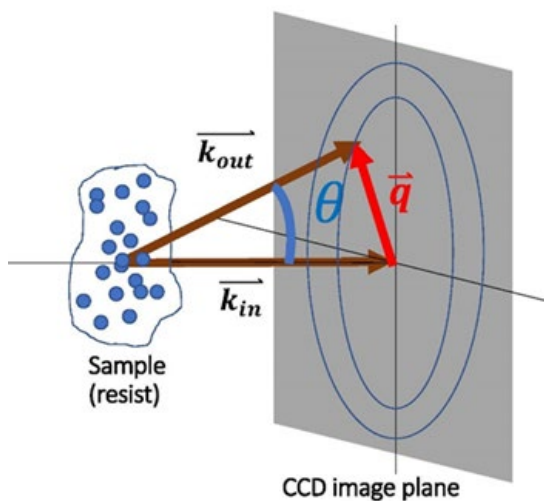


Fig. 3. Scattering vector q .

bonding diffraction image. The RSoXS system at BL-10 beamline of NewSUBARU was used for this experiment [8, 9]. This beamline provides monochromatized energy of the soft X-ray region from 80 to 1000 eV [10].

The scattering vector profiles of PMMA and CA resist are shown in Fig. 4 (a) and 4(b). The Scattering vectors of 0.05 and 0.1 correspond to the structure size of 120 nm and 60 nm, respectively. As

the results, the spatial distributions between the π^* bonding and acrylate group are very similar in PMMA. However, these are quite different in CA resist. Generally, since the LWR of PMMA is smaller than that of CA resist, the results of the scattering vector profiles are consistent to the LWR tendency [11].

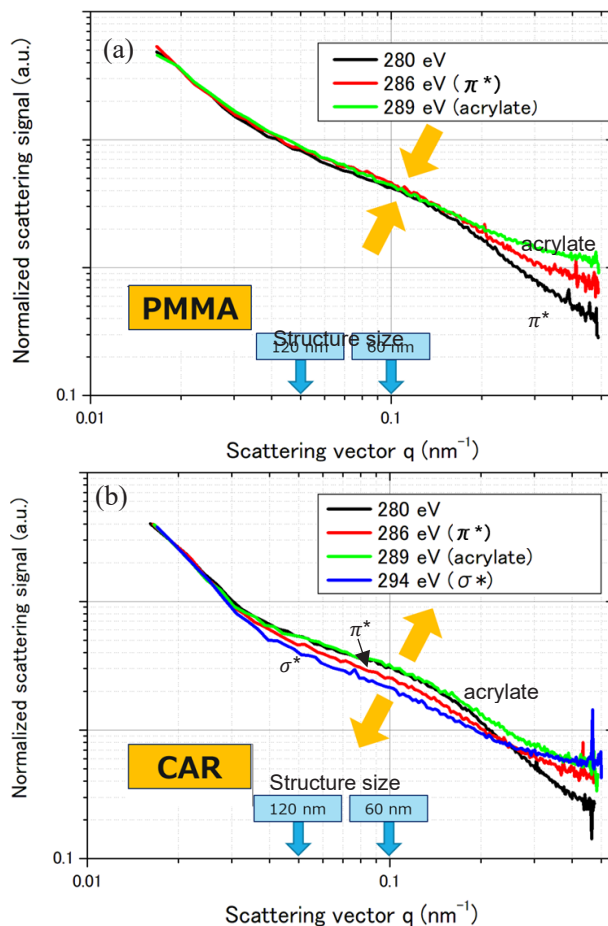


Fig. 4. Scattering vector profiles of (a) PMMA and (b) CAR.

4. Out of Band Systematic Analysis

If the resist exposed by the light which includes the out of band (OoB) light containing the deep UV wavelength region, the OoB lights affects to the LWR of the resist pattern. Thus, reflectance measurement of the mask materials such as Mo/Si multilayer, absorber, and black border (mask substrate surface). Figure 5 shows the beamline setup of the exposure tool and reflectometer by the EUV and OoB lights at BL03A beamline of NewSUBARU. The monochromator setups to enable the EUV at the wavelength of 10 - 80 nm and OoB light at the wavelength of 100 - 200 nm are shown in Fig. 6(a). and Fig. 6(b), respectively. And LiF filter with a thickness of 1 mm were used to cut

the high order lights which is shorter than the wavelength of 100 nm. The reflectance measurement results of the mask materials such as Mo/Si multilayer, absorber, and black border (mask substrate surface) are shown in Fig. 7. The

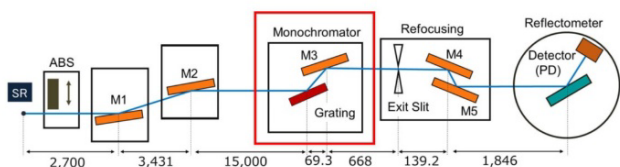


Fig. 5. Beamline setup of the EUV and OoB light exposure tool and reflectometer.

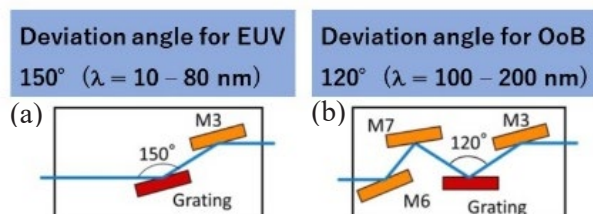


Fig. 6. The monochromator optics for (a) EUV and (b) OoB wavelength regions.

reflectance spectrum of the Mo/Si multilayer was measured completely in the EUV region including high order lights. In the OoB region, the reflectance of Mo/Si multilayer, TaN absorber, and mask substrate as a black border has approximately 30% in maximum. Even if the black border, it has the reflectance of 30%, and the reflectance reduction method should be required.

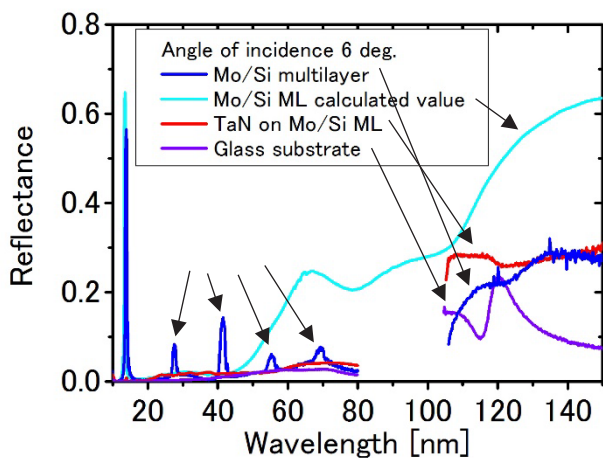


Fig. 7. Reflectance spectra of Mo/Si multilayer, TaN absorber on Mo/Si multilayer, and black border.

5. Preparation of Photo-Electron Emission Microscopy for the Chemical Content Spatial Distribution Analysis

As described in section 3 of RSoXS is one of the methods to observe the chemical-content distribution. However, since the scattering method is used, the averaged distribution is obtained. Instead of this method, we introduce the photoelectron emission microscopy (PEEM) to observe the real chemical content distribution not an averaged one of resist film.

The PEEM system is going to be installed at the BL09A beamline of NewSUBARU. The 3D design and the photography are shown in Figs. 8 and 9, respectively. The PEEM system consists of a load lock chamber to exchange a sample, a sample processing chamber adapted to the ion beam cluster and a sample heating device, and an observation chamber adapted to the PEEM device. In order to prevent vibration and to achieve high spatial resolution in PEEM, a special mechanism is employed.

NewSUBARU is a middle size synchrotron light facility and soft X-ray synchrotron radiation is generated from the 1.0 GeV electron beam storage ring. The soft X-ray absorption spectroscopy in the soft X-ray region is suitable for the chemical analysis of light atomic elements such as carbon, nitrogen, oxygen, and fluorine etc. Thus, the PEEM in the soft X-ray region can observe the chemical imaging of these atomic elements. Since the penetration depth of the soft X-ray is small enough to observe the surface chemical imaging of the resist film, the cluster ion beam tool is employed for the non-damage surface etching of the resist film and enables the chemical imaging in 3D of the resist film.

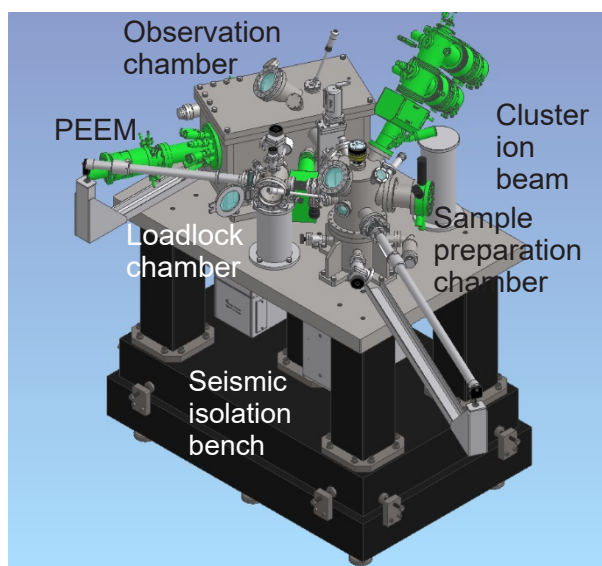


Fig. 8. 3D design of the PEEM system.

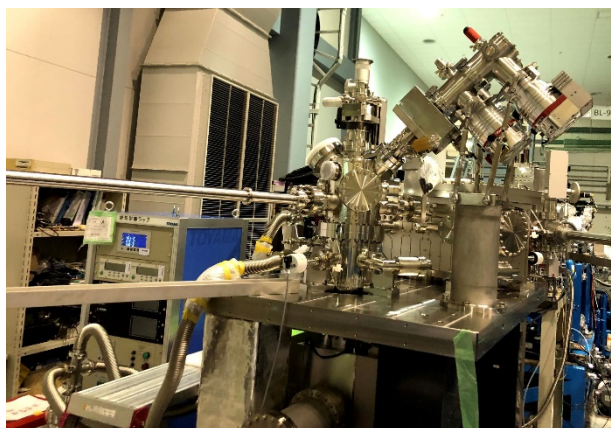


Fig. 9. Photograph of the PEEM system which is installing at the endstation of NewSUBARU 10.8 m long undulator BL09A beamline.

6. New Injector for NewSUBARU

The SPring-8 linear accelerator which had been used as an injection of the electron beam both to SPring-8 and NewSUBARU electron beam storage rings in cooperation of the SPring-8 accelerator team. This linear accelerator was shut down on July 29, 2020. From April to December, the new linear accelerator for NewSUBARU was installed at the beam transportation tunnel. This length of the new linear accelerator has a length of approximately 50-m-long and it is a half-length of the previous one. The new one employed the microwave frequency of approximately 6 GHz (C-band microwave) and it is double frequency of the previous one (S-band microwave) to shortening the length.

The commissioning of NewSUBARU phase II will start from April 20, 2021. After the beamline tuning, user time will be operated at electron beam current of 350 mA in electron energy of 1.0 GeV top-up mode. In addition, 1.5 GeV operation will be started at the same time.

7. Conclusions

The RSoXR method is introduced to evaluate the chemical-layer separation of the CAR, and it is sensitive enough to it. In the single layer resist, the preventing from the pattern collapse at the boundary between the bottom and main body layer might be significant for the fine patterning.

The RSoXS method is introduced to evaluate uniformity of resist material distribution, which can modulate absorption contrast of functional group by changing the incident photon energy around carbon absorption edge. The RSoXS results are clarified the

uniformity of resist material structure, which can highlight the issues to design the low LWR performance.

The out of band systematic analysis tool was prepared at BL03 beamline. In the OoB region, the reflectance of Mo/Si multilayer, TaN absorber, and mask substrate as a black border has approximately 30% in maximum. Even if the black border, it has the reflectance of 30%. And the reflectance reduction method of the OoB lights should be required for the low LWR achievement of the resist patterning.

In order to achieve low LWR, construction of the photo-electron emission microscopy to analyze the chemical content spatial distribution analysis is in progress.

Construction of new injector for NewSUBARU is in progress toward the NewSUBARU phase II operation to start from April 20, 2021.

References

1. *International Symposium on Extreme Ultraviolet Lithography*, (2021) Closing remarks.
2. Web site of NewSUBARU Synchrotron facility, <http://www.lasti.u-hyogo.ac.jp/NS/>
3. M. Nakagawa, *Jpn. J. Polym.Sci. Tech.* **68** (2019) 24 (in Japanese)
4. M. Nakagawa, T. Uehara, Y. Ozaki, T. Nakamura, and S. Ito, *J. Vac. Sci. Technol. B* **36** (2018) 06JF02.
5. T. Ishiguro, J. Tanaka, T. Harada, and T. Watanabe, *J. Photopolym. Sci. Technol.* **32** (2019) 333.
6. K. Tsuji and Y. Muramatsu Ed., “*X-ray Spectroscopy*,” *Spectroscopy Series, The Spectroscopical Society of Japan (in Japanese)*, Kodansya, 2018, ISBN 978-4-06-513038-4.
7. T. Ohta, “*X-ray Absorption Spectroscopy*,” *IPC, in Japanese*, 2017, ISBN 9784901493215.
8. J. Tanaka, T. Ishiguro, T. Harada, and T. Watanabe, *J. Photopolym. Sci. Technol.* **32** (2019) 327.
9. J. Tanaka, T. Ishiguro, T. Harada, and T. Watanabe, *J. Photopolym. Sci. Technol.* **33** (2020) 491.
10. M. Kuki, T. Uemura, M. Yamaguchi, T. Harada, T. Watanabe, Y. Muramatsu, and H. Kinoshita, *J. Photopolym. Sci. Technol.*, **28** (2015) 531.
11. B. Cardineau, P. Garczynski, W. Earley, and R. L. Brainard, *J. Photopolym. Sci. Technol.* **26** (2013) 665.

Randomness of Polymer Microstructure in the Resist Film as Shot Noise

Makoto Muramatsu^{1*}, Arisa Hara², Satoru Shimura², and Hidetami Yaegashi³

¹ *Advanced Technology Development Department, Tokyo Electron Kyushu Ltd.,
 1-1 Fukuhara, Koshi City, Kumamoto 861-1116, Japan*

² *Process Technology Department, Tokyo Electron Kyushu Ltd.,
 1-1 Fukuhara, Koshi City, Kumamoto 861-1116, Japan*

³ *TEL Corporate R&D, Tokyo Electron limited,
 3-1 Akasaka 5-chome, Minato-ku, Tokyo 107-6325, Japan*

*makoto.muramatsu@tel.com

Extreme ultraviolet (EUV) with a wavelength of 13.5 nm has already been mass-produced, but serious technical problems remain an important issue. One of them is the line edge roughness (LER) value for critical dimension (CD). Local variations such as intra-filed CD uniformity and LER are usually identified from the average CD calculated using top-down view observations. However, it is not possible to get an overall picture of LER. In this study, cross-section SEM was applied efficiently to visualize or quantify the basic behavior of the resist. In addition, the resolution limits and minimum structural units that make up the resist pattern associated with LER are discussed.

Keywords: Stochastics, Polymer dynamics, Polymer aggregate, LER, missing defect, EUV, Resolution limit

1. Introduction

It is aggressively discussed that the occurrence of stochastic print failures is an important factor to consider. While two main types of shot noise [1], photons and acids, are generally focused, the backbone polymer of resist materials is less considered, but cannot be negligible. Some random phenomena, as shown in Figure 1, were not first discovered in the EUV era, but before the 248 nm era at the latest. Therefore, the question is whether such randomness is an EUV-specific phenomenon.

In the practical region of the focus exposure matrix (FEM) to derive mean CD, the resist pattern profile is relatively stable, and its randomness is minimal. Therefore, resist pattern profile in the early state with extremely lower dose conditions using negative tone development (NTD) type resist were observed. The main purpose of this observation is to determine the smallest structural unit of the resist pattern. And another important point is to understand the interaction reaction between the resist film and

the underlying layer to find a specific solution for defect reduction.

In This paper, assumptions about the main factors of LER formation and the resolution limits of EUV resists is introduced and mentions important messages of defect induction.

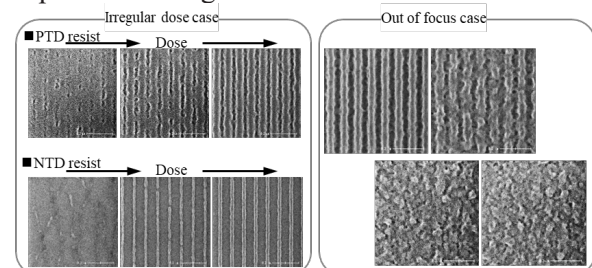


Fig. 1. Various randomness in resist patterning under non optimized condition.

2. Experimental Results and Discussion

2.1. Observation under extreme lower dose

The resist dissolution contrast curve, like FEM, is an important source for easily predicting the basic performance of some lithography. Although

resist pattern profiles can be derived from contrast curves, it is not suitable for more equitable detection of stochastic processes such as resist residues in the resist open space region. In order to accurately observe the microscopic resist behavior, the surface of the contrast curve sample was observed and visualized by cross-section SEM. In this study, NTD type resist [2], which is a negative tone image, was used mainly because it has easier characteristics than a positive tone development (PTD) type resist. Because this NTD type resist was a 193 nm photosensitive material, the 193 nm scanner was selected for this test. The focal region to be visualized was the low dose state before reaching Eth, and the NTD resist film growth process with exposure was characterized by AFM and cross-section SEM images. First, the results of AFM are introduced in Fig. 2 [3-4].

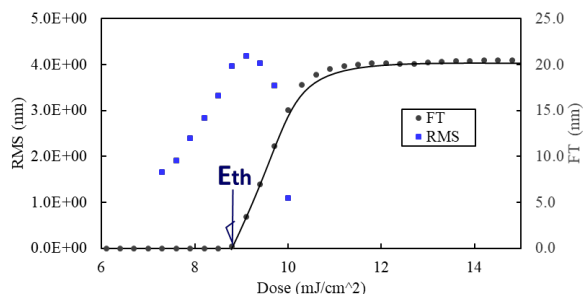
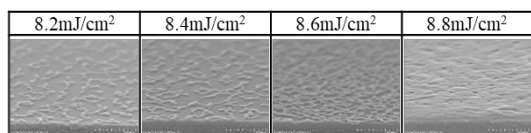
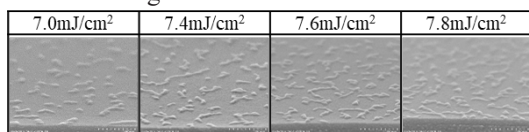


Fig. 2. Roughness trend through exposure does until Eth.

The RMS of surface roughness generated on the substrate increased with the exposure energy up to the Eth point. There may be small objects on the substrate as a resist film that has been photo-reacted and insolubilized. When the visualization results of the insoluble matter are summarized in Table 1, this growth behavior was steadily increasing with small particles generated in some places. Then it was connected in a chain reaction and finally it was filled on the substrate.

Table 1. Polymer aggregates image on under layer surface through dose.



The coverage of the polymer particles on the wafer was plotted in Figure 3 to confirm that the resist film thickness measurement started with a coating point simulation. This point which became thickness measurable corresponds to Eth. Such behavioral analytics must be very important given the specific solutions for defect suppression. Because this test was a macroscopic method, observations of smaller areas under pattern exposure were made.

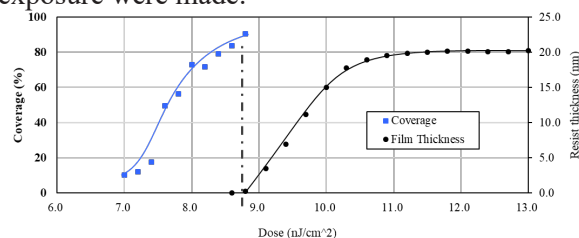


Fig. 3. Coverage trend of polymer aggregates over substrate.

2.2. Preliminary state observation of resist pattern

As the continuous work, the behavior of the resist in the pattern formation during the patterning exposure process step was visualized. The CD trend from patterning to nominal dose is plotted in Figure 4. Since this CD trend has three different phases, the behaviors in each phase were individually characterized.

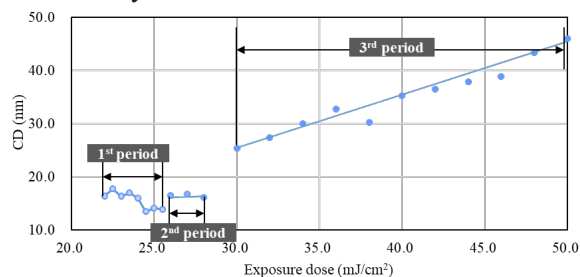
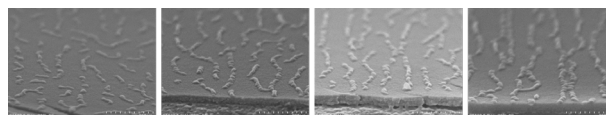


Fig. 4. Resist pattern creation behavior divided in three-periods.

■ 1st period

As shown in Table 2, the generation of the particulate dotted pattern on the substrate is first captured. Since the particles have a weak adhesive force to the substrate, they partially adhered and partially floated.

Table 2. Particulate dotted pattern SEM image in preliminary state at minimum exposure dose.

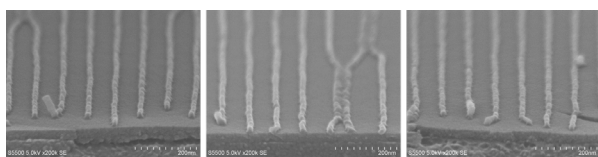


The CD size at this period is about 12 nm, suggesting that it is the smallest structural unit that construct the resist pattern.

■ 2nd period

During this period, the dots are gathered and connected mutually. It looks like a line pattern; however, the adhesive strength is not strong enough and the pattern peeled off in spots. The average CD is kept constant at about 12 nm.

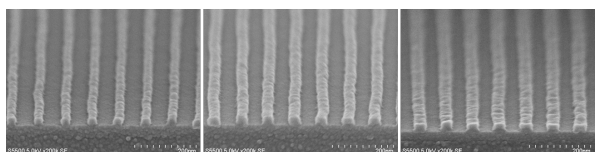
Table 3. Transition state SEM image before enough adhesive force implementation.



■ 3rd period

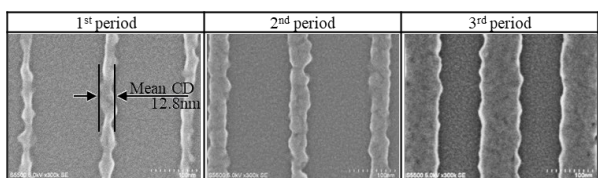
The resist pattern is getting stable and the pattern is growing efficiently. The 3 sigma of CD deviation is also stable, and from this phase, the resist pattern can be visualized by CD-SEM and the CD can be measured.

Table 4. Resist line pattern image on SEM in steady state.



Considering this particle observation work comprehensively, a resist pattern began to be formed from the size of 12 nm in the first phase. The size is assumed to be the smallest structural unit for forming a resist pattern, and the resolution limit of EUV resists should be limited to about 12 nm. Another notable result is the slight appearance of pixelated textures in the resist pattern, as shown in Table 5. The resist pattern seems consists of this 12 nm size structural unit.

Table 5. Top-down image of pixelated elemental unit constructing resist pattern.



2.3. Structural elemental unit of resist film

This section presents the visualization results of polymer aggregates in resist membranes. Assuming the resist pattern is constructed of agglomerated polymer, the carbon density in the space of the polymer agglomerates will be significantly lower. Therefore, removing the part with low carbon density using argon sputtering was tested. With newly specializing sputtering condition [5-7], the low-density part was removed successfully, and an object like a random fingerprint appeared (Figure 5).

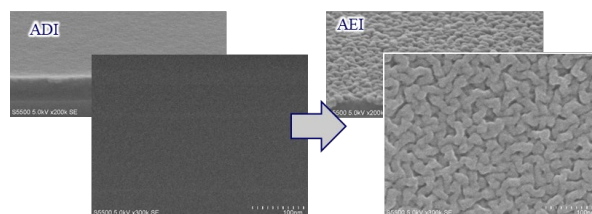


Fig. 5. Successful visualization of linear carbon cluster latent in resist film.

It looks like a fingerprint pattern using Directed Self-Assembly (DSA). When the line width was measured, the average value was 12.6 nm. As shown in Figure 6, the kurtosis of the CD distribution plot is sharp. This special sputtering method also allows carbon agglomerates to float in the tight spaces of a patterned sample, as shown in Figure 7. Interestingly, the winding shape of the LER matches the contour of the linear carbon cluster. Therefore, this cluster can be one of the decisive factors in generating LER and should be minimized.

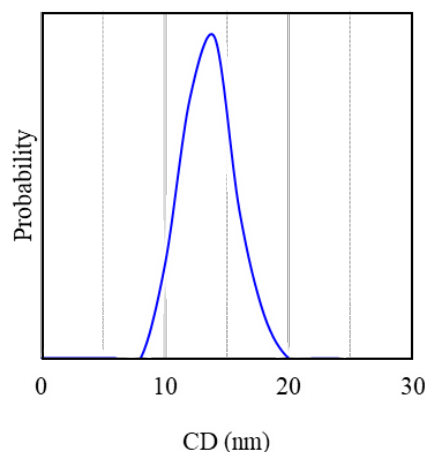


Fig. 6. Line width distribution of carbon cluster.

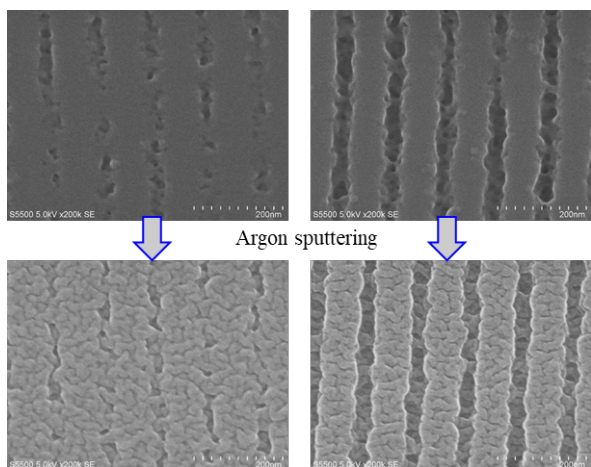


Fig. 7. Carbon cluster appearance on pattern resist sample.

2.4. Exploration of carbon aggregates control factor

This section considers suitable control factors in three technical areas: photochemical reactions, track processes, and resist material design. In this study, a special EUV resist sensitive to 193 nm was used in a 193 nm exposure experimental environment.

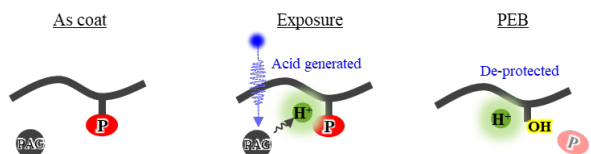


Fig. 8. Simple scheme for the photochemical reaction of chemically amplified resist process.

As shown in the schematic diagram of Figure 8, decomposition occurs by the chemical amplification reaction by UV irradiation and the thermal reaction of the acid in the resist film [8]. The line width of the linear carbon cluster and its distribution were compared at each process step, and the comparison results are shown in Table 6.

Table 6. Variability test result in photo-chemical reaction: appearance, mean CD.

As coat	Exposure	PEB
Mean CD 12.6nm	12.5nm	13.2nm

The appearance of the SEM image at each step did not change, and the CD value did not change at all. This result provides one piece of evidence

that the chemical reaction is not involved in polymer agglutination. Further checks were made on the association of PAG with aggregation by comparing the two types of resists.

One was a nominal resist material and the other was a PAG unmixed test sample. As a result, there was no difference in the appearance of the SEM and the comparison of the average CD value (Figure 9). It can be said that the aggregate is composed only of polymer and has nothing to do with other additives such as PAG.

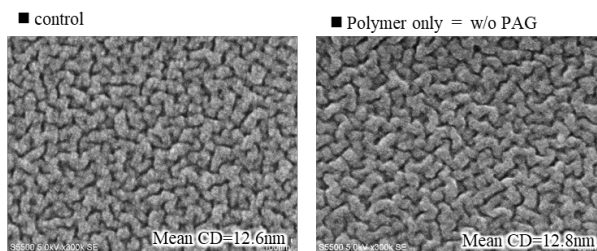


Fig. 9. Variability test result in material composition: nominal resist and polymer without PAG.

Next, the relationship with the track process factor was investigated. Given the conformation of the polymer, in the liquid or solid phase, the stable state is different for each phase. The resist drying and solvent volatilization mechanisms are important in determining the polymer conformation. Comparing the three types of resist drying, nominal spin drying and soft baking, spin drying only and natural drying, no clear difference was found in appearance, texture randomness, or average CD (Figure 10).

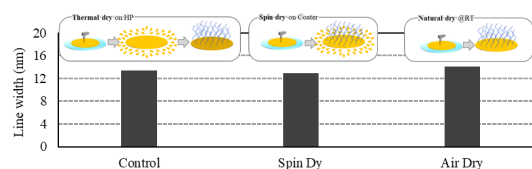


Fig. 10. Variability test result in various resist volatilization method.

According to a paper by Professor Tanaka of Kyushu University, the conformation of the polymer was changed by centrifugal force in the spin casting method as compared with the solvent casting method. The polymer conformation was confirmed throughout the wafer because the stress resisting the film was different at each point throughout the wafer due to centrifugal force. The centrifugal force at the center of the wafer is "0", which is 22.2 N (2.26 kgf) at the

edge position of the 300 mm wafer. The random texture of the polymer aggregate unexpectedly remained in its original condition at each test point (Figure 11). From the same point of view, the relaxation effect of the polymer by thermal annealing was investigated, however none were changed (Figure. 12). According to these test results related to the track process, it must be said that resist tracks do not have effective control over polymer aggregate.

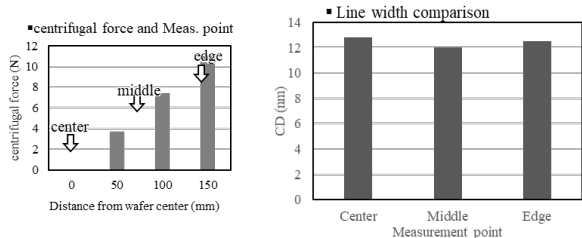


Fig. 11. Examination result of stress impact in resist film formation.

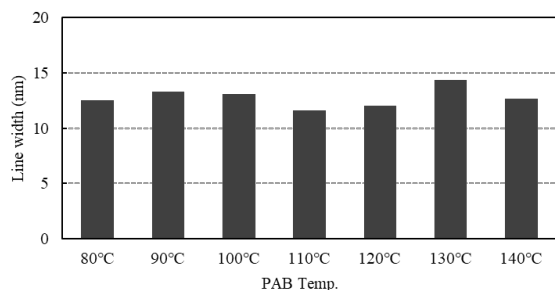


Fig. 12. Annealing effect test result for film stress mitigation related polymer conformation.

The material design of the resist is also important for investigating the conformation of the polymer. In general, EUV backbone polymers are composed of two types of units, an acrylate unit and a PHS (polyhydrostyrene), and the compound ratio is generally optimized by resist synthesis. Therefore, materials with different compound ratios were investigated. One test resist is Acrylate-rich material and other one is PHS-rich type. Obvious mean line width difference, 12.8 nm and 10.9 nm was found in this comparison (Figure 13). Basically, molecular weight is optimized for downward scaling and EUV resist has smaller molecular weight of 193 resist in conventional practice. It seemed that line width of carbon linear cluster was getting smaller in the case of lower molecular weight. In this case, EUV resist had a half molecular weight and then line width varied from 12.6 nm to 9.8 nm (Figure 14).

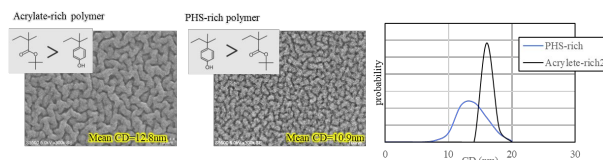


Fig. 13. Variation check result in polymer design in resist material: Acrylate-PHS combination.

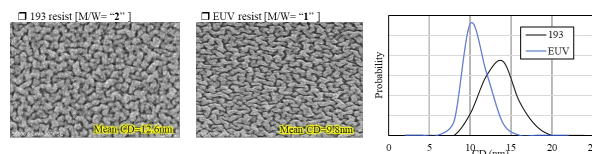


Fig. 14. Variation check result in polymer design in resist material: Molecular weight modification.

The results in this section show that the line width of linear carbon clusters can be changed by minimizing polymer design. Polymer design may be more important than a description of photon and PAG behavior.

2.5. Depth profile of polymer grain of resist film

According to the previous section, there are three important things to reduce LER.

- Resist film construct with linear carbon cluster
- Winding shape of LER match the contour of carbon cluster
- Line width of cluster strongly depends on polymer molecular weight

Since the molecular weight of EUV resist is lower than that of 193 nm resist, the LER of EUV resist should be small. But on the contrary, the LER is worse than 193 nm. Therefore, it should be recognized that another potential factor influences the increase in LER. First, the thickness of EUV resist is thinner than that of 193 nm due to its continuous scaling. The nominal resist thickness in the 193 nm era (about 70 nm) was reduced to less than 20 nm in the EUV era to prevent pattern collapse.

Now, when the resist film is made extremely thin, a particularly interesting phenomenon occurs. That is, the top surface of the resist pattern becomes rough. Based on this result, the depth profile of the carbon cluster was confirmed. For the purpose, various thicknesses of resist films were prepared in the same way as the contrast curve was made, and then the samples were slightly etched with argon plasma as

described above. The appearance of the carbon clusters at each slice level is shown in Figure 15 and the line widths are plotted in Figure 16.

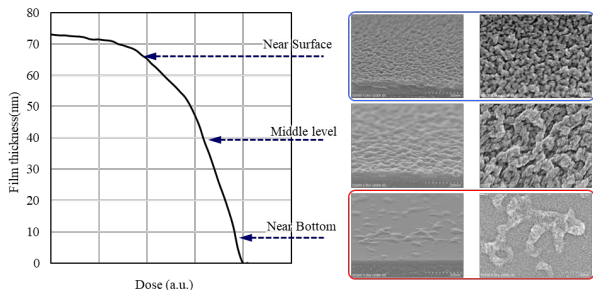


Fig. 15. Depth profile of carbon cluster appearance through resist film.

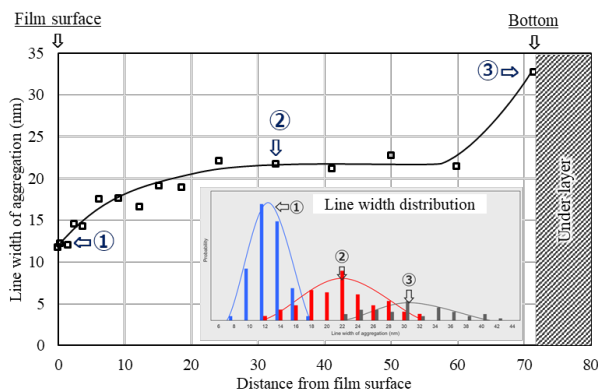


Fig. 16. CD variation in each slice level through resist film.

Line width variation is,

- ◆ Near surface: smallest, around 12 nm,
- ◆ Bulk area: getting bigger to 22 nm,
- ◆ Near bottom: getting bigger more to 33 nm.

As summarized in Figure 17 [9], the significant increase in roughness when thinning the resist can be due to the larger sized carbon clusters formed near the bottom of the resist.

Simply put

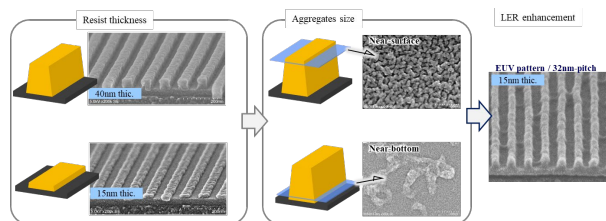
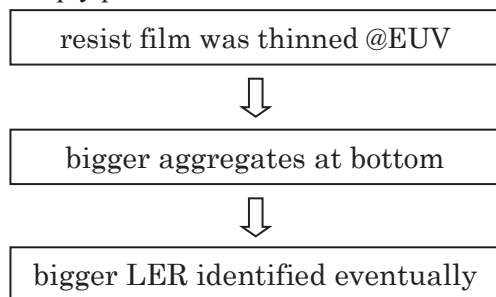


Fig. 17. Assumption of induction factor of LER with resist film thickness.

2.6. Resist behavior in opened space region

The most serious problems today are residual types of defects such as missing holes and bridge lines, and it is really waiting for a solution. To find a solution to minimize defects, the behavior of the resist was investigated by the polymer dynamics aspects, similarly as polymer clusters observation. The focal area of observation is the very low dose state stage before the formation of dotted polymer aggregates, which corresponds to the unexposed open space area of the resist pattern. In this work, as shown in Figure. 18, four types of lower layers with different surface free energies were prepared. The two key factors that make up the surface free energy, the dispersion and polarity components, have changed in the bottom four layers (UL-A to D).

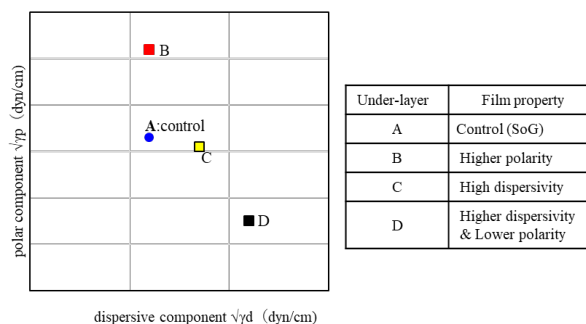


Fig. 18. γ value elements of UL material.

The observation criteria were SEM image acquisition and roughness measurement with an atomic force microscope (AFM). Figure 19 shows an image comparison of defects. UL-A and C defects are large, and UL-B and D are significantly smaller. As previously reported in SPIE [4], UL-B has the advantage of reducing defects over UL-A. Therefore, this result may represent other evidence of defect mitigation capabilities. In addition, the analysis results by X-ray photoelectron spectroscopy (XPS) are also shown in Figure 20. This is a depth profile of the qualitative analysis results comparing the cases of

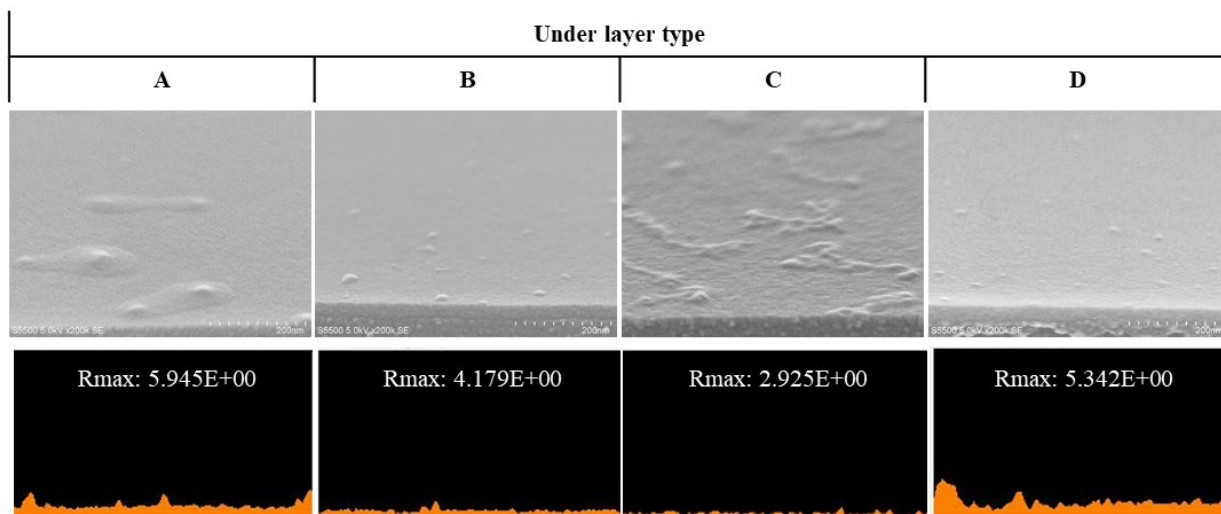


Fig. 19. Resist residue SEM image and AFM profile.

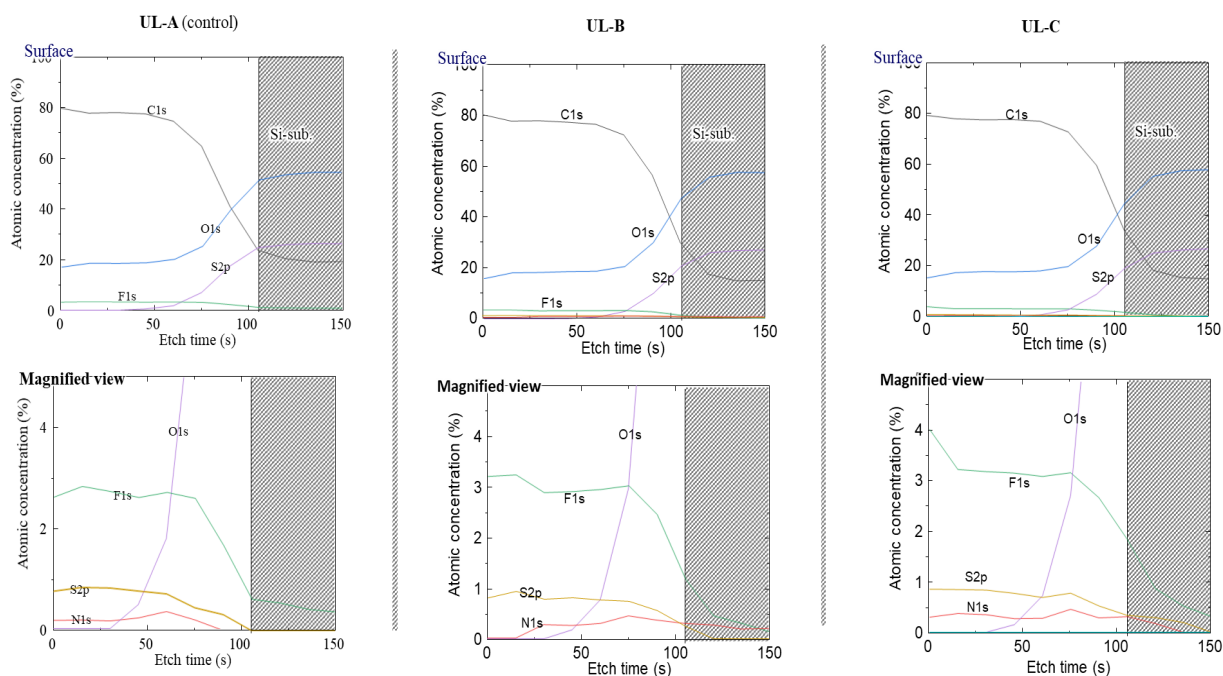


Fig. 20. XPS analytical result comparison in 3 kind of under layer material.

three different under layers. Target elements are sulfur, fluorine, nitrogen and others found in PAG or quencher derivatives and other additives. The additives never move and do not appear to change the surface-to-bottom distribution of the resist under several different underlayer conditions. And it can be understood that the properties of the residue are not due to the influence of the resist additive.

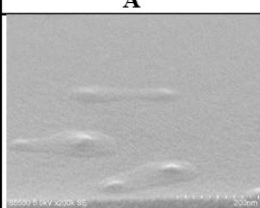
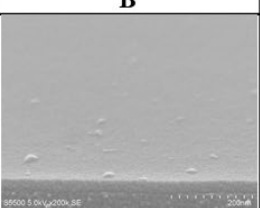
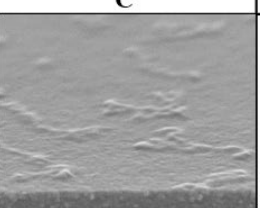
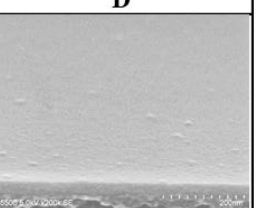
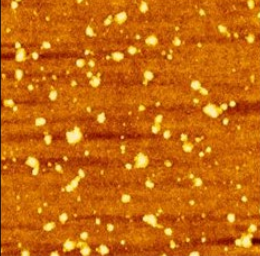
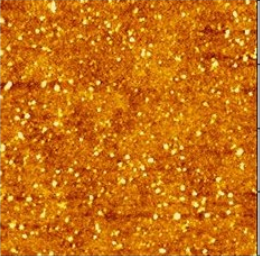
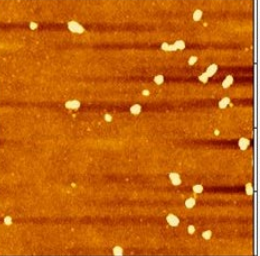
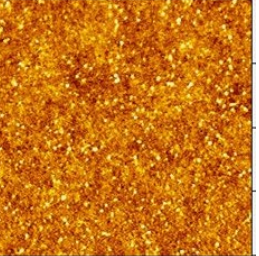
Table 7 summarizes the relevant factors to reduce the number of defects. From this table, it can be pointed out that the adhesive work may be the most effective indicator of affecting defects. The condition with lower adhesive work appears to cause desorption of residues from the substrate.

In addition, the material of the underlayer is also noteworthy. Many defects were found on composite type underlayer but reduced on single component one. The atomic size is microscopic and cannot be measured at present, however, it looks that the elemental formation of the underlayer material was relatively uniform compared to the composite type. Several preferred methods for surface condition analysis may be proposed in the future to replace current contact angle measurement methods.

3. Conclusion

In this paper, several types of randomness were visualized and quantified, targeting any stochastic

Table 7. Summarized comparison of defect density and impacted factor.

Under Layer	A	B	C	D
SEM image on Opening region				
AFM image				
Surface rough	2.799E+00	3.286E+00	6.030E+00	2.925E+00
Adhesive Work	0.9	0.7	1.6	0.7
Film forming	Solvent-casting	Solvent-casting	Solvent-casting	Deposition
Component	Composite	Mono	Composite	Mono

phenomena caused by local variation and residual types defects in the EUV process. The points regarding LER are as follows.

- Resist pattern consists with pixelated polymer aggregates.
- Its pixel size was approximately 12 nm.
- It might correspond to resolution limit.

It can also be said that polymer aggregate must be related with defect density. Important factor may be polymer design in resist synthesis and surface condition of underlayer. Cross-section SEMs were primarily used in this work, but non-destructive methodologies with short turnaround times must be considered in the future.

References

1. Kozawa, T., and Tagawa, S., “Radiation chemistry in chemically amplified resists”, *Jap. J. Appl. Phys.* 49 (2010)
2. Tarutani, S., Tsubaki, H., and Kanna, S., “Development of materials and processes for negative tone development toward 32-nm node 193-nm immersion double-patterning process”, *Proc. SPIE 7273, 72730C* (2009)
3. Cutler, C. A., Mackevich, J. F., Li, J., O’Connell, D. J., Cardinale, G. F., and Brainard, R. L., “Effect of Polymer Molecular Weight on AFM Polymer Aggregate Size and LER of EUV Resists”, *Proc. of SPIE Vol. 5037* (2003)

4. Yaegashi, H., Hara, A., Okada, S., and Shimura, S., “Explorations of missing hole defect in EUV patterning”, *proc. of SPIE 11326-13* (2020)
5. Hohle, C. K., Heckmann, N., Sebald, M., Markert, M., Stepanenko, N., Houlihan, F. M., Romano, A. R., Sakamuri, R., Rentkiewicz, D., and Dammel, R. R., “Surface roughness investigation of 157- and 193-nm polymer platforms using different etch conditions”, *J. Microlith., Microfab., Microsyst.* 4(4), 043009 (2005)
6. Oehrlein, G. S., Phaneuf, R. J., and Graves, D. B., “Plasma-polymer interactions: A review of progress in understanding polymer resist mask durability during plasma etching for nanoscale fabrication”, *J. Vac. Sci. Technol. B* 29 (2011)
7. Takeuchi, T., Corbella, C., Kreul, S. G., Keudell, A. V., Ishikawa, K., Kondo, H., Takeda, K., Sekine, M., and Hori, M., “Development of the sputtering yields of ArF photoresist after the onset of argon ion bombardment”, *Journal of Applied Physics* 113, 014306 (2013)
8. Ito, H., Willson, C. G., Frechet, J. H. J., “New UV resists with negative or positive tone”, *Symposium on VLSI Technology* (1982)
9. Yaegashi, H., Koike, K., “Reconsiderations of LER characterization”, *proc. of SPIE, 10586-8* (2018)

Characterization of Surface Variation of Chemically Amplified Photoresist to Evaluate Extreme Ultraviolet Lithography Stochastics Effects

Eric Liu^{1*}, Amir Hegazy¹, Hyeonseon Choi¹, Maximilian Weires¹
Robert Brainard¹, and Gregory Denbeaux¹

¹ College of Nanoscale Science and Engineering, State University of New York
Polytechnic Institute, 257 Fuller Road, Albany, NY, 12203, USA

*eliu@sunypoly.edu

Extreme ultraviolet (EUV) lithography is required for advanced node semiconductor device fabrication. The stochastic effects in EUV lithography are problematic, especially with regards to pattern roughness and defect formation. In this study, we performed atomic force microscopy (AFM) on an EUV photoresist surface to determine the surface roughness, height histogram, line scan, area ratio, and power spectral density (PSD). Polymethyl methacrylate (PMMA) for nonchemically amplified resist (non-CAR), and poly(4-hydroxystyrene)(t-butyl acrylate) copolymer (PHS:tBA) and poly(4-hydroxystyrene)(polystyrene)(t-butyl acrylate) copolymer (PHSPS:tBA) with/ di-(t-butylphenyl)iodonium perfluorobutane sulfonate (TBPI-PFBS)/tetrabutylammonium lactate (TBAL) for chemically amplified resist (CAR) were examined. In this CAR system, the exposure and dark loss contributed to the surface variation of root mean square (RMS) of 1.5 nm and 0.95 nm under a nominal exposure dosage of 8 $\mu\text{C}/\text{cm}^2$. The contribution of dark loss was further evaluated from the effects of backbone polymer composition and photoacid generator (PAG) loading. The dark loss induced surface roughness can be attributed to the competition of etch selectivity in the resist components. A skewness of the height histogram and change of correlation in PSD are related to the dark loss induced surface variation.

Keywords: EUV, Stochastics effects, AFM, CAR, Non-CAR, Surface roughness.

1. Introduction

In the semiconductor industry, device dimension reduction is one of the most effective strategies to reduce the manufacturing cost and enhance the device performance. A lithography process, known as extreme ultraviolet (EUV) lithography, has been successfully introduced into the advanced logic node device fabrication. Given the novelty of EUV lithography, still several areas require extensive research efforts such as productivity, pattern fidelity, and stochastic effects [1]–[4]. In general, the stochastic effects in EUV lithography include the contributions from the probability distribution between photons, electrons, the photoresist material, and post-exposure treatments [5], [6]. These stochastic effects usually form defects in the devices and introduce pattern variations in the physical features [2], [7]–[10]. The pattern variation is

generally described as line-edge-roughness (LER) in line/space patterns and contact-edge-roughness (CER) in circular patterns. High LER and CER in semiconductor logic devices deteriorate the device performance [11]–[15].

In EUV lithography, the use of photoresist can be categorized into two types: CAR and Non-CAR. CAR generally contains the backbone polymers, PAG, and a base, known as the quencher. The imaging mechanism and reaction of CAR have been well studied in the past [16]–[18]. The complexity of resist material, chemically amplified reaction, and EUV lithography exposure conditions make the estimation of stochastic effects and physical variation in CAR a complex task. To understand the surface variation of photoresist, one of the most common physical characterization methods is AFM. AFM has been widely used for the characterization

of polymer surfaces as well as the EUV photoresists in the past few decades. Several research groups have shown a correlation of surface roughness obtained by AFM to the lithography condition and photoresist type [19]–[26]. The previous study reported an elevated surface roughness in the CAR, which was correlated with dark loss induced surface roughness and resist composition [21]. Another study correlated the surface roughness with device yield and defectivity in the CAR [26]. Most AFM data in previous studies showed just the RMS for the surface roughness. A more detailed data processing can be carried out to construct a complete physical presentation of the photoresist surface such as power spectral density (PSD), area ratio, and histogram of height distribution.

In this study, AFM was used to characterize the surface of photoresist as shown in Fig. 1. The data was then used in the next step of data processing to determine the histogram, area ratio/ particle counts, and PSD. The height distribution, occupied area of peak/valley, and correlation length between two equivalent height signals within the scan area were also extracted. All this information was used to decouple the source of variation from each element in both non-CAR and CAR and to understand the EUV lithography stochastic effects as well as the inhomogeneity behavior of development-induced surface variation.

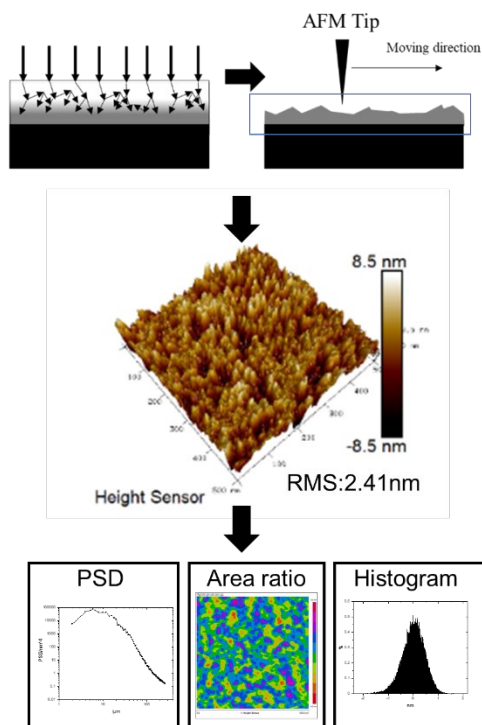


Fig. 1. Illustration of AFM data collection on photoresist surface and data processing.

2. Experimental

2.1. Sample preparation

The CAR was synthesized using 2 wt% of a solid polymer dissolved in propylene glycol methyl ether acetate (PGMEA). The solid polymer is a combination of poly(4-hydroxystyrene) (t-butyl acrylate) copolymer (PHS:tBA) or poly(4-hydroxystyrene)(polystyrene)(t-butyl acrylate) copolymer (PHSPS:tBA) as the backbone polymer, with di-(t-butylphenyl)iodonium perfluorobutane sulfonate (TBPI-PFBS) as the PAG, and tetrabutylammonium lactate (TBAL) as the quencher. PHS:tBA copolymer has a composition ratio of 60:40 and an average molecular weight of 11,500 g/mol. The two types of copolymers PHSPS:tBA, PHSPS:tBA 074 with a composition ratio of 61:24:15 and PHSPS:tBA 075 with a composition ratio of 66:19:15, were obtained from Dow Chemical. The nominal condition of CAR in this study is 83.5 wt% of PHS:tBA or PHSPS:tBA polymer, 15 wt% of TBPI-PFBS as PAG, and 1.5 wt% of TBAL as base. The non-CAR was obtained as a premade 950 k molecular weight PMMA from MicroChem. The chemical structures of both CAR and non-CAR are shown in Fig. 2.

The photoresist was spin-coated onto 4-inch silicon substrates. The spin coat conditions for the CAR are 5 s in 500 rpm, followed by 45 s in 2000 rpm, 5 s in 500 rpm, and 60 s in 1500 rpm for non-CAR. The wafer was subjected to a post-apply bake (PAB) on a hot plate at 120 °C for 60 s for the CAR and 180 °C for 75 s for the non-CAR. The samples were exposed to an electron beam (e-beam) in an Electron-Resist Interaction Chamber (ERIC) at the College of Nanoscale Science and Engineering in Albany, NY, described elsewhere previously [27]–[30]. The e-beam energy was 80 eV, and the nominal dosage of 8 $\mu\text{C}/\text{cm}^2$. After the e-beam exposure, the samples were treated by PEB on a hot plate at 120 °C for 90 s. The CAR samples were rinsed with the developer solution consisting of 0.13 N/0.26 N tetramethylammonium hydroxide (TMAH) at room temperature for 45 s, followed by 30 s of deionized water rinse and drying with nitrogen. For the non-CAR samples, the samples were developed in 1:3 methyl isobutyl ketone/isopropyl alcohol for 30 s at room temperature, followed by deionized water rinse and nitrogen drying. The development-only samples were coated and baked under the PAB conditions. The tested development conditions included a development time from 0 s to 110 s.

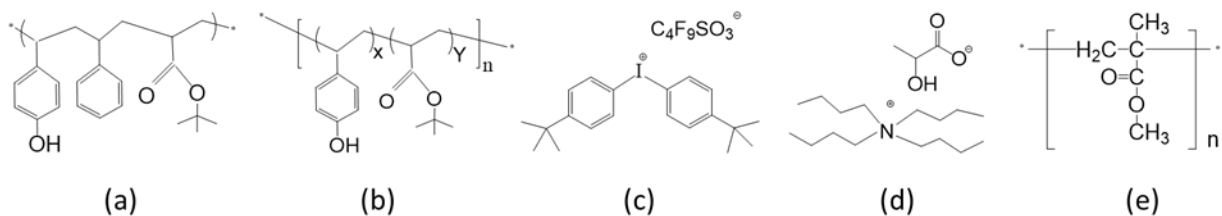


Fig. 2. Chemical structure of CAR (a) PHSPS:tBA, (b) PHS:tBA, (3) TBPI-PFBS, and (d) TBAL and non-CAR (e) PMMA.

2.2. Metrology

The surface roughness was characterized using a Dimension Icon AFM system from Bruker. The measurements were conducted in the noncontact mode of SCANASYST-AIR scan. The tip was made of a triangular shaped silicon nitride with 2 nm tip radius. The scan area was 0.25 μm². The horizontal scan speed was maintained at 500 nm per second, and the step size in vertical direction was <4 nm per step. The results were processed using a NanoScope Analysis software from Bruker using a third-order flattening and noise removal filter to obtain the RMS, PSD, and height distribution histogram by centering the highest point. The AFM images were converted into a quantized color contour image. The area ratio was calculated from a feature with an area of 6 nm and below by normalizing the highest height of each data point. The thickness loss was obtained using a J.A. Woollam M-2000V spectroscopic ellipsometer equipped with a Cauchy thickness model for photoresist on the silicon substrate.

3. Results and discussion

3.1. Surface roughness of PHSPS:tBA CAR vs PMMA non-CAR

To separate different sources of surface roughness on the resist, a simplified model was used assuming that each process is an independent source of roughness. Under the assumption of independent parameter, this simple view of EUV lithography stochastic effects on surface roughness is shown as Equations (1) and (2) for the non-CAR and CAR cases

$$\sigma_{Total\ of\ Non-CAR}^2 = \sigma_{Coat}^2 + \sigma_{Exp}^2 + \sigma_{Dev}^2 \quad (1)$$

$$\sigma_{Total\ of\ CAR}^2 = \sigma_{Coat}^2 + \sigma_{Exp}^2 + \sigma_{Dev}^2 \quad (2)$$

$\sigma_{Total\ of\ Non-CAR}$ and $\sigma_{Total\ of\ CAR}$ are the photoresist surface roughness in non-CAR and CAR, respectively. σ_{Coat} is the surface roughness after coating, representing the surface roughness before exposure. This includes the contributions from

resist conformity, uniformity, and film adhesion to the substrate. σ_{Dev} is the surface roughness after the development process includes dark loss induced deprotection reaction variations in the developing process. σ_{Exp} is the surface roughness from the exposure step. This represents the contributions from shot noise and chemical amplified reaction in CAR. This embodies the contributions from material inhomogeneity and Poisson probability distribution in the chemical amplified reaction. This includes photon– electron interaction from the incoming photons, electron cascade within the photoresist material, acid quantum yield, acid diffusion, acid–base neutralization, and the degree of deprotection reaction.

The RMS of surface roughness was collected on both the PMMA as the non-CAR sample and the PHSPS:tBA+TBPI-PFBS+TBAL as the CAR sample in each processing step. The AFM images of both topview and tilt view for the non-CAR and CAR surfaces are shown in Fig. 3. The RMS of both samples significantly decreased after coating in the following processes. In the non-CAR material, dark loss contributed to the RMS degradation from 0.4 nm to 0.5 nm. Further degradation to 0.8 nm can be explained by a combination of dark loss and e-beam exposure. Using Equation 1, the σ_{Exp} was calculated as 0.63 nm in RMS to the overall roughness. In the CAR, the dark loss contributed to the RMS of 0.95 nm. The RMS roughness further degraded to 1.8 nm due to the contributions from the exposure and chemical amplified reaction. Using Equation 2, the contribution of σ_{Exp} was calculated as 1.5 nm in RMS. The contribution of each term is shown in Fig. 4. In the CAR system, the exposure and dark loss can be attributed to the major portion of overall surface variation in this formulation.

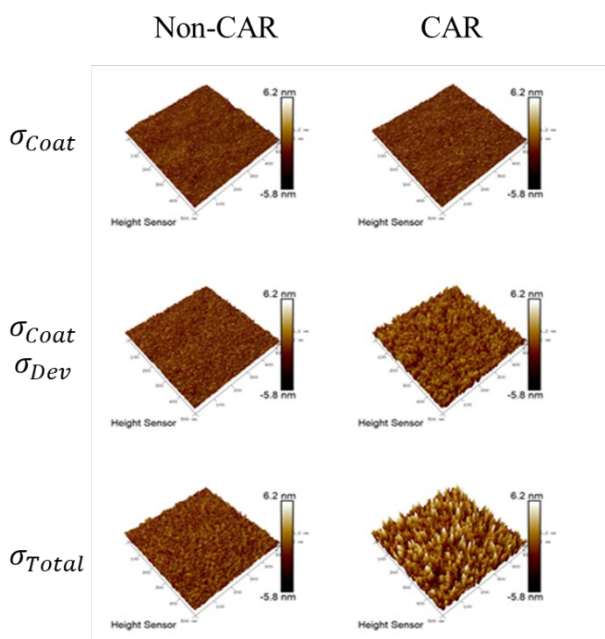


Fig. 3. AFM images of resist surface of PMMA and PHSPS:tBA+TBPI-PFBS+TBAL

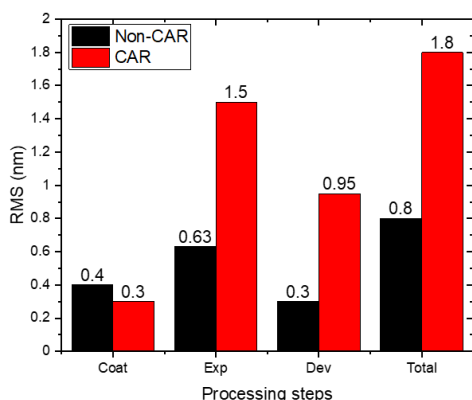


Fig. 4. Contribution of PMMA (Non-CAR) and PHSPS:tBA+TBPI-PFBS+TBAL (CAR) to surface roughness.

3.2. Dark loss induced surface variation in PHS:tBA system

In the following sections, the dark loss induced contribution of resist compositions to surface roughness is discussed, especially the effect of polymer system and PAG loading. The first evaluated CAR sample was PHS:tBA as the backbone polymer. Fig. 5 (a) shows the thickness loss regarding development time. The sample had no PAG and quencher, resulting in the fastest etch rate of >2 nm/s. The presence of PAG and quencher effectively reduced the etch rate to 0.5 A/s. PAG worked as a development inhibitor and reduced the etch rate as well as the backbone polymer, as reported previously [31], [32]. No distinct

difference in term of etch rate was observed between the presence of 1.5 wt% quencher with PAG in PHS:tBA. Fig. 5(b) shows the RMS performance regarding development time. The sample with PHS:tBA-only shows no roughness response with the development time. The film was mostly removed in the first 10 s of development. The AFM measurement was most likely conducted on the silicon substrate but not on the photoresist. The samples with PAG and quencher and without quencher show a similar trend as the surface roughness increases with the development time. Fig. 6 shows the surface evolution with development time. The RMS increased from 0.29 nm after coating to 2.52 nm after 110 s of development.

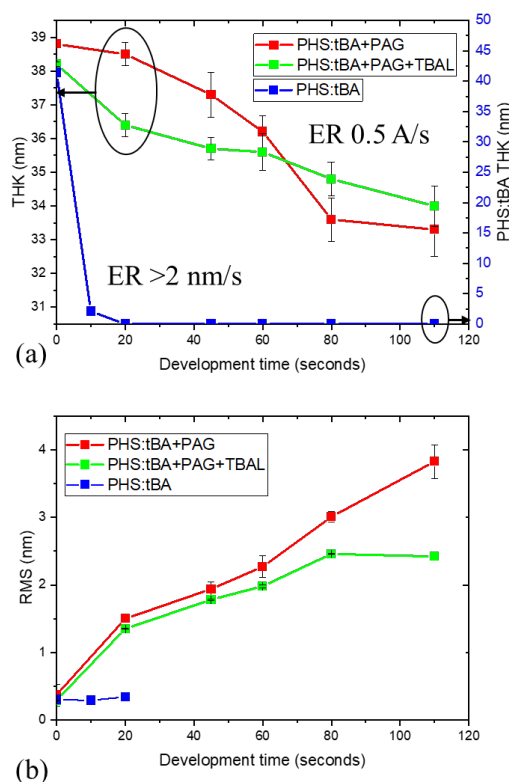


Fig. 5. (a) Film thickness change and (b) RMS change with the development time in the resist system of PHS:tBA

Fig. 7 (a) and (b) show an AFM line scan comparison between the development time and comparison of height histogram. The surface roughness or variation is clearly associated with the development time as well as “valley” formation. The “valley” is classified as a big trench on the resist surface. The implication of “valley” formation is

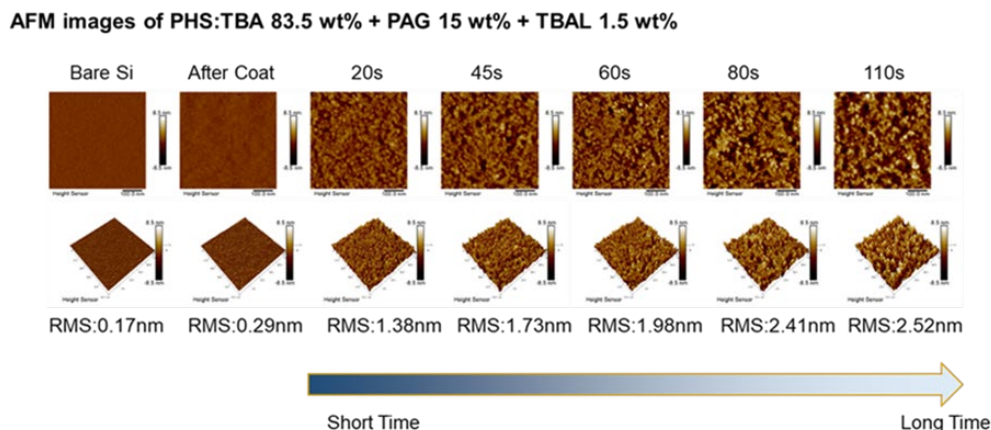


Fig. 6. AFM images of PHS:tBA with 15 wt% of PAG and 1.5 wt% of TBAL with the development time.

shown as a localized material loss with a relatively faster etch rate than the adjacent site and resulted in a rough surface. A similar result was observed in the height histogram. The histogram was started in the shape of a normal distribution in 0 s and then progressed into a skewness into the region of negative height. This indicates a localized dissolution rate difference that tends to be correlated with the resist component and inhomogeneity of resist structure.

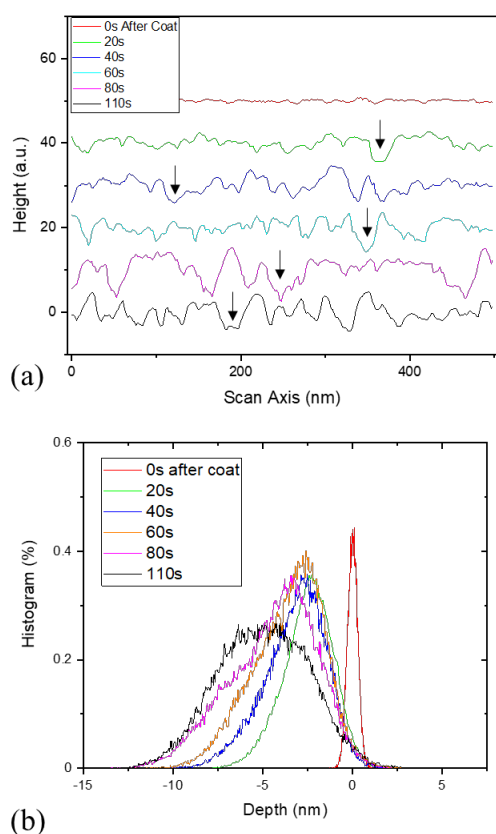


Fig 7. (a) Line scan and (b) height histogram of PHS:tBA with 15 wt% of PAG and 1.5 wt% of TBAL with the development time. The black arrows show examples of valley formation.

Fig. 8 shows the ratio of valley area to the total scan area with the development time. A clear valley area expansion was associated with the development time. In the first 20 s, the valleys were created locally and accounted only <10% of the total scan area. The area increased with the development time. At 80 s of development, the valleys account for close to 65% of the scan area of the resist and show a few features that protruded out of the surface. At 110 s of development, the valley area was slightly reduced to around 55% from the possible undercut etch and the isotropic etch behavior of the wet dissolution.

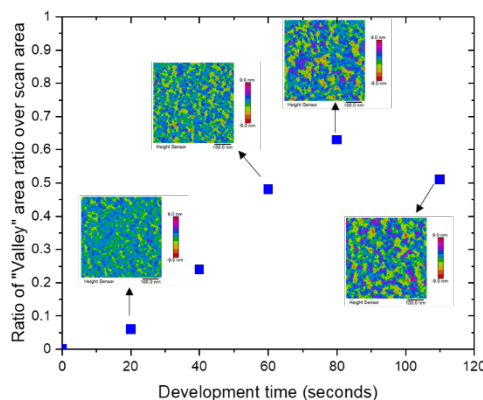


Fig 8. Ratio of “valley” area over the scan area with the development time.

3.3. Dark loss induced surface variation in PHSPS:tBA system and PAG loading

In this section, the role of backbone polymers and PAG loading to dark loss induced surface variation is discussed. Fig. 9 (a) shows the thickness loss of tested samples with the development time. The PHS:tBA sample with PAG and quencher had an etch rate of about 0.5 Å/s. The other tested samples had an etch rate of <0.1 Å/s or no average film loss.

The development rate on these tested samples was effectively reduced by changing the polymer system from PHS:tBA to PHSPS:tBA. The presence of polystyrene in the copolymer system tends to alleviate the film loss during the wet process because it does not contain a polar group in the structure. One commercially available CAR resist was also included in the comparison with equivalent development condition. No noticeable thickness change was observed in this resist.

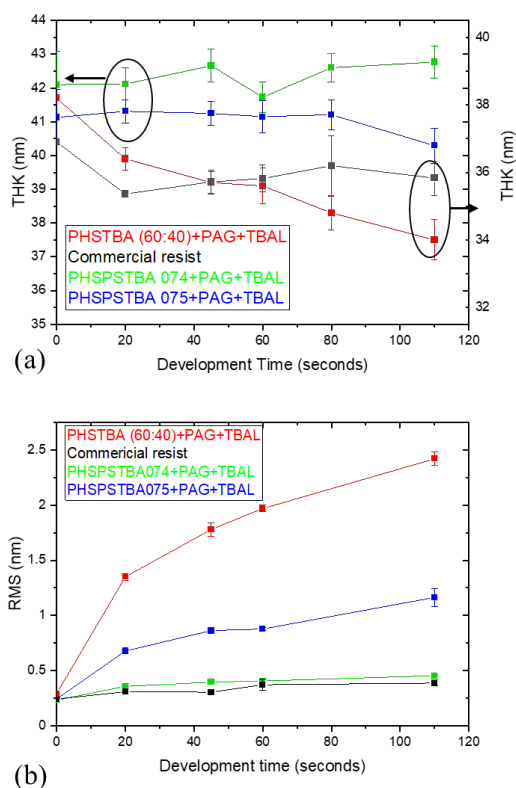


Fig. 9. (a) Film thickness change and (b) RMS change with the development time.

Fig. 9 (b) shows the progression of surface roughens with development time in PHS:tBA, PHSPS:tBA 074, PHSPS:tBA 075, and the commercial resist. The general trend was observed as the surface roughness increased with the development time among all the tested samples. The reduction in film loss in the presence of polystyrene can also be attributed to a reduction in the degradation of surface roughness. The amount of polystyrene in the two PHSPS:tBA systems also significantly affected the surface roughness. PHSPS:tBA 074 has 24% of polystyrene than 19% in 075 in the copolymer system, resulting in an RMS difference from 0.4 nm to 1.01 nm under 110 s of development process. The presence of PAG and

polystyrene works as a dissolution inhibitor, corresponding to a slower etch rate in the development process than the PHS:tBA system. The etch selectivity between the components of the resist is clearly associated with the dark loss induced surface roughness. In the PHSPS:tBA system, both components of backbone polymer and PAG had a relatively slower etch rate, thus resulting in a minor degradation of surface roughness with the development process. In the PHS:tBA system, the backbone polymer and PAG had a significant difference in etch rate. The faster etch rate component tends to be removed first, and the slow etch rate components tend to remain on the surface for creating a rough surface. The commercially available resist had a similar surface roughness as PHSPS:tBA 074 system with minor dark loss induced surface roughness.

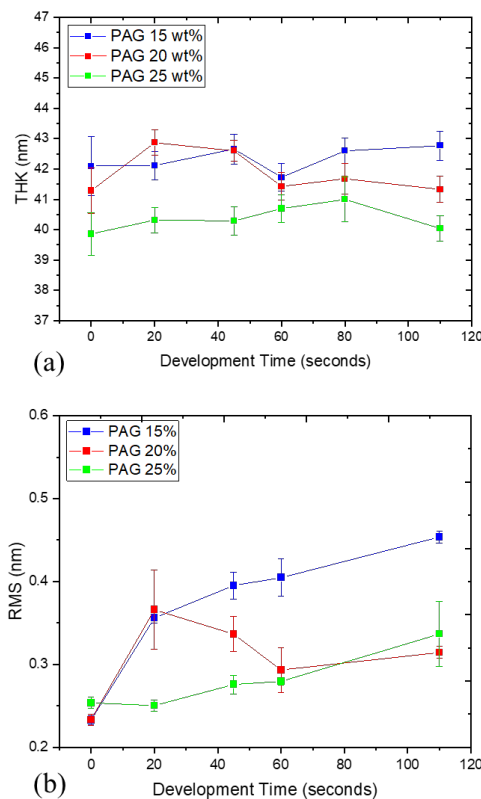


Fig. 10. PAG loading to (a) film thickness change and (b) RMS change with the development time in the resist system of PHSPS:tBA 074 with TBAL.

Fig. 10 (a) shows the film loss with development time in the PHSPS:tBA 074 resist with 1.5 wt% of TBAL and PAG loading of 15, 20, and 25 wt%. Similar results are also observed in Fig. 9 (a). No obvious film loss was observed with the increase of

development time. The change in film thickness was within the sample variation. Fig. 10 (b) shows the RMS performance with the development time between the PAG loading tested conditions. In general, the surface roughness increased with development time. The high concentration of PAG has the lowest RMS. PAG was added to reduce the etch selectivity between resist components. Fig. 11 shows a PSD comparison between the PAG loading tested conditions. The tested condition with 15 wt% of PAG had a high PSD within the most frequency domain. The correlation length beyond 100 nm was not considered due the lack of data points within the limited scan area. By increasing the PAG loading from 15 wt% to 25 wt%, a change in correlation length in spatial frequency was observed. The correlation length increased from 33 nm to close to 100 nm. The presence of PAG affects both average surface roughness and the spatial frequency of surface topography from the PSD observation.

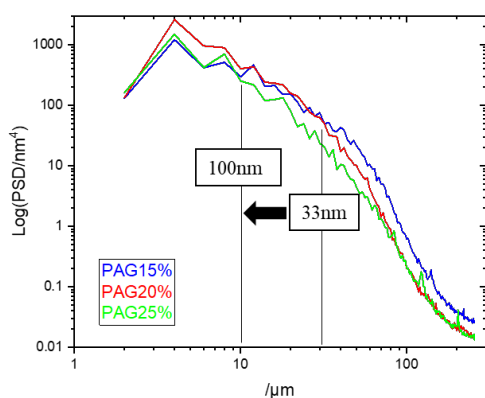


Fig. 11. PSD comparison of PAG loading tested conditions in the resist system of PHSPS:tBA 074 and TBAL at development of 45 s.

4. Summary and Conclusion

In summary, the surface topography of an EUV photoresist was characterized by AFM. In a particular CAR system, the photochemistry and dark loss were the main contributors to the overall surface variation. An extensive study was conducted to evaluate the effect of dark loss including the backbone polymer system and PAG loading. The AFM data was processed and extracted to determine the height histogram, line scan, area ratio calculation, and PSD. From this information, the dark loss induced surface roughness can be attributed to the competition of etch selectivity in resist components. When the etch selectivity is relatively low as well as low film loss, the dark loss

induced surface roughness remains relatively smooth. In the case of a high etch selectivity between the components, a substantial difference in etch rate in the deprotection front led to a high surface roughness as well as a change of correlation length in PSD and skewness in the height histogram.

Acknowledgement

This work was funded in part by Semiconductor Research Corporation (SRC) Nanomanufacturing and Processes (NMP) research program, and it was performed at the State University of New York Polytechnic Institute, College of Nanoscale Science and Engineering at Albany, NY. We would like to thank Sandra Schujman for her in-depth knowledge and valuable help in the AFM measurements.

References

1. H. J. Levinson and T. A. Brunner, *Proc. SPIE*, **10809** (2018) 1080903.
2. P. De Bisschop, *J. Micro/Nanolithography, MEMS, MOEMS*, **16** (2017) 1.
3. P. P. Naulleau, C. N. Anderson, L.-M. Baclean, P. Denham, S. George, K. A. Goldberg, G. Jones, B. McClinton, R. Miyakawa, S. Rekawa, and N. Smith, *Proc. SPIE*, **7972** (2011) 797202.
4. S. Bhattarai, A.R. Neureuther, and P. P. Naulleau, *J. Vac. Sci. Technol. B, Nanotechnol. Microelectron. Mater. Process. Meas. Phenom.*, **35** (2017) 061602.
5. C. A. Mack, *Proc. SPIE*, **11147** (2019) 111470A.
6. J. W. Thackeray, *Proc. SPIE*, **7972** (2011) 797204.
7. L. Meli, K. Petrillo, A. De Silva, J. Arnold, N. M. Felix, C. Robinson, B. Briggs, Y. Mignot, J. Shearer, B. Hamieh, K. Hontake, L. Huli, C. Lemley, D. Hetzer, T. Shimoaoki, Y. Hashimoto, H. Ichinomiya, A. Kai, S. Kawakami, K. Tanaka, A. Jain, B. Saville, C. Lenox, S. Matham, E. Liu, K. Akiteru, and H. Choi, *Proc. SPIE*, **10583** (2018) 105830E.
8. Raley, C.A. Mack, E. Liu, S. Thibaut, and A. Ko, *Proc. SPIE*, **10809** (2018) 1080915.
9. Ashim Dutta, J. Church, J. Lee, L. Meli, C. Chun Liu, S. Sharma, K. Petrillo, C. Murray, E. Liu, K. Lutker-Lee, Q. Lou, C. Cole, A. Raley, A. Ko, S. Kal, J. Kaminsky, A. Mosden, H. Zhang, S. Hu, L. Huli, N. Shibata, D. Hetzer, and C.-Y. Hsieh, *Proc. SPIE*, **11323** (2020) 113230V.
10. E. Liu, S. Thibaut, A. Ko, and P. Biolsi, *Proc. SPIE*, **10963** (2019) 109630R.
11. A. H. Gabor, A. Brendler, T. A. Brunner, X.

- Chen, J. Culp, and H. Levinson, *Proc. SPIE*, **10583** (2018) 105830C.
12. D. De Simone, V. Rutigliani, G. Lorusso, P. De Bisschop, Y. Vesters, V. M. Blanco Carballo, and G. Vandenberghe, *Proc. SPIE*, **10583** (2018) 105830G.
 13. E. Liu, A. Ko, R.A. Farrell, D. O'Meara, C.-Y. Hsieh, and P. Biolsi, *Proc. SPIE*, **10584** (2018) 1058408.
 14. D. Nagy, G. Indalecio, A. J. Garcia-Loureiro, M.A. Elmessary, K. Kalna, and N. Seoane, *IEEE J. Electron Devices Soc.*, **6** (2018) 332.
 15. Y. Luo and P. Gupta, *Proc. SPIE*, **10588** (2018) 105880O.
 16. Robinson and R. Lawson, *Materials and Processes for Next Generation Lithography* (2016).
 17. K. Nakamura, "Photopolymers: Photoresist Materials, Processes, and Applications" (2014).
 18. U. Okoroanyanwu, *Chemistry and Lithography* (SPIE, 2010).
 19. M. Toriumi, K. Kaneyama, S. Kobayashi, and T. Itani, *Proc. SPIE*, **6923** (2008) 69230L.
 20. T. Yoshimura, H. Shiraishi, J. Yamamoto, and S. Okazaki, *Appl. Phys. Lett.*, **63** (1993) 764.
 21. C. A. Cutler, J. F. Mackevich, J. Li, D. J. O'Connell, G. F. Cardinale, and R. L. Brainard, *Proc. SPIE*, **5037** (2003) 406.
 22. T. Yoshimura, H. Shiraishi, J. Yamamoto, and S. Okazaki, *Jpn. J. Appl. Phys.*, **32** (1993) 6065.
 23. N. Kubota, T. Hayashi, T. Iwai, H. Komano, and A. Kawai, *J. Photopolym. Sci. Technol.*, **16** (2003) 467.
 24. I. U. Ahad, M. A. Obeidi, B. Budner, A. Bartnik, H. Fiedorowicz, and D. Brabazon, *AIP Conf. Proc.*, **1896** (2017) 200008.
 25. B. C. Park, Y. J. Cho, I. Kim, and J. Yeo, *Proc. SPIE*, **8681** (2013) 86812K.
 26. D. Schmidt, K. Petrillo, M.A. Breton, J. Fullam, S. Hand, J. Osborne, W. Wang, and D. Fey, *Proc. SPIE*, **11325** (2020) 113250T.
 27. C. Mbanaso, S. Kruger, C. Higgins, Y. Khopkar, A. Antohe, B. Cardineau, and G. Denbeaux, *Proc. SPIE*, **7969** (2011) 79692J.
 28. S. Grzeskowiak, A. Narasimhan, E. Rebeyev, S. Joshi, R. L. Brainard, and G. Denbeaux, *J. Photopolym. Sci. Technol.*, **29** (2016) 453.
 29. Narasimhan, S. Grzeskowiak, B. Srivats, H. Herbol, L. Wisheart, C. Kelly, W. Earley, L.E. Ocola, M. Neisser, G. Denbeaux, and R.L. Brainard, *Proc. SPIE*, **9422** (2015) 942208.
 30. S. Grzeskowiak, A. Narasimhan, M. Murphy, L. Napolitano, D. A. Freedman, R. L. Brainard, and G. Denbeaux, *Proc. SPIE*, **10146** (2017) 1014605.
 31. B. Kumar and D.L. Goldfarb, *Proc. SPIE*, **10586** (2018) 1058604.
 32. H. Ito, D.-F. Alexander, and G. Breyta, *J. Photopolym. Sci. Technol.* **10** (1997) 397.

New Approaches to EUV Photoresists: Studies of Polyacetals and Polypeptoids to Expand the Photopolymer Toolbox

Jingyuan Deng¹, Florian Kaefer¹, Sean Bailey¹, Yusuke Otsubo^{1,2}

Zoey Meng³, Rachel Segalman³ and Christopher K. Ober^{*,1}

¹Materials Science and Engineering, Cornell University,
Ithaca 14853, NY, USA

²JSR, Corp. 100 Kawajiri-cho, Yokkaichi, Mie, 510-8552, Japan

³Chemical Engineering and Materials, UC Santa Barbara, Santa Barbara, CA, 93106-5080

*cko3@cornell.edu

Low stochastics, high sensitivity photoresists remain a goal for EUV lithography. Here we present studies of two polymer systems that attempt to make improvements to these resist characteristics using two different chemical approaches. In one system we work on scissionable poly(phthalaldehyde) modified to enable incorporation of photoactive units on each repeat unit of the polymer chain. In a second system we explore peptoid polymers that possess identical molecular size and composition with much higher molecular uniformity than possible by conventional synthetic techniques. We report the results of exposure of these materials to EUV exposures and the chemical changes that occur.

Keywords: Scissionable polymers, EUV photolithography, stochastics control, peptoid

1. Introduction

An ongoing challenge in the development of EUV photoresists is solving the issue of stochastics, that is, the random probability distributions of exposure, molecular size and molecular composition which ultimately lead to imperfections in pattern formation. For example, in a classical chemically amplified photoresist there is: i) heterogeneity in polymer composition and ii) in the blending of the photoresist and photoactive additives [1]. The effect of inhomogeneity is believed to contribute to line edge roughness and defect formation among other issues. In most polymer preparation methods in which several building blocks are incorporated, further compositional heterogeneity results from the statistical nature of random copolymerization.

A very effective approach in producing high resolution photoresists has been to create nanoparticle lithographic systems where the basic building blocks are so small that molecular homogeneity becomes simpler to achieve [2]. Nevertheless, there remain advantages in working with polymer systems if stochastics can be

addressed. In this report we discuss two approaches, one based on a polymer that depolymerizes and a second in which synthetic chemistry is used that enables the preparation of polymers chains that are identical in composition and identical in molecular weight.

Chain scissionable polymers are polymers that will depolymerize under different stimuli including acid, base, and free radicals [3]. These polymers have been investigated in the development of photoresists and other degradable materials [4]. The scissionable polymer family we have studied, based on poly(phthalaldehyde), (PPA), has been previously used in high resolution photolithography as, for example, mask making [5] and is of interest as a substrate material in the new field of vanishing electronics. The PPA backbone consists of acetal linkages that are very sensitive to acids. Upon exposure to acids, the polymer chain depolymerizes to its corresponding monomers.

In our study we have modified the basic building block by adding a substituent in order to incorporate units that make the basic polymer both more susceptible to EUV exposure and more likely to

depolymerize after exposure while remaining stable in the absence of radiation. Each chain is made of identical building blocks and by using anionic polymerization has a very narrow molecular weight. Our premise is that while the polymer itself may not be of uniform molecular size (although with narrow dispersity as it is made by living polymerization methods), this is less important because the patterning mechanism involves depolymerization (conversion of polymer to monomer) and removal of the polymer in the exposed area.

In a second resist material, we explore the construction of polymers derived from peptoid units [6]. This polymer family, prepared using a robot synthesizer system originally developed for protein synthesis, is produced on a polymer substrate and can be made in gram quantities. Attachment to a substrate enables exquisite control of the polymer formation chemistry. The number of units in each chain is identical and the average composition is identical, thus minimizing issues of compositional statistics. The efficiency of peptoid preparation (compared to peptides) means that resist molecules ranging from 10 to 20 or more repeat units are easily produced. Recent simulations by researchers at Lawrence Berkeley have shown very interesting scission behavior of amide bonds under EUV radiation [7]. Both the potential for molecular weight control and these simulations prompt our studies.

Our expectation is that these approaches to EUV lithography will help to limit the defects present in an EUV patterning regime, by minimizing the stochastic nature of light-matter interactions through extreme homogeneity in chemical structure and resulting chemical reactivity [8]. At the same time these strategies take advantage of the inherent flexibility of molecular design afforded by polymer synthesis and do not require completely new processes or entirely new molecular systems.

Studies of the results of exposure to EUV radiation and preliminary studies of the lithographic performance of these resist systems have been carried out and will be discussed.

2. Experimental

All reagents were purchased from Sigma Aldrich, Millipore Sigma, TCI America, and Oakwood Products at the highest purity available and used without further purification.

2.1. Synthesis of polyphthalaldehyde (PPA) scissionable polymers

To a Schlenk flask phthalaldehyde monomer and

alcoholic initiator were added. The solids were dissolved in THF and then solution cooled to $-78\text{ }^{\circ}\text{C}$. Base initiator was then added and the reaction stirred while maintaining at $-78\text{ }^{\circ}\text{C}$ for 3 h. End group reagents and pyridine were added and the mixture stirred overnight at $-78\text{ }^{\circ}\text{C}$. The resulting polymer was precipitated in methanol and washed using methanol. The polymers were further purified by dissolving in dichloromethane and re-precipitating into methanol. The synthesis is shown in Figure 1.

Photoresist solution containing 5 wt.% polymer in cyclohexanone blended with PAG was prepared in varying ratios of 10-20 wt.% to PPA. The solution was then spin coated onto a silicon wafer at 3000 rpm for 1 min and post baked at $90\text{ }^{\circ}\text{C}$ for 1 min to remove excessive solvent.

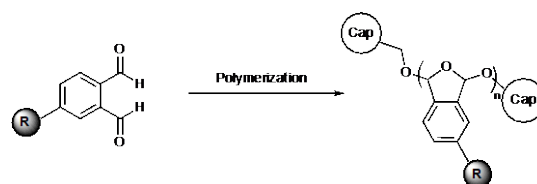


Fig. 1. Synthesis of PPA polymers. R represents a substituent group chosen for a specific functionality or reactivity.

2.2. Synthesis of peptoid photoresists

To start the preparation, 500 mg of 2-chlorotriethyl chloride resin with a loading of 1.7 mmol g^{-1} was swelled in dichloroethane (DCE) and washed with dimethyl-formamide (DMF). The first bromoacetylation step was carried out by adding 10 mL of 0.15 M bromoacetic acid (BAA) in DCE and 1 mL of *N,N*-diisopropylethylamine (DIPEA) to the resin and bubbling with nitrogen for 45 minutes. The resin was then washed repeatedly with DMF. Amination was performed by reacting the acylated resin with 2 M of the amine in DMF for 60 minutes. Additional bromoacetylation steps were conducted with 1.2 M BAA and 1.4 M *N,N'*-diisopropyl carbodiimide (DIC) in DMF. Cleavage was accomplished by treatment with 20% hexafluoroisopropanol in dichloromethane (DCM). The resin was filtered, and the solution was concentrated via rotary evaporation. The resulting solid was dissolved in 1:1 acetonitrile/water and lyophilized to powder. Product purity was evaluated using LC-MS with an acetonitrile-water gradient.

2.3. Lithographic characterization

DUV exposure was conducted on ASML PAS 5500/300C DUV Wafer Stepper. E-beam lithography was carried out on a JEOL 6300 e-beam

lithography tool. The resulting patterns were characterized by, for example, us of an Asylum-MFP3D-Bio-AFM-SPM.

3. Results and discussion

3.1. Phthalaldehyde scissionable polymers

In this study, we focus on the synthesis of PPA derivatives, via metal-free anionic polymerization of phthalaldehyde derivatives. Not only can this method produce linear PPAs with tunable molecular weights and low dispersity, but also provides the possibility to introduce extra functional groups at the chain ends.

We focused on the investigation of substituted PPA photoresists, which are designed to minimize stochastic issues present in multicomponent EUV resists by direct attachment of PAG units along the backbone. The performance of PPAs as photoresist materials were investigated by means of DUV (Figure 2a) and e-beam (Figure 2b) photolithography.

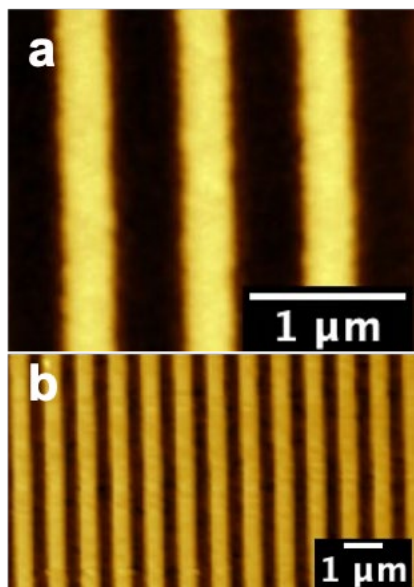


Fig. 2. Line pattern measured using AFM; (a) after DUV exposure ($\sim 50 \text{ mJ/cm}^2$), feature size 512 nm, (b) after exposure to $75 \text{ } \mu\text{C/cm}^2$ e-beam radiation. feature size of 400 nm.

As seen in Figure 2, both 512 nm and 400 nm lines were easily resolved under DUV and e-beam exposure, respectively. Studies of EUV exposures will also be reported.

3.2. Controlled length peptoid photoresists

Resolution in photoresists is controlled by the solubility difference between exposed and unexposed regions. Similarly, line edge roughness

has been correlated to inhomogeneities in regions of the resist possessing both soluble and insoluble components after exposure [9]. These inhomogeneities are partially the result of stochastics in the initial distribution of photoacid generators and solubility change groups [10]. Minimizing such variations via control of the polymer's molecular size is crucial to achieving the lithography performance requirements set by the IEEE IRDS [11]. As resolution and line edge roughness requirements approach the size of sub 10 nm traditional photoresist design or more recent orthogonal methods employing electrochemistry and photochemistry [12] may be inadequate for developing future generations of photoresists.

Peptoids possess repeat units built from *N*-substituted glycines. Compared to peptides, peptoids present numerous advantages including a wider range of functional groups and lower-cost. More efficient synthesis enables production of higher molecular weights with high precision when compared to protein synthesis in molecular weight ranges suitable for photoresists [13]. While peptoids can be produced via ring opening polymerization of *N*-carboxyanhydrides, perfect precise molecular weight control requires the use of solid-phase supports. The most well-developed solid-phase method is the submonomer synthesis (SMS), which combines two types of repeat units, primary amines and bromoacetic acid, in a stepwise manner (Figure 3).

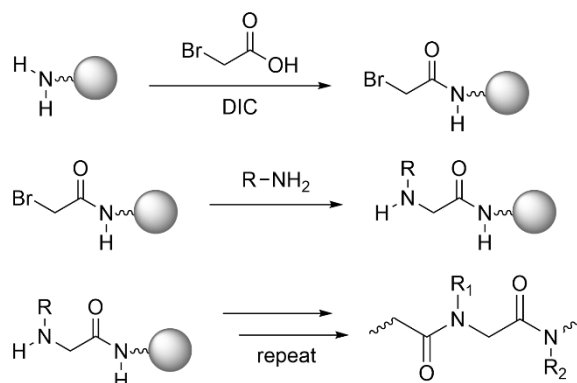


Fig. 3. Sub-monomer synthesis of a peptoid.

The extensive number of commercially available primary amines and the ease of synthesizing novel ones enable a high degree of molecular complexity to be implemented into peptoids. SMS is also an easily scalable process that allows gram-scale synthesis of peptoids of up to 100 repeat units. Anecdotally, amides are thought to interfere with the chemical amplification process from experience

in its early years, due to vulnerability to poisoning by NMP; yet current resist formulations purposely add tertiary amines to prevent dark losses. Recent research has demonstrated that amides can accelerate deprotonation of radical cations [14] that form along the polymer backbone upon exposure to EUV. This feature helps to prevent recombination with other radicals and increases acid generation, thereby enhancing sensitivity [15].

Our goal in these studies was to design peptoids that incorporate chemical moieties adapted to functions such as adhesion to the underlying substrate, etch resistance, and solubility switching. As the peptoids examined are 10-mers, the structure of the side chains is also carefully chosen to avoid crystallization and tune the glass transition temperature. Protecting groups serving as solubility switches were selected with the goal of groups that possessed a high radical cation acidity, a property previously shown to correlate closely with the sensitivity of EUV resists. While these initial results show the potential of peptoids as photoresist materials, the ongoing research is still at an initial stage.

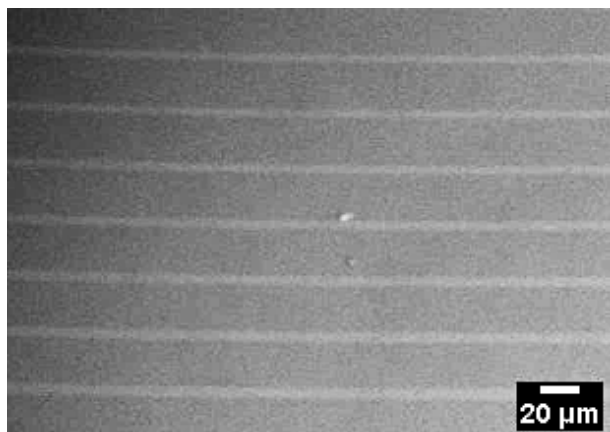


Fig. 4. SEM image of peptoid pattern formed after exposure to 248 nm radiation and development.

4. Conclusion

To summarize, these photopolymers are being investigated to explore methods for producing high resolution, high sensitivity photoresists that minimize stochastic issues through macromolecular design. Results of the preparation and lithographic patterning of these materials will be presented.

Acknowledgements

In this work we thank JSR Corp. for support of Y. Otsubo as a visiting scientist who outlasted the

pandemic during his stay in Ithaca, NY. We also thank JSR for support of F. Kaefer, during the initial stages of this project.

We are grateful to Intel Corp for support of J. Deng through an SRC project and for support of Z. Meng through its CINEMA program.

References

1. A. Lio, *Proc. SPIE*, **97760V-14** (2016) 9776.
2. H. Xu, K. Sakai, K. Kasahara, V. Kosma, K. Yang, H. C. Herbol, J. Odent, P. Clancy, E. P. Giannelis, C. K. Ober, *Chem. Mater.*, **30** (2018) 4124.
3. R. E. Yardley, A. R. Kenaree, and E. R. Gillies, *Macromolecules*, **52** (2019) 6342.
4. H. L. Hernandez, S.-K. Kang, O. P. Lee, S.-W. Hwang, J. A. Kaitz, B. Inci, C. W. Park, S. Chung, N. R. Sottos, J. S. Moore, J. A. Rogers, and S. R. White, *Adv. Mater.*, **26** (2014) 7637.
5. F. Wang and C. E. Diesendruck, *Macromol. Rapid Commun.*, **39** (2018) 1700519.
6. M. E. Barry, E. C. Davidson, C. Zhang, A. L. Patterson, B. Yu, A. K. Leonardi, N. Duzen, K. Malaviya, J. L. Clarke, J. A. Finlay, A. S. Clare, Z. Chen, C. K. Ober, and R. A. Segalman, *Macromolecules*, **52** (2019) 1287.
7. J. Ma, *2021 EUVL Workshop Abstract*, Oct. 23-28, 2021.
8. D. De Simone, Y. Vesters G. Vandenberghe, *J. Photopolym. Sci. Technol.*, **31** (2018) 651.
9. T. Kozawa and S. Tagawa, *Jpn. J. Appl. Phys.*, **49** (2010) 030001.
10. P. D. Ashby, D. L. Olynick, D. F. Ogletree and P. P. Naulleau, *Advanced Materials*, **27** (2015) 5813.
11. M. Neisser, H. Levinson, *Proc. SPIE*, **11323, XI** (2020).
12. M. J. Supej, B. M. Peterson, B. P. Fors, *Chem.*, **6** (2020) 1794.
13. N. Gangloff, J. Ulbricht, T. Lorson, H. Schlaad, R. Luxenhofer, *Chem. Rev.*, **116** (2016) 1753.
14. T. Susa, K. Okamoto, T. Ishida, H. Yamamoto, T. Kozawa, R. Fujiyoshi, K. Umegaki, *SPIE* (2014) 9051.
15. S. Fujii *et al.* *Jpn. J. Appl. Phys.*, **56** (2017) 06GD01.

Investigating High Opacity and Increased Activation Energy in the Multi-Trigger Resist

C. Popescu^a, G. O'Callaghan^a, A. McClelland^a, J. Roth^b, T. Lada^b, T. Kudo^c,
R. Dammel^c, M. Moynour^c, Y. Cao^c, and A.P.G. Robinson^a

^a*Irresistible Materials, Birmingham Research Park, Birmingham, UK*

^b*Nano-C, 33 Southwest Park, Westwood, MA, USA.*

^c*EMD Performance Materials Corp, 70 Meister Ave., Somerville, NJ 08876, USA*
a.p.g.robinson@bham.ac.uk

The development of novel EUV resists is widely agreed to be one of the highest priority challenges for the deployment of high-NA EUV lithography. One potential approach is the multi-trigger concept wherein a reaction will only occur when multiple elements of the resist are initiated concurrently and in close spatial proximity. The multi-trigger material presented consists of a novel MTR molecule and a crosslinker, which represent the resist matrix, together with a photoacid generator (PAG). Research is continuing to upgrade this resist, in particular focusing on improving resist opacity and crosslinking density. Here we present results from further work focused on the enhancement of the high-opacity MTR resist. A new high-Z crosslinker molecule, mark III, has been synthesized and formulated in the MTR resist to make the high opacity MTR compatible with the ethyl lactate and PGMEA casting solvents. We report results obtained using the new MTR system containing this high-Z cross-linker mark III, with a variation of process conditions and formulation variations. The lithographic performance of a formulation containing this crosslinker, at pitch 32nm patterned on an NXE3350 is presented. Furthermore, we have also investigated increasing the activation energy of the self-quenching aspect of the MTR system. In the case presented, MTR8 has a higher activation energy than MTR4. Having a higher activation energy is predicted to allow the introduction of PEB to increase crosslinking and reduce pattern collapse, whilst simultaneously preserving the self-quenching behaviour. We present results which show a decrease in dose and Z-factor using MTR8 at this formulation ratio compared to MTR4.

Keywords: EUV lithography, Photoresist, Molecular resist, Multi-trigger resist, Chemical amplification, Crosslinking

1. Introduction

As EUV lithography becomes established in high volume manufacturing it has been necessary to address many challenges with the tool and the materials. EUV photoresists that have the appropriate capability to support future roadmap requirements remain a challenging topic. Currently traditional chemically amplified resists (CAR) are being used, but several novel approaches are being investigated to support future patterning needs for high resolution and sensitivity and low line width roughness and stochastic defects. [1–3]. It is, however, well-known that these resist metrics are fundamentally linked in a tradeoff relationship, and improvements to one often comes at a cost to

another. For instance, the resolution of a CAR can be improved by reducing the addition diffusion length with base additives or bulky acids, but with a detrimental effect on the required dose and/or the line width roughness. Defectivity due to line collapse, bridging or line breaks is an increasingly common failure mode at pitches below 32nm.

Irresistible Materials (IM) is developing novel resist systems based on the multi-trigger concept. In a multi-trigger resist multiple elements of the resist must be simultaneously activated to enable the catalytic reactions to proceed. In high dose areas the resist therefore behaves like a traditional CAR, whilst in low dose areas, such as line edges, the reaction is second-order increasing the chemical

gradient. Effectively there is a dose dependent quenching-like behavior built into the resist, enhancing chemical contrast and thus resolution and reducing roughness, whilst eliminating the materials stochastic impact of a separate quencher.

In a chemical amplified resist (CAR) (see Figure 1, left hand diagram) the photoacid (H^+) reacts with a resist molecule and is immediately regenerated. The resist molecule is altered from unexposed to exposed in a single step. Quenchers and catalytic inefficiencies remove H^+ , or reactions stop at the end of the PEB, but otherwise the reaction will continue indefinitely. In a multi-trigger material, resist exposure proceeds via a catalytic process in a similar manner to a chemically amplified resist. However, instead of a single photoacid causing a single resist exposure event and then being regenerated, in the multi-trigger resist multiple photoacids activate multiple acid sensitive molecules, which then react with each other to cause a single resist event while also regenerating the photoacids (Figure 1, right hand diagram). In areas with a high number of activated photoacids (higher dose areas, for instance at the centre of a pattern feature) resist components are activated in close proximity and the multistep resist exposure reaction proceeds, ending with photoacids regeneration and thus further reactions, ensuring high sensitivity. In areas with a low number of activated photoacids (lower dose areas, for instance at the edge of a pattern feature), the activated resist components are too widely separated to react, the photoacids are not

released and are thus removed, stopping the catalytic chain. The multi-trigger resist creates an increase in the chemical gradient at the edge of patterned features, and reduces undesirable acid diffusion out of the patterned area.

The multi trigger effect is due to the synergistic combination of two main reaction pathways together with a number of lesser pathways. We can control the weighting of these pathways through formulation choices. In effect there are six different aspects of the resist formulation that can be varied to affect the performance, see figure 2. In the MTR platform previously presented [4-10] it is possible to vary the relative importance (or ratio) of each aspect with a relatively high degree of flexibility, to achieve various performance changes. Whilst performance can be modulated through the formulation ratios, further enhancements are possible by optimizing the functional groups.

Research has been undertaken to improve this resist, in particular focusing on improving resist opacity and crosslinking density. Higher absorption is a potential route to overcome the photon shot noise limit in EUV lithography as well as potentially improving the sensitivity to enable high volume manufacturing at current source power output. IM have added a high *Z non-metal* element onto the crosslinker component of the resist. The formulations that has been tested often also does not include an additional quencher which further reduces the chemical stochasticity, whereas a extrinsic quencher was necessary with the standard

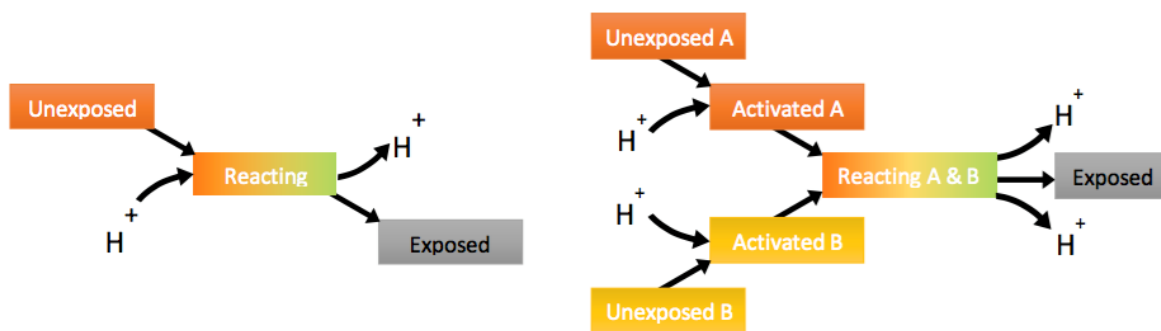


Fig. 1. on left: Traditional Chemical Amplification; on right: Multi Trigger Concept.

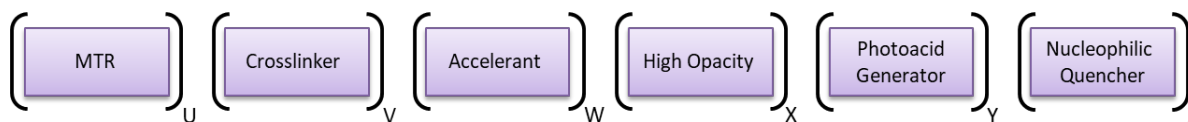


Fig. 2: Aspects of resist formulation that can be varied.

crosslinker to minimize LWR.

The results presented here show the third iterations of this high opacity crosslinker. A mark III high-Z crosslinker was synthesized with a modified chemical structure in order to improve the solubility in industry recommended solvents.

2. Experimental

The resist samples were prepared by dissolving the individual components in ethyl lactate or PGMEA. The solutions were then combined in various weight ratios and concentrations to give a range of formulations.

The resist was spun onto a commercial underlayer, Brewer Scientific E2 STACK AL412-302. After spin-coating of the resist the samples received a post application bake (PAB) of 80 °C for 1 minute, when using a track for film deposition, or 60 °C for 3 minutes at PSI. EUV exposures were performed using the XIL-II interference lithography tool at the Paul Scherrer Institute, Switzerland [7], and using an ASML NXE3350 scanner. After exposure most samples did not receive a post exposure bake but were developed in n-butyl acetate for 60 seconds followed by 15 seconds of MIBC rinse unless stated. Some of the samples received a post exposure bake of up to 80 °C for 1 minute where noted in the results section. For the NXE3350 results, the patterning was observed using CD-SEM and the LWR and LER values are biased values unless otherwise stated, and where the all LER and LWR numbers are unbiased, 3 σ , they are measured using Fractilia software. At PSI, exposed samples were analyzed with a scanning electron microscope (SEM) in top-down view. Critical dimension (CD), LWR and LER were calculated from the SEM

images with SMILE software. The baseline for the optimization is the previously introduced xMT resist system, shown in Figure 3, from which the MTR1 series resist was developed. The molecular resin has been modified, to increase the glass transition temperature (T_g) (MTR2) and to modify the activation energy of the molecule (MTR4 and MTR8). A cross-linking molecule, which incorporates a non-metal high-Z element, was introduced in the system for increased optical density. Triphenylsulfonium tosylate, which acts as a photo-decomposable quencher in epoxy-based systems, was added. [8].

3. Results and discussion

3.1. High Z crosslinker (mark III)

The Mark I high-Z Crosslinker chemical structure previously presented [11] was once more modified to enable solubility in industry accepted solvents Ethyl (-L) lactate and PGMEA, and the lithographic performance at pitch 32 nm patterned on an NXE3350 containing this crosslinker is presented in Figures 4 and 5.

The film thickness is 22.5 nm and no PEB was used. A biased LWR of 4.2 nm for a line width of 15.1 nm was shown. Using Fractilia software, an unbiased LWR value of 3.82nm was calculated at best dose / best focus and the dose-to-size is

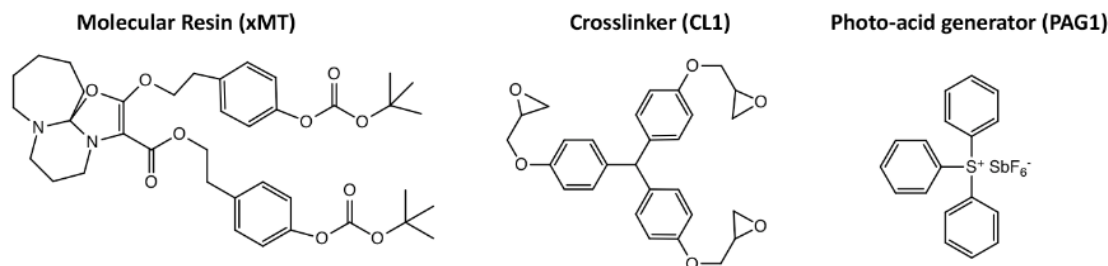


Fig. 3. Resist components in the baseline xMT system.

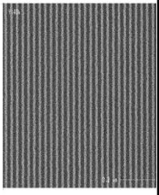
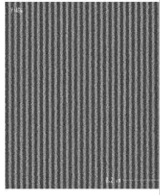
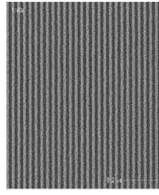
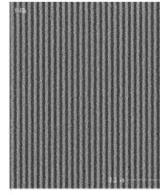
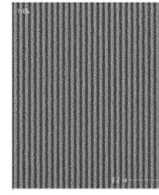
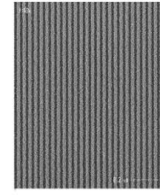
Dose (mJ/cm ²)	42	45	48	51	54	57
Rectangular Scan						
CD (nm)	12.41	13.28	14.15	15.07	15.58	16.68
LWR (nm)	4.70	4.65	4.60	4.22	4.48	4.18

Fig. 4. MTR4L3Y(2)-0 negative tone resist patterned at pitch 32 nm.

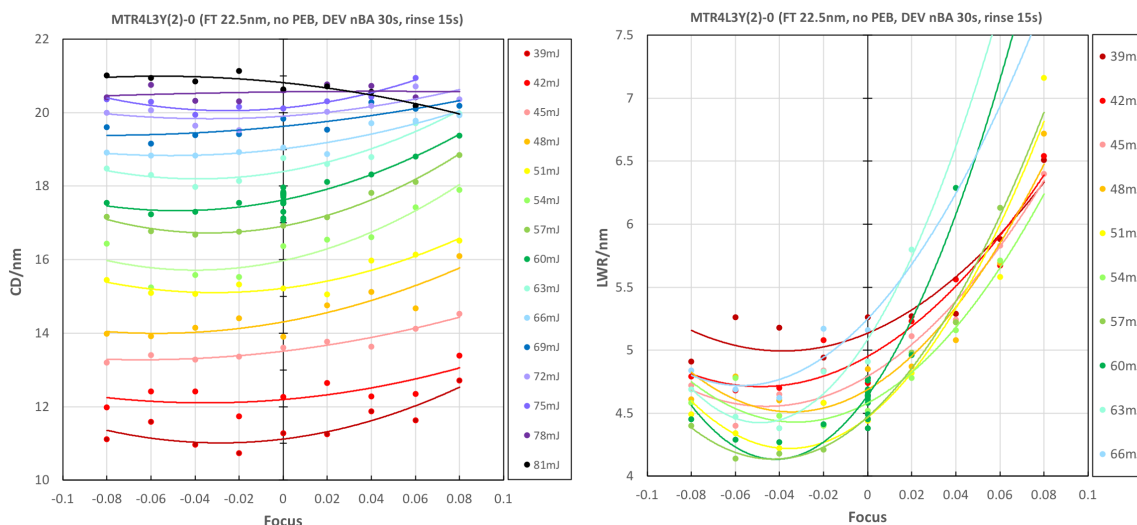


Fig. 5. For MTR4L3Y(2)-0: Left: Focus versus critical dimension; Right: Focus versus LWR.

54mJ/cm². There are some bridging defects still seen at higher doses, so further improvements to the formulation, including ways increase the purity of the formulation are being undertaken. Trackside process variations to evaluate their effects on bridging, include underlayer choice, and developer and rinse conditions are underway. One process variation which was explored was introducing a post exposure bake (PEB). A PEB of 60 °C resulted in a reduction in dose to 46mJ/cm² however the LWR increased by 0.2nm at pitch 32nm. A further increase in PEB temperature to 80 °C resulted in a further dose to size decrease to 41mJ/cm² and a further 0.3nm LWR increase. Overall, the lowest Z factor conditions occur with a PEB of 60°C and is 4.1 x 10⁻⁸ using biased LWR values.

3.2 Process variation – film thickness for MTR4L3Y(2)

The thickest film thickness tested using the NXE3350 was 22.5 nm. A film thickness of 20nm negatively affected LWR, so increasing the film thickness could be favourable at p32 using the NXE scanner. At PSI, 12 nm lines on a 28 nm pitch were patterned with an LWR of 2.07 nm using a film thickness of 25 nm. This used a 60 °C PEB and the analytics were carried out by SMILE software. Also patterned at PSI were 13 nm lines on a 26 nm pitch using an 18 nm film thickness. These results are shown in figure 6.

3.3 Comparing MTR molecules with different activation energies

MTR4 and MTR8 molecules were synthesised

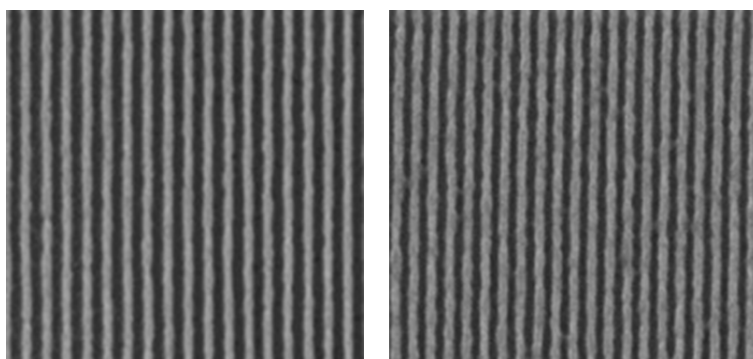


Fig. 6. Patterning of dense line spaces at PSI. Left: pitch 28 nm, dose: 37.2 mJ/cm², CD: 12.2 nm, LWR: 2.07nm, Film Thickness 25 nm. Right: pitch 26 nm, Dose: 37.2 mJ/cm², CD: 13.2 nm, LWR: 2.58 nm, Film Thickness 18 nm.



Fig. 7. Comparing MTR4 and MTR8 dose to size, LWR and Z factor.

to increase the activation energy of MTR system. In this case, MTR8 has a higher activation energy than MTR 4. In the MTR2 resist it is seen that a PEB is beneficial to mitigating pattern collapse, but detrimental to LWR. Having a higher activation energy should allow introduction of a PEB to increase crosslinking and reduce pattern collapse whilst avoiding an increase in LWR. The results shown in figure 7 show a decrease in dose and Z-factor using MTR8 at this formulation ratio compared to MTR4, when tested at PSI. The results also show a Z factor improvement when using a 60 °C PEB, and initial results indicate that higher activation energies do not show the significant rise in LWR with PEB that was previously observed in lower activation energy formulations.

4. Conclusion

It has been shown previously that Multi-Trigger chemistry enhances the chemical gradient without

quenchers. Previous formulations have shown little benefit from PEB. The high-Z MTR chemistry however can be driven using external factors such as PEB. New synthesis procedures have been developed to produce novel molecules capable of improving the Irresistible Materials Multi Trigger resist which had previously shown 16 nm patterning on an NXE3300 scanner. Improved absorption, reduced material stochastics and improved crosslinking are being addressed, and the materials' patterning capabilities have been shown at PSI, at the MET and on an NXE3350 scanner using EUV lithography.

In this study, a new high-Z crosslinker molecule, mark III, has been synthesized and introduced in the MTR resist to make the high opacity MTR compatible with ethyl lactate and PGMEA casting solvents. We report results obtained using the new MTR system containing the high-Z cross-linker mark III, with a variation of process conditions and

formulation variations. The lithographic performance at pitch 32 nm patterned on an NXE3350 containing this crosslinker is presented A biased LWR of 4.2 nm for a line width of 15.1 nm is shown. Introducing a PEB induces performance changes for the MTR4L3Y(2) resist. The sensitivity improves by over 20% with 80 °C PEB. However, the LWR does increase with PEB by 12%. Overall, the lowest Z factor (using biased LWR) occurs with a 60 °C PEB temperature. The Z factor is also significantly lower with FT 22.5 nm compared to 20 nm. The thickest film tested using the NXE3350 is 22.5 nm. However, at PSI, 12 nm lines on a 28 nm pitch were patterned with an LWR of 2.07 nm using a film thickness of 25nm.

We have also increased the activation energy of the MTR system. In this case, MTR8 has a higher activation energy than MTR4. Having a higher activation energy should allow introduction of PEB to increase crosslinking and reduce pattern collapse. We present results which show a decrease in dose and Z-factor using MTR8 at this formulation ratio compared to MTR4, when tested at PSI. The results also show a Z factor improvement when using a 60 °C PEB.

Acknowledgements

The authors would like to thank Ms Michaela Vockenhuber, Dimitrios Kazazis, Tim Allenet and Chia-Kai Yeh from PSI for their assistance with the EUV exposures. Part of this work was performed at Swiss Light Source (SLS), Paul Scherrer Institute, 5232 Villigen, Switzerland. The authors would like to thank Marie Krysak (Intel) and Warren Holcomb and Chanin King (Lawrence Berkeley National Laboratory) for their help with EUV exposures. The authors would like to thank Lidia van Lent-Protasova, Jara Santa Garcia (ASML) for their help with EUV exposures. The authors would like to thank the Engineering and Physical Sciences Research Council (EPSRC) for support of this project. The authors thank Irresistible Materials Ltd. and Nano-C for support and provision of resist materials. This project has received funding from the EU-H2020 research and innovation program under grant agreement No 654360 having benefitted from the access provided by Paul Scherrer Institute in Villigen, Switzerland within the framework of the NFFA-Europe Transnational Access Activity.

References

- [1] S. Nagahara, C. Que Dinh, K. Yoshida, G. Shiraishi, Y. Kondo, K. Yoshihara, K. Nafus, J. S. Petersen, D. De Simone, P. Foubert, G. Vandenberghe, H-J. Stock, and B. Meliorisz, *Proc. SPIE*, **11326** (2020) 113260A.
- [2] A. Shirotori, M. Hoshino, D. De Simone, G. Vandenberghe, and H. Matsumoto, *Proc. SPIE*, **11517** (2020) 115170D.
- [3] S. K. Sharma, R. Kumar, M. Chauhan, M. G. Moinuddin, J. Peter, S. Ghosh, C. P. Pradeep, and K. E. Gonsalves, *Proc. SPIE*, **11326** (2020) 1132604.
- [4] Y. Vesters, A. McClelland, C. Popescu, G. Dawson, J. Roth, W. Theis, D. de Simone, G. Vandenberghe, and A. P. G. Robinson, *Proc. SPIE* **10586** (2018).
- [5] C. Popescu, D. Kazazis, A. McClelland, G. Dawson, J. Roth, W. Theis, Y. Ekinici, and A. P. G. Robinson, *Proc. SPIE*, **10583** (2018) 10583.
- [6] G. O'Callaghan, C. Popescu, A. McClelland, D. Kazazis, J. Roth, W. Theis, Y. Ekinici, and A. Robinson, *Proc. SPIE* **10960** (2019)
- [7] W. Montgomery, A. McClelland, D. Ure, J. Roth, and A. Robinson, *Proc. SPIE*, **10143** (2017) 1014328.
- [8] C. Popescu, A. McClelland, D. Kazazis, G. Dawson, R. Roth, Y. Ekinici, W. Theis, and A. P. G. Robinson, *Proc. SPIE*, **10775** (2018) 10775-02.
- [9] Y. Ekinici, M. Vockenhuber, B. Terhalle, M. Hojeij, L. Wang, and T. R. Younkin, *Proc. SPIE*, **8322** (2012) 83220W.
- [10] R. A. Lawson, A. Frommhold, D. X. Yang, and A. P. G. Robinson, "Negative-tone organic molecular resists," in Robinson A.P.G., Lawson R.A. editors. *Materials and Processes for Next Generation Lithography*. Oxford, Elsevier (2016).
- [11] C. Popescu, G. O'Callaghan, A. McClelland, J. Roth, T. Lada, and A. P. G. Robinson, *Proc. SPIE*, **11326** (2020) 11326-11.

EUV Photochemistry of α -Substituted Antimony Carboxylate Complexes

Michael Murphy, Maximilian Weires, Nitinkumar S. Upadhyay, Philip Schuler, Shaheen Hasan, Greg Denbeaux, and Robert L. Brainard*

College of Nanoscale Science and Engineering, SUNY Polytechnic Institute, Albany, NY 12203

*rbrainard@sunypoly.edu

We present a new class of EUV antimony carboxylate photoresists with enhanced reactivity and contrast, through the substitution of heteroatoms into the carboxylate. The lithographic performance of $(C_6H_5)_3Sb(O_2CCH_2X)_2$ photoresists in which X = methoxy, bromine or iodine is presented. The addition of iodine to the photoresist greatly improves dissolution contrast. Utilizing in-situ mass spectrometry, we show how the identity and degree of volatile photoproducts created during EUV exposure change with the composition of the heteroatom.

Keywords: EUV, Photoresist, MORE, Antimony, Photomechanism, α -Bromoacetate

1. Introduction

As EUV begins its incorporation into high volume manufacturing, research is still required to create better performing photoresists [1-5]. Many novel chemical technologies are being studied in an effort to create EUV photoresists capable of high resolution, high sensitivity and low line-edge roughness (LER) [1-8]. Since 2011, our group has been developing Molecular Organometallic Resists for EUV (MORE) [5-9]. One of the primary objectives of this program has been to synthesize and study compounds prepared from elements in the periodic table that strongly absorb EUV light (Figure 1A). This work has led to the development of several EUV resist platforms containing platinum, palladium, cobalt, bismuth, antimony and tin [9-13].

One of our most successful MORE platforms is composed of antimony complexes of the type, $R_3Sb(O_2CR')_2$ (Figure 1B). We have prepared and evaluated dozens of molecules within this platform in which R and R' are aromatic, aliphatic, and in many instances contain olefins [13-15]. Recently, we have focused on the mechanisms of EUV photolysis of non-olefinic antimony-carboxylates by comparing variations in the structure of these complexes with (1) the composition of the nonvolatile photoproducts using TOF-SIMS [8-9] and (2) the composition of the volatile photoproducts using mass spectroscopy [12-15].

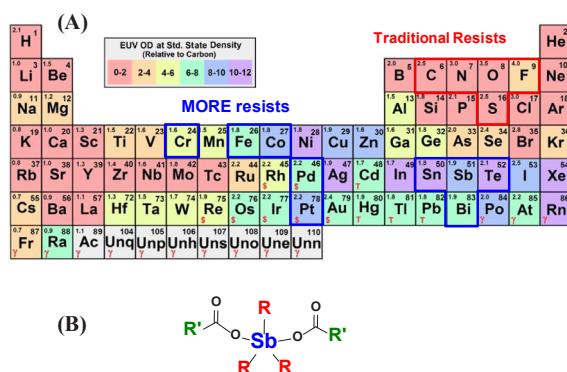


Fig. 1. (A) The periodic table illustrating the relative EUV optical density of the elements. (B) General schematic of pentacoordinate antimony carboxylate photoresists.

Using ToF-SIMS, we determined that the non-volatile EUV photolysis products were oxygen-rich high molecular weight antimony polymers [8-9]. Using mass spectroscopy, we investigated a number of interesting mechanistic pathways leading to the formation of CO_2 , benzene and phenol (Figure 2). In particular, using isotopic labelling techniques, we have shown that the hydrogens that originate in the α -positions of acetate ligands become the O-H bonds in phenols but do not become C-H bonds in benzene. To further explore the reactivity of the α -position in acetate ligands, we have explored the

effect of substituting one of the hydrogens with a heteroatom [16].

Here, we present a new group of antimony carboxylate resists containing α -substituted acetate ligands with improved reactivity. We evaluate the EUV photochemistry of derivatives of triphenyl-antimony(diacetate) (**JP-18**) in which the α -position has been substituted with iodine (**PS-15**), bromine (**PS-13**), cyanide (**PS-12**), and methoxy (**PS-14**) (Figure 3). Additionally, we present mass spectroscopic study of the compounds outgassed by the bromo-derivative.

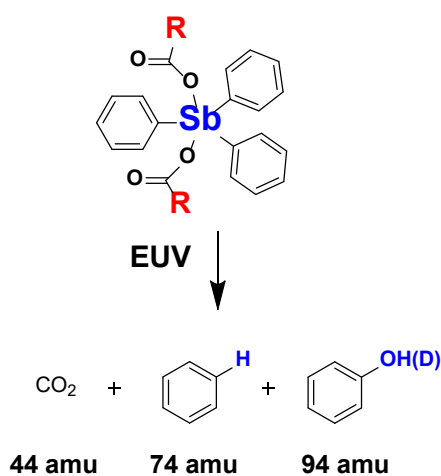


Fig. 2. Exposure of **JP-18** ($R = \text{CH}_3$) to EUV light yields CO_2 , benzene and phenol. Exposure of d_6 -**JP-18** ($R = \text{CD}_3$) to EUV light yields CO_2 , and greater than 95% isotopically pure d_0 -benzene and d_1 -phenol [16].

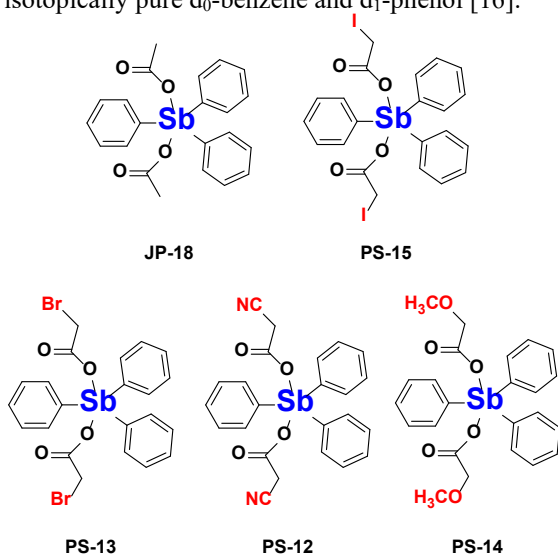


Fig. 3. α -Substituted compounds studied in this paper.

2. Experimental

2.1. General

1,2-dichloroethane, hexanes, toluene, propylene glycol monomethyl ether acetate, dichloromethane, 2-butanone and hexanoic acid were purchased from

Sigma Aldrich and used without further purification. 0.26 N Tetramethyl-ammonium hydroxide, water and 2-propanol were provided by the facility where the exposures were performed.

2.2. Photoresist Formulation & Coating

All photoresist films were formulated at 1.5-2 wt.% solids in 1,2-dichloroethane. Once solubilized the formulations were filtered through 0.45 μm PTFE filters and spincoated onto 4-inch silicon wafers, precoated with an adhesion-promoting film (crosslinked hydroxyethyl methacrylate/methyl methacrylate copolymers). The spin conditions were 2000 rpm for 45 seconds. No pre- or post-exposure bakes were performed unless specified.

2.3. Instruments

Film thicknesses were measured using a J. A. Woollam M-2000 fixed angle ellipsometer equipped with Complete Ease software. The thicknesses were fitted using a Cauchy model for the photoresist and underlayer. The dense line patterning exposures were characterized by a LEO 1550 SEM and a Zeiss Supra 55VP at 1–2 keV accelerating voltage using an in-lens detector.

2.4. PSI XIL-II EUV Interference Lithography Beamline

EUV exposures performed at the Paul Scherrer Institut XIL-II beamline. 13.5 nm light was generated by an undulator synchrotron source and illuminated the photoresist samples as a spatially-coherent beam of EUV light. Contrast curve samples were composed of twenty-five exposures through a 1.7 mm x 1.7 mm open frame in a serpentine pattern with an index dose for reference. High resolution periodic features were patterned on photoresists by interference lithography exposures using suspended silicon nitride membranes patterned by electron beam lithography. Periodic images were created on the photoresist film by interference of two or more diffracted coherent beams [17]. The aerial image produced with first-order diffracted beams is half the period of the original mask grating period. Our interference exposures used a photomask capable of printing 50-, 40-, 30- and 22-nm half-pitch dense lines. Review of recent advances in inorganic photoresists.

3. Results and Discussion

3.1. Lithographic Analysis of α -Halo Carboxylate Resists

Our baseline compound,

triphenylantimony(diacetate) (**JP-18**), produces an acceptable contrast curve when developed in water, but shows no contrast when developed in hexanes. However, triphenylantimonybis(iodoacetate) (**PS-15**) provides dual enhancement in the form of halogen reactivity and EUV absorptivity from two iodine atoms per molecule. When developed in water, the EUV contrast curve of **PS-15** is very similar to that of the unsubstituted triphenylantimony diacetate (**JP-18**). However, when developed in hexanes, **PS-15** exhibits excellent contrast whereas **JP-18** shows no contrast at all (Figure 4). Thus, the substitution of a single iodine atom in the α -position of the carboxylate dramatically changed the photoresists photo-response. This result is surprising as no other $(C_6H_5)_3Sb(O_2CR)_2$ resists have high contrast in both organic and aqueous developers unless they contain olefins.

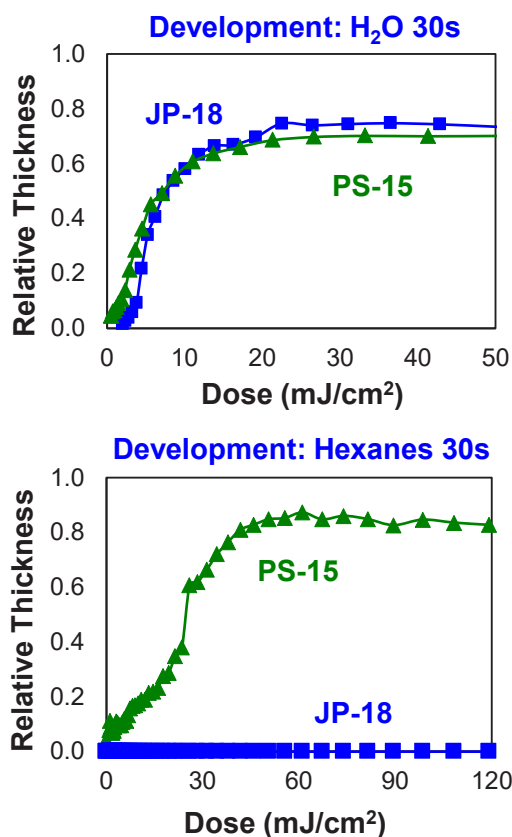


Fig. 4. α Contrast curves of triphenylantimonybis(iodoacetate) (**PS-15**) developed in hexanes (green) or H₂O (blue) compared to **JP-18**. **PS-15** is developable in both hexanes and H₂O with good contrast.

After the success of **PS-15**, we prepared derivatives in which bromine (**PS-13**), cyano (**PS-12**) and methoxy (**PS-14**) were substituted in the α -position of the acetic acid ligands. Each compound was exposed to EUV light and developed

in water and hexanes. Using aqueous development, compounds containing bromo-, iodo- and cyanoacetate ligands produced very similar contrast curves to that of **JP-18** with its unsubstituted acetate (Figure 5A). However, the compound prepared with methoxyacetate (**PS-14**), had poorer contrast and did not reach full thickness at Emax. Emax is defined as the energy to maximum thickness in a contrast curve.

Carboxylate ligands with R' composed solely of alkyl chains or aromatic rings without olefin groups have no dissolution contrast when developed in organic solvents. However, we find that the complexes prepared with acetate ligands with methoxy, bromo, or iodo in the α -position show remarkably good contrast when developed in hexanes (Figure 5B).

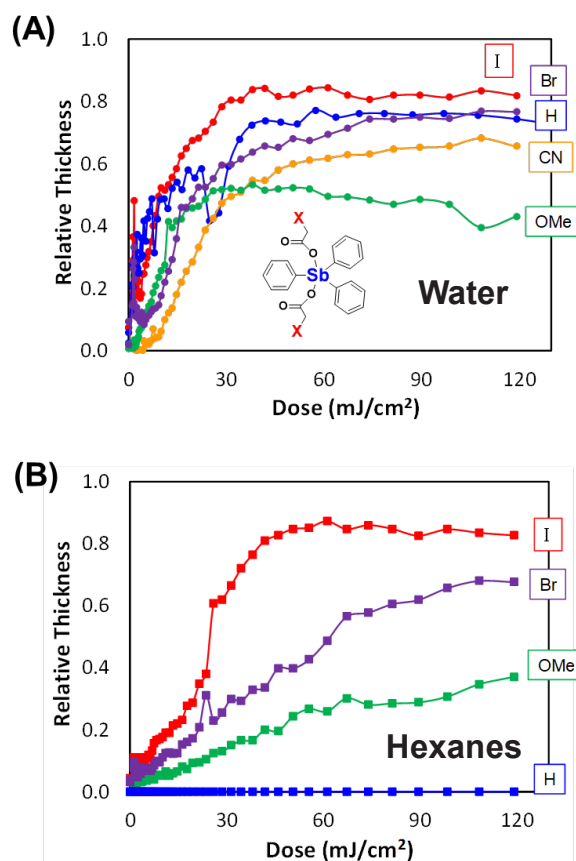


Fig. 5. (A) Contrast curves of α -substituted $(C_6H_5)_3Sb(O_2CCH_2X)_2$ resists developed for thirty seconds in H₂O. Some heteroatom substitutions improve performance (e.g. iodoacetate, bromoacetate) while others degrade performance (e.g. cyanoacetate). (B) Contrast curves of α -substituted $(C_6H_5)_3Sb(O_2CCH_2X)_2$ resists developed for twenty seconds in hexanes. Heteroatom substitutions improve dissolution contrast in hexanes.

3.2. EUV Outgassing of α -Substituted Antimony

Complexes

Prior EUV outgassing studies examined the production of dominant volatile species within a series of alkyl and aryl triphenylantimonydicarboxylate resists. The generation of CO₂, benzene and phenol were found to correlate with antimony-carboxylate bond strength [16]. In the present study, we re-examine the in-situ mass spectra of several triphenyl-antimonycarboxylate resists to investigate carboxylate decomposition pathways.

Our research has shown that EUV photolysis of antimony carboxylates may occur by pathways involving the cleavage of three different bonds (Figure 6). Bond 1: cleavage of the antimony-oxygen bond leading to the formation CO₂ and a R' radical. Bond 2: cleavage of the oxygen-carbonyl bond yielding an acylium ion and an oxygen atom bound to antimony. Bond 3: cleavage of the bond α to the carbonyl yielding an unstable intermediate that can form a ketene through cleavage of the oxygen-carbonyl bond. Deoxygenation and α-cleavage reaction pathways can lead to crosslinked antimony-oxide networks, as determined by ToF-SIMS [16].

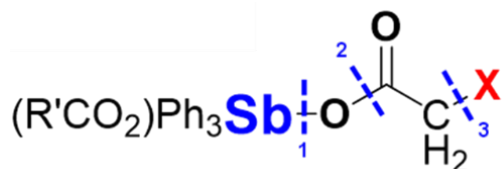


Fig. 6. Photolytic decomposition of organometallic carboxylates may undergo three potential reaction pathways: (1) cleavage of the antimony-oxygen bond, (2) cleavage of the oxygen-carbonyl bond or (3) cleavage of bond α to the carbonyl.

Previous studies of the d₀ and d₂ derivatives of triphenylantimonybis(isobutyrate) (*MM-49* and d₂-*MM-49*, respectively) provide a good background for understanding these three bond-cleavage reactions [16]. This compound yields dimethylketene (1) and acylium ion (2) upon exposure to EUV (Figure 8). The mass spectrum shows 2-methyl-isopropanoyl ion at 71 amu with further structural corroboration by the tracking of the d₁-isopropanoyl ion at 72 amu from exposure of d₂-*MM-49*. Furthermore, dimethyl ketene is observed in both *MM-49* and d₂-*MM-49* at 70 amu which identifies the site of hydrogen abstraction as alpha to the carbonyl.

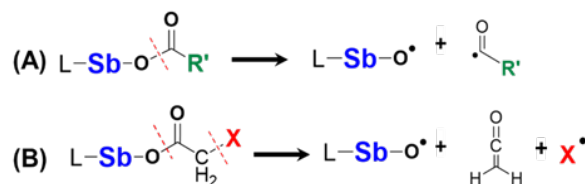


Fig. 7. Formation of (A) acylium ions and (B) ketene both involve cleavage of the oxygen-carbonyl bond resulting in a reactive oxygen site on the antimony core a potential initiation site for the creation of crosslinked antimony oxide networks.

Mass spectral analysis of the volatile EUV photoproducts *PS-13* showed a large quantities of bromo-ketene and bromo-acylium ion (Figure 9A). These volatile products are consistent with the volatile products produced during the exposure of compound *MM-49*, and suggest a mechanistic pathway involving the cleavage of bond 2.

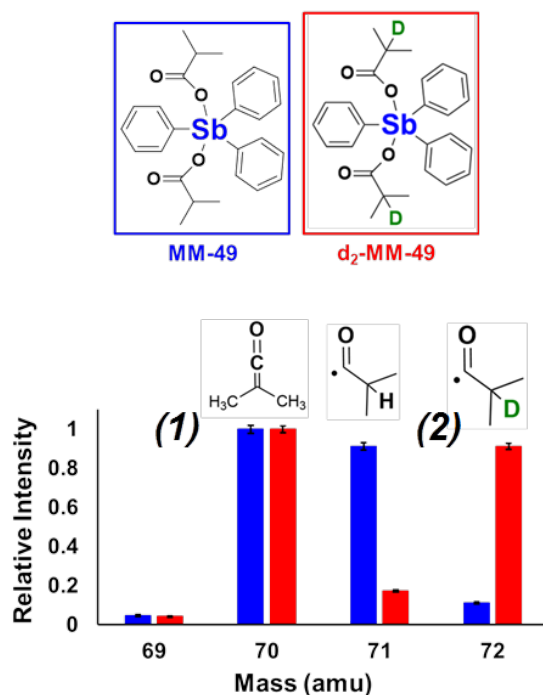


Fig. 8. Dimethyl ketene and 2-methyl-isopropanoyl ions are generated during EUV exposure of *MM-49*. Selective deuterium labelling of the alpha-hydrogen site of the isobutyrate ligand (d₂-*MM-49*) substantiates the compositions of the photoproducts and cleavage of the alpha-hydrogen to form dimethyl ketene (1) (70 amu).

Mass spectroscopy of the volatile products also showed the creation of bromobenzene (Figure 9B), suggesting the breaking of bond 3. This result is quite surprising because previous work showed that cleavage of bond 3 when X = H to create benzene occurred < 3% of the time during the photolysis of *JP-18* and occurred < 30% of the time during the photolysis of *MM-49*. Therefore, it appears that α -cleavage of a C-Br bond is much more likely than the α -cleavage of a C-H bond.

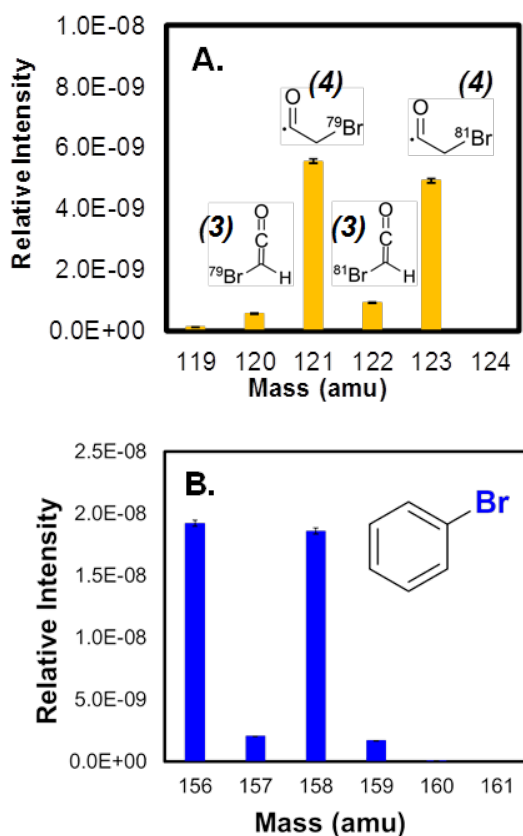


Fig. 9. Mass spectra of volatile products produced during the EUV exposure of triphenylantimonybis(bromoacetate). (A) One of the products are upon EUV exposure illustrating the formation of bromo-ketene (3) and bromo-ketenyl ions (4) identified through the isotopic signature of ^{79}Br and ^{81}Br . (B) Another volatile product is bromobenzene.

4. Conclusion

We have shown that the addition of heteroatoms in the α -position of acetate ligands can generate antimony EUV photoresists with high sensitivity and high contrast. In particular, triphenylantimonybis(iodoacetate) (*PS-15*) shows excellent contrast when developed with either water or hexanes.

Evaluation of new antimony photoresists

containing heteroatom-functionalized carboxylates has revealed a large potential for deoxygenation and α -cleavage reaction pathways that occur during EUV. Specifically, the compound substituted with bromine (*PS-13*) outgasses significant amounts of bromobenzene, bromo-ketene (3) and bromo-ketenyl ion (4). We think that a halogen in the α -position of the carboxylate ligand competes with hydrogen for abstraction and generation of volatile photoproducts. Additionally, this competition reaction favors deoxygenation vs. decarboxylation and would therefore increase the concentration of reactive antimony–oxygen bonds and the potential for an insoluble oxide network. This conclusion is in agreement with the lithographic performance demonstrated for α -halo substituted carboxylate photoresists.

References

1. B. Turkot, S. L. Carson, A. Lio, T. Liang, M. Phillips, B. McCool, E. Stenehjem, T. Crimmins, G. Zhang, and S. Sivakumar, *Proc. SPIE*, **9776**, (2016) 977602.
2. T. Manouras, and P. Argitis, *Nanomaterials*, **10** (2020) 1593.
3. A. Mallik, W. Vansumere, J. Ryckaert, A. Mercha, N. Horiguchi, S. Demuyne, J. Bömmels, T. Zsolt, G. Vandenberghe, K. Ronse, A. Thean, D. Verkest, H. Lebon, and A. Steegen, *Proc. SPIE*, **8679** (2013) 86792Y.
4. H. Nakagawa, T. Naruoka, and T. Nagai, *J. Photopolym. Sci. Technol.*, **27** (2014) 739.
5. S. Tagawa, S. Enomot, and A. Oshima, *J. Photopolym. Sci. Technol.*, **26** (2013) 825.
6. P. P. Naulleau, C. N. Anderson, L. M. Baclea-an, P. Denham, S. George, K. A. Goldberg, G. Jones, B. McClinton, R. Miyakawa, S. Rekawa, and N. Smith, *Proc. SPIE*, **7972** (2011) 797202.
7. C. D. Higgins, C. R. Szmanda, A. Antohe, G. Denbeaux, J. Georger, R. L. Brainard, *Jpn. J. Appl. Phys.*, **50** (2011), 036504.
8. J. Stowers and D. A. Keszler, *Microelectron. Eng.*, **86** (2009) 730.
9. M. Krysak, M. Trikeriotis, E. Schwartz, N. Lafferty, P. Xie, B. Smith, P. Zimmerman, W. Montgomery, E. Giannelis, and C. K. Ober, *Proc. SPIE*, **7972** (2011) 79721C.
10. M. Sortland, J. Hotalen, R. Del Re, J. Passarelli, M. Murphy, T. S. Kulmala, Y. Ekinici, M. Neisser, D. A. Freedman, and R. L. Brainard, *J. Micro. Nanolithogr. MEMS MOEMS*, **14** (2015) 043511.

11. M. Wilklow-Marnell, D. Moglia, B. Steimle, B. Cardineau, H. Al-Mashat, P. Nastasi, K. Heard, A. Aslam, R. Kaminski, M. Murphy, R. Del Re, M. Sortland, M. Vockenhuber, Y. Ekinici, R. L. Brainard, D. A. Freedman, *J. Micro/Nanolith. MEMS MOEMS*, **17** (4) (2018) 043507.
12. J. Passarelli, M. Sortland, R. Del Re, B. Cardineau, C. Sarma, D. A. Freedman, and R. L. Brainard, *J. Photopolym. Sci. and Technol.*, **27** (2014) 655.
13. J. Passarelli, M. Murphy, R. Del Re, M. Sortland, J. Hotalen, L. Dousharm, R. Fallica, Y. Ekinici, M. Neisser, D. A. Freedman, and R. L. Brainard, *J. Micro. Nanolithogr. MEMS MOEMS*, **14** (2015) 043503.
14. R. Del Re, J. Passarelli, M. Sortland, B. Cardineau, Y. Ekinici, E. Buitrago, M. Neisser, D. A. Freedman, and R. L. Brainard, *J. Micro. Nanolithogr. MEMS MOEMS*, **14** (2015) 043506.
15. M. Murphy, A. Narasimhan, S. Grzeskowiak, J. Sitterly, P. Schuler, J. Richards, G. Denbeaux and R. L. Brainard, *J. Photopolym. Sci. Technol.*, **30** (2017) 121.
16. M. Murphy, J. Sitterly, S. Grzeskowiak, G. Denbeaux and R. L. Brainard, *J. Photopolym. Sci. Technol.*, **31** (2018) 233.
17. E. Buitrago, T. S. Kulmala, R. Fallica, Y. Ekinici, *Front. of Nanosci.*, **11** (2016) 135.

Non-chemically Amplified Negative Molecular Resist Materials using Polarity Change by EUV Exposure

Kohei Fujisawa¹, Hiroyuki Maekawa¹, Hiroto Kudo^{1*},
Kazumasa Okamoto², and Takahiro Kozawa²

¹ Department of Chemistry and Materials Engineering, Faculty of Chemistry, Materials and Bioengineering, Kansai University, 3-3-35, Yamate-cho, Suita-shi, Osaka, 564-8680, Japan

² Institute of Scientific and Industrial Research, Osaka University, 8-1 Mihogaoka, Ibaraki, Osaka 567-0047, Japan

*kudoh@kansai-u.ac.jp

We examined the synthesis, physical properties, and resist property of the molecular non-chemically amplified resist materials. By the condensation reaction of tri(4-hydroxyphenyl)methane (HPM) and various bisphenols (BisA, BisAF, HPE, and TDP) with 4-bromoethoxyphenyl methyl sulfide (BEPMS), the compounds (HPM-BEPMS, BisA-BEPMS, BisAF-BEPMS, HPE-BEPMS, and TDP-BEPMS) containing sulfide moieties were synthesized. These were reacted with silver trifluoromethanesulfonate and iodomethane, yielding corresponding compounds HPM-BEPMS_{ion}, BisA-BEPMS_{ion}, BisAF-BEPMS_{ion}, HPE-BEPMS_{ion}, and TDP-BEPMS_{ion}, respectively. They have good physical properties (solubility, film-forming ability, and thermal stability) and high nega-type resist sensitivity in an extreme ultraviolet (EUV) exposure tool, indicating these were good candidate to offer higher resolution resist pattern.

Keywords: Molecular resist, n-CAR, Extreme ultraviolet, Negative-type resist

1. Introduction

Development of large-scale integration using EUV lithography system has been examined and just reached the early practical stage. However, a suitable resist material for EUV has been under consideration to offer higher resolution (R), lower roughness of resist pattern (L), and higher sensitivity under exposure tool (S). Then, there is still no resist material satisfying these three resist properties at the same time, i.e., the relationship of R, L, and S is well known as a trade-off issue [1]. At the present time, the chemically amplified resist (CAR) system has been useful method to form high-resolution resist patterns, and there are many reports concerning EUV resist materials [2]. Among them, the molecular resist materials have also been examined as higher resolution resist material and expected to improve the trade-off issue as mentioned above, due to that their sizes are smaller compared to those of polymers and they have also no molecular weight distribution. For example,

Ueda et al. synthesized calix[4]resorcinarene with pendant *t*-butyloxycarbonyl group as a molecular resist and it's a thin film could offer a resist pattern with 1.5 μm L/S using UV exposure tool [3]. Our research group has also reported the development of molecular resist materials based on ladder cyclic oligomer noria ("noria" = water wheel in Latin) [4 - 12], tannic acid derivative [13], and tellurium-containing materials [14, 15]. These molecular resists have been considered to achieve higher sensitivity, but their roughness of resist pattern could not improve. Very recently, the improving roughness of resist pattern would be the most important issue in the development of high-resolution resist material. Furthermore, the resolution of next generation EUV resist pattern has been expected to offer under about 15nm, which might not be applicable in CAR system, presumably because of that EUV exposure might cause some reactions to reach the unexposed area. Therefore, non-chemically amplified resist (n-CAR) system

has been attracting for next-generation EUV resist material [16 - 22]. Thakur et al. synthesized molecular n-CAR material having a fluorene skeleton in the aromatic core and introducing a sulfonium triflate group, and evaluated the resist performance using i-line, DUV, and electron beam (EB) as the exposure source. As a result, it showed 20 nm lines of resist patterns and LER was 5.69 ± 0.2 nm [23].

In this time, we synthesized the molecular resist materials containing sulfonium triflate skeletons which were expected to change polarity exposed by EUV light. The physical properties (solubility, film-forming, and thermal stability) and resist property (sensitivity) of synthesized molecular resist materials were examined to offer higher resolution in n-CAR system under EUV exposure tool.

2. Experimental

2.1. Materials

N,N-Dimethylformamide (DMF) and acetonitrile were dried with calcium hydride (CaH_2) and purified by distillation under reduced pressure. Chloroform (CHCl_3), hexane, diethyl ether, hydrochloric acid (HCl), potassium carbonate (K_2CO_3), cesium carbonate (Cs_2CO_3), tetrabutylammonium bromide (TBAB), 4-(methylthio)phenol, 1,2-dibromoethane, tri(4-hydroxyphenyl)methane (HPM), 2,2-bis(4-hydroxyphenyl)propane (BisA), 2,2-bis(4-hydroxyphenyl)hexafluoropropane (BisAF), di(4-hydroxyphenyl) ether (HPE), iodomethane (stabilized with Copper chip), silver trifluoromethanesulfonate, and propylene glycol monomethyl ether (PGME) were used as commercially available.

2.2. Measurements

Infrared (IR) spectra were taken with a JASCO FT/IR4200. The $^1\text{H-NMR}$ spectra were recorded on JEOL ECS-400K (400 MHz for $^1\text{H-NMR}$) instruments in $\text{DMSO-}d_6$ and CDCl_3 with Me_4Si (TMS) as an internal standard. Thermal analysis was performed on a Shimadzu thermogravimetric analyzer (TGA) TGA-50/50H at a heating rate of 10 $^\circ\text{C}/\text{min}$ under nitrogen.

2.3 Condensation reaction of 4-(methylthio)phenol and 1,2-dibromoethane [synthesis of 4-bromoethoxyphenyl methyl sulfide (BEPMS)]

Typical procedure: A solution of 4-

(methylthio)phenol (22.0 mmol, 3.12 g), K_2CO_3 (85.0 mmol, 11.71 g), in acetonitrile (75 mL) was stirred at 60 $^\circ\text{C}$ for 2 h. Then, 1,2-dibromoethane (69.0 mmol, 12.9 g) was added, and the reaction mixture was stirred at 60 $^\circ\text{C}$ for 24 h. After completion of the reaction, K_2CO_3 was separated from the reaction mixture by filtration on a membrane filter (Millipore LAWPO 4700 pore size 0.45 μm) and the resultant filtrate was evaporated under a rotary evaporator. The pure crystalline white solid of BEPMS was obtained after the purification of reaction mixture through silica gel column chromatography (Eluent: chloroform). Yield = 1.43 g (28 %). IR (KBr, cm^{-1}): 2916 (ν - CH_2 - of methylene), 1492 (ν C=C of aromatic), 1249 (ν -S- CH_3 of sulfide). $^1\text{H-NMR}$ (400 MHz, CDCl_3 , TMS) δ (ppm): 2.38 (s, 3H, - CH_3), 3.74 (t, 2H, $J = 5.6$ Hz, - CH_2 -), 4.24 (t, 2H, $J = 5.6$ Hz, - CH_2 -), 6.89 - 7.19 (m, 4H, aromatic H).

2.4 Condensation reaction of BEPMS and HPM (synthesis of HPM-BEPMS)

Typical procedure: A solution of HPM (0.5 mmol, 0.146 g), tetrabutylammonium bromide (TBAB) (0.2 mmol, 0.064 g), and Cs_2CO_3 (2.0 mmol, 0.651 g), in DMF (7.0 mL) was stirred at 80 $^\circ\text{C}$ for 2 h. Then, BEPMS (2.0 mmol, 0.493 g) was added, and the reaction mixture was stirred at 80 $^\circ\text{C}$ for 24 h. The resulting mixture was poured into a large amount of 0.1 N hydrogen chloride solution to precipitate a solid, which was collected by filtration on a membrane filter (Millipore LAWPO 4700 pore size 0.45 μm) and washed with water. The obtained product was dried *in vacuo* at 60 $^\circ\text{C}$ for 24 h to afford a cream powder. Yield = 0.34 g (85 %). IR (KBr, cm^{-1}): 2916 (ν - CH_2 - of methylene), 1492 (ν C=C of aromatic), 1239 (ν -S- CH_3 of sulfide). $^1\text{H-NMR}$ (400 MHz, CDCl_3 , TMS) δ (ppm): 2.43 (s, 3H, - CH_3), 4.28 (s, 12H, - CH_2 -), 5.40 (s, 1H, $>\text{CH}$ -), 6.84 - 7.27 (m, 24H, aromatic H).

2.5 Condensation reaction of BEPMS and BisA (synthesis of BisA-BEPMS)

Reaction of BEPMS and BisA was carried out in the same way for the reaction of BEPMS and HPM. Yield = 0.85 g (80 %). IR (KBr, cm^{-1}): 2924 (ν - CH_2 - of methylene), 1494 (ν C=C of aromatic), 1240 (ν -S- CH_3 of sulfide). $^1\text{H-NMR}$ (400 MHz, CDCl_3 , TMS) δ (ppm): 1.62 (s, 6H, - CH_3), 2.43 (s, 6H - CH_3), 4.27 (s, 8H, - CH_2 -), 6.71 - 7.26 (m, 16H, aromatic H).

2.6 Condensation reaction of BEPMS and BisAF

(synthesis of BisAF-BEPMS)

Reaction of BEPMS and BisAF was carried out in the same way for the reaction of BEPMS and HPM. Yield = 0.60 g (47 %). IR (KBr, cm^{-1}): 2924 (ν -CH₂- of methylene), 1494 (ν C=C of aromatic), 1240 (ν -S-CH₃ of sulfide). ¹H-NMR (400 MHz, CDCl₃, TMS) δ (ppm): 2.44 (s, 6H, -CH₃), 4.31 (s, 8H, -CH₂-), 6.88 - 7.34 (m, 16H, aromatic H).

2.7 Condensation reaction of BEPMS and HPE (synthesis of HPE-BEPMS)

Reaction of BEPMS and HPE was carried out in the same way for the reaction of BEPMS and HPM. Yield = 0.70 g (69 %). IR (KBr, cm^{-1}): 2924 (ν -CH₂- of methylene), 1494 (ν C=C of aromatic), 1240 (ν -S-CH₃ of sulfide). ¹H-NMR (400 MHz, CDCl₃, TMS) δ (ppm): 2.45 (s, 6H, -CH₃), 4.29 (s, 8H, -CH₂-), 6.86 - 7.28 (m, 16H, aromatic H).

2.8 Condensation reaction of BEPMS and TDP (synthesis of TDP-BEPMS)

Reaction of TDP and BEPMS was carried out in the same way for the reaction of BEPMS and HPM. Yield = 1.30 g (84 %). IR (KBr, cm^{-1}): 2921 (ν -CH₂- of methylene), 1490 (ν C=C of aromatic), 1238 (ν -S-CH₃ of sulfide). ¹H-NMR (400 MHz, CDCl₃, TMS) δ (ppm): 2.38 (s, 6H, -CH₃), 4.25 (s, 8H, -CH₂-), 6.91 - 7.28 (m, 16H, aromatic H).

2.9 Synthesis of HPM-BEPMS_{ion}

Typical procedure: A solution of HPM-BEPMS (0.10 mmol, 0.079 g) and silver trifluoromethane sulfonate (0.40 mmol, 0.10 g) in acetonitrile (5.0 mL) was stirred at room temperature. Then methyl iodide (0.4 mmol, 0.025 ml) added drop wise to the above reaction mixture over a period of 10min for 24 h in dark conditions. The resulting mixture was separated with membrane filter (Millipore LAWPO 4700 pore size 0.45 μm) and the obtained filtrate was evaporated under a rotary evaporator to obtain the solid HPM-BEPMS_{ion}. Yield = 0.103 g (81 %). IR (KBr, cm^{-1}): 2979 (ν C-H of methyl), 1725 (ν C=O of ester), 1205 (ν C-O of ether). ¹H-NMR (400 MHz, DMSO-*d*₆, TMS) δ (ppm): 3.17 (s, 9H, -CH₃), 4.33 (d, 12H, *J* = 8Hz, -CH₂-), 5.42 (s, >CH-), 6.86 - 7.98 (m, 24H, aromatic H).

2.10 Synthesis of BisA-BEPMS_{ion}

Reaction of BisA-BEPM was carried out in the same way for the reaction of HPM-BEPMS_{ion}. Yield = 0.75 g (95 %). IR (KBr, cm^{-1}): 2935 (ν -

CH₂- of methylene), 1499 (ν C=C of aromatic), 1255 (ν -S-CH₃ of sulfide). ¹H-NMR (400 MHz, DMSO-*d*₆, TMS) δ (ppm): 1.52 (s, 6H, -CH₃), 3.14 (s, 6H, -CH₃), 4.33 (d, 8H, *J* = 8Hz, -CH₂-), 6.60 - 7.96 (m, 16H, aromatic H).

2.11 Synthesis of BisAF-BEPMS_{ion}

Reaction of BisA-BEPM was carried out in the same way for the reaction of HPM-BEPMS_{ion}. Yield = 0.40 g (62 %). IR (KBr, cm^{-1}): 2935 (ν -CH₂- of methylene), 1499 (ν C=C of aromatic), 1255 (ν -S-CH₃ of sulfide). ¹H-NMR (400 MHz, DMSO-*d*₆, TMS) δ (ppm): 3.18 (s, 6H, -CH₃), 4.39 (d, 8H, *J* = 8Hz, -CH₂-), 7.04 - 7.97 (m, 16H, aromatic H).

2.12 Synthesis of HPE-BEPMS_{ion}

Reaction of HPE-BEPMS was carried out in the same way for the reaction of HPM-BEPMS_{ion}. Yield = 0.42 g (50 %). IR (KBr, cm^{-1}): 2924 (ν -CH₂- of methylene), 1499 (ν C=C of aromatic), 1255 (ν -S-CH₃ of sulfide). ¹H-NMR (400 MHz, DMSO-*d*₆, TMS) δ (ppm): 3.18 (s, 6H, -CH₃), 4.34 (d, 8H, *J* = 8Hz, -CH₂-), 6.71 - 7.98 (m, 16H, aromatic H).

2.13 Synthesis of TDP-BEPMS_{ion}

Reaction of TDP-BEPMS was carried out in the same way for the reaction of HPM-BEPMS_{ion}. Yield = 0.80 g (82 %). IR (KBr, cm^{-1}): 2939 (ν -CH₂- of methylene), 1495 (ν C=C of aromatic), 1253 (ν -S-CH₃ of sulfide). ¹H-NMR (400 MHz, DMSO-*d*₆, TMS) δ (ppm): 3.18 (s, 6H, -CH₃), 4.30 - 4.42 (m, 8H, -CH₂-), 6.92 - 7.97 (m, 16H, aromatic H).

2.14. Resist sensitivity

Solutions of synthesized molecular resist materials were filtered through a 0.20 μm PTFE syringe filter prior to spin-coating on 6-inch silicon wafers. Spin-coating was performed at 3300 rpm for 30 sec. to form thin films on the silicon wafers. Then these spin-coated films were prebaked at 90 °C for 60 sec. The film thickness was adjusted to 50 nm. The resulting films were exposed to EUV lithography (energetic EQ-10M). The area of exposure was approximately 1 \times 1 cm². After the exposure, the silicon wafer was developed by dipping in deionized water at room temperature for 30 sec. then rinsed in deionized water before drying. The resist film thickness was measured with an ellipsometry to obtain sensitivity curves.

3. Results and discussion

3.1. Synthesis of molecular n-CAR materials

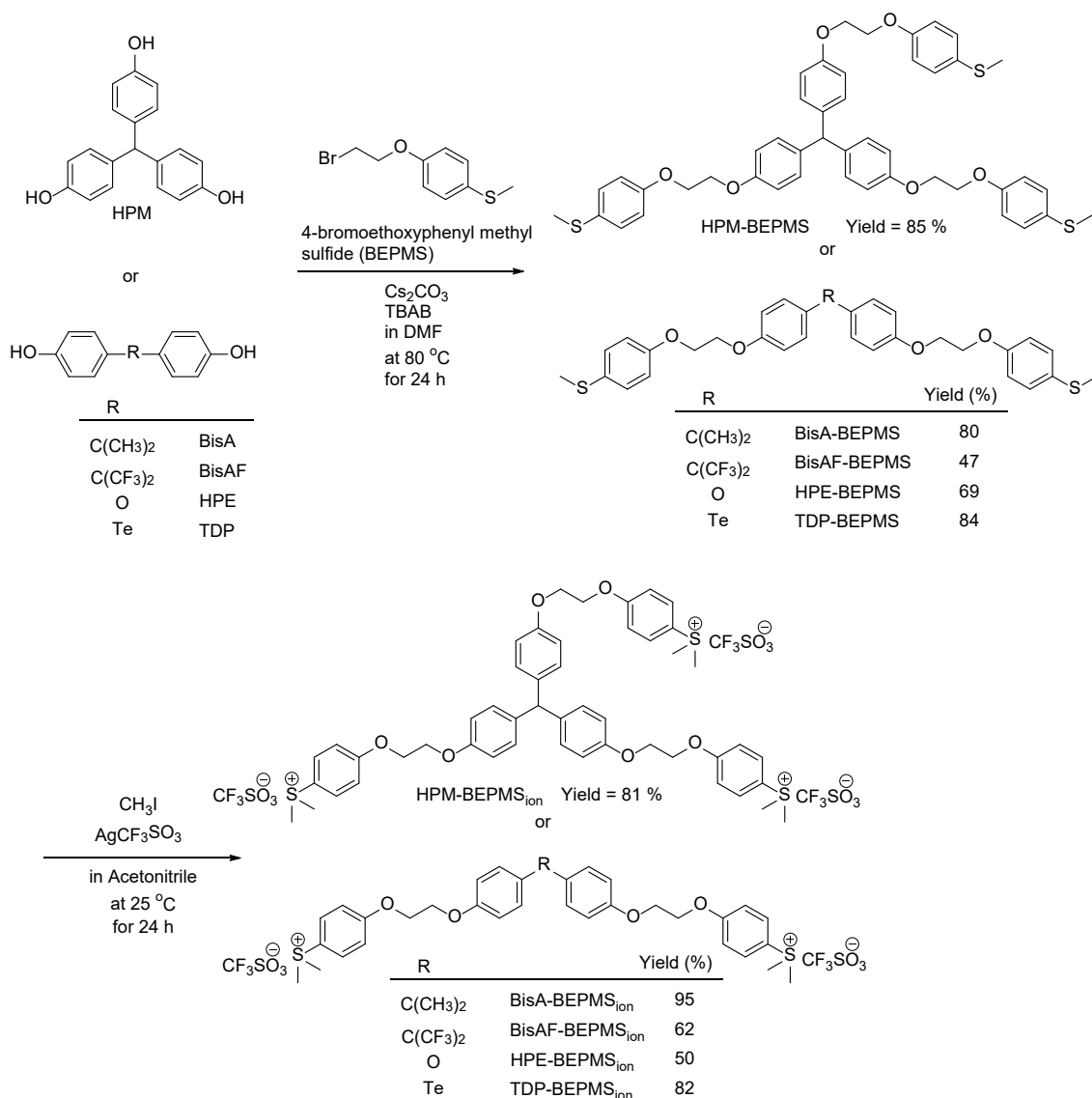
HPM-BEPMS_{ion}, BisA-BEPMS_{ion}, BisAF-BEPMS_{ion}, HPE-BEPMS_{ion}, and TDP-BEPMS_{ion}

Condensation reaction of HPM and BEPMS was examined using cesium carbonate as a base in DMF at 80 °C for 24 h in the presence of TBAB as a catalyst, to give a corresponding compound HPM-BEPMS containing sulfide moieties in 85 % yield. Its structure was confirmed by ¹H-NMR and FT-IR spectroscopy. In the same way, the reaction of various bisphenols (BisA, BisAF, HPE, and TDP) and BEPMS was performed to give the corresponding compounds BisA-BEPMS, BisAF-BEPMS, HPE-BEPMS, and TDP-BEPMS in 47 ~ 84 % yields. Next, the reaction of HPM-BEPMS with silver trifluoromethanesulfonate and

iodomethane was carried out in acetonitrile at room temperature for 24 h, to give a corresponding compound HPM-BEPMS_{ion} in 81 % yield. Its structure was confirmed by ¹H-NMR and FT-IR spectroscopy. In the same way, BisA-BEPMS_{ion}, BisAF-BEPMS_{ion}, HPE-BEPMS_{ion}, and TDP-BEPMS_{ion} were synthesized in 50 ~ 95 % yields. These synthetic procedures are illustrated in Scheme 1.

3.2. Physical properties (solubility, film-forming ability, and thermal stability)

Physical properties of the synthesized molecular n-CAR materials HPM-BEPMS_{ion}, BisA-BEPMS_{ion}, BisAF-BEPMS_{ion}, HPE-BEPMS_{ion}, and TDP-BEPMS_{ion} relevant to their applicability as EUV-resist materials were examined.



Scheme 1. Synthetic procedure of molecular n-CAR materials HPM-BEPMS_{ion}, BisA-BEPMS_{ion}, BisAF-BEPMS_{ion}, HPE-BEPMS_{ion}, and TDP-BEPMS_{ion}

Solubility. HPM-BEPMS_{ion}, BisA-BEPMS_{ion}, BisAF-BEPMS_{ion}, HPE-BEPMS_{ion}, and TDP-BEPMS_{ion} were soluble in polar solvents such as water, DMSO, DMF, NMP, methanol, and acetone. Furthermore, they were soluble in PGME, which is usually used when the resist materials are spin-coated on the silicon wafer. They were also insoluble in non-polar organic solvents such as ethyl acetate, ethyl ether, CHCl₃, toluene, hexane. These are summarized in Table 1.

Film-forming ability. The film-forming ability was examined by spin coating a solution of synthesized molecular resist materials 50 mg in PGME 1.0 ml on silicon wafer, and drying the wafer *in vacuo* at room temperature. All molecular resist

materials showed good film-forming abilities.

Thermal stability. The thermal properties of the synthesized molecular resist materials were examined by means of TGA. The initial weight loss temperature was measured by means of TGA, to be in the range between 190 and 280 °C, which are also summarized in Table 1. These are adequate for application as photo-resist materials.

3.3. Resist sensitivity

Resist sensitivity of molecular n-CAR materials HPM-BEPMS_{ion}, BisA-BEPMS_{ion}, BisAF-BEPMS_{ion}, HPE-BEPMS_{ion}, and TDP-BEPMS_{ion} were examined using EUV exposure tool. Solutions of these compounds in PGME were spin-coated on silicon wafers to prepare thin films of about 50 ~ 80 nm thickness.

Next, the silicon wafer allows development by dipping in deionized water at room temperature for 30 sec. The value of the thickness of remained thin film was measured by means of ellipsometer after the lithography process. These results are illustrated in Fig. 1.

The thin films of HPM-BEPMS_{ion}, BisA-BEPMS_{ion}, BisAF-BEPMS_{ion}, and HPE-BEPMS_{ion} were fully insoluble in deionized water after 20, 18, 30, and 30 mJ/cm², respectively, i.e., E₁₀₀ (value of resist sensitivity)'s were in the range between 18 and 30 mJ/cm². Furthermore, the photoresist contrast values γ could be extracted from these sensitivity curves and their values of HPM-BEPMS_{ion}, BisA-BEPMS_{ion}, BisAF-BEPMS_{ion}, and HPE-BEPMS_{ion} were 20.75, 6.91, 4.60 and 20.41 respectively. These are also summarized in Table 2. These results indicate that HPM-BEPMS_{ion}, BisA-BEPMS_{ion}, BisAF-BEPMS_{ion}, HPE-BEPMS_{ion} are applicable to negative type EUV

Table 1. Solubility and thermal stability of molecular n-CAR materials HPM-BEPMS_{ion}, BisA-BEPMS_{ion}, BisAF-BEPMS_{ion}, HPE-BEPMS_{ion}, and TDP-BEPMS_{ion}

(R)-BEPMS _{ion}	R				
	HPM	BisA	BisAF	HPE	TDP
water	++	++	++	++	++
DMSO	++	++	++	++	++
NMP	++	++	++	++	++
DMF	++	++	++	++	++
methanol	++	++	++	++	++
acetone	++	++	++	++	++
THF	--	--	--	--	--
ethyl acetate	--	--	--	--	--
diethyleter	--	--	--	--	--
chloroform	--	--	--	--	--
toluene	--	--	--	--	--
hexane	--	--	--	--	--
PGME	++	++	++	++	++
PGMEA	--	++	--	++	++
2.38wt% TMAH	++	++	++	++	++
T _d ^{a, b} (°C)	280	190	279	263	247

^a++; Soluble at room temperature. --; Insoluble in at room temperature. PEGME; Propyleneglycol monomethyl ether. PEGMEA; Propyleneglycol monomethyl ether acetate. TMAH; Tetramethyl ammonium hydroxide. ^bT_dⁱ; Initial thermal decomposition temperature.

Table 2. E₁₀₀ (value of resist sensitivity) and contrast value γ of HPM-BEPMS_{ion}, BisA-BEPMS_{ion}, BisAF-BEPMS_{ion}, HPE-BEPMS_{ion}, and TDP-BEPMS_{ion}

	E ₁₀₀	γ
HPM-BEPMS _{ion}	20	20.75
BisA-BEPMS _{ion}	18	6.91
BisAF-BEPMS _{ion}	30	4.6
HPE-BEPMS _{ion}	30	20.41
TDP-BEPMS _{ion}	^a	^a

^aNot determined.

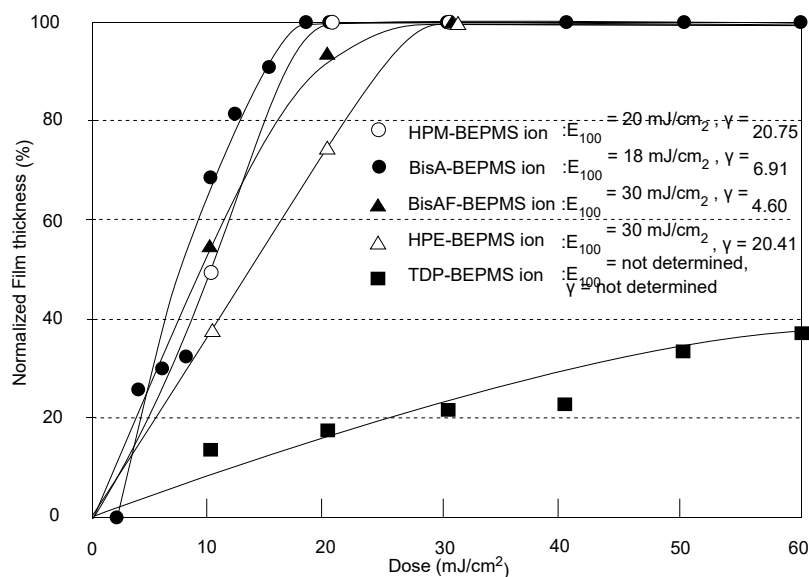


Fig. 1. Sensitivity curves of resist materials based on molecular n-CAR materials HPM-BEPMS_{ion}, BisA-BEPMS_{ion}, BisAF-BEPMS_{ion}, HPE-BEPMS_{ion}, and TDP-BEPMS_{ion}.

resist materials. However, a good sensitivity curve could not be obtained in the case of TDP-BEPMS_{ion}. Presumably because of that transparency of TDP-BEPMS_{ion} might be low due to tellurium, which has high EUV absorption efficiency^{14,15}.

4. Conclusion

In summary, we examined the condensation reaction of trisphenol (HPM) and various bisphenols (BisA, BisAF, HPE, and TDP) with BEPMS, and the corresponding compounds (HPM-BEPMS, BisA-BEPMS, BisAF-BEPMS, HPE-BEPMS, and TDP-BEPMS) containing sulfide moieties were obtained. The synthesized HPM-BEPMS, BisA-BEPMS, BisAF-BEPMS, HPE-BEPMS, and TDP-BEPMS were reacted with silver trifluoromethanesulfonate and iodomethane to give the molecular n-CAR materials HPM-BEPMS_{ion}, BisA-BEPMS_{ion}, BisAF-BEPMS_{ion}, HPE-BEPMS_{ion}, and TDP-BEPMS_{ion}. Their physical properties (solubility, film-forming ability, and thermal stability) could show good results, meaning that they are adequate for application as photo-resist materials. Furthermore, resist sensitivity of HPM-BEPMS_{ion}, BisA-BEPMS_{ion}, BisAF-BEPMS_{ion}, HPE-BEPMS_{ion}, and TDP-BEPMS_{ion} were examined using EUV exposure tool. All compounds except for TDP-BEPMS_{ion} could show the applicable to negative-type resist material, and their sensitivities (E_{100}) were in the range between 18 and 30 mJ/cm².

Acknowledgement

This work was partly supported by Cooperative Research Program "Network Joint Research Center for Materials and Devices".

References

1. V. Bakshi, "EUV Lithography", John Wiley & Sons, Inc. (2009).
2. Y. Morikawa, K. Arimitsu, T. Gunji, Y. Abe, and K. Ichimura, *J. Photopolym. Sci. Technol.*, **16** (2003) 81.
3. K. Young-Gil, J. B. Kim, T. Fujigaya, and M. Ueda, *J. Mater. Chem.*, **12** (2002) 53.
4. H. Kudo, R. Hayashi, K. Mitani, T. Yokozawa, N. C. Kasuga, and T. Nishikubo, *Angew. Chem. Int. Ed.*, **45** (2006) 7948.
5. M. Tanaka, A. Rastogi, H. Kudo, D. Watanabe, T. Nishikubo, and C. K. Ober, *J. Mater. Chem.*, **19** (2009) 4622.
6. H. Kudo, D. Watanabe, T. Nishikubo, K. Maruyama, D. Shimizu, T. Kai, T. Shimokawa, and C. K. Ober, *J. Mater. Chem.*, **18** (2008) 3588.
7. X. André, J. K. Lee, A. DeSilva, C. K. Ober, H. B. Cao, H. Deng, H. Kudo, D. Watanabe, and T. Nishikubo, *Proc. SPIE*, **6519** (2007) 65194B.
8. T. Nishikubo, H. Kudo, Y. Suyama, H. Oizumi, and T. Itani, *J. Photopolym. Sci. Technol.*, **22** (2009) 73.
9. H. Kudo, Y. Suyama, H. Oizumi, T. Itani, and T. Nishikubo, *J. Mater. Chem.*, **20** (2010) 4445.
10. N. Niina, H. Kudo, H. Oizumi, T. Itani, and T. Nishikubo, *Thin Solid Films*, **534** (2013) 459.
11. H. Kudo, M. Jinguji, T. Nishikubo, H. Oizumi,

- and T. Itani, *J. Photopolym. Sci. Tech.*, **23** (2010) 657.
12. H. Seki, Y. Kato, H. Kudo, H. Oizumi, T. Itani, and T. Nishikubo, *Jpn. J. Appl. Phys.*, **49** (2010) 06GF06-1
13. H. Kudo, S. Ohori, H. Takeda, H. Ogawa, T. Watanabe, H. Yamamoto, and T. Kozawa, *J. Photopolym. Sci. Technol.*, **31** (2018) 221.
14. M. Fukunaga, H. Yamamoto, T. Kozawa, and T. Watanabe, H. Kudo, *J. Photopolym. Sci. Technol.*, **30** (2017) 103.
15. H. Kudo, M. Fukunaga, T. Yamada, S. Yamakawa, T. Watanabe, H. Yamamoto, K. Okamoto, and T. Kozawa, *J. Photopolym. Sci. Technol.*, **32** (2019) 805.
16. S. Enomoto and T. Kozawa, *J. Vac. Sci. Technol. B*, **36** (2018) 031601
17. S. Enomoto, T. Yoshino, K. Machida, and T. Kozawa, *Jpn. J. Appl. Phys.*, **58** (2019) 016504.
18. S. Enomoto, T. Yoshino, K. Machida, and T. Kozawa, *Jpn. J. Appl. Phys.*, **58** (2019) 056504.
19. J. Peter, M. G. Moinuddin, S. Ghosh, S. K. Sharma, and K. E. Gonsalves, *ACS Appl. Polym. Mater.*, **2** (2020) 1790.
20. V. S. V. Satyanarayana, F. Kessler, V. Singh, F. R. Scheffer, D. E. Weibel, S. Ghosh, and K. Gonsalves, *ACS Appl. Mater. Interfaces*, **6** (2014) 4223.
21. P. Kumar, P. G. Reddy, S. K. Sharma, S. Ghosh, C. P. Pradeep, and K. E. Gonsalves, *Microelectron. Eng.*, **194** (2018) 100.
22. X. Shi, P. Prewett, E. Huq, D. M. Bagnall, A. P. G. Robinson, and S. A. Boden, *Microelectron. Eng.*, **155** (2016) 74.
23. N. Thakur P. G. Reddy, S. Nandi, M. Yogesh, S. K. Sharma, C. P. Pradeep, S. Ghosh, and K. E. Gonsalves, *J. Micromech. Microeng.*, **27** (2017) 125010.

Study on Irradiation Effects by Femtosecond-pulsed Extreme Ultraviolet in Resist Materials

Yuji Hosaka^{1,2}, Hiroki Yamamoto¹, Masahiko Ishino^{1,3}, Thanh-Hung Dinh³,
Masaharu Nishikino³, Akira Kon^{4,5}, Shigeki Owada^{4,5}, Yuichi Inubushi^{4,5},
Yuya Kubota^{4,5}, and Yasunari Maekawa¹

¹ Takasaki Advanced Radiation Research Institute, National Institutes for Quantum and Radiological Science and Technology (QST),
1233 Watanuki, Takasaki, Gunma 370-1292, Japan

² Institute for Advanced Synchrotron Light Source, National Institutes for Quantum and Radiological Science and Technology (QST), 1-1-1 Kouto, Sayo, Hyogo 679-5148, Japan

³ Kansai Photon Science Institute (KPSI), National Institutes for Quantum and Radiological Science and Technology (QST), 8-1-7 Umemidai, Kizugawa, Kyoto 619-0215, Japan

⁴ Japan Synchrotron Radiation Research Institute (JASRI), 1-1-1, Kouto, Sayo-cho, Sayo-gun, Hyogo 679- 5198, Japan

⁵ RIKEN SPring-8 Center, 1-1-1, Kouto, Sayo-cho, Sayo-gun, Hyogo 679-5148, Japan
yamamoto.hiroki@qst.go.jp

Irradiation effects of poly(methyl methacrylate) (PMMA) induced by femtosecond-pulsed extreme ultraviolet (EUV) were investigated using Soft X-ray free electron laser (SXFEL) for realization of next generation extreme ultraviolet free electron laser (EUV-FEL) lithography. The sensitivity of PMMA upon exposure to femtosecond-pulsed SXFEL was much higher than that measured for conventional nanosecond-pulsed EUV source. The sensitivity enhancement upon exposure to femtosecond-pulsed SXFEL is similar to the result obtained using laser-induced-plasma based Soft X-ray laser (SXRL) (picosecond-pulsed EUV). This result speculates the reactions induced by femtosecond-pulsed SXFEL and picosecond-pulsed XRL were almost same, but it was different from those induced by nanosecond-pulsed EUV.

Keywords: Extreme Ultraviolet, Resist materials, Free-electron laser, Poly(methyl methacrylate), X-ray laser

1. Introduction

It is essential for our lives to use electronic devices. Lithography technique is very important for producing them. ArF immersion lithography has mainly used for the high-volume production of the forefront of electronic devices [1, 2]. However, ArF immersion lithography has reached the limit of nanofabrication and thereby a new technique has been urgently required [3].

Extreme ultraviolet (EUV) lithography, whose wavelength is 13.5 nm, has been recently adopted by the semiconductor industry as the advanced lithography technology to achieve further device scaling. However, EUV lithography also has

approached the limits imposed by single exposure. Therefore, we must replace EUV with next generation lithography candidates including High-NA EUV lithography [4], next generation EUV with the wavelength of 6.x [5], extreme ultraviolet free electron laser (EUV-FEL) lithography [6, 7], and so on. Among them, it is thought that high power EUV-FEL will improve both nano fabrication cost and throughput [7]. One of the important characteristics of EUV-FEL is its short temporal pulse duration, which arises from the interaction between the ultrashort electron bunch and electromagnetic field. Recently, FEL which generates pulsed soft X-ray (EUV) such as

SPring-8 Angstrom Compact FEL (SACLA) has been developed all over the world [8].

Main-chain-scission-type resists have been widely used for the fabrication of nano-devices because they could fabricate in principle ultrafine structures to the dimensions of the monomers they consist of. Among them, poly(methyl methacrylate) (PMMA) is a typical main-chain-scission-type resist [9-13]. PMMA has the capability for fabricating sub-10 nm half-pitch, although its applications are limited due to its poor etch resistance [14, 15]. The reaction mechanism of PMMA upon exposure to radiation and electron beam has been reported as follows [16-18]. Upon exposure to radiation such as EUV and electron beam, PMMA molecules are ionized and their radical cations results in. After the detachment of side chains from the radical cations, β -scission of PMMA molecules occurs. However, the irradiation effects induced by EUV with a short pulse width and high power intensity in PMMA have not yet been elucidated.

In order to make clear the irradiation effects by EUV with a short pulse width and high power intensity, the morphological and chemical changes in PMMA induced by picosecond-pulsed EUV were investigated using a laser-induced-plasma based Soft X-ray laser (SXRL) in Kansai Photon Science Institute (KPSI) [19]. It has been reported that the sensitivity of PMMA upon exposure to picosecond-pulsed SXRL was much enhanced in comparison with using conventional EUV sources [20]. The short-pulsed ionizing radiation causes a unique reaction because of the high dose rate.

Further investigation of short-pulsed EUV-induced reactions in resist materials are strongly needed for realizing EUV-FEL lithography. An important feature of EUV-FEL is the short pulse width on the order of femtoseconds. Because EUV with a pulse width of less than picoseconds is a novel light born in recent scientific and technological developments, physical events and chemical reactions in resist materials induced by the short-pulse EUV are not sufficiently understood. Therefore, it is very important for EUV-FEL resist design to understand femtosecond-pulsed EUV-induced reaction in PMMA.

In this study, the sensitivity of PMMA upon exposure to femtosecond-pulsed EUV was investigated by using soft X-ray free electron laser (SXFEL) in SACLA in order to make clear whether the resist sensitivity of PMMA enhances or

not upon exposure to femtosecond-pulsed-EUV.

2. Experimental

Ultrashort-pulsed soft X-ray of SACLA BL1 was used as femtosecond-pulsed EUV source [21]. SXFEL is generated by 800 MeV electron beam passing through an undulator. The pulse width was 70 fs and the energy was 92 eV, which is equal to wavelength of 13.5 nm. The horizontal spot size was 4.47 μm and vertical spot size was 3.67 μm (FWHM). Because the maximum fluence on target is approximately 100 $\text{J}/\text{cm}^2/\text{shot}$, SXFEL was attenuated below the ablation threshold. The SXFEL shots were attenuated to suitable intensity by using Zr filters having various thicknesses (0.1, 0.2, 0.5, 1.0, and 2.0 μm thickness or these combination). Details of the system have been reported elsewhere [22-24].

PMMA (Sigma-Aldrich, Mw = 350,000) were dissolved in toluene, spin-coated on Si wafer chips at 2500 rpm (min^{-1}), and baked at 220 $^{\circ}\text{C}$ for 15 minutes in air. The thicknesses of the spin-coated PMMA samples can be controlled by changing the concentration of PMMA solution. The samples with the thickness of approximately 66 nm and 350 nm were prepared. PMMA films were exposed to femtosecond-pulsed EUV. The irradiated samples were developed in a developer (methyl isobutyl ketone (MIBK): isopropyl alcohol (IPA) 1:3) for 60 s at room temperature (22 $^{\circ}\text{C}$).

The surface change due to development was observed by using atomic force microscope (AFM) (AFM5300E, Hitachi High-Tech Science Corporation) in the atmosphere. The three-dimensional profiles of PMMA surface were obtained.

3. Results and discussion

SXFEL-irradiated PMMA surface was observed

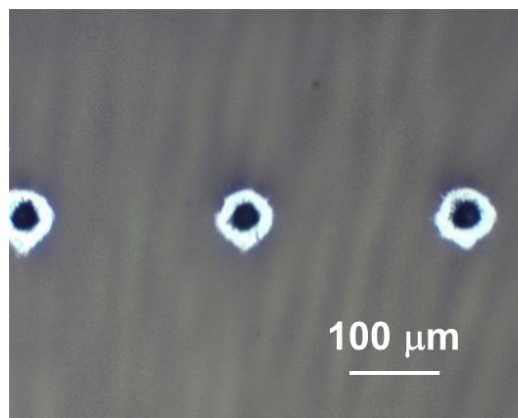


Fig. 1. Optical microscope image of a surface of SXFEL-irradiated PMMA film without attenuation before development.

without attenuation as already reported [23]. Large craters with several tens of μm were produced on samples as shown in Fig. 1 and used as a mark to search the position of development experiment.

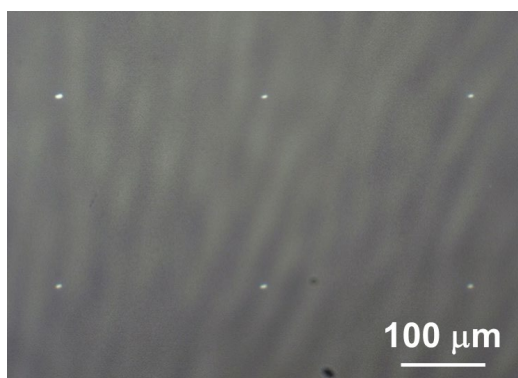


Fig. 2. Optical microscope image of a surface of SXFEL-irradiated PMMA film with attenuation after development.

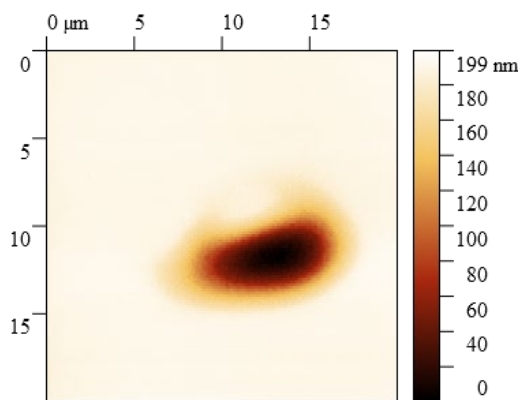


Fig. 3. AFM image of a hole on SXFEL-irradiated 66 nm thick PMMA film with attenuation after development.

Subsequently, in order to investigate resist performance of PMMA, SXFEL was attenuated to suitable intensity by using Zr filters. PMMA samples (initial thickness: 350 nm) were irradiated by one shot of SXFEL and total exposure dose was change by the combination of Zr filters. We confirmed no holes or damages was observed with microscope on the irradiated PMMA surface when the intensity was attenuated to about 1/1000 using Zr filters. Then, the sample was developed in for 60 s at room temperature (22 °C). Small holes were observed after development. The holes appeared after development on the irradiated PMMA sample as shown in Fig. 2. Also, AFM image of the hole on the 66 nm thick sample are shown in Fig. 3. Relatively well-formed profiles were obtained after development by using SXFEL. The hole size was consistent with SXFEL spot size.

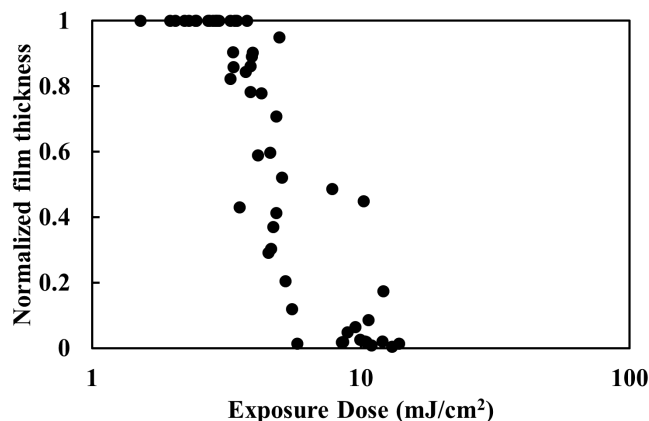


Fig. 4. Sensitivity curve of SXFEL-irradiated 66 nm thick PMMA film after development.

The EUV pulse width of SXFEL in SACLA is approximately 80 fs, which is much shorter than conventional EUV and laser-induced-plasma based SXRL pulse widths. In order to confirm whether the resist sensitivity of PMMA enhances or not upon exposure to femtosecond-pulsed-EUV compared with conventional EUV and SXRL, we evaluated the resist performance of PMMA. Sensitivity of PMMA for SXFEL irradiation was measured. Fig. 4 shows sensitivity curve of PMMA with 66 nm film thickness after development. The sensitivity of a positive-tone resist is defined as the dose required to entirely remove the resist layer after development. The sensitivity of PMMA for femtosecond-pulsed SXFEL was determined to be approximately 6–8 mJ/cm^2 . It has been reported that the sensitivity of PMMA for typical EUV and SXRL was approximately 50 mJ/cm^2 and 2 mJ/cm^2 , respectively [19, 20]. PMMA can be developed with lower energy deposition for femtosecond-pulsed SXFEL than typical EUV. On the other hand, the sensitivity enhancement upon exposure to femtosecond-pulsed EUV is similar to the result obtained using laser-induced-plasma based SXRL. Surprisingly, the sensitivity enhancement is common to result obtained using picosecond-pulsed SXRL. It has been already reported that SXRL irradiation induced the decomposition of both the main and side chains in PMMA [20]. In femtosecond-pulsed SXFEL, the same reaction in PMMA as SXRL might be induced, so that the sensitivity of PMMA for SXFEL irradiation was enhanced compared with using typical EUV sources. Further investigation of these detailed mechanisms are in progress.

4. Conclusion

In order to investigate the physical and chemical

reactions in resists for next generation lithography using short-pulsed EUV-FEL, irradiation effects by femtosecond-pulsed SXFEL in PMMA were performed. When using SXFEL with a pulse width of femtoseconds, PMMA film was removed by development after exposure of only 6–8 mJ/cm². Sensitivity of PMMA for SXFEL was much higher than the value that measured for conventional EUV. The sensitivity enhancement is common to result obtained using picosecond-pulsed SXRL. These results suggest the importance of a specific resist design for next-generation EUV-FEL lithography, which is short-pulsed EUV.

Acknowledgement

This work was partly supported by JSPS KAKENHI Grant number JP 18K18308 and JP 20H02489. EUV-FEL experiments were performed at the BL1 of the SACLA-SPring-8 facility by the approval of the Japan Synchrotron Radiation Research Institute (JASRI) (Proposal No. 2018B8042).

References

1. R. H. French and H. V. Tran, *Annu. Rev. Mater. Res.*, **39** (2009) 93.
2. S. Tarutani, H. Tsubaki, and S. Kanna, *J. Photopolym. Sci. Technol.*, **21** (2008) 685.
3. L. Li, X. Liu, S. Pal, S. Wang, C. K. Ober, and E. P. Giannelis, *Chem. Soc. Rev.*, **46** (2017) 4855.
4. O. R. Wood II, *J. Photopolym. Sci. Technol.*, **30** (2017) 599.
5. T. G. Oyama, A. Oshima, M. Washio, and S. Tagawa, *J. Vac. Sci. Technol. B*, **31** (2013) 041604.
6. C. Pagani, E. L. Saldin, E. A. Schneidmiller, and M. V. Yurkov, *Nucl. Instrum. Meth. A*, **463** (2001) 9.
7. E. R. Hosler, O. R. Wood, W. A. Barletta, P. J. S. Mangat, and M. E. Preil, *Proc. SPIE*, **9422** (2015) 94220D.
8. M. Yabashi, H. Tanaka, and T. Ishikawa, *J. Synchrotron Rad.*, **22** (2015) 477.
9. S. Yasin, D. G. Hasko, and H. Ahmed, *Appl. Phys. Lett.*, **78** (2001) 2760.
10. E. A. Dobisz, S. L. Brandow, R. Bass, and J. Mitterender, *J. Vac. Sci. Technol. B*, **18** (2000) 107.
11. D. R. S. Cumming, S. Thoms, S. P. Beaumont, and J. M. R. Weaver, *Appl. Phys. Lett.*, **68** (1996) 322.
12. M. Khoury and D. K. Ferry, *J. Vac. Sci. Technol. B*, **14** (1996) 75.
13. W. Chen and H. Ahmed, *Appl. Phys. Lett.*, **62** (1993) 1499.
14. W. C. Hu, K. Sarveswaran, M. Lieberman, and G. H. Bernstein, *J. Vac. Sci. Technol. B*, **22** (2004) 1711.
15. D. R. S. Cumming, S. Thoms, J. M. R. Weaver, and S. P. Beaumont, *Microelectron. Eng.*, **30** (1996) 423.
16. T. Kozawa, S. Tagawa, T. Kai, and T. Shimokawa, *J. Photopolym. Sci. Technol.*, **20** (2007) 577.
17. T. Ichikawa and H. Yoshida, *J. Polym. Sci. A*, **28** (1990) 1185.
18. G. Geuskens and C. David, *Makromol. Chem.*, **165** (1973) 273.
19. M. Ishino, T. Dinh, Y. Hosaka, N. Hasegawa, K. Yoshimura, H. Yamamoto, T. Hatano, T. Higashiguchi, K. Sakaue, S. Ichimaru, M. Hatayama, A. Sasaki, M. Washio, M. Nishikino, and Y. Maekawa, *Applied Optics*, **59** (2020) 3692.
20. Y. Hosaka, T. G. Oyama, H. Yamamoto, M. Ishino, T.-H. Dinh, M. Nishikino, and Y. Maekawa, *Appl. Phys. Lett.*, **115** (2019) 073109.
21. S. Owada, K. Togawa, T. Inagaki, T. Hara, T. Tanaka, Y. Joti, T. Koyama, K. Nakajima, H. Ohashi, Y. Senba, T. Togashi, K. Tono, M. Yamaga, H. Yumoto, M. Yabashi, H. Tanaka and T. Ishikawa, *J. Synchrotron Radiat.*, **25** (2018) 282.
22. T.-H. Dinh, N. Medvedev, M. Ishino, T. Kitamura, N. Hasegawa, T. Otobe, T. Higashiguchi, K. Sakaue, M. Washio, T. Hatano, A. Kon, Y. Kubota, Y. Inubushi, S. Owada, T. Shibuya, B. Ziaja, and M. Nishikino, *Communication Physics*, **2** (2019) 150.
23. K. Mikami, M. Ishino, T.-H. Dinh, S. Motokoshi, N. Hasegawa, A. Kon, Y. Inubushi, S. Owada, H. Kinoshita, and M. Nishikino *Opt. Lett.*, **45** (2020) 2435.
24. T. Shibuya, T. Takahashi, K. Sakaue, T.-H. Dinh, H. Hara, T. Higashiguchi, M. Ishino, Y. Koshiba, M. Nishikino, H. Ogawa, M. Tanaka, M. Washio, Y. Kobayashi, and T. Kuroda, *Appl. Phys. Lett.*, **113** (2018) 171902.

Evolution of Secondary Electrons Emission During EUV Exposure in Photoresists

Roberto Fallica^{1,*}, Stefano Nannarone², Nicola Mahne², Andrea Marco Malvezzi²,
Andrea Berti², Danilo De Simone¹

¹ IMEC, Leuven, Belgium

² CNR-IOM Trieste, Italy

*roberto.fallica@imec.be

Low energy electronic processes are key to chemical reactions during exposure of photoresists in extreme ultraviolet lithography. To understand and optimize the functionality of photoresists, it is of paramount importance to assess the magnitude of the electron distribution inside the material. While photoemission spectroscopy is being widely used, vacuum barrier crossing and nonideal photoemissivity alter the measured spectra in a way that prevents meaningful assessment of very low energy electrons. In this work we propose a model to account for the physics of photoemission effects and to reliably estimate the distribution from solid state matter. The model also provides a quantitative value for the occupation function and density of state. We tested the model on the photoemission spectra acquired on a prototype EUV photoresist and report here the results.

Keywords: EUV lithography, Electronic processes, Secondary electrons, Photoemission, Photoresist, Photoelectron spectroscopy

1. Introduction

Recent experimental evidence indicates that scattering processes involving electrons of very low kinetic energy $\ll 10$ eV are the main driver for chemical reactions in organic molecules [1]. Specific examples including electron scattering studies on isolated molecules in gas phase [2,3] and their role in desorption mechanisms [4] indicate how electronic processes triggered by low energy (\sim eV) electrons are at the base of most lithographically relevant phenomena. For electron attachment and dissociation where a molecule is taken in the scattering process into an unstable excited state with modified electronic and structural configuration resulting in fragmentation and desorption.

Low-energy electron-induced reactions have substantial technological importance in Extreme Ultra-Violet (EUV) optical lithography which uses light beams with photons of energy well above the ionization threshold and smaller wavelengths that allow a jump in the high-resolution patterning of thin organic polymer-based photoresist films. Contrary to previous optical lithography

technologies such as deep ultraviolet (DUV), in EUV the amount of incident photons is about one order of magnitude lower than it was when UV or longer wavelength photons were used. As a result, the exposure mechanism that leads to the lithographic process is ascribed to the electron cascade generated by the primary photoelectron filling up the formerly empty electronic states in absence of illumination more than the photoelectron creation itself.

Photoresists (PR) for EUV lithography consist of, as in previous technology, an organic polymer backbone plus small percentages of photoacid generator (PAG) and acid quencher to catalyze or slow down the deprotection reaction, respectively. These compounds are therefore known as chemically amplified resists (CAR) since their invention [5]. Due to the nature of EUV light and electronic structure of photoresist material, photo-absorption mostly involves electrons energetically located in the valence band occupying molecular orbitals involving atomic O, C and H states whose excitation triggers the production of primary, high-energy electrons [6].

In case of PR made up of atomic species with electron binding energies lower than photon energies photo-electrons due to core level excitation and related Auger electrons have to be added to this scenario, a case which is not at issue here.

Owing to the electron mean free path of photoelectrons, most of the kinetic energy and momentum of primaries is transferred to PR through multiple inelastic electron-electron scattering events in sub-picosecond timescale, which generate a substantially larger amount of electrons bond to occupy low energy electronic states [8]. All this experimental evidence leads to the conclusion that low energy electrons are the main responsible in starting chemical reactions in the photoresist at variance with the early expectations. For lithography engineers, the amount and distribution of secondary electrons in photoresists during exposure to EUV light is therefore key to assess the efficiency of the litho process.

Though it is not yet entirely quantitatively assessed the way these electronic processes translate into lithographic performance (conventionally described in terms of figures of merit such as sensitivity, roughness, resolution [9], and defectivity). Present contribution is devoted to the presentation of an experimental method and the model it stems from aims at establishing a protocol to assess the total amount of low energy electron production and their distribution among electronic states inside the PR during light exposure. Experimentally, the PR is exposed to the working photon energy of $\hbar\omega = 92$ eV and the distribution in kinetic energy of emitted electrons per incident photon $N_{ext}(E_k)$ is measured in the region spanning from the electron emission onset of secondary electrons up to a few tens of eV. The $N_{ext}(E_k)$ distribution is modeled in terms of PR parameters and the figure of merit of the rate of production of low energy electrons expressed by an out-of-equilibrium occupation function $f^*(E)$, formerly empty in absence of illumination.

Furthermore, it is worth to stress that the distribution in kinetic energy and momentum of the emitted electrons is deformed in energy, E , and momentum caused by the PR-vacuum barrier height χ , resulting in a net energy change, and reduction of the normal component of momentum and consequent electron diffraction. Because of the barrier cutoff, the low energy end of electron states with energies lower than χ is experimentally inaccessible, a limitation which is overcome performing a suitable extrapolation of the

occupation function obtained for the electron energy above the barrier range. We believe that this procedure provides a reliable estimation of the energy distribution of electrons inside the photoresist when the material is under illumination in the light patterning phase of the photolithographic process. The underlying assumptions are discussed in light of the known literature of photoemission from organic molecules in the solid-state layers and some examples are presented.

2. Experimental

Low energy electron emission yield studies of EUV photoresists were carried out by electron yield spectroscopy at the CNR-IOM synchrotron beamline BEAR [10] (Elettra, Trieste-Italy) using a photon beam of EUV light ($\lambda=13.5$ nm wavelength, $\hbar\omega=91.9$ eV) of $\approx 200 \mu\text{m}^2$ cross section area whose intensity was calibrated by an absolute photodiode AXUV-100. In this apparatus, samples were loaded through an interlock onto a motorized stage located in a vacuum chamber which had been evacuated at a base pressure in the 10^{-10} mbar range for the entire duration of the experiment. The distribution $N_{ext}(E_k)$ in kinetic energy of electrons emitted from the sample surface was measured using an hemispherical electron analyzer with resolution $\Delta E = 0.1$ eV positioned in normal emission with the light impinging at 45° in s -polarization incidence. During the measurement, the samples were also biased to a voltage of -30 V (kinetic electrons energy where obtained rescaling by 30 eV) to get an almost parallel electron beam in the region of fly in vacuum and then to maximize the electron trajectories collected by the electron analyzer. Kinetic energy distribution of emitted electrons was then acquired in the very low energy range starting from the secondary emission onset and covering a kinetic energy range ~ 15 eV.

Photoresist samples consisted of a EUV-patternable blend of polymer (82.7 wt.%) and photoacid generator (PAG) (17.3 wt.%). The polymer was poly(hydroxystyrene) (PHS) modified with 50% *t*-Butyloxycarbonyl (*t*BOC) protecting group, $\text{C}_{16}\text{O}_3\text{H}_{18}$. The PAG was a triphenylsulfonium salt, $\text{C}_{23}\text{O}_3\text{H}_{17}\text{S}_2\text{F}_9$. Molecular structures are shown in Figure 1.

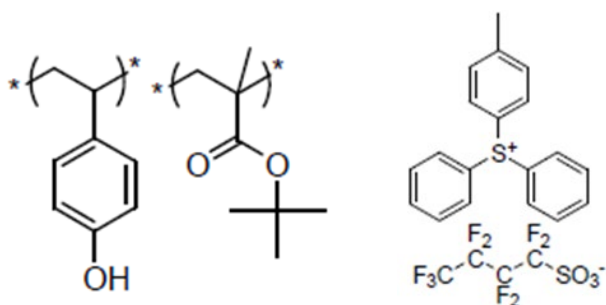


Fig. 1. Structure of the photoresist investigated, consisting of a poly(hydroxystyrene) backbone with t-Butyloxycarbonyl protecting groups (left) and a triphenylsulfonium salt as photoacid generator (right).

The material was spin coated on blank silicon wafers of 4" diameter, then baked at 100 °C for 60 s on a hot plate to remove the remaining solvent. By tuning the spin coating speed, uniform film of 35 ± 1 nm thickness was obtained by ellipsometry. The silicon substrate was then cleaved into 2×2 cm² dices and kept in low vacuum until their loading in the vacuum chamber.

The measurement procedure consists of a first measurement of sample in pristine condition ('unexposed'). Count rate was obtained sitting with the light spot at a fixed surface point with an acquisition time of 1s which resulted in ~ 2s of illumination per kinetic energy point corresponding to a dose ~ 1 mJ/cm² per kinetic energy point resulting in a total dose ~ 10 mJ/cm² for 10 points.

Best effort was taken to minimize the sample exposure which, according to the photon flux and duration of the acquisition, is estimated to be ≈ 0.7 mJ/cm² (much lower than the dose to clear and thus negligible from the point of view of the chemical changes induced). Afterwards, the sample was also measured after having been exposed to increasing amount of EUV light and comparable to the typical dose-to-size for this class of photoresists.

3. Analytical model of outside versus inside electron energy distribution

An essential account of the model is given here, referring the reader to a future publication for details. First, the model accounts for the crossing of the vacuum barrier which makes the electron lose part of their energy, E , and momentum component along the normal to the surface, z , with subsequent refraction. The zero of energy distribution inside the material is taken as the bottom of the conduction band or LUMO (Lowest Unoccupied Molecular Orbital,) according to the terminology of solids or molecular aggregates (similarly, valence band top is

reported as HOMO – Highest Occupied Molecular Orbital). The vacuum level is taken as zero of kinetic energy of electrons emitted in vacuo according to the relation:

$$E = E_K + \chi$$

The material is assumed to be in stationary conditions at an out of equilibrium temperature T^* . The occupation of states by charge carriers is described by an occupation function $f^*(T^*)$.

The physical parameters in the model are the position of the quasi-Fermi level inside the gap, E_F , the electronic affinity, χ , and the temperature T^* of the electron gas in the conduction band which is as first trial entry assumed as a free electron gas with a density of states $g(E) \propto \sqrt{E}$, as supported by previous theoretical result [11].

The $N_{ext}(E_k)$ distribution of emitted electrons results modeled through an integral on the z -coordinate normal to the surface on the portion of light excited and out of equilibrium portion of material of a combination of functions describing the light attenuation, electron transport to the surface and barrier crossing at its turn integrated on the polar angle between electron momentum and

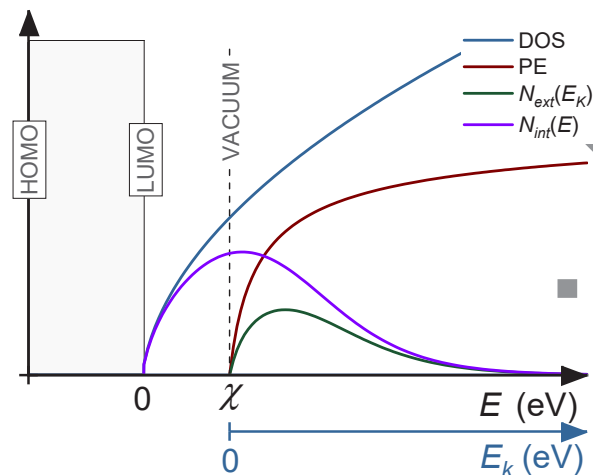


Fig. 2. Plot of the functions involved in the analytical model for photoemission. HOMO: highest occupied molecular orbital and top of the valence band. LUMO: lowest unoccupied molecular orbital and bottom of the conduction band. HOMO and LUMO are separated by a bandgap. Vacuum level is aligned to the electronic affinity χ (i.e., the barrier for photoemission). E is the energy of carriers inside the material. E_k is the kinetic energy of photoemitted photoelectrons. The electronic distribution inside the material, $N_{int}(E)$ is determined by density of states (DOS) and occupation function ($f^*(E)$, not shown). The distribution of photoemitted electrons is $N_{ext}(E_k)$ and it is a function of internal distribution in the photoresist $N_{int}(E)$ and of the photoemission model PE.

surface normal with the rate of emission at a given kinetic energy band weighted by the occupation function f^* . The functions involved in the model are depicted Fig. 2. It should be noted that the model does not require the modeling of the dynamics of the cascade of secondary electrons being just devoted to inferring from the experimental secondary emission at what extent the low electron energy levels in the material become occupied through the electron cascade mechanism.

4. Results

The experimental distribution $N_{ext}(E_k)$ of photoelectrons emitted from a polymer + PAG photoresist film as a function of the kinetic energy E_k is shown in Fig. 3a. The spectrum presents the typical overall shape of secondary electron emission with a slowly decaying tail for $E_k > 4$ eV and a peak approaching the kinetic energy zero. The electron affinity in model calculation is assumed to be $\chi = 2$ eV and as a result the LUMO and band gap are highlighted at $E_k \leq -\chi$.

As entry value for the quasi-Fermi level, the work using a linear assumption behavior of material work function using the value $E_F = -2.5$ eV with respect to the LUMO level. Using a minimization routine to fit to the experimental $N_{ext}(E_k)$, the temperature T^* of the electron gas was found to be $T^* = 15073$ K. However, we could not find a satisfactory fit in the very low kinetic energy portion of the spectrum as evidenced by comparing the fit function dashed line in Figure 3a with experiment. This disagreement can be ascribed to a deviation of the density of states from that of the free electron gas because of the presence of localized molecular orbital(s) close to the vacuum level. The large electron mean free path of low E electrons can also be responsible of overweighting the contribution of emission from low energy states or even from substrate. This effect, ignored in the model, might imply an electron yield higher than PR.

Under the hypothesis of localized molecular orbital(s), an additional term $\delta(E)$ to the density of states $g(E)$ can be introduced to take this extra emission into account. The $f^*(E)$ function presented here is obtained with this correction to the free electron gas density of states. This calls for specific theoretical calculations of density of states of empty orbitals in this energy range to validate or reject this kind of hypothesis.

In summary, the fitting function in the thermal approximation seems to be able to provide insight into the occupation of states in the conduction band

close to energy bottom in the region from LUMO up to a few eV above vacuum level. Provided the $g(E)$ from theory or experiment, the amount of the electronic states of the photoresist that are occupied during the stationary exposure to the EUV beam can be estimated, as shown in Figure 3b.

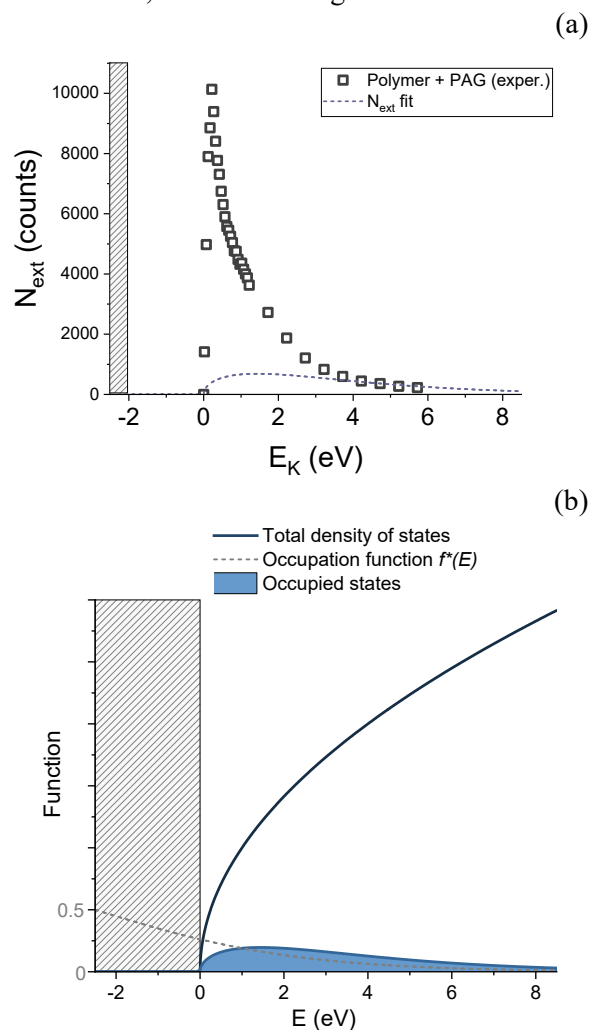


Fig. 3. (a) Experimental photoemission data (black squares) and model fitting (dashed blue line). (b) Total density of states (dark blue line), occupation function $f^*(E)$ (dashed yellow line) and resulting occupied states in the conduction band of the photoresist (shaded light blue area). The quasi-Fermi level is located at $E_F = -2.5$ eV, and the vacuum level is located at $E = \chi = 2$ eV. The highlighted region below $E = 0$ eV (LUMO) is the bandgap.

5. Conclusions

In this work we present an analytical model to determine the inner distribution of electrons in a material during exposure to EUV light from the experimental secondary electron distribution in kinetic energy close to the emission onset. Our

approach gives insight into the occupation of low energy electronic states in the region spanning from the LUMO and extrapolated data and up to states in the vacuum level region.

Although there are aspects to understand and refine, we believe that this method shows promising validity and represents an example of how one can experimentally determine and monitor the distribution of very low energy electrons generated in a photoresist under stationary EUV radiation exposure conditions in the photoresist which have energies below the vacuum threshold, i.e., that cannot be measured experimentally. This model provides for the first time a complete picture of very low energy electrons, which are relevant for lithographic purposes.

Acknowledgements

Photoresist manufacturers are kindly acknowledged for the providing test materials. The authors also wish to thank Vasiliki Kosma and Ivan Pollentier (imec) for fruitful discussions. Stimulating discussion with J. Rezvani are acknowledged, A. Giglia and K. Koshmak are thanked for their support in data acquisition.

References

1. "Low-Energy Electrons: Fundamentals and Applications" edited by Oddur Ingólfsson, Jenny Stanford Publishing; 1st edition (2019). ISBN-13: 978-9814800006.
2. R. M. Thorman, R. K. T. P., D. H. Fairbrother, and O. Ingólfsson, *Beilstein J. Nanotechnol.*, **6** (2015) 1904.
3. I. I. Fabrikant, S. Eden, N. J. Mason, and J. Fedor, *Advances In Atomic, Molecular, and Optical Physics*, **66** (2017) 545.
4. M. Bertin, I. Martin, F. Duvernay, P. Theule, J. B. Bossa, F. Borget, E. Illenberger, A. Lafosse, T. Chiavassa, and R. Azria, *Phys. Chem. Chem. Phys.*, **11** (2009) 1838.
5. H. Ito, C. G. Willson, and J. M. J. Frechet, *Digest of Technical Papers of 1982 Symposium on VLSI Technology* (1982) 86.
6. A. Narasimhan et al., *J. Micro/Nanolith. MEMS MOEMS* **14**(4) (2015) 043502.
7. R. Fallica, S. J. Rezvani, S. Nannarone, S. Borisov, D. De Simone, S. Babin, G. Lorusso, and G. Vandenberghe, *Proc. SPIE*, **10960** (2019) 1096009.
8. R. E. Chase, W. L. Gordon, and R.W. Hoffman, *Applications of Surface Science*, **4** (1980) 271.
9. G. M. Gallatin, P. Naulleau, D. Niakoula, R. Brainard, E. Hassanein, R. Matyi, et al., *Proc SPIE*, **6921** (2008) 69211E.
10. S. Nannarone, F. Borgatti, A. DeLuisa, B. P. Doyle, G. C. Gazzadi, A. Giglia, P. Finetti, N. Mahne, L. Pasquali, M. Pedio, G. Selvaggi, G. Naletto, M. G. Pelizzo, and G. Tondello, *AIP Conference Proceedings* **705**(1) (2004) 450. <http://www.elettra.trieste.it/elettra-beamlines/bear.html>.
11. S. Serra, E. Tosatti, S. Iarlori, S. Scandolo, and G. Santoro, *Phys. Rev. B*, **62**, (2000) 7.

The Measurement of the Refractive Index n and k Value of the EUV Resist by EUV Reflectivity Measurement Method

Yosuke Ohta^{1*}, Atsushi Sekiguchi¹, Tetsuo Harada², and Takeo Watanabe²

¹ *Litho Tech Japan Co., Ltd., 2-6-6 Namiki, Kawaguchi, Saitama 332-0034, Japan*

² *Center for EUV Lithography, Laboratory of Advanced Science and Technology for Industry, University of Hyogo, 1-1-2 NewSUBARU, Kouto Kamigori, Ako-gun, Hyogo 678-1205, Japan*

*ohta.yosuke@ltj.co.jp

Up to now, we have been researching methods for measuring the simulation parameters of EUV resist. These parameters include the development parameter, the Dill C parameter, the diffusion length of acid generated from PAG, and the deprotection reaction parameter. By using these parameters, we have attempted to simulate EUV resist. As a result, we could investigate the conditions for reducing LER and for enhancing resolution. We hereby report on the methods of calculating the refractive index n and k values of photoresist with EUV light (13.5 nm), which has been difficult to measure until now, and the Dill B parameter, which is an absorption parameter. The three types of photoresists we investigated are the main chain scission type resist, chemically amplified resist, and metal resist.

Keywords: EUV reflectance measurement method, Refractive index, Dill B parameter, Main chain scission type resist, EUV chemically amplified resist, Metal resist

1. Introduction

As candidates for next-generation lithography with a half pitch (hp) of 15 nm or below, the ArF immersion multi-patterning technique and EUV lithography are the strongest. As it uses multiple masks and an etching technique, the multi-patterning technique is capable of obtaining high resolution, but its cost is high. On the other hand, the EUV lithography technique (hereinafter referred to as “EUVL”) is advantageous in terms of cost because a single exposure is possible. Research on the photoresist suitable for EUV lithography requires cost and time. As a method for solving this issue, application of such photoresists to resist research using lithography simulation is useful. Up to now, we have studied the methods for measuring the simulation parameters of EUV resist.

These parameters include the development parameter [1], the Dill C parameter [2, 3], the diffusion length of acid generated from PAG [4], and the deprotection reaction parameter [5, 6]. By using these parameters, we have attempted to simulate EUV resist. As a result, we could investigate the conditions for reducing LER and for

enhancing resolution [7, 8]. We hereby report on the methods of calculating the refractive index n and k values of photoresist with EUV light (13.5 nm), which has been difficult to measure until now, and the Dill B parameter, which is an absorption parameter, by focusing on the reflectance measurement method. The three types of

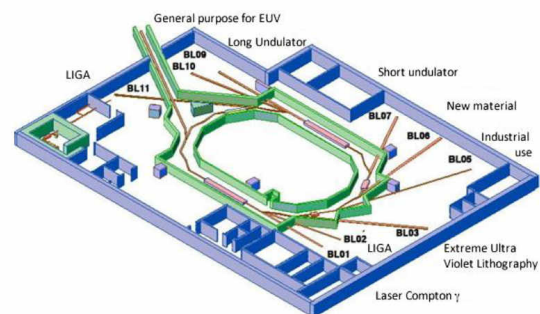


Fig. 1. NewSUBARU synchrotron radiation facility.

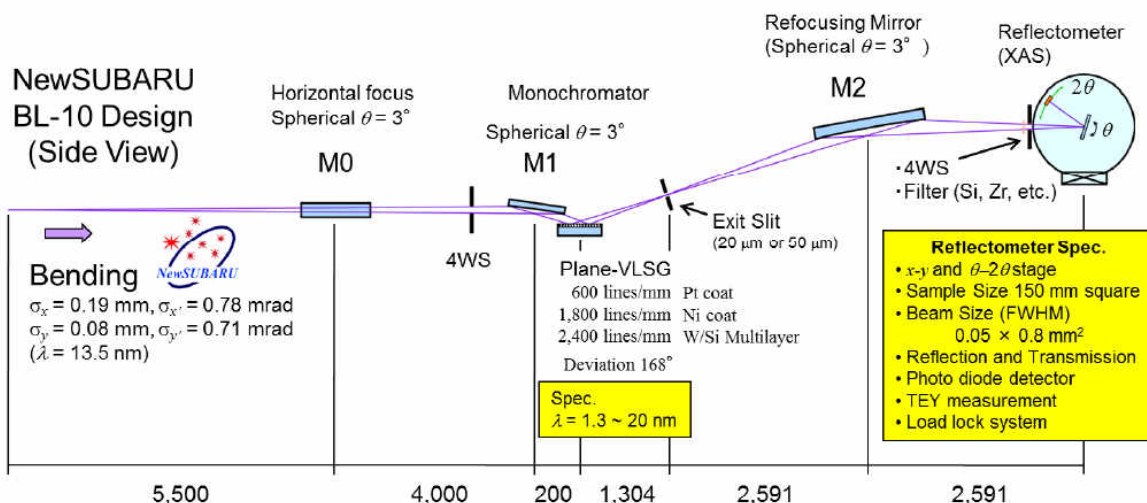


Fig. 2. Concept of reflectivity measurement system in BL-10.

photoresists for EUV we investigated are the main chain scission type resist, chemically amplified resist, and metal resist.

2. Experiment equipment

An overview of the reflection measurement system [9] in BL10 of the NewSUBARU Synchrotron Radiation Facility is provided in Figures 1 and 2. SR light emitted from a deflection magnet is monochromatized by a grating spectroscop to obtain EUV light with a wavelength of 13 to 14 nm. By arranging a 250 nm-thick silicone filter downstream of the grating, it is possible to irradiate the sample with EUV light.

Specifically, irradiated light is focused on the slit through the plane-VLSG by means of the M0 mirror horizontally and the M1 mirror vertically, and then focused horizontally and vertically on the measurement point in the chamber by means of the

M2 mirror. The radiated light is then monochromatized into EUV light by this system and made usable for the experiment. The size of the focused beam is 0.8 mm (H) × 0.1 mm (V).

Figure 3 shows an appearance of EUV reflectance measurement equipment. The intensity of the EUV light irradiated on the resist was measured by a photodiode.

3. Measurement principle

Figure 4 shows the measurement principle of the reflection angle and reflection intensity. A sample is placed on the rotary stage and irradiated with a 13.5 nm-wavelength beam, then the reflection intensity is measured while the reflection angle is changed. An SXUV 100 is used as the detector photodiode, and the measurement condition is an oblique incidence angle in the range of 0 to 90°. By this method, it is possible to measure the reflection spectrum at a wavelength of 13.5 nm. The

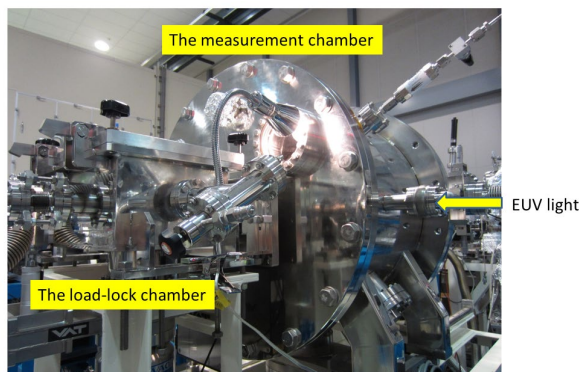


Fig. 3. Appearance of transmittance measurement system.

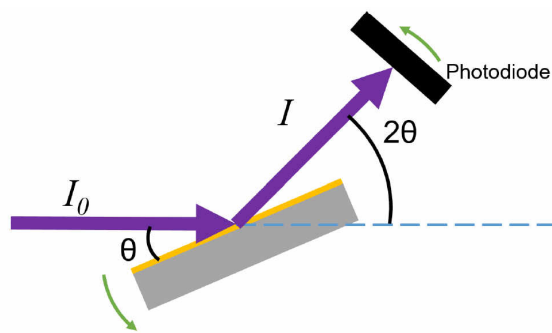


Fig. 4. Principle of reflection intensity measurement.

reflectance R can be obtained by Formula (1).

$$R = \frac{I}{I_0} \quad (1)$$

Where, I represents reflection light intensity and I_0 represents incident light intensity.

4. Experiment

We measured the refractive indexes n and k of the main chain scission type electron beam resist ZEP-520A (manufactured by Zeon Corporation), the acryl resin-based EUV resist SEVR-140 (manufactured by Shin-Etsu Chemical), and the ZrO_2 metal resist (manufactured by Litho Tech Japan) with a wavelength of 13.5 nm.

Resists were applied to Si substrates with film thickness of 25, 50, 75, and 100 nm.

The process conditions are shown in Table 1.

Figure 5 and Figure 6 show the reflection

Table 1. Film information conditions.

	Pre-bake	
	Temperature (°C)	Time (s)
ZEP-520A	180	90
SEVR-140	130	90
ZrO ₂ -MMA	110	90

spectrums of SEVR-140 and ZrO_2 -MMA resists by the reflection angles respectively.

In both measurements, we could confirm a fringe structure and obtain reflection angle spectrums. We calculated the n and k values by means of fitting. The fitting calculation to the measured spectrum was performed by IMD software program [10]. At that point, we conducted an analysis of the resist as a single-layer film, but this was not successful. Then, we employed a two-layer model, and the analysis was successful. With a two-layer model, we could observe the existence of a thin film layer with a different refractive index of 2 to 4 nm near the

SEVR-140

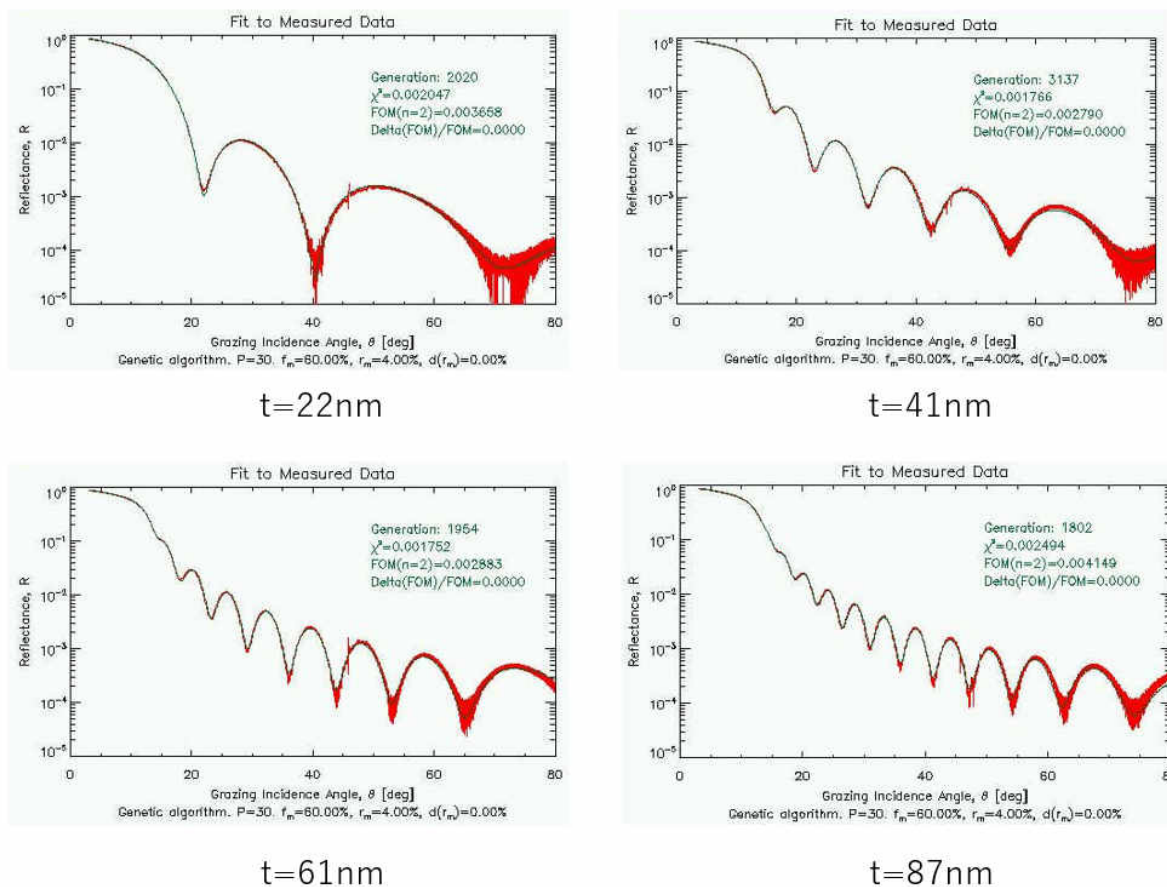


Fig. 5. Angle reflection spectrums of SEVR-140.

ZrO₂-MMA

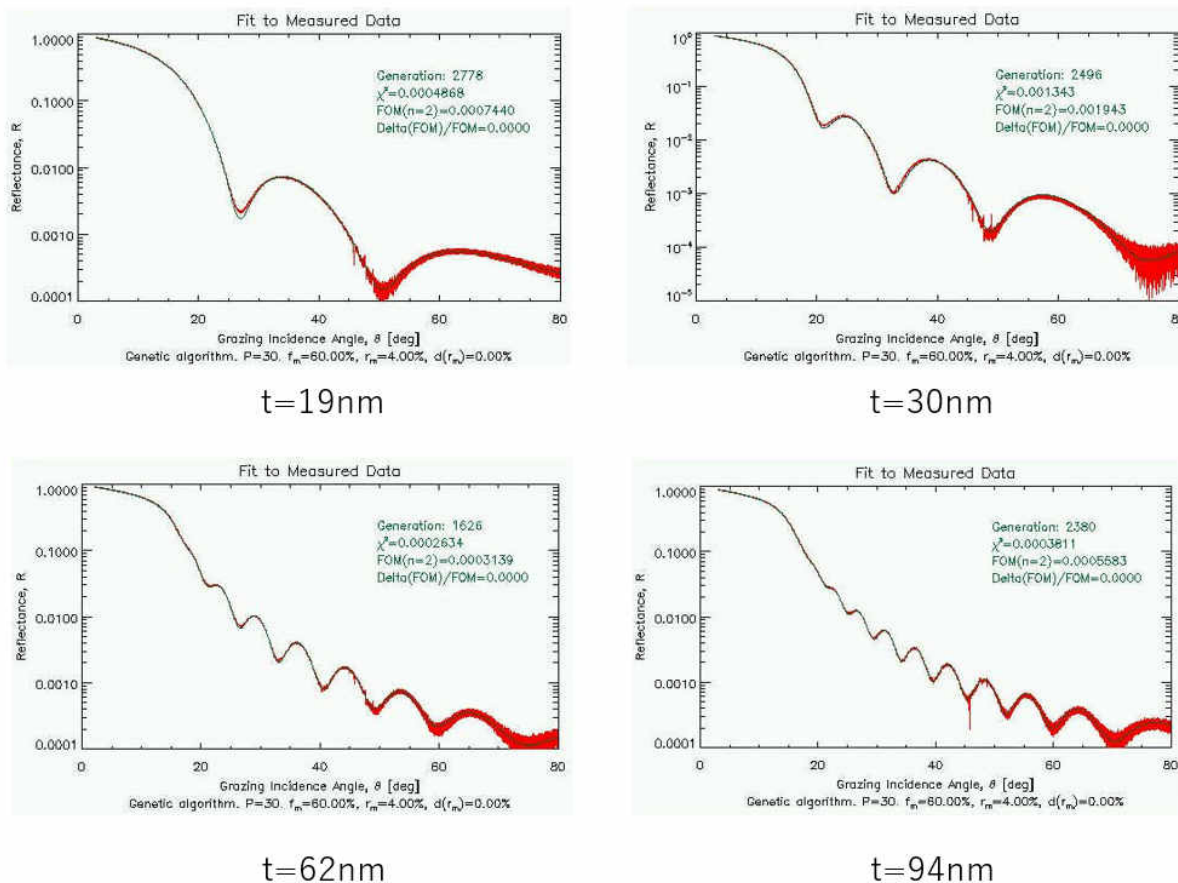


Fig. 6. Angle reflection spectrums of ZrO₂-MMA.

substrate. Figure 7 shows the relationship between the refractive index n and the film thickness in each resist.

The refractive index values n of SEVR-140 and

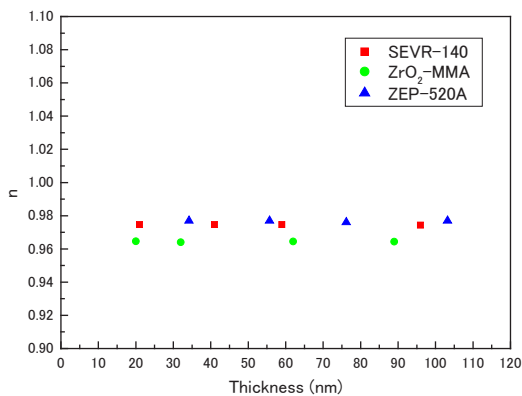


Fig. 7. Relationship between film thickness and refractive index.

ZEP-520A were similar, and the value of ZrO₂-MMA was slightly lower.

Figure 8 shows the relationship between the extinction coefficient k and the film thickness in each resist.

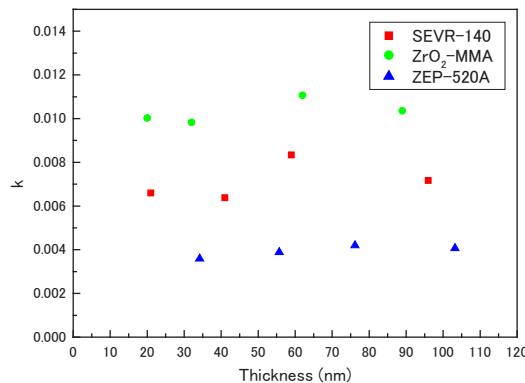


Fig. 8. Relationship between film thickness and extinction coefficient.

The extinction coefficient k was highest in ZrO₂-MMA, followed by SEVR-140 and ZEP-520A in that order. Concerning ZrO₂-MMA, it was confirmed that the refractive index n is lower compared to polymer-based resist. As metal resists generally absorb EUV light, the extinction coefficient k in ZrO₂-MMA is considered to be high [11].

5. Calculation of absorption coefficient

As the intensity of light is proportional to the square of the absolute value of the electric field amplitude, it is expressed by Formula (2).

$$I \propto |E|^2 = E_0^2 e^{-\frac{2\omega kx}{c}} \quad (2)$$

Where, ω represents angular velocity, k represents extinction coefficient, and c represents light velocity. This formula indicates that when light travels through objects, the light attenuates as it is absorbed by the objects.

The absorption coefficient is a scale which is representing the strength of absorption by an object, and the change in this strength can be expressed by the Formula (3) in accordance with Lambert-Beer's law.

$$I = I_0 e^{-\alpha x} \quad (3)$$

Where, α represents the absorption coefficient. The relationship between the absorption coefficient α and the extinction coefficient k is expressed as Formula (4) in comparison with Formulas (2) and (3).

$$\alpha = \frac{2\omega k}{c} = \frac{4\pi k}{\lambda} \quad (4)$$

Where, λ represents wavelength. The wavelength at this point is 13.5 nm. Therefore, based on the extinction coefficient k , it is possible to calculate the absorption coefficient α . At this point, when Formula (3) is deformed, it is possible to obtain Formula (5) which expresses the transmittance T .

$$T = \frac{I}{I_0} = e^{-\alpha x} \quad (5)$$

When the path length x is equal to the film thickness d , the absorption coefficient α serves as the Dill B parameter and the parameter can be generally

Table 2. Measurement results of Dill B parameter.

	B(μm ⁻¹)
SEVR-140	6.14
ZrO ₂ -MMA	9.34
ZEP-520A	3.75

expressed by Formula (6) [12-15].

$$B = -\frac{1}{d} \log T \quad (6)$$

Table 2 shows the obtained Dill B parameters of each resists. When the Dill B parameters of respective resists were compared, the parameter of ZrO₂-MMA is the highest, followed by those of SEVR-140 and ZEP-520A. This experiment also confirmed that metal resists have a higher absorption of EUV compared to polymer resists.

6. Summary

By using EUV light (13.5 nm), we measured the refractive indexes n and extinction coefficients k of resists by the reflectance measurement method. We also calculated the Dill B parameters based on the extinction coefficients.

As a result, we confirmed that the refractive index of metal resist ZrO₂-MMA is lower than that of polymer resists and also confirmed that EUV light absorption by ZrO₂-MMA is higher than that of polymer resists. This result is considered to be derived from the metal. In the future, we plan to measure n and k of metal resists containing HfO₂ and TeO₂ when EUV light is irradiated.

Acknowledgements

We gratefully acknowledge Mr. Motofumi Kashiwagi at Zeon Corporation and Mr. Jun Hatakeyama at Shin-Etsu Chemical for providing polymer materials.

References

1. A. Sekiguchi and Y. Sensu, *Proc. SPIE*, **8682** (2013) 55.
2. A. Sekiguchi, Y. Matsumoto, H. Konishi, K. Moriyasu, and Y. Morimoto, *Proc. SPIE*, **7972** (2011).
3. A. Sekiguchi, Y. Matsumoto, and J. J. Biafor, *Proc. SPIE*, **8682** (2013).
4. A. Sekiguchi and Y. Matsumoto, *Proc. SPIE*, **9051** (2014).

5. A. Sekiguchi, T. Watanabe, and H. Kinoshita, *J. Photopolym. Sci. Technol.*, **27** (2014) 623.
6. A. Sekiguchi, Y. Kono, and Y. Senu, *J. Photopolym. Sci. Technol.*, **16** (2003) 209.
7. M. Yanagihara, J. Cao, M. Yamamoto, A. Arai, S. Nakayama, T. Mizuide, and T. Namioka, *Applied Optics*, **30** (1991) 2807.
8. M. Yoshifuji, S. Niihara, T. Harada, and T. Watanabe. *Jpn. J. Appl. Phys.*, **58** (2019).
9. Y. Fukushima, T. Watanabe, T. Harada, and H. Kinoshita. *J. Photopolym. Sci. Technol.*, **22** (2009) 85.
10. T. Ishiguro, J. Tanaka, T. Harada, and T. Watanabe. *J. Photopolym. Sci. Technol.*, **32** (2019) 333.
11. B. Cardineau, R. D. Re, H. Al-Mashat, M. Marnell, M. Vockenhuber, Y. Ekinci, C. Sarma, M. Neisser, D. A. Freedman, and R. L. Brainard, *Proc. SPIE*, **9051** (2014).
12. A. Sekiguchi, T. Harada, and T. Watanabe, *Proc. SPIE*, **10143** (2017).
13. A. Sekiguchi, Y. Matsumoto, M. Isono, M. Naito, Y. Utsumi, T. Harada, and T. Watanabe, *Proc. SPIE*, **10583** (2018).
14. F. H. Dill, W. P. Hornberger, P. S. Hauge, and J. M. Shaw, *IEEE Trans. Electron Devices*, **22** (1975) 445.
15. F. H. Dill, *IEEE Trans. Electron Devices*, **22** (1975) 440.

Affinity Analysis of Photoacid Generator in the Thin Film of Chemical Amplification Resist by Contact Angle Measurement

Shinji Yamakawa^{1*}, Ako Yamamoto¹, Seiji Yasui², Takeo Watanabe¹, Tetsuo Harada¹

¹ Center for EUV Lithography, Laboratory of Advanced Science and Technology for Industry, University of Hyogo, 1-1-2 NewSUBARU, Kouto, Kamigori, Ako-gun, Hyogo 678-1205, Japan

² San-Apro Ltd., 11-1, Ikkyo Nomoto-cho, Higashiyama-ku, Kyoto 605-0995, Japan
*s.ymkw@lasti.u-hyogo.ac.jp

In extreme ultraviolet (EUV) lithography development, the reduction of line width roughness (LWR) is a one of the significant issues. It has been reported that the LWR of photoacid generator (PAG) bounded resist is lower than that of PAG blended resist. It is considered that the chemical composition distribution of PAG bounded resist is more uniform than PAG blended resist. However, it has not been evaluated systematically and experimentally. In this study, we introduced the contact angle measurement method for the evaluation of the chemical composition distribution between PAG blended resist and PAG bounded resist. It is clarified that the resist thin film has a different chemical composition distribution from the center to the outside of wafer regardless of the type of resists. In particular, the chemical composition distribution of the bounded resist showed the opposite behavior to that the blended one.

Keywords: Contact angle measurement, PAG bounded resist, PAG blended resist, Chemical amplification resist

1. Introduction

Extreme ultraviolet (EUV) lithography has been used for the production of 7-nm node semiconductor devices in 2019 and for high volume mass production of 5-nm-logic devices in 2020. However, the semiconductor industry continuously requires more advanced device nodes. The next generation EUV photoresist is needed to satisfy with half pitch of smaller than 10 nm, sensitivity of higher than 15 mJ/cm², and low line width roughness (LWR) of lower than 1 nm [1].

The origins of LWR have been considered such as photon shot noise, acid diffusion for photoacid generator (PAG) in the chemical amplification resist (CAR), and the chemical composition distribution in the resist thin film. Especially, several methods of the chemical composition distribution analysis for the resist thin film have been reported applying TOF-SIMS analysis [2-6], MC-SIMS [7], and the resonant soft X-ray scattering (RSoXS) [8, 9]. In these reports, it has been considered that the chemical composition distribution of the resist thin film is not uniform in the nano-scale. However, the

consideration of the photoresist design satisfied with low-LWR has not been achieved yet.

Generally, it is known that there are two types of the CARs, such as PAG-blended resist (blend resist) and PAG-bounded resist (bound resist). The blend resist is a mixture of the base-resin (polymer or molecule), PAG, and amine additive in the solvent. On the other hands, the bound resist is not a mixture, because the PAG unit is contained in the base polymer. The difference of the blend and bound resists has been reported by many researchers [10-18], and especially, Watanabe et al. have reported that the bound resist is more less line edge roughness (LER) than blend resist [11]. The reason of low LER for bound resist is expected that the uniformity of bound resist is better than blend one, however, the chemical composition distribution analysis has not been evaluated.

Thus, this paper is proposed that a method of the contact angle measurement for the composition distribution of the bound resist and the blend resist thin films on the silicon wafer. The base polymer used in positive-tone CARs mainly has hydroxy

and the degree of introduction of PAG group in the polymer was calculated from the ¹H NMR peak area ratio using the following eq (1), and (2).

$$[\text{PHS unit}] / ([\text{PHS unit}] + [\text{TBA unit}]) = (\text{phenyl} / 4) / [(\text{phenyl} / 4) + \{\text{alkyl} - (\text{phenyl} / 4) \times 3\} / 12] \quad (1)$$

$$[\text{PAG unit}] = \text{PAG} / 18 \times [\text{PHS unit}] \quad (2)$$

The signals and their positions are as follows: ¹H NMR: δ 8.19-7.39 (PAG), 7.20-6.06 (phenyl) and 2.05-0.0 (alkyl); ¹⁹F {¹H} NMR: δ -77.7 (CF₃).

2.4. Photo resist thin layer coating on the silicon wafer

The resist solutions were filtered through a 0.22 μm PTFE syringe filter prior to spin-coating on silicon wafers which were treated by the adhesion process by HMDS. Spin-coating was performed at 3000 rpm for 30 s to form HMDS thin films on silicon wafers. Then these spin-coated films were prebaked at 130 °C for 90 s. Then, the solutions of sample #1-6 in PGMEA and sample #7 in γ-butyl lactone were spin-coated on the silicon wafer to prepare corresponding thin films. Spin-coating was performed at 2500 rpm for 45 s to form thin films on silicon wafers. Then these spin-coated films were prebaked at 110 °C for 60 s. The resist thickness was measured by the optical-interference-type film thickness measurement tool (NanoSpec6100, NANO metrics Inc.).

The average film thickness and the degree of introduction (DI) of PAG (mol%) in each of the prepared samples show in Table 2.

Table 2. Summary of prepared resist samples.

Sample	Thickness (nm)	PAG structure	DI of PAG (mol%)	Resist type
1	41	-	0	Polymer
2	45	PAG-1	2.2	Blended
3	45	PAG-1	4.3	Blended
4	43	PAG-2	2.2	Blended
5	43	PAG-3	2.2	Blended
6	43	PAG-4	2.2	Blended
7	22	PAG-5	5.2	Bounded

2.5. Contact angle measurement on the resist thin layer surface

The contact angle was measured by the sessile

drop method. The measurement points on a 4 inch silicon wafer show in Fig. 1 (blue dot). Ultrapure water (18.2 MΩ) was used as a measurement solvent, and the liquid volume was 2.0 μl (the liquid diameter was calculated 1.6 mm when contact angle = 90 °). The θ/2 method was used to calculate the contact angle. The droplet images were captured 10 s after dripping. The average value and standard deviation of the measured values at each distance (0, 20, 40 mm) from a wafer center were calculated and plotted.

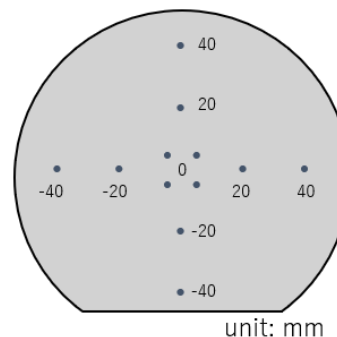


Fig. 1. Measurement points (blue dots) of the contact angle on a silicon wafer.

3. Results and discussion

3.1. Introduction of PAG-5 into base polymer (synthesis of bound resist)

The reaction of PHS-TBA with PAG-5 was carried out using EDC · HCl as a condensation reagent under DMAP as a base catalyst at r.t. for 22 h, obtaining the polymer with $M_n = 4,500$ ($M_w/M_n = 1.88$) at 79% yield. The DI of PAG-5 as calculated by ¹H NMR spectroscopy was found to be 5.2 mol%. Obtained polymer having PAG was poorly dissolved in PGMEA, acetonitrile, and diethyl ether, however, dissolved in γ-butyllactone, THF, and DMSO. Thus, γ-butyllactone was chosen as solvent for the preparation of resist thin film.

3.2. Contact angle measurement of samples with different DI of PAG.

Figure 2-a) summarizes the results of contact angle measurement of samples #1-3 with different DI of PAG. The horizontal axis and the vertical axis show the distance from the center of silicon wafer and the contact angle of droplet, respectively. The contact angle on polymer sample #1 (black triangle) is $79.8 \pm 1.5^\circ$ in the vicinity of the center. However, the case of the blend resists sample #2 (red circle), and #3 (brown circle) are $81.3 \pm 1.4^\circ$ and $83.3 \pm 1.6^\circ$, respectively. As the results, it indicates that blend resists are more hydrophobic than polymer without PAG. PHS-TBA as a base polymer has hydroxy groups derived from hydroxystyrene unit.

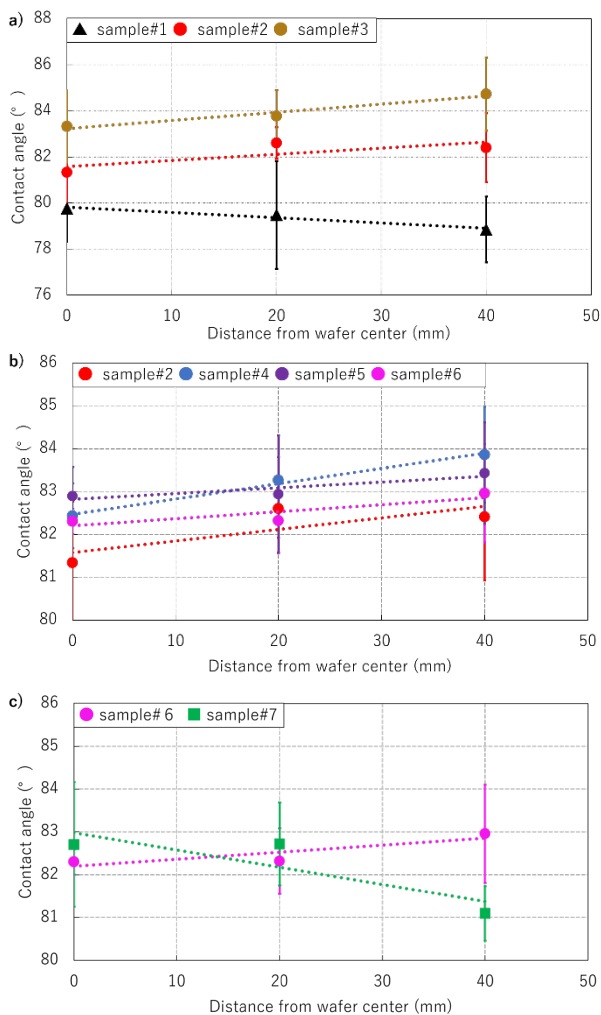


Fig. 2. Contact angle results of sample resists of a) sample #1-3, b) sample #2, and #4-6, and c) sample #6 and #7. Polymer (▲), blend resist (●), and bound resist(■).

However, PAG is without hydroxy groups. Therefore, it is considered that the reason of the increasing of hydrophobicity on the blend resist thin film is derived from PAG.

Interestingly, comparison of the contact angle between the center and the outside of the wafer, the contact angle tended to be smaller in polymer without PAG and larger in blend resist. Kawai *et al.* measured the refractive index and contact angle of resist thin films composed of novolak resin and naphthoquinone diazide after the spin coating, and it is reported that the refractive index and contact angle increased as the amount of residual solvent in the thin film decreased [19, 20]. Furthermore, the refractive index and the contact angle increase from the center to the outside of the silicon wafer. Therefore, it was considered that the difference in the amount of residual solvent was caused by the difference in the drying speed of the solvent between the center and the outside of the wafer.

Actually, the contact angle of the blend resist increased from the center of the wafer to the outside in our results too. However, the result of polymer without PAG showed opposite behavior as shown Fig. 2-a). As the results, it means that the contact angle behavior changes between presence and absence of PAG. It is suggested that the differences in hydrophobicity between PAG and polymer caused by the differences in the distribution of contact angles on the resist thin film surface.

3.3. Contact angle measurement of samples with different PAG structure.

Next, the effect of the difference of PAG structures was evaluated. The contact angle measurement results of blend resists with different PAG structures are summarized as shown in Fig. 2-b). The contact angle of each samples increased from the center of the wafer to the outside. Focusing on the structure of the cations, samples #2 and 4 (blue circle) using PAG having three phenyl groups had an approximate curve slope of 0.02 °/mm or larger. On the other hand, the slopes of the approximate curves of samples #5 (purple circle) and 6 (pink circle) using PAG having four phenyl groups were relatively small to be 0.013 °/mm to 0.016 °/mm, respectively. Furthermore, when focusing on the structure of the anion, it was shown that the slope of the approximate curve of $C_4F_9SO_3^-$ (samples #2, 5) tends to be smaller than that of $CF_3SO_3^-$ (samples #4, 6). As the results, it means that the chemical composition of the surface also changes depending on the structure of cations and anions of PAG, and it is considered that it is affected by the difference in molecular size or hydrophobicity of PAG. In other words, the chemical composition of the thin film surface can be adjusted by the structure of PAG. Since the chemical composition of the thin film surface is more uniform as the slope of the approximate curve is smaller, it is predicted that sample #5 has the most uniform chemical composition in samples #2, 4, 5, and 6.

3.4. The comparison of the contact angle between a blend resist and a bound resist.

In the above, the blend resist was mainly described however, the comparison with the bound resist will be explained below. Fig. 2-c) shows the comparison results of the blend resist sample #6 and the bound resist sample #7 (green square), which have the same cation and anion of PAG structure. Surprisingly, the contact angle of sample #7 did not increase from the center of the wafer to outside, which is different behavior of sample #6. This difference indicates the resist type introducing PAG

into the base polymer affects the chemical composition on the resist thin film surface. This is significant result suggesting that the chemical composition distribution of the blend resist and the bound resist are different.

4. Conclusion

In this paper, we evaluated the effects of differences in PAG structure, the types of resist on the thin film surface on the chemical composition distribution using the contact angle measurement method. The contact angle behavior of the blend resists increased from the center of the wafer to the outside. The chemical composition of the surface changes depending on the structure of cations and anions of PAG. The contact angle behavior of the base polymer and the bound resist decreased from the center of the wafer toward the outside. It is clarified that the resist thin film has different chemical composition distributions from the center to the outside of wafer regardless of the type of resists. Especially, the difference behavior of the contact angles between blend resists and bound resist are significant to understand the differences in LWR performance. In the future, we will measure the LWR of blend resists and bound resists after EB or EUV exposure to examine the correlation with the uniformity.

References

1. K. Ronse, *International Symposium on Extreme Ultraviolet Lithography* (2018) Closing remarks.
2. N. Man, H. Okumura, H. Oizumi, N. Nagai, H. Seki, and I. Nishiyama, *Appl. Surf. Sci.*, **231** (2004) 353.
3. T. Hirayama, D. Shiono, S. Matsumaru, T. Ogata, H. Hada, J. Onodera, T. Arai, T. Sakamizu, A. Yamaguchi, H. Shiraishi, H. Fukuda, and M. Ueda, *Jpn. J. Appl. Phys.*, **44** (2005) 5484.
4. T. Hirayama, D. Shiono, J. Onodera, A. Yamaguchi, and H. Fukuda, *Polym. Adv. Technol.*, **17** (2006) 116.
5. T. Hagiwara, T. Ishibashi, M. Terai, T. Kumada, N. Shirota, O. Yokokoji, T. Matsunobe, N. Man, K. Yoshikawa, Y. Tanahashi, and T. Hanawa, *J. Photopolym. Sci. Technol.*, **21** (2008) 647.
6. N. Man, A. Sekiguchi, and Y. Matsumoto, *Proc. of SPIE*, **9425** (2015) 94251H-1.
7. X. Hou, M. Li, M. J. Eller, S. V. Verkhoturov, E. A. Schweikert, and P. Trefonas, *J. Micro/Nanolith. MEMS MOEMS*, **18** (2019) 033502.
8. J. Tanaka, T. Ishiguro, T. Harada, and T. Watanabe, *J. Photopolym. Sci. Technol.*, **32** (2019) 327.
9. J. Tanaka, T. Ishiguro, T. Harada, and T. Watanabe, *J. Photopolym. Sci. Technol.*, **33** (2020) 491.
10. M. D. Stewart, H. V. Tran, G. M. Schmid, T. B. Stachowiak, D. J. Becker, and C. G. Willson, *J. Vac. Sci. Technol. B*, **20** (2002) 2946.
11. M. Thiagarajan, K. Dean, and K. E. Gonsalves, *J. Photopolym. Sci. Technol.*, **18** (2005) 737.
12. T. Watanabe, Y. Fukushima, H. Shiotani, M. Hayakawa, S. Ogi, Y. Endo, T. Yamanaka, S. Yusa, and H. Kinoshita, *J. Photopolym. Sci. Technol.*, **19** (2006) 521.
13. M. Wang, N. D. Jarnagin, C. T. Lee, C. L. Henderson, W. Yueh, J. M. Roberts, and K. E. Gonsalves, *J. Mater. Chem.*, **16** (2006) 3701.
14. Y. Fukushima, T. Watanabe, R. Ohnishi, H. Kinoshita, H. Shiotani, S. Suzuki, M. Hayakawa, Y. Endo, T. Yamanaka, and S. Yusa, *J. Photopolym. Sci. Technol.*, **20** (2007) 419.
15. R. D. Allen, P. J. Brock, Y.-H. Na, M. H. Sherwood, H. D. Truong, G. M. Wallraff, M. Fujiwara, and K. Maeda, *J. Photopolym. Sci. Technol.*, **22** (2009) 25.
16. S. Tarutani, H. Tamaoki, H. Tsubaki, T. Takahashi, H. Takizawa, and H. Takahashi, *J. Photopolym. Sci. Technol.*, **24** (2011) 185.
17. H. Yamamoto, T. Kozawa, and S. Tagawa, *J. Photopolym. Sci. Technol.*, **25** (2012) 693.
18. H. Yamamoto, T. Kozawa, and S. Tagawa, *Proc. SPIE*, **8682**, (2013) 86821B-2.
19. K. Nagata, and A. Kawai, *J. Adhesion Soc. of Jpn (in Japanese)*, **31** (1995) 187.
20. Web site of laboratory of Kawai group, <http://kawai.nagaokaut.ac.jp/miniseminar1.htm>

Polymerizable Olefins Groups in Antimony EUV Photoresists

Michael Murphy, Nitinkumar S. Upadhyay, Munsaf Ali, James Passarelli, Jodi Grzeskowiak, Maximillian Weires, and Robert L. Brainard*

College of Nanoscale Science and Engineering, SUNY Polytechnic Institute,
Albany, NY 12203

*rbrainard@sunypoly.edu

Many antimony-carboxylate complexes containing polymerizable olefins are highly sensitive EUV photoresists. Herein we report two approaches by which we explored the reactivity of polymerizable olefin antimony carboxylate photoresists to improve lithographic performance. First, we explored the effect of replacing three phenyl groups with methyl groups in an effort to increase the relative concentration of olefins vs. size of the molecule. Second, we explored the effect of increasing the number of polymerizable olefins from two to five. This approach examines the use of tris(4-vinylphenyl)antimony-dicarboxylate complexes as photoresists and the developer chemistry capable of patterning highly crosslinked substrates.

Key Words: EUV, Photoresist, Antimony, Carboxylate, Olefin, Crosslinked.

1. Introduction

To achieve the best possible resolution, line-edge roughness (LER) and sensitivity, many groups around the world are developing EUV photoresists containing elements in the periodic table that strongly absorb EUV light [1-15]. Our group has developed multiple organometallic resist platforms including metals such as platinum, palladium, cobalt, bismuth, antimony and tin [4-8]. We have developed palladium oxalates that exhibit positive-tone imaging, developed tin carboxylates that exhibit very low line-edge roughness, and developed antimony-carboxylates that exhibit excellent photospeed [4-8].

Two of the first antimony resists developed by our group were triphenylantimonydiacrylate (**JP-20**) and triphenylantimonybis(4-vinylbenzoate) (**JP-30**) [7]. Upon exposure to EUV light, **JP-20** produces contrast curves with high photosensitivity and high contrast (Figure 1A). This resist also resolves negative-tone dense-line patterns down to 16-nm half-pitch at very low doses using either hexanes or water as developers (Figure 1B).

Unfortunately, however, the dense-line patterns of **JP-20** are very sensitive to SEM electrons (~1 keV) such that the dense lines evaporate after two scans. **JP-30** is also a fairly sensitive photoresist, but it is not quite as sensitive as **JP-20**. It provides contrast curves exhibiting high speed and high contrast, and prints dense-line patterns with resolution down to 22 nm (Figure 2). Unlike **JP-20**, however, **JP-30** is very stable in the SEM.

JP-20 and **JP-30** demonstrate a performance trade-off. Both compounds contain two olefins, but vary greatly in molecular weight and carbon content. The smaller **JP-20** is faster, but evaporates quickly in the SEM; the larger **JP-30** is about three times slower, but is perfectly stable in the SEM. Additional work by our group demonstrated a strong correlation between the sensitivity of olefin-containing antimony resists and the relative concentrations of olefins in the compound, known as the Polymerizable Olefin Loading (POL) [7]. The POL value is equal to the number of polymerizable olefins in a molecule divided by the number of atoms excluding hydrogen.

In this paper, we explored the extremes of our sensitivity/POL correlation using two approaches. First, we increased the relative olefin concentration (POL) in the resists by replacing the three aromatic groups bound directly to antimony with methyl groups. Second, we increased the number of olefins from two to five (Figure 3).

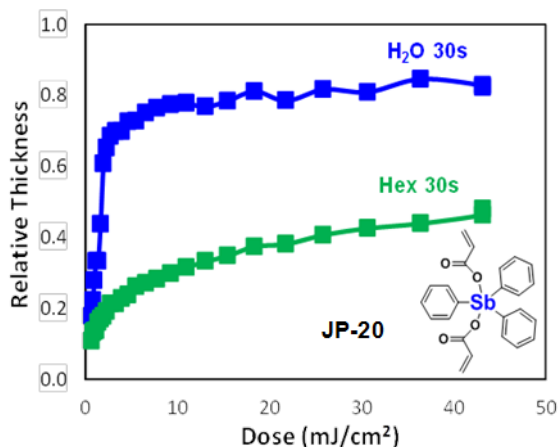


Fig. 1. Contrast curves of *JP-20* developed in water and in hexanes. The patterning capabilities of *JP-20* developed in hexanes and water. High resolution was achieved with exceptional photosensitivity although pattern collapse dominated below 30-nm half-pitch.

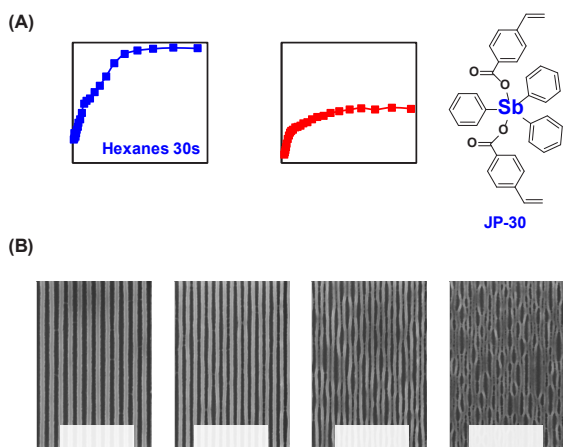


Fig. 2. (A) Contrast curves of triphenylantimony-(4-vinylbenzoate)₂ (*JP-30*) developed thirty seconds in hexanes and one hundred eighty seconds in H₂O. (B) Dense pattern imaging of *JP-30* (“h/p” means half-pitch) [17].

2. Experimental

2.1. General

1, 2-dichloroethane, hexanes, toluene, propylene glycol monomethyl ether acetate, dichloromethane, 2-butanone and hexanoic acid

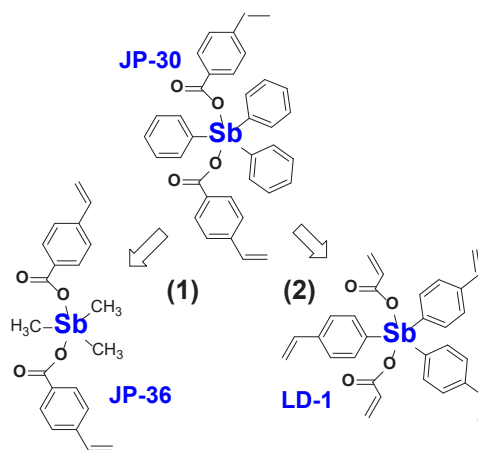


Fig. 3. Two strategies were explored to improve upon the performance vs. *JP-30*: (1) Enhance photoreactivity by decreasing the size of the R group. (2) Increase the number of olefins/molecule.

were purchased from Sigma Aldrich and used without further purification. 0.26 N Tetramethylammonium hydroxide, water and 2-propanol were provided by the facility where the exposures were performed.

2.2. Photoresist Formulation & Coating

All photoresist films were formulated at 1.5-2 wt.% solids in 1,2-dichloroethane. Once solubilized the formulations were filtered through 0.45 μm PTFE filters and spincoated onto 4-inch silicon wafers, precoated with an adhesion-promoting film (crosslinked hydroxyethyl methacrylate/methyl methacrylate copolymers). The spin conditions were 2000 rpm for 45 seconds. No pre- or post-exposure bakes were performed unless specified.

2.3. Instruments

Film thicknesses were measured using a J. A. Woollam M-2000 fixed angle ellipsometer equipped with Complete Ease software. The thicknesses were fitted using a Cauchy model for the photoresist and underlayer. The dense line patterning exposures were characterized by a LEO 1550 SEM and a Zeiss Supra 55VP at 1–2 keV accelerating voltage using an in-lens detector.

2.4. PSI XIL-II EUV Interference Lithography Beamline

EUV exposures performed at the Paul Scherrer Institut XIL-II beamline. 13.5 nm light was generated by an undulator synchrotron source and illuminated the photoresist samples as a spatially-coherent beam of EUV light. Contrast curve samples were composed of twenty-five exposures

through a 1.7 mm x 1.7 mm open frame in a serpentine pattern with an index dose for reference. High resolution periodic features were patterned on photoresists by interference lithography exposures using suspended silicon nitride membranes patterned by electron beam lithography. Periodic images were created on the photoresist film by interference of two or more diffracted coherent beams [16]. The aerial image produced with first-order diffracted beams is half the period of the original mask grating period. Our interference exposures used a photomask capable of printing 50-, 40-, 30- and 22-nm half-pitch dense lines. Review of recent advances in inorganic photoresists.

3. Results and Discussion

3.1. $(\text{CH}_3)_3\text{Sb}(\text{O}_2\text{CR}')_2$ Photoresists

To increase the olefin concentration and the EUV optical density of our mononuclear antimony resists, we explored the possibility of replacing the phenyls in compounds such as *JP-20* and *JP-30* with smaller alkyl groups (R). Thus, we synthesized a series of $\text{R}_3\text{Sb}(\text{O}_2\text{CR}')_2$ photoresists and lithographically evaluated each to observe their performance relative to $(\text{C}_6\text{H}_5)_3\text{Sb}(\text{O}_2\text{CR}')_2$ photoresists. The change from aromatic R-groups to alkyl groups such as methyl, ethyl and isopropyl resulted in $\text{R}_3\text{Sb}(\text{O}_2\text{CR}')_2$ complexes that were nonvolatile as bulk solids but too volatile as thin films. $(\text{CH}_3)_3\text{Sb}(\text{O}_2\text{CR}')_2$ compounds where $\text{R}' = -\text{CH}_3$, $-\text{C}(\text{CH}_3)_3$, $-\text{CHCH}_2$ or $-(\text{CH}_2)_4\text{CH}_3$ all lost considerable film thicknesses at ambient pressure and almost instantaneously lost all film thickness under vacuum. The only way to compensate for this volatility problem was to use large carboxylate ligands such as benzoate or its derivatives. We found that trimethylantimonybis(4-vinylbenzoate) (*JP-36*) can be coated into an amorphous film that does not evaporate under vacuum.

Trimethylantimonybis(4-vinylbenzoate) (*JP-36*) has fifteen fewer carbon atoms than *JP-30* and based on our POL sensitivity correlation was predicted to have an $E_{\text{max}} < 2 \text{ mJ/cm}^2$ [6, 18]. However, contrast curves of *JP-36* show the E_{max} (dose to achieve maximum thickness) to be about 40-50 mJ/cm^2 (Figure 4A). This result is in direct contradiction to the POL correlation and points to an important role played by the aromatic groups that are bound directly to antimony in the EUV exposure mechanism.

The methyl R-groups improve dissolution selectivity over phenyl ligands. *JP-36* can be successfully developed in H_2O , hexanes and PMA

with all developments exhibiting similar contrast and minimal top-loss. $(\text{C}_6\text{H}_5)_3\text{Sb}(\text{O}_2\text{CR}')_2$ photoresists do not have similar performance when developed in hexanes vs. water, and most have no dissolution contrast in more aggressive organic solvents such as PMA. *JP-36* resolves patterns down to 30-nm half-pitch with minimum pattern collapse when developed for forty-five seconds in hexanes (Figure 4B). Characterization by SEM of *JP-36* had no pattern degradation even with the large reduction in carbon-content relative to *JP-30*. This result further illustrates that the carboxylate ligand plays a significant role in the photoresists stability.

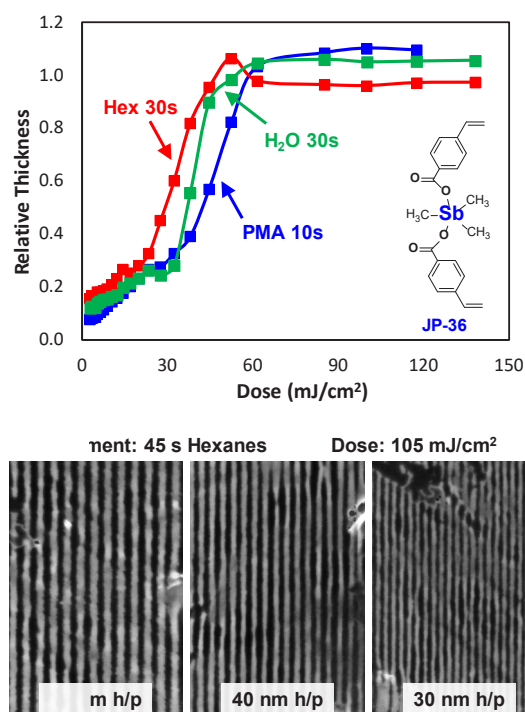


Fig. 4. (A) Contrast curves of *JP-36* developed in various solvents. All three development conditions provide similar sensitivity and contrast unlike that seen for $(\text{C}_6\text{H}_5)_3\text{Sb}(\text{O}_2\text{CR}')_2$ photoresists. (B) Dense line patterning of *JP-36* developed in hexanes [17]. The dose to pattern does not follow the POL sensitivity trend suggesting the R-group composition plays a significant role in the FRP mechanism.

3.2. Increasing Olefin Content

To explore the capability of resists with 3-5 olefins/molecule, we made molecules in which the phenyls that are bound to antimony are replaced by styrene [15]. A series of $(4-\text{C}_8\text{H}_7)_3\text{Sb}(\text{O}_2\text{CR}')_2$ photoresists were synthesized ranging in olefin content from three to five per molecule. Unfortunately, unexposed thin films of

tristyreneantimony-dibenzoate (**JP-41**) and tristyreneantimonydiacrylate (**LD-1**), with three and five olefins respectively, cannot be dissolved in water, hexanes or PMA after contrast-curve exposures (Figure 5). A wide range of organic and alcohol developers were tested on additional contrast-curve samples without success. Our hypothesis is that the increase in olefins allow for uncontrolled polymerization to occur into the unexposed regions of the film preventing dissolution in standard solvents.

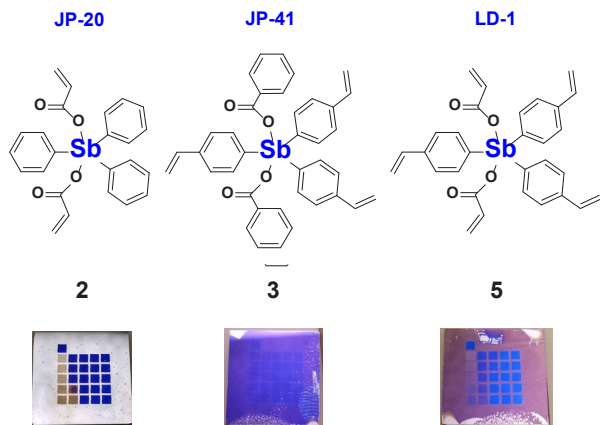


Fig. 5. Photographs of contrast-curve samples for three resists. Dicarboxylate complexes (e.g. **JP-20**) upon development in hexanes solution fully develop away the unexposed regions. Tristyreneantimony-dicarboxylate complexes containing three–five olefins do not develop in hexanes solution presumably due to enhanced cross-linking interactions. More reactive developer solutions were required to successfully pattern these photoresists.

Reactive developers containing strong acid or base were used to successfully develop these high olefin-containing complexes. Reactive developers are well known in the IC industry with tetramethylammonium hydroxide (TMAH) being one of the most common developers [1]. In addition, previous work by our group has shown the potential for acidic developers to have dramatic changes on organometallic photoresist performance depending on the acid used [15].

The combination of highly crosslinked photoproduct and aggressive solvents provided the means to pattern dense lines down to 22-nm half-pitch with less line collapse and higher sensitivity than di-olefin photoresists (Figure 6). Fine-tuning of acid or base concentration, and the solvent may allow for even higher resolution patterning.

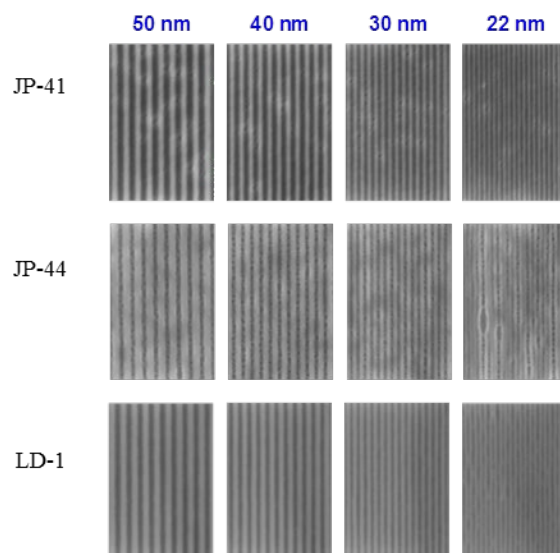


Fig. 6. A series of $(C_8H_7)_3Sb(O_2CR)_2$ photoresists and their lithographic capabilities upon development in reactive solvents [17]. Development conditions: For **JP-41**, **JP-44**; Dose: 8.2 mJ/cm²; 10% IPA in 0.26 N TMAH in 5 min with water rinse. For **LD-1**; Dose: 8.2 mJ/cm²; 10% hexanoic acid in hexanes for 45 s.

4. Conclusion

The incorporation of olefins into antimony complexes provides EUV resists with excellent photospeed. **JP-20** (triphenylantimonydiacrylate) prints dense lines with sizing doses as low as 5-9 mJ/cm², but evaporated quickly when exposed to SEM electrons. **JP-30** (triphenylantimonybis(4-vinylbenzoate)) is capable of resolving dense line patterns down to 22 nm half-pitch at moderate doses with no discernable pattern degradation during SEM characterization.

Here, we explored the limits of our POL correlation by (1) reducing the size of the ligands bound to antimony and by (2) creating antimony compounds with 3-5 olefins/molecule. We found that the replacement of phenyl groups with methyl groups produced photoresists that did not follow the sensitivity vs. olefin concentration (POL) correlation that we had established earlier. Instead, the trimethylantimony complexes were about 25 times slower than was expected. This result points to the importance of the role played by phenyl groups when bound directly to antimony in the EUV exposure mechanism.

We also found that resists prepared using three or more olefins were so fast that resist films that unexposed films could not be fully cleared using conventional developers. We found that these resist could provide good images with reactive developers were used.

Notes and References

1. R. Brainard, M. Neisser, G. Gallatin, A. Narasimhan, *SPIE Press*, 2018, Chapter 8, pp. 493.
2. J. Stowers and D. A. Keszler, *Microelectron. Eng.*, **86** (2009) 730.
3. M. Krysak, M. Trikeriotis, E. Schwartz, N. Lafferty, P. Xie, B. Smith, P. Zimmerman, W. Montgomery, E. Giannelis, and C. K. Ober, *Proc. SPIE*, **7972** (2011) 79721C.
4. M. Sortland, J. Hotalen, R. Del Re, J. Passarelli, M. Murphy, T. S. Kulmala, Y. Ekinici, M. Neisser, D. A. Freedman, and R. L. Brainard, *J. Micro. Nanolithogr. MEMS MOEMS*, **14** (2015) 043511.
5. M. Wilklow-Marnell, D. Moglia, B. Steimle, B. Cardineau, H. Al-Mashat, P. Nastasi, K. Heard, A. Aslam, R. Kaminski, M. Murphy, R. Del Re, M. Sortland, M. Vockenhuber, Y. Ekinici, R. L. Brainard, D. A. Freedman, *J. Micro/Nanolith. MEMS MOEMS*, **17** (2018) 043507.
6. J. Passarelli, M. Sortland, R. Del Re, B. Cardineau, C. Sarma, D. A. Freedman, and R. L. Brainard, *J. Photopolym. Sci. Technol.*, **27** (2014) 655.
7. J. Passarelli, M. Murphy, R. Del Re, M. Sortland, J. Hotalen, L. Dousharm, R. Fallica, Y. Ekinici, M. Neisser, D. A. Freedman, and R. L. Brainard, *J. Micro. Nanolithogr. MEMS MOEMS*, **14** (2015) 043503.
8. R. Del Re, J. Passarelli, M. Sortland, B. Cardineau, Y. Ekinici, E. Buitrago, M. Neisser, D. A. Freedman, and R. L. Brainard, *J. Micro. Nanolithogr. MEMS MOEMS*, **14** (2015) 043506.
9. M. Evans, M. Santappa, and N. Uri, *J. Photopolym. Sci. Technol.*, **7** (1951) 243.
10. M. S. Matheson, E. E. Auer, E. B. Bevilacqua, E. J. Hart, *J. Am. Chem. Soc.*, **73** (1951) 5395.
11. P. J. Flory, *J. Am. Chem. Soc.*, **59** (1937) 241.
12. M. Koton, and F. Florinskii, *Dokl. Akad. Nauk SSSR*, **169** (1966) 598.
13. J. W. Thackeray, *J. of Micro. Nanolithogr. MEMS MOEMS*, **10** (2011) 1.
14. C. Luo, C. Xu, L. Lv, H. Li, X. Huang and W. Liu, *RSC Adv.*, **10** (2020) 8385.
15. J. Hotalen, M. Murphy, W. Earley, M. Vockenhuber, Y. Ekinici, D. A. Freedman, and Robert L. Brainard, *Proc. SPIE*, **10143** (2017) 1014309.
16. E. Buitrago, T. S. Kulmala, R. Fallica, Y. Ekinici, *Front. of Nanosci.*, **11** (2016) 135.
17. All SEM images show dense-line (line/space = 1:1) patterns. Line size is shown as h/p or half-pitch.
18. The Polymerizable Olefin Loading (POL) of $(\text{CH}_3)_3\text{Sb}(\text{C}_6\text{H}_4\text{CH}=\text{CH}_2)_2$ (**JP-36**) = 100% * 2 olefins / 26 non-hydrogen atoms = 7.7%. When compared to the POL plot in Ref 6, the predicted E_{max} is $< 2 \text{ mJ/cm}^2$.

Instructions to Authors

Journal of Photopolymer Science and Technology is devoted to the publication of articles on the scientific progress and the technical development of photopolymers.

1. General Paper, Communication, Technical Paper, and Review are published.
2. All contributions should be written in English.
3. All the articles must contain an abstract and 3~6 keywords. The abstract should be a single paragraph (50~250 words) that summarizes the content of the article.
4. Communication is short submission of 4~6 pages which contain new results. The contents of Communication may be republished with more details.
5. Manuscripts should be prepared with following the Manual for Manuscript Writing.
6. The day on which the manuscript arrives at the editorial office shall be the received date.
7. The authors bear full responsibility for the content of their articles.
8. All the papers submitted are reviewed by the referee system of the Journal. The editorial board requests to revise the manuscript when the reviewer's

comments have good reason. The revised manuscript should be submitted before the deadline proposed by the editorial board.

9. To support a part of the cost of publication of journal pages, the author's institution is requested to purchase reprints.
10. The authors of manuscripts for the Journal should follow the document. Submit the manuscripts to Editorial Manager.

The Editorial Office

Haruyuki Okamura

Journal of Photopolymer Science and Technology
Department of Applied Chemistry, Osaka Prefecture
University, 1-1 Gakuen-cho, Naka-ku, Sakai, Osaka
599-8531, Japan

E-mail: okamura@chem.osakafu-u.ac.jp

11. The electronic file may be used for the electric publication of the Journal and for the direct printing process of publication. Note: In all cases the Editorial Office reserves the right to decide whether to use a manuscript from authors' files or not.

Manual for Manuscript Writing

All the papers submitted are reproduced as they are. For this reason, manuscript should be prepared according to the items given below.

Size of sheet

White A4 sheets, 210 mm × 297 mm in size, should be used for submissions, and the manuscript be clearly prepared. The total pages of manuscript are recommended to be even.

Format

Manuscript should be started from the title, author's name, affiliation, address including e-mail address, abstract, and text. The manuscript should be prepared by using a word software with the font "Times New Roman" for Windows series or "Times" for Macintosh series. The font-size and the line spacing should be set 11 point and 13 point, respectively except title (18 point and 18 point), abstract, keywords, figure and table captions (10 point and 12 point). Use the bold face for author's name and keywords, and the italic for affiliation and address including e-mail address (See Table 1). The

first letter of each important word in the title should be capitalized. Math and Equations should be written using either the Microsoft Equation Editor or the MathType commercial add-on for MS Word for all math objects in your paper. Number of equations should be placed consecutively after the equation with numbers in parentheses with the margin, as in (1). Be sure that the symbols in your equation are defined before or immediately after the equation. The example of equation (1) is shown as follows:

$$R_p = \frac{d[M]}{dt} = k_p[M](f\phi_{abs})^{0.5}k_t^{-0.5} \quad (1)$$

The word processing software recommended is MS Word which is used for the preparation of the example of manuscript. The layout of the paper is shown in Figs. 1-3. The right and left columns end in the same line.

For the separation of sections in the manuscript, use the following system,

3. Result

3.1.

3.1.1.

3.1.1.1.

All the figures and tables with captions should be pasted directly on the sheets of manuscript at the appropriate place in the text where they are cited. Do not collect them at the end of your paper.

Table 1. Font sizes, styles and line spacing.

Type size/line spacing (pts)	Regular	Bold	Italic
10/12	Abstract, figure captions, table text, figure text	Keywords	
11/13	Main text, secondary and tertiary section headings	Author's name, a primary section heading	Address and affiliation
18/18	Title of the paper		

Electronic submission

The editorial office strongly recommends the electronic submission via <https://www.editorialmanager.com/photopolymer/default.aspx> for fast publication.

The submission of files of main text (.doc or .docx), Journal Check List, and Copyright Transfer Agreement are mandatory. The files of main text (.pdf), Reprint Order Form, and supplementary information are optional. If you have any trouble in electronic submission, the contents of the Web site "<http://www.editorialmanager.jp/faqen>" will help you before the contact to the editorial office. Especially, the author should note that electronic

submission should be completed after "[Approve Submission]" action.

Conclusion

Conclusion is one of the most important parts of a paper. Please give careful consideration to this section.

References and footnotes

References and footnotes are to be indicated by Arabic numbers in brackets, []. They should be arranged in sequences and summarized at the last part of the text. All of the authors of the references should be written. The use of "et al." is not allowed because of the requirement for electronic publication. More than 20 references should be cited in a paper. Examples of references are written below.

1. T. Omote, "Polyimides", M. Ghosh, and K. L. Miital, Eds., Dekker, New York, 1996, p.121.
2. S. Hayase, K. Takano, Y. Mikogami, and Y. Nakano, *J. Electrochem. Soc.*, **138** (1979) 3625.
3. T. Omote, K. Koseki, and T. Yamaoka, *Macromolecules*, **23** (1990) 4788.
4. T. Omote, S. Hayashi, K. Ishii, K. Naito, and T. Yamaoka, *Adv. Technol.*, **4** (1993) 277.
5. D. N. Khanna and W. H. Mueller, *Polym. Eng. Sci.*, **29** (1989) 954.
6. H. Ahne, R. Rubner, and E. Kuhn, EP0023626, to Siemens, 1980.
7. R. Rubner, *Adv. Mater.*, **2** (1990) 452.
8. T. Yamaoka, N. Nakajima, K. Koseki, and Y. Maruyama, *J. Polym. Sci. Polym. Chem.*, **28** (1990) 2517.
9. H. Ahne, E. Kuhn, and R. Ruber. U.S. patent No. 4,395,482 (1985).
10. M. Ueda, K. Seki, and Y. Imai, *Macromolecules*, **15** (1982) 17.

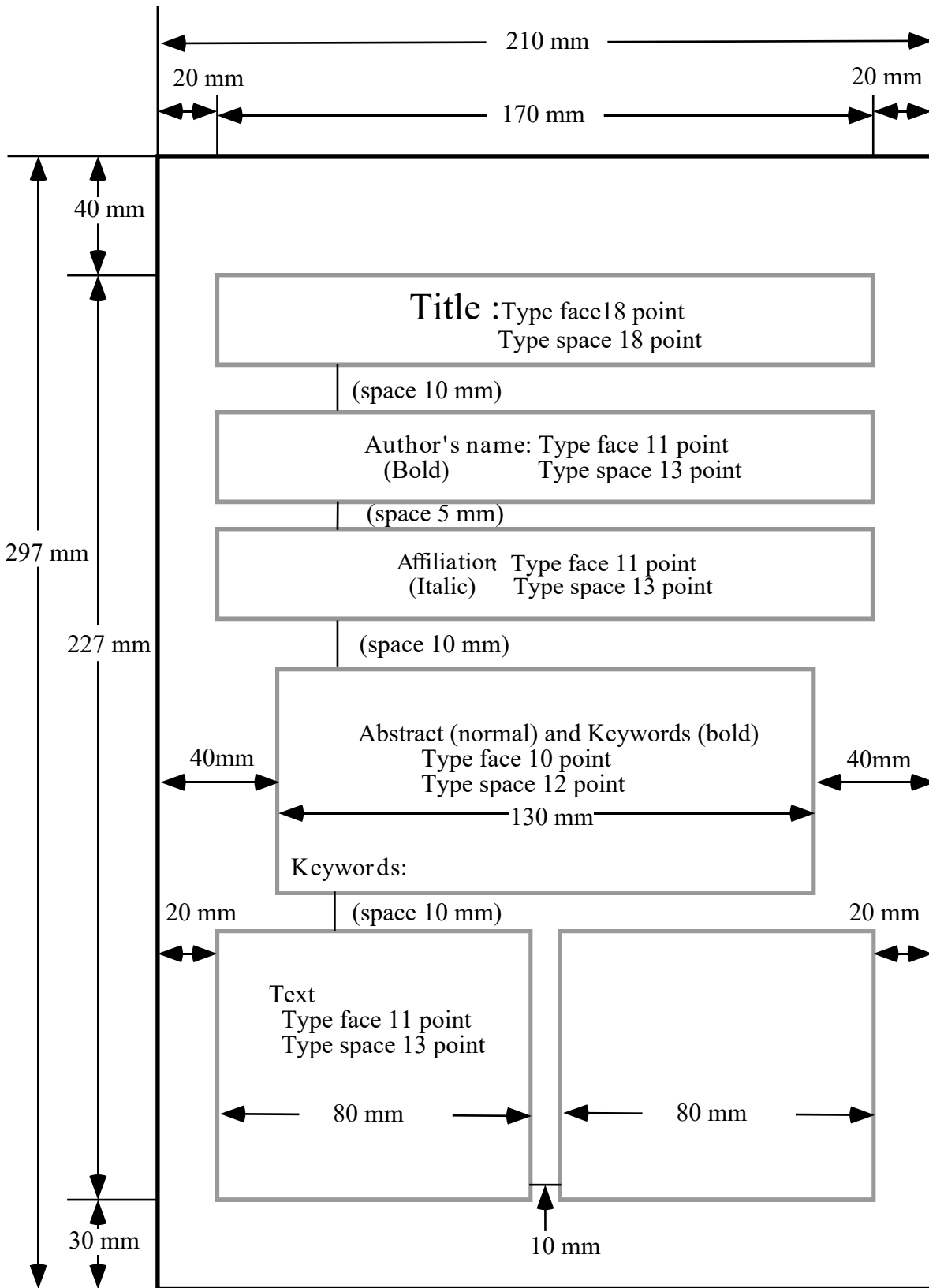


Fig. 1. The First Sheet of Manuscript. Type within the dotted block using "Times New Roman" font .

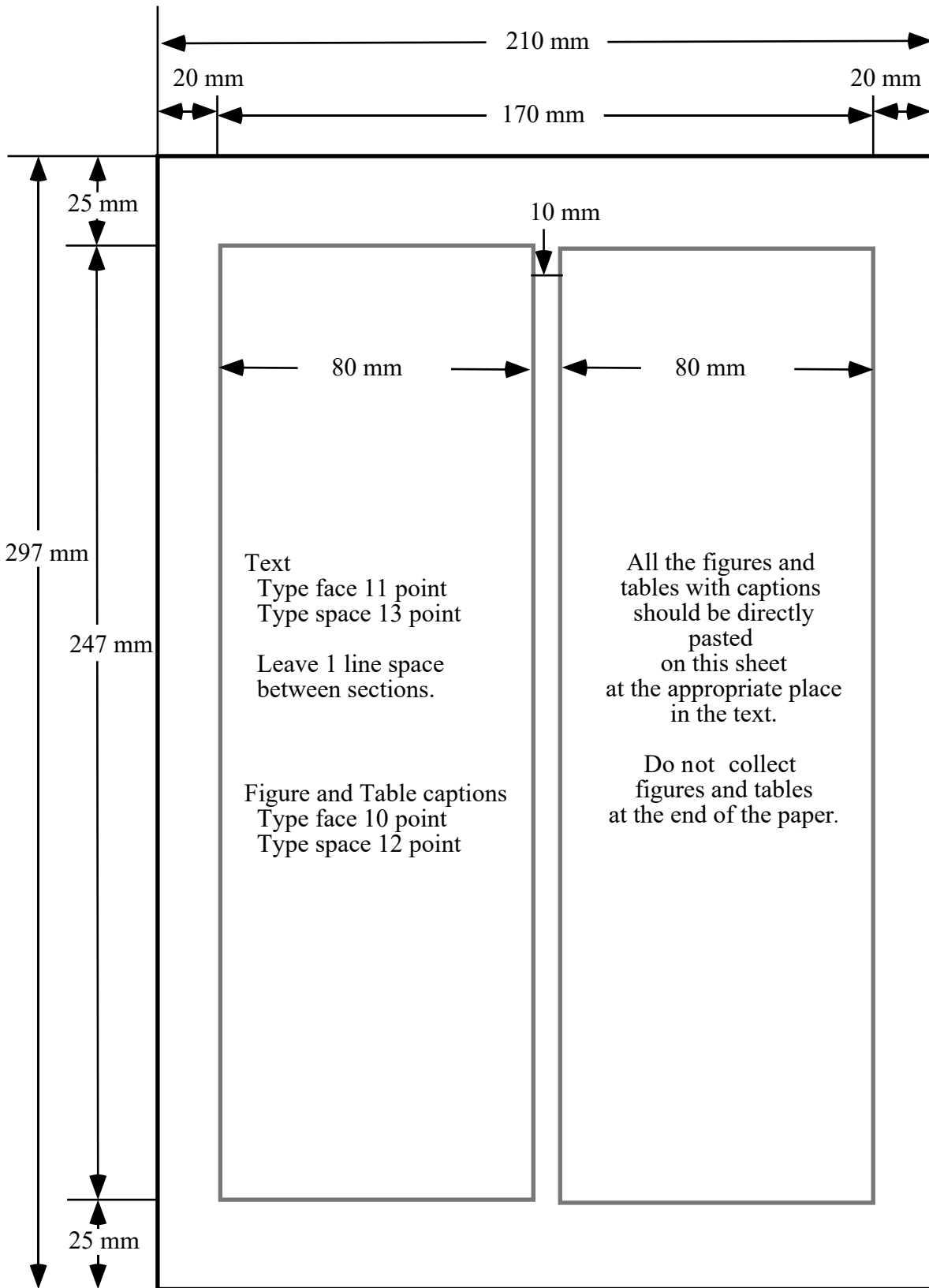


Fig. 2. Following Sheets of Manuscript

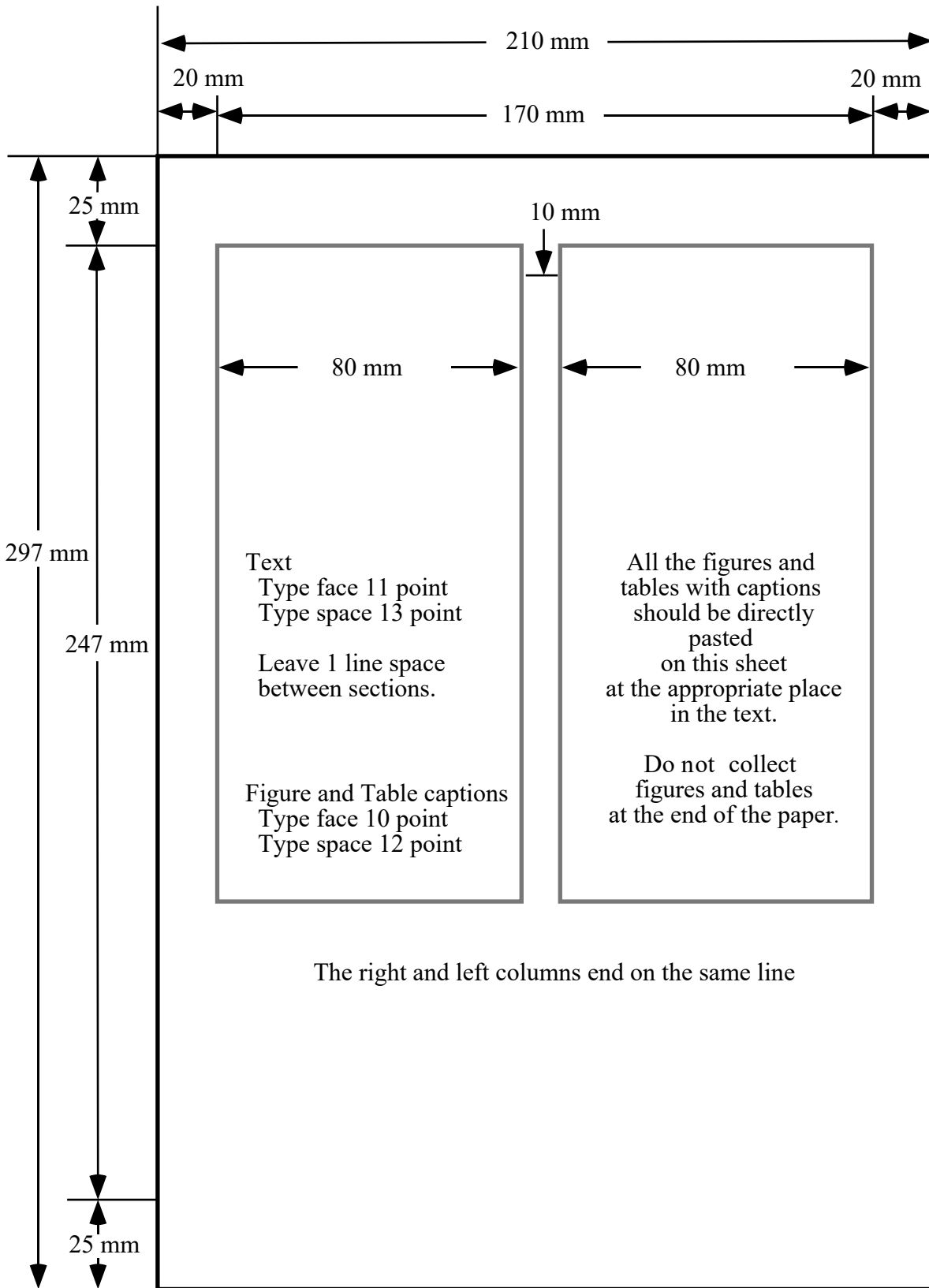


Fig. 3. Last page partly occupied

Photoresists for Screen Printing Plates with High Resolution and Sensitivity Using Thiol-ene Reaction

Haruyuki Okamura^{1*}, Keiko Muramatsu², Hideyuki Nakajiri²,
Masamitsu Shirai¹, and Akikazu Matsumoto¹

¹ Department of Applied Chemistry, Graduate School of Engineering,
Osaka Prefecture University, 1-1 Gakuen-cho, Naka-ku, Sakai, Osaka 599-8531, Japan

² Research and Development Center, Nakanuma Art Screen Co., Ltd.,
23 Uzumasa Yasui Okuhata-cho, Ukyo-ku, Kyoto 616-8082, Japan

*okamura@chem.osakafu-u.ac.jp

Photoresists for high resolution screen printing plates was devised using thiol-ene reaction. New resist formulation contains a base polymer which contains acid-labile tetrahydropyranyl-protected carboxylic acid, hydroxyl and methacrylic functions. As crosslinkers, multifunctional acrylates and multifunctional thiols were employed. Photoacid generators were used for pattern formation. A 6- μm feature size of resist on a SUS screen plate was obtained on irradiation at 365 nm and followed by development. Post-exposure curing using 254 nm light with photoradical generators improved the mechanical characteristics of the resist patterns. Addition of a multifunctional thiol compound was effective to improve flexibility of the cured resist and resist sensitivity.

Keywords: Screen printing plate, Photoresist, Thiol-ene reaction, High resolution, High sensitivity

1. Introduction

Screen printing is a promising method to fabricate small feature size patterning of circuits for the production of electronic devices in terms of not only economical but also environmental issues compared to conventional lithographic methods. In this point of view, we have developed the photoresists for screen printing plates with high resolution [1-5]. The fabrication process of the screen plates is depicted in Fig. 1. The photoresist patterns contained a base polymer, a crosslinker, a photoacid generator (PAG) [6], and a photoradical generator (PRG) [7].

In this work, high-resolution screen printing plates were devised based on the findings previously reported [1-5]. New resist formulation contains a base polymer, which consists of acid-labile tetrahydropyranyl-protected carboxylic acid, hydroxyl, and methacrylic functions. As crosslinkers, multifunctional acrylates and thiols were employed. PAGs were used for pattern formation. Curing reactions of the acrylates are strongly inhibited in the presence of oxygen. The

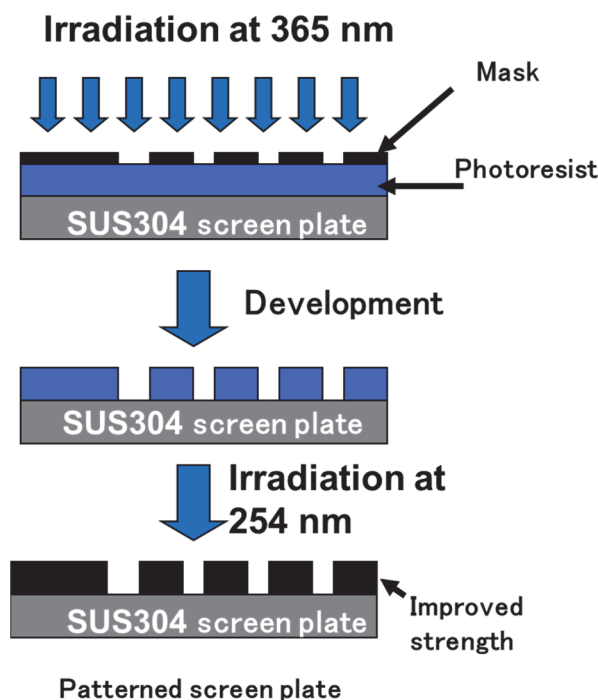
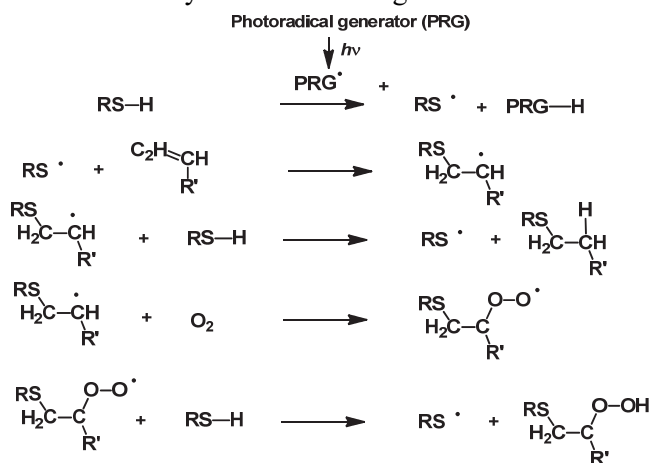


Fig. 1. Schematic illustration for the fabrication of screen plates.

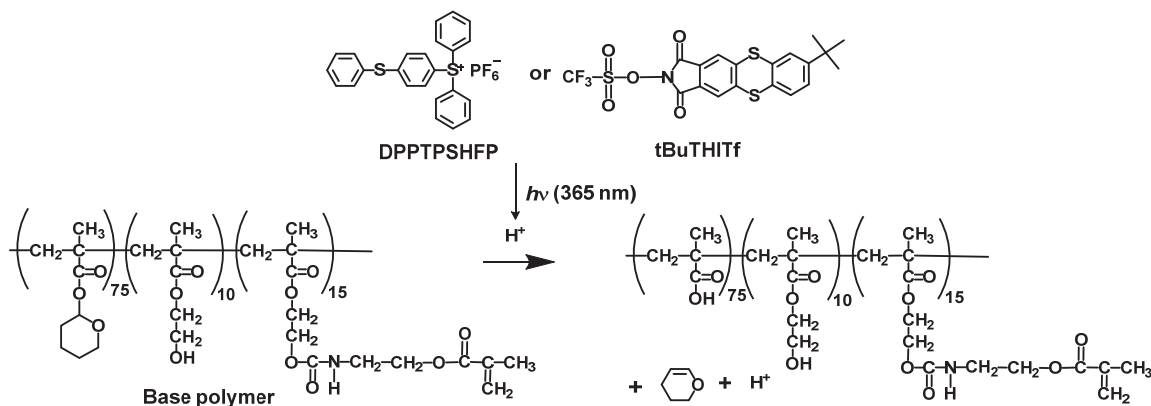
oxygen inhibition was effectively suppressed by the use of thiol-ene photocuring system due to regeneration of thiol radical in the presence of oxygen [8-10] (Scheme 1). Thus, application of thiol-ene system may afford high resist sensitivity and durability. Effect of the structures of thiol compounds on flexibility of the cured resist and resist sensitivity was also investigated.



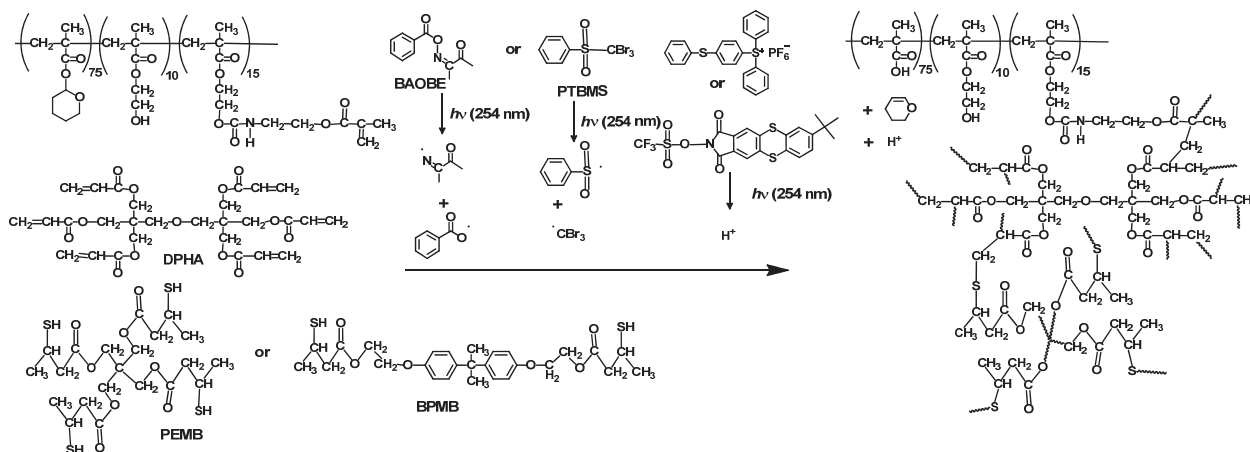
Scheme 1. Mechanism of thiol-ene reaction.

2. Experimental

The PAG diphenyl[4-(phenylthio)phenyl]sulfonium hexafluorophosphate (DPPTPSHFP) (product name: CPI-100P) (49 wt% propylene carbonate solution) was obtained from San-Apro Ltd. *N*-Trifluoromethanesulfonyloxy-7-*tert*-butylthianthrene-2,3-dicarboxylic imide (tBuTHITf) [11,12] (product name: SIN-11) was kindly donated by Sanbo Chemical Ind., Ltd. The PRG phenyl tribromomethyl sulfone (PTBMS) (Nacalai Tesque) was used as received. *O*-Benzoyl diacetone monooxime (BAOBE) [13] was prepared according to the literature. The crosslinkers DPHA (product name: A-DPH), and base polymer (product name: AP-HAR-201) were donated from Shin-Nakamura Chemical Co., Ltd. The difunctional thiol 1,1'-[(1-methylethylidene)-bis(4,1-phenylene-oxy-2,1-ethanediyl)] bis(3-mercaptopbutylate) (BPMB) and the tetrafunctional thiol pentaerythritol tetrakis(3-mercaptopbutylate) (PEMB) were obtained from Showa Denko K.K. and used as received. Chemical structures of the compounds are included in Schemes 2 and 3.



Scheme 2. Reaction mechanism of pattern formation on irradiation at 365 nm.



Scheme 3. Reaction mechanism of crosslinking on irradiated at 254 nm.

All sample films were prepared on silicon wafer by spin-casting or on poly(ethylene terephthalate) (PET) film (Cosmoshine A4100, 125 μm , Toyobo Co., Ltd.) by bar-coating from solutions of toluene containing the base polymer, the crosslinker, and a PAG and a photoradical generator. The sample films were dried on a hot plate at 90 $^{\circ}\text{C}$ for 1 min. The thickness of films was about 0.5 μm . Irradiation was performed in air at 254 nm using a low-pressure mercury lamp (Ushio ULO-6DQ, 6 W) without a filter, at 365 nm using a Xenon lamp (Asahi Spectra MAX-301, 300 W) with a band-path filter for 365 nm, and at 230-420 nm using the Xenon lamp with a mirror which passes the light below 420 nm. The intensity of the light was measured with an Orc Light Measure UV-M02 and Ushio USR-45VA. Insoluble fraction was determined by comparing the film thickness before and after dipping into 2.38 wt% tetramethylammonium hydroxide (TMAH) solution or toluene for 10 min. Thickness of films was measured by interferometry (Nanometrics Nanospec M3000). The measurement of pencil hardness goes from the lowest to the highest pencil in order to determine the maximum hardness for scratching the surface of the film on silicon wafer (Method: JIS K 5600-5-4). The hardness of the film was determined relative to a standard set of pencil leads. The surface hardness is determined by scratching the leads across the coating at a controlled angle of 45 $^{\circ}$. The pencil hardness was measured using a pencil hardness tester (Imoto Machinery Co., Ltd.) with UNI pencil series supplied by Mitsubishi Pencil (Japan). Flexibility was evaluated in a cylindrical mandrel test according to JIS K5600-5-1. This test is performed using equipment in which the film coated on a PET film is attached and bent over a 5-mm-diameter glass rod. Flexibility is evaluated observing the presence or absence of cracks or defects in the film.

UV-vis spectra were taken on a Shimadzu UV-2400 PC. The patterns of the resists were observed using a Keyence digital microscope VHX-200. Screen printing was carried out using a screen-printing machine (LZ-1232, Newlong Seimitsu Kogyo Co., Ltd).

3. Results and discussion

3.1. Strategy

We selected the protected poly(methacrylic acid) by cyclic acetal units with methacryl side chains as a base polymer. The polymer widely used as a

positive type photoresist using photoinduced-acid catalyzed deprotection of the cyclic acetal units [14] as shown in Scheme 2. Durability of the resist was improved by radical crosslinking reaction between the methacrylic group in the side chain of the base polymer and the crosslinkers with the thiol as shown in Scheme 3. Addition of thiol compounds affords the high efficiency of the crosslinking reaction.

Selection of PAG and PRG of the resists was very important in addition to the choice of light sources. We selected 365 nm-light which is emitted from a medium-pressure mercury lamp and 254 nm-light from a low-pressure mercury lamp. It is required that PRG did not affect the pattern formation by the decomposition of the PAGs on irradiation at 365 nm. Thus, the absorbance of the PRG at 365 nm must be much lower than that of PAGs on the resist formulations. Figure 2 shows the UV-vis spectra of the PAGs (DPPTPSHFP and tBuTHITf) and the PRGs (BAOBE and PTBMS) in acetonitrile. As shown in Fig. 2, the absorbance of the tBuTHITf was larger than that of DPPTPSHFP at 365 nm. The absorbance of BAOBE was larger than that of PTBMS.

On irradiation at 254 nm, the PRGs and PAGs absorb the light to form radicals [6,13,15] and acids [7,11,16-21], respectively. The produced acid promotes the deprotection reaction of tetrahydropyranyl-protected units to form 3,4-dihydro-2H-pyran, which affects not only the crosslinking reactions including thiol-ene reaction but also the mechanical properties of the resist.

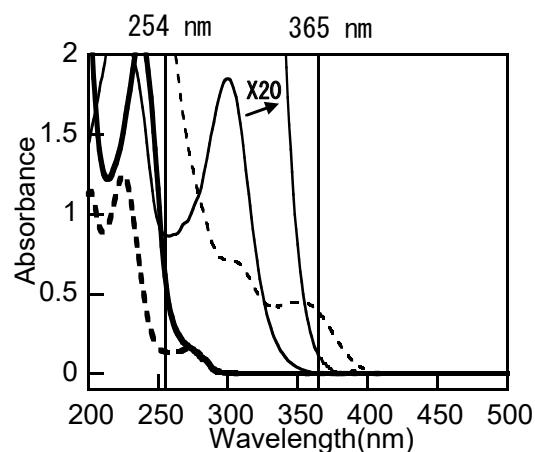


Fig. 2. UV-vis spectra of DPPTPSHFP (solid line), tBuTHITf (broken line), BAOBE (bold line), and PTBMS (bold and dotted line) in acetonitrile (1.0×10^{-4} M). For comparison, UV-vis spectrum of DPPTPSHFP (2.0×10^{-3} M) is also shown.

Table 1. Effect of formulation on sensitivity and mechanical property of the resist.

Base polymer	Composition (weight ratio)							Irradiation wavelength (nm)	Sensitivity (mJ/cm ²)			
	DPHA	PEMB	BPMB	DPPTPSHFP	tBuTHITf	PTBMS	BAOBE		Dissolution in alkali ^a	Solvent resistance ^b	Flexibility ^c	Hardness ^d
100	14			4			1.2	365	1400	- ^e	- ^e	- ^e
100	14			4			1.2	254	- ^e	1200	- ^e	- ^e
100	14	7		4			1.2	365	700	- ^e	- ^e	- ^e
100	14	7		4			1.2	254	- ^e	800	- ^e	- ^e
100	14	10		4			1.2	365	400	- ^e	- ^e	- ^e
100	14	10		4			1.2	254	- ^e	400	- ^e	- ^e
100	14	14		4			1.2	365	400	- ^e	- ^e	- ^e
100	14	14		4			1.2	254	- ^e	400	- ^e	- ^e
100	14			4			1.2	365	1400	- ^e	- ^e	- ^e
100	14			4			1.2	254	- ^e	200	50	- ^e
100	14	14		4			1.2	365	400	- ^e	- ^e	- ^e
100	14	14		4			1.2	254	- ^e	< 50	< 25	- ^e
100	10	10		2			1.2	365	1400	- ^e	- ^e	- ^e
100	10	10		2			1.2	254	- ^e	< 10	< 15	100
100	10	10		2			1.2	230-420 ^f	- ^e	400	2000	84000
100	10		10	2			1.2	365	1400	- ^e	- ^e	- ^e
100	10		10	2			1.2	230-420 ^f	- ^e	28000	2000	2800 ^g
100	7	14		2			1.2	365	1000	- ^e	- ^e	- ^e
100	7	14		2			1.2	254	- ^e	< 10	100	700
100	7	14			2		1.2	365	< 100	- ^e	- ^e	- ^e
100	7	14			2		1.2	254	- ^e	< 10	100	700

^a Minimum irradiation dose for 95 wt% dissolution in 2.38 wt% TMAH for 10 min.

^b Minimum irradiation dose for 95 wt% insolubilization in toluene for 10 min.

^c Maximum irradiation dose to pass cylindrical mandrel test with 5 mm diameter.

^d Minimum irradiation dose to obtain 4H pencil hardness. ^e Not measured.

^f Light source: Xenon lamp. ^g 2H.

Thus, the balance of the generation of radicals and acids is important to improve the resist performance.

3.2. Formulation

To improve the performance of the resist, optimization of the resist formulation was required. The effect of PAGs, PRGs and thiols on resist performance was investigated. Especially, role of thiol compounds against the resist performance was mainly discussed.

We summarized the effect of formulation on sensitivity and mechanical property of the resist in Table 1. In this work, the methacryl monomer DPHA having six functionalities was employed. It is known that the crosslinker having high functionalities is effective to crosslink and enhance the hardness of the resists.

The effect of formulation on sensitivity on irradiation at 365 nm was investigated. The best sensitivity was obtained using tBuTHITf as a PAG, which is due to the strong absorption at 365 nm as shown in Fig. 2. In addition of the thiol compound PEMB increase the sensitivity because PEMB acts as a dissolution promotor and PEMB increases the flexibility of the resist, which enhances the

deprotection reaction of the base polymer. Addition of the PRGs PTBMS and BAOBE did not affect the resist sensitivity, which indicates that the PRGs do not absorb 365 nm-light. Thus, thiol-ene reaction does not occur on irradiation at 365 nm.

The effect of formulation on solvent resistance, flexibility, and hardness of the crosslinked resist on irradiation at 254 nm was investigated. Solvent resistance of the crosslinked resist increased with irradiation dose for all formulations. Addition of PEMB drastically increased the solvent resistance. BAOBE was more effective than PTBMS due to larger absorption at 254 nm. When the formulation of the resist was [base polymer]/[DPHA]/[PEMB]/[DPPTPSHFP]/[BAOBE] = 100/7/14/2/1.2 by weight, the highest sensitivity (< 10 mJ/cm²) for the solvent resistance was observed among the all formulations.

Using BAOBE as a PRG, flexibility of the crosslinked resist was investigated. Crosslinked resist loses its flexibility with irradiation dose due to high crosslinking density. Flexibility is very important for printing. The flexibility was enhanced by the addition of PEMB which incorporate the flexible units in the crosslinked resist with high solvent resistance. The high

flexibility was also appeared by the pencil hardness of the crosslinked resist. Structures of PAGs did not affect the mechanical properties.

The effect of the structure of the thiols on the sensitivity and the mechanical properties of the resist were investigated using PEMB and BPMB. The formulation of the resist was fixed to [base polymer]/[DPHA]/[thiol]/[DPPTSHFP]/[BAOBE] = 100/10/10/2/1.2 by weight. On irradiation at 365 nm, the resist sensitivity using PEMB was similar with that using BPMB, which is due to no interference on the photoinduced-acid catalyzed deprotection reaction as shown in Scheme 2. On irradiation at 254 nm, the effect of the structures of the thiols was not appeared due to the high sensitivity of the thiol-ene system. Thus, a xenon lamp which emits continuous spectra between 230-420 nm was used. The resist containing PEPM showed higher performance than that of BPMB on the solvent resistance and hardness. The resist containing PEMB showed the same flexibility as that of BPMB. Thus, we conclude that the tetrafunctional thiol PEMB is better than BPMB having two functionalities.

3.3. Evaluation of screen plate

The effect of thiols on resist performance was investigated by the fabrication of screen plates on stainless steel screens. Three kinds of resist formulations were investigated. Table 2 shows the resist formulations and the sensitivity of the resist on irradiation at 365 nm for the formation of line and space pattern as shown in Fig. 3. The sensitivity was strongly affected by the content of DPHA and DPPTSHFP. Addition of PEMB in the resist formulation did not affect the sensitivity of the resist. The optical microscope images of top side and bottom side of screen plates in Fig. 3 revealed that line and space patterns with the resolution of 11.5 and 8.5 μm was clearly observed. Some defects were appeared in only the screen plate containing PEMB. The results indicate that PEMB gives negative effect on resist resolution due to some side reaction. Optimization of the formulation of the resist may circumvent the problem.

We have successfully fabricated the screen plates with 6- μm resolution as shown in Fig. 4. Durability of the screen plates was also investigated using the finest screen plates with 6- μm line and space widths. Figure 4 shows the optical microscope images of the screen plate with (a) and without ((b), (c)) PEMB before and after printing

100 sheets.

Before printing, 6- μm line and space patterns were clearly obtained for the both resists. After printing 100 sheets, the damages of the resist without PEMB pattern were clearly observed as shown in Fig 4 (c). On the other hand, no damage was observed for the screen plate without PEMB. Thus, the addition of PEMB enhances the toughness of the resist on the screen plates. The result is consistent to the observation of enhanced flexibility and hardness of the crosslinked resists in addition of PEMB.

Table 2. Resist formulation and sensitivity the resist for screen plate.

Base polymer	Composition (weight ratio)				Sensitivity (mJ/cm ²)
	DPHA	PEMB	DPPTSHFP	BAOBE	
100	33		5	1.0	2810
100	10		2	1.2	7190
100	10	10	2	1.2	8440

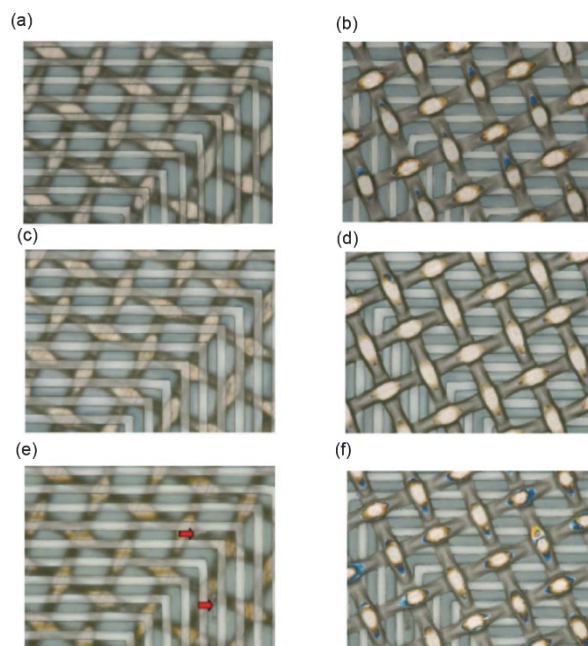


Fig. 3. Optical microscope images of top side ((a), (c), (e)) and bottom side ((b), (d), (f)) of screen plates.

L/S width: 11.5/8.5 ($\mu\text{m}/\mu\text{m}$).

Formulation: (a), (b); [base polymer]/[DPHA]/[DPPTSHFP]/[BAOBE] = 100/33/5/1 by weight.

(c), (d); [base polymer]/[DPHA]/[DPPTSHFP]/[BAOBE] = 100/10/2/1.2 by weight.

(e), (f); [base polymer]/[DPHA]/[PEMB]/[DPPTSHFP]/[BAOBE] = 100/10/10/2/1.2 by weight.

Arrows in (e) represent the positions of defects.

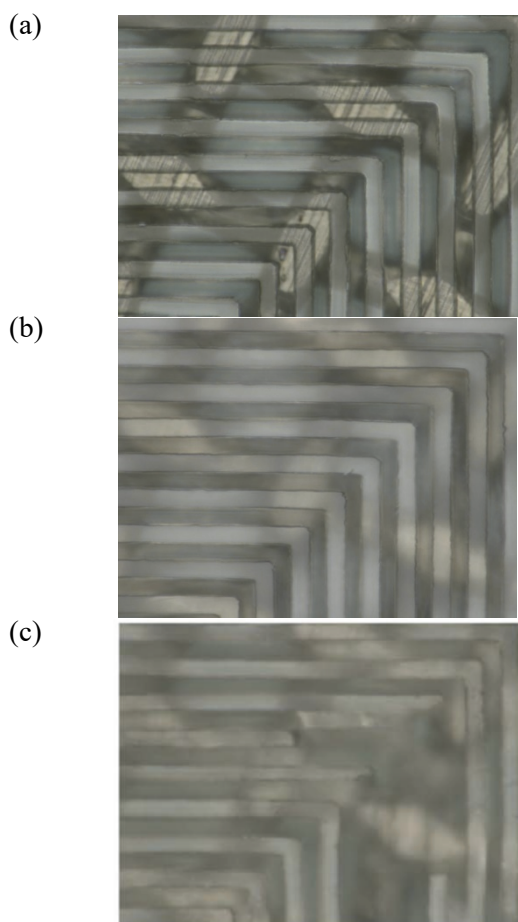


Fig. 4. Optical microscope images of screen plate before ((a), (b)) and after (c) printing 100 sheets.

L/S width: 6/6 ($\mu\text{m}/\mu\text{m}$).

Formulation: (a) [base polymer]/[DPHA]/[PEMB]/[DPPTSHFP]/[BAOBE] = 100/10/10/2/1.2 by weight.

(b), (c); [base polymer]/[DPHA]/[DPPTSHFP]/[BAOBE] = 100/10/2/1.2 by weight.

4. Conclusion

A 6- μm feature size of resist on a SUS screen plate was obtained on irradiation at 365 nm and followed by development with aqueous alkaline solution. Highest sensitivity was accomplished using tBuTHITf as a PAG. Post-exposure curing using 254 nm light with the PRG improved the mechanical characteristics of the resist patterns. BAOBE was more sensitive than PTBMS as the PRG. Resist durability was enhanced by the addition of thiols. PEMB having 4 functionalities was effective to enhance the resist durability.

Acknowledgement

This work was partly supported by a Grant-in-Aid for projects to support the advancement of strategic core technologies in contingency reserve

of fiscal 2010, from MITI, Japan.

References

1. H. Okamura, M. Kayanoki, K. Takada, H. Nakajiri, K. Muramatsu, M. Yamashita, and M. Shirai, *Polym. Adv. Technol.*, **23** (2012) 1151.
2. K. Takada, J. Hamuro, T. Matoba, M. Yamashita, M. Shirai, and H. Okamura, Japan Patent JP 2015-59160A (2015).
3. K. Takada, J. Hamuro, T. Matoba, M. Yamashita, M. Shirai, and H. Okamura, Japan Patent JP2016-172811A (2016).
4. K. Takada, *Mater. Stage*, **15** (2015) 16.
5. L. Wang, J. Pfeifer, C. Balázsi, I. M. Szilágyi, and P. I. Gouma, *Proc. SPIE*, **6769** (2007) 6769E1.
6. J. V. Crivello and E. Reichmanis, *Chem. Mater.*, **26** (2014) 533.
7. B. M. Monroe and G. C. Weed, *Chem. Rev.*, **93** (1993) 435.
8. C. E. Hoyle, T. Y. Lee, and T. Roper, *J. Polym. Sci. Part A: Polym. Chem.*, **42** (2004) 5301.
9. Q. Li, H. Zhou, and C. E. Hoyle, *Polymer*, **50** (2009) 2237.
10. C. E. Hoyle and C. N. Bowman, *Angew. Chem. Int. Ed.*, **49** (2010) 1540.
11. H. Okamura, H. Naito, and M. Shirai, *J. Photopolym. Sci. Technol.*, **21** (2008) 285.
12. M. Shirai, H. Okamura, and M. Takahashi, Japan Patent JP5126873B (2012).
13. S. I. Hong, T. Kurosaki, and M. Okawara, *J. Polym. Sci. Polym. Chem. Ed.*, **12** (1974) 2553.
14. G. N. Taylor, L. E. Stillwagon, F. M. Houlihan, T. M. Wolf, D. Y. Sogah, and W. R. Hertler, *Chem. Mater.*, **3** (1991) 1031.
15. D. L. Fields, Jr. and H. Shechter, *J. Org. Chem.*, **51** (1986) 3369.
16. J. L. Dektar and N. P. Hacker, *J. Am. Chem. Soc.*, **112** (1990) 6004.
17. M. Shirai, *J. Photopolym. Sci. Technol.*, **20** (2007) 615.
18. H. Yamamoto, T. Asakura, Y. Nishimae, A. Matsumoto, J. Tanabe, J.-L. Birbaum, P. Murer, T. Hinterman, and M. Ohwa, *J. Photopolym. Sci. Technol.*, **20** (2007) 637.
19. T. Asakura, H. Yamato, and M. Ohwa, *J. Photopolym. Sci. Technol.*, **13** (2000) 223.
20. M. Shirai and M. Tsunooka, *Prog. Polym. Sci.*, **21** (1996) 1.
21. H. Okamura, “Hikari-kagaku no jiten”, Asakura Pub. Co., Tokyo (2014) p. 190 (in Japanese).

TRANSFER OF COPYRIGHT AGREEMENT

Copyright to the article entitled

by

All Authors

Type of Paper (Mark below)

General Paper Communication Technical Paper Review

is hereby transferred to the Society of Photopolymer Science and Technology (SPST), effective if and when the article is accepted for publication in **Journal of Photopolymer Science and Technology**

However, the authors reserve the following rights:

- (1) All proprietary rights other than copyright, such as patent rights.
- (2) The right to grant or refuse permission to third parties to republish all or part of the article or translations thereof. In the case of whole articles, such third parties must obtain SPST's written permission as well. However, such permission will not be refused by SPST except at the direction of the authors. SPST may grant rights with respect to journal issues as a whole.
- (3) The right to use all or part of this article in future works of their own, such as lectures, lecture notes, press releases, reviews, textbooks, or reprint books.
- (4) In the case of a "work made for hire," the right of the employers to make copies of this article for their own use, but not for resale.

To be signed by at least one of the authors (who agrees to inform the others, if any) or, in the case of a "work made for hire", by the employer.

Signature

Name (Print)

Title, if not Author

Institution or Company

Date

The signed statement must be received by the Editorial office before the manuscript can be accepted for publication. Address requests for further information or exceptions to the Editorial Office, c/o Assoc. Prof. Haruyuki OKAMURA, Department of Applied Chemistry, Osaka Prefecture University, 1-1 Gakuen-cho, Naka-ku, Sakai, Osaka 599-8531, Japan. Phone +81-72-254-9291, Fax +81-72-254-9291, e-mail: okamura@chem.osakafu-u.ac.jp

Investigating High Opacity and Increased Activation Energy in the Multi-Trigger Resist	75
<i>C. Popescu, G. O'Callaghan, A. McClelland, J. Roth, T. Lada, T. Kudo, R. Dammel, M. Moinpour, Y. Cao and A.P.G. Robinson</i>	
EUV Photochemistry of α -Substituted Antimony Carboxylate Complexes	81
<i>Michael Murphy, Maximilian Weires, Nitinkumar S. Upadhyay, Philip Schuler, Shaheen Hasan, Greg Denbeaux and Robert L. Brainard</i>	
Non-chemically Amplified Negative Molecular Resist Materials using Polarity Change by EUV Exposure	87
<i>Kohei Fujisawa, Hiroyuki Maekawa, Hiroto Kudo, Kazumasa Okamoto and Takahiro Kozawa</i>	
Study on Irradiation Effects by Femtosecond-pulsed Extreme Ultraviolet in Resist Materials	95
<i>Yuji Hosaka, Hiroki Yamamoto, Masahiko Ishino, Thanh-Hung Dinh, Masaharu Nishikino, Akira Kon, Shigeki Owada, Yuichi Inubushi, Yuya Kubota and Yasunari Maekawa</i>	
Evolution of Secondary Electrons Emission During EUV Exposure in Photoresists	99
<i>Roberto Fallica, Stefano Nannarone, Nicola Mahne, Andrea Marco Malvezzi, Andrea Berti and Danilo De Simone</i>	
The Measurement of the Refractive Index n and k Value of the EUV Resist by EUV Reflectivity Measurement Method	105
<i>Yosuke Ohta, Atsushi Sekiguchi, Tetsuo Harada and Takeo Watanabe</i>	
Affinity Analysis of Photoacid Generator in the Thin Film of Chemical Amplification Resist by Contact Angle Measurement	111
<i>Shinji Yamakawa, Ako Yamamoto, Seiji Yasui, Takeo Watanabe and Tetsuo Harada</i>	
Polymerizable Olefins Groups in Antimony EUV Photoresists	117
<i>Michael Murphy, Nitinkumar S. Upadhyay, Munsaf Ali, James Passarelli, Jodi Grzeskowiak, Maximillian Weires and Robert L. Brainard</i>	

JOURNAL OF PHOTOPOLYMER SCIENCE AND TECHNOLOGY

Volume 34, Number 1, 2021

Experimental Evaluation and Modeling of Adsorption Phenomena of Nanoliposomes on Poly(dimethylsiloxane) Surfaces	1
<i>Sylvan Sunny Koyagura, Virendra Majarikar, Hiroaki Takehara and Takanori Ichiki</i>	
Polymer-Based Near-Infrared Afterglow Fluorescent Complex of Dye and Rare-Earth-Doped Ceramics	7
<i>Shengjie Fang, Masakazu Umezawa, Kyohei Okubo and Kohei Soga</i>	
Multifunctional Top-Coats Strategy for DSA of High- χ Block Copolymers	11
<i>Xavier Chevalier, Cindy Gomes Correia, Gwenaelle Pound-Lana, Philippe Bézard, Matthieu Sérégé, Camille Petit-Etienne, Guillaume Gay, Gilles Cunge, Benjamin Cabannes-Boué, Célia Nicolet, Christophe Navarro, Ian Cayrefourcq, Marcus Müller, Georges Hadziioannou, Ilias Iliopoulos, Guillaume Fleury and Marc Zelsmann</i>	
Resist Thickness Dependence of Latent Images in Chemically Amplified Resists Used for Electron Beam Lithography	17
<i>Takahiro Kozawa and Takao Tamura</i>	
Investigations of Matrix-Exposure Lithography Using Stacked Linear Arrays of Squared Optical Fibers	27
<i>Toshiyuki Horiuchi, Jun Watanabe, Jun-ya Iwasaki and Hiroshi Kobayashi</i>	
Research on a New Lithography Method Utilizing Laser Speckles for Printing Random Patterns	35
<i>Hiroshi Kobayashi, Iwaoka Tomoki, Kazuki Oi and Toshiyuki Horiuchi</i>	
Development of Materials Informatics Platform	41
<i>Yasumitsu Orii, Shuichi Hirose, Akihiro Fujita and Masakazu Kobayashi</i>	
Fundamental Evaluation of Resist on EUV Lithography at NewSUBARU Synchrotron Light Facility	49
<i>Takeo Watanabe, Tetsuo Harada and Shinji Yamakawa</i>	
Randomness of Polymer Microstructure in the Resist Film as Shot Noise	55
<i>Makoto Muramatsu, Arisa Hara, Satoru Shimura and Hidetami Yaegashi</i>	
Characterization of Surface Variation of Chemically Amplified Photoresist to Evaluate Extreme Ultraviolet Lithography Stochastics Effects	63
<i>Eric Liu, Amir Hegazy, Hyeonseon Choi, Maximilian Weires, Robert Brainard and Gregory Denbeaux</i>	
New Approaches to EUV Photoresists: Studies of Polyacetals and Polypeptoids to Expand the Photopolymer Toolbox	71
<i>Jingyuan Deng, Florian Kaefer, Sean Bailey, Yusuke Otsubo, Zoey Meng, Rachel Segalman and Christopher K. Ober</i>	